Conformational control of organic molecules by azobenzene-based photoswitches – a spectroscopic study

Dissertation
zur Erlangung des Doktorgrades
der Naturwissenschaften

vorgelegt beim Fachbereich 14
der Johann Wolfgang Goethe-Universität
in Frankfurt am Main

von
Sabrina Steinwand
aus Goslar

Frankfurt 2016
(D30)

vom Fachbereich 14 der
Johann Wolfgang Goethe-Universität als Dissertation angenommen.

Dekan:	Prof. Dr. Michael Karas
Gutachter:	Prof. Dr. Josef Wachtveitl
	Prof. Dr. Alexander Heckel
Datum der Disputation:	

Zusammenfassung

Conformational control of organic molecules by azobenzene-based photoswitches – a spectroscopic study

von Sabrina Steinwand

Für die Optimierung sowie Entwicklung lichtsteuerbarer Systeme für biologische Anwendungen oder neue Materialien für z.B. Energiespeicherung ist ein detailliertes Verständnis der zugrunde liegenden komplexen, lichtinduzierten Prozesse eine Voraussetzung. Die Verwendung von Photoschaltern in z.B. Makromolekülen ermöglicht eine zeitliche und örtliche Kontrolle über strukturelle Änderungen sowie die entsprechend folgenden (biologischen) Funktionen durch die Verwendung von Licht als externem Auslöser.

Ein wichtiger Bestandteil dieser Arbeit befasst sich mit der Entwicklung eines auf Licht reagierenden Riboschalters, welcher die gezielte Kontrolle über Genexpression ermöglicht. Hierzu wurde eine spektroskopische Charakterisierung von verschiedenen Photoschaltern bezüglich einer Verwendung als biologischer Ligand sowie der Wechselwirkungen zwischen Azobenzolen und RNA, auch hinsichtlich ihrer Bindungsdynamiken durchgeführt. Zunächst wurde die hohe Abhängigkeit der (photo-)chemischen Eigenschaften der Azobenzole von der Wahl der Substituenten, wie z.B. Sulfonamide oder Hydroxygruppen, untersucht, wobei besonders die Anwendung in wässrigem Milieu betrachtet wurde. In einer detaillierten (zeitaufgelösten) Studie wurde der positionsabhängige Einfluss der Hydroxy-Substitution von Azobenzolen auf die Photoisomerisierung in wässriger Lösung untersucht. Für eine *ortho*-Substitution ergab sich hierbei ein alternativer Deaktivierungskanal nach Photoanregung, welcher stärker ausgeprägt ist, als die *trans*- zu *cis*-Isomerisierung. Hierbei wird ein intramolekularer Protontransfer im angeregten Zustand (ESIPT) von der Hydroxy- zur Azogruppe beobachtet, welcher mit einer Zeitkonstante von 0.3 ps beschrieben werden kann und in einer Keto-Spezies resultiert. Diese Keto-Enol-Tautomerie konnte ebenfalls für die *para*-Hydroxy-Substitution beobachtet werden, welche hier allerdings schon im Grundzustand ermöglicht wird. Somit können beide Spezies gezielt adressiert werden. Durch Acetylierung der Hydroxygruppe verlangsamt sich die thermische Relaxation des *cis*-Isomer zu dem entsprechenden *trans*-Isomer signifikant ohne den Photoisomerisierungsmechanismus zu beeinträchtigen. Dementsprechend ermöglicht eine solche Acetylierung die Verwendung von bekannten Azobenzolderivaten, wie z.B. Sulfasalazin, als Photoschalter.

Zudem werden in dieser Arbeit zwei verschiedene Herangehensweisen in der Entwicklung eines Riboschalters beschrieben, welcher sich durch Licht regulieren lässt. Diese sind durch kovalentes bzw. nicht-kovalentes Einbringen eines Azobenzolderivats in die RNA Struktur charakterisiert. Ein neuer Linker, welcher auf einer Desoxyribose-Struktur beruht, wird für die kovalente Anbindung des Azobenzols an den RNA Strang präsentiert, welcher eine licht-induzierte Dehybridisierung eines RNA

Doppelstranges ermöglichen soll. Eine außergewöhnlich hohe Schaltamplitude mit einem *cis*-Gehalt von etwa 90% konnte für das Azobenzol im RNA Einzelstrang schon bei Raumtemperatur ermittelt werden. Zudem wurde der Einfluss des Photoschalters sowie der benachbarten Nukleotide in der RNA auf die Stabilität der RNA Doppelhelix untersucht. Die zweite Vorgehensweise beruht auf einer nicht-kovalenten Bindung zwischen einem Azobenzolderivat und einem RNA Aptamer, welche lediglich für eines der Photoisomere ermöglicht wird, wodurch eine örtliche und zeitliche Kontrolle der Ligandenbindung der RNA erfolgt. Im Rahmen dieser Arbeit war es möglich zwei verschiedene RNA Aptamere zu identifizieren und zu untersuchen, bei welchen eine Ligandenbindung lediglich für das *trans*-Azobenzol ausgebildet wird. Diese weisen eine hohe Spezifität und Affinität mit einer Dissoziationskonstanten von 3.5 μM z.B. im Fall des RNA Aptamers 42_{trunc} und des Chloramphenicol-Azobenzol-Liganden auf. Zudem wurde die Photoisomerisierung des Azobenzols innerhalb der RNA Struktur sowie daraus resultierende lichtinduzierte Konformationsänderungen der RNA mittels zeitaufgelöster Anreg-/Abtastspektroskopie untersucht. Die daraus resultierende Dynamik der photoinduzierten Ligandenbindung sollte eine weitere gezielte Optimierung lichtschaltbarer biologischer Systeme erlauben.

Der zweite Teil dieser Arbeit beschäftigt sich mit der zeitaufgelösten Untersuchung eines photoschaltbaren Foldamers. Diese Verbindungen sind z.B. für die Entwicklung neuer Materialien bezüglich der ultraschnellen Speicherung von z.B. Energie interessant. Speziell wurde der strukturelle Übergang des OmPE-Foldamers $\mathbf{10_5}$ zwischen einer definierten helikalen und einer ungefalteten Konformation auf Grund der Photoisomerisierung der, in das Rückgrat integrierten, Azobenzole untersucht. Dabei konnten die frühen (Ent-)Faltungsmechanismen des Foldamers im sub-Nanosekunden-Zeitbereich beobachtet werden, welche durch quantenmechanische Rechnungen unterstützt werden konnten. Darüberhinaus, war es möglich einen Anregungsenergietransfer vom PE-Rückgrat des Foldamers auf die Azobenzole nachzuweisen, welcher die Lebensdauer der angeregten Zustände des Systems signifikant verkürzt.

Diese Arbeit liefert wichtige Informationen zu den Reaktionspfaden, den gezielten Wechselwirkungen zwischen Photoschaltern und größeren organischen Molekülen, sowie den daraus resultierenden lichtinduzierten strukturellen Änderungen durch die Anwendung einer Vielzahl an (zeitaufgelösten) spektroskopischen Methoden. Diese Ergebnisse tragen zum weiteren Verständnis komplexer Prozesse in biologischem sowie nicht-biologischem Zusammenhang und somit zu einer weiterführenden Entwicklung neuer Systeme bei.

Abstract

Conformational control of organic molecules by azobenzene-based photoswitches – a spectroscopic study

by Sabrina Steinwand

The optimization and development of new photo-responsive systems for (biological) use and materials for e.g. energy storage requires a detailed understanding of complex processes. The use of photoswitches in e.g. macromolecules allows a spatial and temporal control of structural changes and consequently modulation of (biological) functions by using light as an external trigger.

One major part of this thesis is the development of a photo-responsive riboswitch, which allows a spatial and temporal control of gene expression. A spectroscopic characterization of photoswitches as ligands and further the interactions between the azobenzene-type ligands and RNA were investigated, especially regarding their binding dynamics. Firstly, the high dependence of the (photo-)chemical properties of the photoswitch azobenzene on the choice of substituents, like sulfonamides and hydroxy-groups, was studied with the focus on the application in aqueous solution. In a detailed (time-resolved) spectroscopic study, the position-dependent influence of the hydroxy-substitution of azobenzenes in aqueous solution on the isomerization behavior was investigated. In case of *ortho*-substitution, an alternative deactivation pathway was observed, which is even more pronounced than the *trans*-to-*cis*-isomerization. Here, an excited state intramolecular proton transfer (ESIPT) from the hydroxy-group to the azo-group was determined, which proceeds with a lifetime of 0.3 ps and results in a keto-species of azobenzene. This keto-enol-tautomerism could also be observed for the hydroxy-substitution in *para*-position, however, already in the ground state. Consequently, both species can be specifically addressed by excitation. Upon acetylation of the hydroxy-group, the thermal relaxation from the *cis*-isomer to the *trans*-isomer is decelerated significantly without affecting the photo-isomerization mechanism. Consequently, acetylation of hydroxy-groups enables the use of known azobenzene-derivatives, like Sulfasalazine, as photoswitches.

Furthermore, two different approaches for the development of a photo-responsive riboswitch are described in this work, which imply the covalent and the non-covalent incorporation of azobenzene-derivatives in the RNA structure. A new linker, which consists of a desoxyribose unit, for a covalent implementation in the RNA strand is presented, which is designed to achieve a light-induced dehybridization of RNA helices. An extraordinarily high switching amplitude of about 90% of the azobenzene within the RNA strand was obtained already at room temperature. Moreover, the influence of the azobenzene as well as of the neighboring nucleotides in the RNA on the stability of the RNA double helix was investigated. The second approach implies a non-covalent binding of azobenzene derivatives to RNA aptamers in only one of the isomeric forms of the photoswitch, which allows a spatio-temporal control of

the ligand binding of RNA. In the course of this thesis, two different RNA aptamers were obtained and studied, which bind specifically the *trans*-isomer of an azobenzene ligand. They exhibit a high specificity and affinity e.g. with a dissociation constant of 3.5 μM for the RNA aptamer 42_{trunc} and the chloramphenicol-azobenzene ligand. Moreover, the dynamics of the isomerization process within the RNA aptamer as well as the light-induced conformational changes were investigated by time-resolved pump/probe experiments. These results provide insights in the photo-induced ligand binding and allow a further distinct optimization of the corresponding biological systems.

The second part of this thesis presents the investigation of a photoswitchable foldamer. This compound is interesting for the development of new materials for applications as e.g. energy storage media. Here, the conformational changes of the O*m*PE-foldamer $\mathbf{10_5}$ from a defined helical structure into a random coil conformation upon photo-isomerization of the embedded azobenzenes were investigated. These results reveal insights in the early (un-)folding dynamics in the sub-ns time regime, which could be supported by quantum-chemical calculations. Moreover, an excitation energy transfer was observed from the PE-backbone structure to the azobenzenes, which decreases the lifetime of the excited states significantly.

This thesis provides important information on the distinct interactions between the photoswitch and larger organic molecules as well as the consequent photo-induced structural changes by using a variety of (time-resolved) spectroscopic techniques. These results help understanding the complex processes in a biological as well as in a non-biological context and should aid further development of new photo-controlled systems.

Contents

III Results

IV Concluding Remarks

Chapter 1

Introduction

One of the major goals in the research field of natural science as well as material science is the detailed understanding of complex (biological) reactions and the consequent relationship between a defined structure and the corresponding function. This knowledge is especially essential for the optimization and the development of a variety of new substances or materials for biological as well as non-biological applications as e.g. therapeutics in oncology or storage media for data or energy.

For a detailed understanding of the essential steps of the ultrafast reaction pathways, time-resolved spectroscopic methods can be used to observe processes in real time and therefore to achieve insights into the complex mechanisms. Consequently, ultrafast laser pulses are required to obtain and record the fast changes in the electronic or the molecular structure. While fast processes, like electron transfer or excited state dynamics, already occur on a time scale of femto- to picoseconds, conformational changes, especially of macromolecules can range from nanoseconds to minutes. This high diversity of differently fast reactions requires a number of experimental setups for the ultraviolet, the visible and infrared region on different time scales. Investigations in the ultraviolet and visible spectral region provide information about the electronic behavior, which give insights into reaction mechanism and pathways. In addition, structural information can be obtained by experiments in the infrared region, which deliver information about the vibrational pattern and consequently structural changes. Using the pump/probe spectroscopy technique with ultrashort laser pulses, the electronic as well as vibrational changes in the fs/ps-time scale upon photo-excitation can be observed in real time. Consequently, a combined analysis of investigations in the visible and infrared spectral region on different time scales can supply a complete set of information on subsequent reactions upon photoexcitation.

The focus of this thesis is the spatial and temporal control of conformational changes in biological and non-biological systems by the use of the photoswitch azobenzene. Implementation of azobenzenes in a larger molecule enables the transmission of conformational transitions from the photoswitch onto the macromolecule upon photoisomerization.

A major aspect is the development of a light-responsive riboswitch, which allows a spatio-temporal control on gene expression. Therefore, gene expression should

only occur for one specific photo-isomer of azobenzene, which is covalently or non-covalently incorporated in the RNA aptamer, which serves as a sensor domain for a riboswitch, while for the second photo-isomer transcription/translation is terminated. This highly cooperative project implies the development of a photoswitch with optimal (photo-)chemical properties, which binds specifically in one isomeric form and with high affinity to a RNA sequence, that is obtained by a systematic search (SELEX). Consequently, depending on the isomeric state of the photoswitch, gene expression occurs and a required substance is produced. This allows new approaches for the design of photo-responsive riboswitches in the field of oncology or wound healing.

Moreover, the distinct control over conformational changes and consequent functions is also an important aspect in the development of new materials, especially for their application regarding energy or data storage. As a model system, the photoswitchable foldamer $\mathbf{10_5}$ is studied to get insights in the photo-induced conformational changes between a helical and a random coil structure. In combination with an energy transfer along the chain of the foldamer, this would allow a photo-controlled energy transfer and consequently the development of systems, which could be used for the application for energy transport and storage.

In the first part of this thesis (part I), the theoretical framework is presented, which includes the methodology as well as the the theoretical background of the studied photoswitches.

In chapter 2, the general background of spectroscopic methods in the visible (UV/vis-absorption, circular-dichroism spectroscopy) and the IR-region (FTIR-spectroscopy) are explained (section 2.1). Moreover, different aspects of the line broadening of absorption spectra as well as relaxation processes after photo-excitation, including radiative and non-radiative deactivation processes, are discussed. Detailed insights into time-resolved pump/probe spectroscopy are given in this chapter, which also implies the generation of ultrashort laser pulses as well as non-linear optics (section 2.2). Furthermore, important aspects of quantum mechanics, like the Schrödinger equation and the Born-Oppenheimer approximation, as well as *ab initio* approaches, like the density functional theory, are briefly introduced (section 2.3).

In chapter 3 the general principles of photoswitches are shortly introduced. Moreover, the theoretical background of the photoswitch azobenzene is given, which includes the spectral properties, isomerization mechanisms and substituent effects.

In part II, used materials, like azobenzene derivatives and buffered solutions, are presented. Moreover, experimental methods, which were applied in this work, are shortly discussed. Here, the illumination procedure is explained as well as the detailed setup and alignment of the different (time-resolved) spectroscopic techniques.

In part III, the results obtained in this work are presented. A spectroscopic characterization of a variety of azobenzene derivatives for the biological use in aqueous solution is presented in chapter 5. Moreover, a detailed study on the influence of hydroxy-substitution on the isomerization behavior of azobenzenes in aqueous media is presented. These results, which rely on time-resolved studies in the visible spectral range

and which are supported by quantum-chemical calculations, allow not only insights in the complex mechanism of isomerization and keto-enol-tautomerism, but also provides guidelines for a distinct optimization of azobenzene derivatives regarding their photo-chemical properties, like for the therapeutic Sulfasalazine.

Based on these results in chapter 6 two different approaches are presented for the development of a photo-responsive aptamer. In section 6.1, the covalent incorporation of azobenzene derivatives in the RNA strand of a model oligomer via a desoxyribose linker is presented. Beside the spectroscopic characterization of the azobenzene derivative as monomer and within RNA single strands, the influence of the azobenzenes within the RNA strand on the stability of a RNA double strand is discussed. Also, the non-covalent incorporation via interactions of azobenzene derivatives in a RNA aptamer structure, which resulted from a SELEX process, is introduced in section 6.2. These azobenzene derivatives were obtained in the detailed study presented in chapter 5. Furthermore, the isomerization mechanism as well as the photo-induced conformational changes of the RNA structure were investigated by (time-resolved) studies in the visible and infrared spectral region.

As a non-biological application of azobenzene, the photo-switchable foldamer structure $\mathbf{10_5}$ was studied as a model system, especially regarding the photo-induced conformational changes between a helical and a random coil conformation (chapter 7). The early (un-)folding process was investigated by time-resolved studies in the visible and infrared region, which was supported by theoretical calculations on the vibrational structure. Moreover, clear evidence for an excitation energy transfer within the foldamer structure is presented.
In chapter 8 the results of this thesis are summarized and an outlook for further projects is presented.

Part I

Theoretical Framework

Chapter 2

Theoretical Background and Spectroscopic Methods

Optical spectroscopy is an important technique for characterization of molecular structure, properties and even dynamics, based on which predictions about photochemical reactions or the influence of structural modifications can be made.

A powerful tool is the spectroscopy in the ultraviolet and visible spectral range, the UV/vis-absorption spectroscopy, which allows investigations on the electronic structure of the molecules by regarding electronic transitions or even investigations on the secondary or tertiary structures of large biomolecules by using CD-spectroscopy in the UV/vis-range (see subsection 2.1.1). Besides the common use of UV/vis-absorption spectroscopy in the analytical chemistry for quantitative determination of substrates, the even more important application is the use for the determination of kinetics of (photo-)chemical reactions by measuring the time-dependent changes in the composition of absorbance bands of the starting material and the photo-product. Moreover, kinetics can also be monitored by investigations on the vibrational structure of a molecule using IR-spectroscopy (see subsection 2.1.2).

In contrast to UV/vis-spectroscopy, the IR-spectroscopy delivers information on the molecular structure. Consequently, by monitoring time-dependent changes of the highly characteristic vibrations, conclusions can be drawn about the molecular structure of the molecules, which are included in the chemical (photo-)reaction. Both spectroscopy techniques, UV/vis- and IR-spectroscopy, can be performed in a time-resolved manner to obtain rate constants of (photo-)chemical reactions (see section 2.2). While for slow reactions in the time range longer than seconds, an UV/vis-absorption or a FTIR-spectrometer can be used, respectively, in case of ultrafast chemical processes in the fs/ps-time range, ultrashort laser pulses are required (see subsection 2.2.1). In a pump/probe-experiment (see subsection 2.2.3), the molecule is excited by one ultrashort laser pulse with a defined wavelength in the UV/vis-spectral range, which is generated by non-linear optical processes (see subsection 2.2.2). The second laser pulse, the probe pulse, with a broad spectral range either in the UV/vis or in the IR is used to detect the absorbance differences of the electronic or the vibrational absorption bands, respectively, before and after excitation. This can be done at varying delay times between pump and probe pulse. These time-resolved experiments can deliver information on the photo-chemical and dynamical properties of the intermediate of

the photo-reaction. Due to these results, photo-chemical reactions can be investigated and a reaction mechanism can be proposed.

For the interpretation of experimental data – UV/vis- or IR-absorption spectra, rate constants and reaction mechanism – quantum mechanical approaches based on *ab initio* methods are a powerful tool to understand the dynamics on a molecular/atomistic level using a theoretical description. An exact solution of the Schrödinger-equation (see subsection 2.3.1) would describe the energy and the properties of the molecular system exactly. However, due to the many-particle problem, a variety of approximations, starting with the Born-Oppenheimer approximation (see subsection 2.3.2) are necessary. *Ab initio*-approaches, like the Hartree-Fock-approach and the density functional theory (see subsections 2.3.3 and 2.3.4), can be used as approximations for the solution of the Schrödinger-equation. In the following chapter, the theoretical background of the used spectroscopic and *ab initio* methods and setups will be presented.

2.1 Spectroscopic Background

In this section, the theoretical background of the general principle of optical spectroscopy, the absorption of a photon by a molecule, is explained. Moreover, the theory, including selection rules for a distinct transition, is discussed not only for UV/vis-absorption technique (see subsection 2.1.1), which involves CD-spectroscopy, but also for IR-spectroscopy (see subsection 2.1.2). Although the absorption of a photon with a distinct energy implies only a spectral line, the usual absorption spectrum contains absorption bands with a defined spectral width. The main reasons for the line broadening – the natural linewidth, the pressure and the Doppler broadening – are discussed in subsection 2.1.3. After absorption of a photon, a variety of processes are possible for the relaxation back into the electronic ground state and the release of the excess energy. The different radiative and non-radiative deactivation processes are shown in subsection 2.1.4.

The electromagnetic spectrum of light consists of a spectral range of more than 10^{12} meters, with wavelengths ranging from meters (radio waves) to picometers (Gamma Rays). Dependent on the range of the electromagnetic spectrum, particular spectroscopic techniques are present to analyse the molecular behavior, which occurs due to excitation by light of a defined energy referring to this spectral range.

In general, four different energies of a molecule can be distinguished: energy in translation, rotation, vibration and electronic states. The translational motion of a molecule cannot be addressed by light directly, while the motions of rotation and vibration as well as electronic states can be influenced by light. Referring to the Planck-Einstein relation (Eq. 2.1), the energy of a photon is quantized and can be characterized by e.g. the wavelength λ or the wavenumber $\tilde{\nu}$ of light

$$E = h\nu = \frac{hc}{\lambda} = hc\tilde{\nu} \tag{2.1}$$

where h is Planck's constant and c describes the speed of light.

The absorption of a photon with a defined energy E, which is resonant to the energy difference between two states ΔE_m and ΔE_n, induces a transition from an occupied to an unoccupied state. This essential relation is called *Bohr's frequency condition*.

$$\Delta E = E_n - E_m = h\nu \tag{2.2}$$

In this work, only molecular transitions in a spectral range between 200 and 700 nm (6.2 - 1.8 eV) and 1000 and 1800 cm^{-1} (0.12 - 0.22 eV) have been studied using spectroscopic techniques in the ultraviolet (UV)/visible as well as in the infrared (IR) region.

2.1.1 UV/vis-Absorption Spectroscopy

The spectral range from 200 to 400 nm (nm $= 10^{-9}$ m), referring to the middle and near ultraviolet, is covering an energy range from 6.2 to 3.1 eV. The adjacent *visible* range corresponds to a spectral range from 400 to 700 nm (3.1 to 1.8 eV). Light with an energy within these two spectral ranges coincide with the typical energy difference between electronic states. Therefore, the electronic structure of molecules or the reaction between two molecules, resulting in formation or breaking of bonds, can be analysed by UV/vis-spectroscopy.

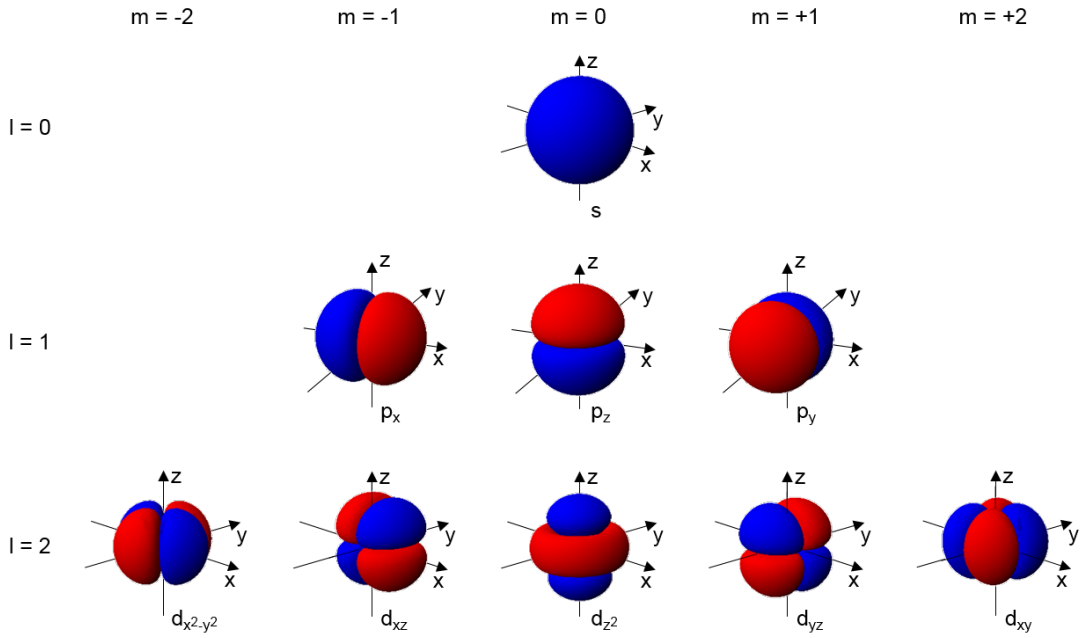

Figure 2.1: Atomic orbitals (n=3) for varying azimuthal quantum numbers $l = 0, 1, 2$ and magnetic quantum number $m = -l \ldots 0 \ldots + l$.

Electrons are located in a defined space around the nucleus, which is called *orbital*.[1,2] This orbital displays the probability density of an electron. Each atomic orbital (AO) is characterized by a specific set of three quantum number - the principal (n), the azimuthal (l) and the magnetic (m) quantum number (Fig. 2.1). These values

refer to the energy of the electron, the angular momentum and the magnetic quantum number. Every orbital contains two electrons at the maximum, which need to differ in their spin quantum number. A general assignment of atomic orbitals with an azimuthal quantum number of $l = 0, 1, 2, 3$ are the s-, p-, d- and f-orbitals, referring to sharp, principal, diffuse and fundamental, due to historical reasons.

In case of suitable symmetries and energies, a linear combination of atomic orbitals (LCAO) can result in a formation of a molecular bond and therefore, in a molecular orbital (MO). Molecular orbitals can be divided into binding (σ and π), non-binding (n) and anti-binding (σ^* and π^*) orbitals. While σ-MOs, referring to the properties of the s-orbital, have no nodal planes, π-MOs have one nodal plane etc. Excitation of an electronic transition of a molecule can have a crucial effect on the electronic structure. Thus, an electronic transition of an electron from a binding orbital into an anti-binding MO, for example, usually leads to an elongation of the molecular bond. Dependent on the state of the MOs, the energies of a transition can be found in the visible range (e.g. $n\pi^*$) to the UV (e.g. $\pi\pi^*$) and to even higher energies for e.g. $\sigma\sigma^*$-transitions.

The coincidence of the energy difference of the electronic transition with the energy of the incident photon does not necessarily result in an electronic transition. A variety of selection rules have to be obeyed.

- Conservation of multiplicity: Electronic transitions are only considered as allowed transition, if the multiplicity does not change. The multiplicity of the system describes the total number of spins by $M = 2S + 1$, where S is the total spin angular momentum. Therefore, a system with only paired electrons ($S = 0$) results in a multiplicity of 1 and is called singlet. In case of triplets ($M = 3$), the spin of one electron is inverted ($S = 1$). Consequently, an electronic transition from a singlet into a triplet state or *vice versa*, is formally forbidden.

- Laporte rule:[3] Electronic transitions, in which the parity of a centrosymmetric system is obtained, are forbidden. The parity describes the symmetry of a centrosymmetric molecule. If the orbital is symmetric with respect to the inversion center, the orbital is called even or *gerade* (*g* as an index). In cases of antisymmetric behavior it is called odd or *ungerade* (*u* as an index). An electronic transition is allowed, when the parity (*g* and *u*) changes.

However, forbidden electronic transitions can still occur to a small amount due to vibronic coupling, which describes a combination of electronic and vibrational transitions. The energy between vibrational states is significantly smaller than the energy, which is necessary for an electronic transition. Therefore, a transition from an electronic ground state into an electronically excited state usually results in a vibrationally excited state on the electronically excited state. The vibrational transition, and therefore, also the vibronic coupling, can be written in a Taylor-series expression.[4] For a forbidden transition, some intensity can be obtained from an allowed transition due to a mixing of the states.

During a transition from the ground state (*i*) into an excited state (*f*) of the molecular system, the charge density is displaced, which can be described by the transition dipole moment μ_{fi} (Eq. 2.3)

$$\mu_{fi} = \int \Psi_f^* \, \mu \, \Psi_i \, d\tau \tag{2.3}$$

where μ describes the dipole operator. Due to the Born-Oppenheimer approximation (subsection 2.3.2) and the resulting separation of the total wave function $\Psi(R, r) = \psi(r)\,\phi(R)$, the magnitude of a transition probability is determined by the overlap integral of the nuclear wave functions of the initial and the final state ϕ_i and ϕ_f, respectively. Even for fulfillment of the mentioned requirements, a negligible overlap integral could lead to a forbidden transition (Eq. 2.4).

$$\int \phi_f^* \, \phi_i \, d\tau \neq 0 \tag{2.4}$$

The squared transition dipole moment displays the probability of a transition, which is connected to the oscillator strength f by Eq. 2.5[4]

$$f = \frac{8\pi^2 \, m_e \, \nu_{fi}}{3h \, e^2} \, |\mu|^2 \tag{2.5}$$

where m_e is the mass of an electron, ν_{fi} displays the frequency of the transition and e is the elementary charge.[5] The probability of a transition and the oscillator strength are proportional to the extinction coefficient ϵ, which displays the strength of a transition on a macroscopic scale (Eq. 2.6)

$$f \sim \frac{\epsilon_{max} \, \Delta\bar{\nu}_i}{2.5 \cdot 10^8} \tag{2.6}$$

with ϵ_{max} as the extinction coefficient at the maximum of an absorbance band and $\Delta\bar{\nu}_i$ as the full-width at half maximum of the absorbance band. This wavelength-dependent extinction coefficient ϵ_λ plays an important role in Lambert-Beer's law (Eq. 2.7), which describes the absorption behavior

$$A = \epsilon_\lambda \, c \, d = -\log T = -\log \frac{I}{I_0} \tag{2.7}$$

where c is the concentration and d the thickness of the sample. The transmission T describes the ratio of the intensity of the transmitted light I and the intensity of the incident light I_0. The Lambert-Beer's law is only valid in a distinct concentration range, due to effects of e.g. aggregation, changes in the refractive index or electrostatic interactions at higher concentrations.

Circular-Dichroism Spectroscopy

A particular kind of absorbance spectroscopy in the ultraviolet (UV) and visible range is the circular-dichroism (CD) spectroscopy, which is a powerful tool for determination of conformations and structural changes of chiral molecules.[6] Important applications can especially be found for large biomolecules, like proteins or nucleic acids.

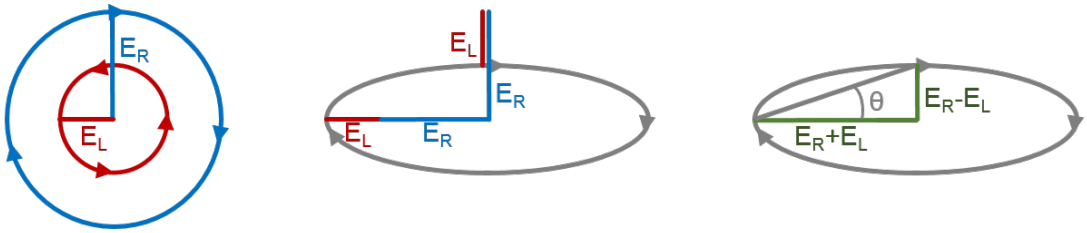

Figure 2.2: Scheme of ellipticity Θ of circular polarized light, which results from different absorbance of left-handed and right-handed circular polarized light by a substance; modified after ref. [7].

Superposition of two linearly polarized light beams with perpendicular electric field vectors and a phase shift of $\pm\pi/2$ results in a helical shape of the polarization, which is called circular polarized. The resulting left-handed circular polarized light (L-CPL) and right-handed circular polarized light (R-CPL) are mirror-images and therefore, non-superimposable. A CD-signal is observed, if the absorbance behavior of a molecule is different for L-CPL or R-CPL. This is usually true for every molecule with at least one chiral chromophore. If the absorbed amount of L-CPL is more pronounced than for R-CPL, the resulting CD-signal is positive (Eq. 2.8). However, also negative CD-signals are common for a more pronounced absorbance of R-CPL.

$$CD = \Delta A\,(\lambda) = A\,(\lambda)_{L-CPL} - A\,(\lambda)_{R-CPL} \tag{2.8}$$

In case of different absorbance of the L-CPL and the R-CPL, the emerging light behind the sample is elliptically polarized (Fig. 2.2). The angle Θ, describing the ellipticity,[8]

$$\Theta = \arctan\frac{b}{a} \tag{2.9}$$

can be rewritten, using the fact that the transmission is proportional to the squared electric field vector, resulting in Eq. 2.10.

$$\tan\Theta = \frac{b}{a} = \frac{\sqrt{T_{R-CPL}} - \sqrt{T_{L-CPL}}}{\sqrt{T_{R-CPL}} + \sqrt{T_{L-CPL}}} \tag{2.10}$$

By extension with $\sqrt{T_{R-CPL}} + \sqrt{T_{L-CPL}}$, Eq. 2.10 changes to

$$\tan\Theta = \frac{T_{R-CPL} - T_{L-CPL}}{T_{R-CPL} + 2\cdot\sqrt{T_{R-CPL}\cdot T_{L-CPL}} + T_{L-CPL}} \tag{2.11}$$

Since the difference between T_{R-CPL} and T_{L-CPL} and therefore the angle Θ is very

small, Eq. 2.11 is approximated to

$$\Theta \approx \frac{1}{4}\,\frac{\Delta T}{\bar{T}} \quad [rad] \tag{2.12}$$

Using a Taylor-series expression to first order of $\bar{T} + \Delta T$ and the Lambert-Beer's law (Eq. 2.7), the absorbance difference between L-CPL and R-CPL can be written as

$$\Delta A = A_{L-CPL} - A_{R-CPL} = \frac{1}{\ln 10}\frac{\Delta T}{\bar{T}} \tag{2.13}$$

By combining Eq. 2.12 and Eq. 2.13, the ellipticity Θ can be directly determined by the absorbance difference ΔA (Eq. 2.14).

$$\Theta \approx \frac{\ln 10}{4}\,\Delta A \approx \frac{360^\circ}{2\pi}\frac{\ln 10}{4}\,\Delta A \approx 33^\circ\,\Delta A \quad [deg] \tag{2.14}$$

2.1.2 Infrared Absorption Spectroscopy

Performing spectroscopy in the spectral region of the middle infrared (mid-IR), information about the vibrational behavior of a molecule can be obtained. Light with an energy between 0.05 and 0.5 eV (400-4000 cm^{-1}) can induce a transition between vibrational levels of a molecule. However, this interaction only leads to a transition in cases of changes in the dipole, which includes not necessarily only permanent dipoles. These vibrations are therefore called "IR-active".[9]

Vibrations can be regarded as displacements of atoms from the stable rest position. For the case of a diatomic molecule, harmonic oscillations can be described by a harmonic potential $V\,(r)$ (Eq. 2.15), which refers to Hooke's law,

$$V\,(r) = \frac{1}{2}\,k\;(r - r_0)^2 \tag{2.15}$$

where k describes the force constant, r is the distance of the two atoms included in the vibration and r_0 is the distinct equilibrated distance. The frequency ν of the harmonic oscillator is described by Eq. 2.16

$$\nu = \frac{1}{2\pi}\,\sqrt{\frac{k}{\mu}} \tag{2.16}$$

with the reduced mass $\mu = \frac{m_1 \cdot m_2}{m_1 + m_2}$. Due to quantum mechanics, only discrete energies are feasible

$$E = \left(v + \frac{1}{2}\right)\,h\nu \tag{2.17}$$

for the vibrational quantum numbers $v = 0, 1, 2, \ldots$. Regarding Eq. 2.17, the lowest energy level is located at $E_0 = \frac{1}{2}\,h\nu$, which is the zero-point energy of the system. For a harmonic oscillator, only transitions fulfilling the selection rule $\Delta v = \pm 1$ are allowed.

However, vibrations of molecules do not comply with the harmonic oscillator, since an intense displacement of one atom during a vibrations will inevitably lead to a breaking of the molecular bond. Therefore, for a realistic description of a vibration of a molecule, an anharmonic potential, or Morse-potential, is used (Eq. 2.18)

$$V(r) = D_e \left[1 - e^{\alpha (r_e - r)}\right]^2 \tag{2.18}$$

with D_e as the dissociation energy, r_e as the equilibrium bond distance and the stiffness parameter $\alpha = \sqrt{\frac{k_e}{2D_e}}$, where k_e is the force constant at the minimum of the well. The permitted energy levels are no longer equidistant (Eq. 2.19)

$$E(v) = \left(v + \frac{1}{2}\right) h\nu - \left(v + \frac{1}{2}\right)^2 x_e\, h\nu \tag{2.19}$$

with the anharmonic constant $x_e = \frac{h\nu}{4\,D_e}$, which causes a decrease of the energy difference with increasing energy. The selection rule for a transition in the anharmonic case is extended to $\Delta v = \pm 1, \pm 2, \pm 3, \ldots$.

In general, vibrations can be differentiated by the change of the molecule during the process. Vibrations, which change the distance along the atom bond, are called valence or stretching vibrations. In case of a changing shape of the molecule, a deformation vibration occurs, like an out-of-plane motion. Moreover, a vibration can further be categorized in symmetric or antisymmetric vibrations, which is depending on the general change of the symmetry of the molecule.

A molecule with *N* atoms has *3N* degrees of freedom, reflecting the coordinates *x*, *y* and *z* in space. However, a translation of the molecule can be described by three degrees of freedom, as well as the rotation of a non-linear molecule, while for a linear molecule only two rotational degrees of freedom are regarded, since a rotation around a molecular bond has no effect on the coordinates of the molecule. Therefore, $3N - 6$ vibrations can be found for a non-linear molecule ($3N - 5$ vibrations for linear molecules). These vibrations are called *normal modes*.

2.1.3 Line Broadening

Although the energies of electronic transitions are quantized, the electronic spectrum of a distinct transition does not consist of only one line, but is displayed by a Lorentzian or Gaussian profile. This can be caused by a variety of physical reasons, which will partly be explained in the following.

- Natural linewidth: The reason for the broadening of a spectral line can be found in Heisenberg's uncertainty principle,[10] which states the impossibility of determining two complementary properties of one particle exactly. In spectroscopy, especially, the two properties of energy and time play an important role (Eq. 2.20).

$$\Delta E\, \Delta t \geq \frac{\hbar}{2} \tag{2.20}$$

The excitation into an excited state is followed by a relaxation into an energetically lower state, which furthermore emits a photon. Therefore, each excited state has a finite lifetime τ. Due to the certain lifetime, the emitting photons do not possess the same exact energy, but differ around an averaged value in a Lorentzian shape (Eq. 2.21) with the natural line width of $\gamma = \Delta\omega = \frac{1}{\tau}$ or $\Delta\nu = \frac{\gamma}{2\pi} = \frac{1}{2\pi\tau}$.

$$\frac{I(\nu)}{I_0} = \frac{\frac{\gamma}{2\pi}}{(\nu - \nu_0)^2 + \left(\frac{\gamma}{2}\right)^2} \tag{2.21}$$

Consequently, independent of the conditions, this spectral line width is inevitable and therefore called *natural linewidth*.

- Pressure broadening: The pressure broadening, or also called collision broadening, is a result of collisions between molecules.[11] When the thermal motion of the particles increases, e.g. at high pressures, a higher frequency of collisions $\bar{\nu}$ and therefore, the number of collision-induced transitions from state m to state n is the result.

  A distortion of the energy levels of the molecule is the result, which broadens the Lorentzian shape due to inelastic collisions and shifts the Lorentzian curve because of elastic collisions. Due to a quenching behavior of the inelastic collisions, the lifetime of the excited state decreases, which results in a broadened spectrum, similar to the natural linewidth.

$$\frac{I(\nu)}{I_0} = \frac{c}{\pi} \frac{n\pi\bar{\nu}a^2}{(\nu - \nu_0)^2 + (n\pi\bar{\nu}a^2)^2} \tag{2.22}$$

  with n as the number of atoms per cm^3, a as the collision radius and $\bar{\nu}$ as the mean velocity of the atoms. The half-width of the pressure broadening is displayed by $2n\pi\bar{\nu}a^2$.

- Doppler broadening: The broadening of a spectral line can also be caused by the Doppler-effect,[12] which describes the dependence of a frequency ν on the movement and the velocity of a source and a receiver. Therefore, a change in frequency is detected for a movement of an absorbing atom v_{atom} towards or backwards the detector (Eq. 2.23).

$$\nu = \nu_0 \left(1 \pm \frac{v_{atom}}{c}\right) \tag{2.23}$$

  In terms of spectroscopy, a change in frequency $\Delta\nu$, the Doppler-shift, is depending on the thermal motion or the velocity of an absorbing molecule.

$$\Delta\nu = \nu_0 \frac{v_{atom}}{c} \tag{2.24}$$

Referring to the Maxwell-Boltzmann-distribution, the shape of the spectral line due to Doppler broadening can be described by Eq. 2.25

$$\phi(\nu) = \frac{1}{\Delta\nu_D \sqrt{\pi}} e^{\left(-\frac{(\nu-\nu_0)^2}{\Delta\nu_D^2}\right)} \tag{2.25}$$

where $\Delta\nu_D = {}^{\nu_0}/_{c} \cdot \left({}^{2k_B T}/_{m}\right)^{1/2}$ is describing the Doppler width. The full width at half maximum (FWHM) of the Gaussian profile is given by Eq. 2.26.

$$\Delta\nu = \frac{\nu_0}{c} \sqrt{\frac{8k_B T \ln 2}{m}} \tag{2.26}$$

Unlike the natural and collision broadening, the Doppler broadening is an inhomogeneous broadening, which affects all molecules unequally. Moreover, the Doppler broadening is linearly proportional to the frequency ν_0 and is temperature-dependent. Consequently, the FWHM increases with higher temperatures and is especially high for molecules with a small mass.

The combination of the Lorentzian functions describing the natural linewidth and the pressure broadening and the Gaussian profile resulting from the Doppler broadening is described by a Voigt profile $P(x,y)$ (Eq. 2.27), which is the convolution of a Gaussian and a Lorentzian curve.[13]

$$P(x,y) = \frac{1}{\alpha_D} \left(\frac{ln2}{\pi}\right)^{\frac{1}{2}} \frac{y}{\pi} \int_{-\infty}^{\infty} \frac{e^{-t^2}}{y^2 + (x-t)^2} dt \tag{2.27}$$

where $y = \frac{\alpha_L}{\alpha_D} (ln2)^{\frac{1}{2}}$ as the ratio of Lorentz and Gaussian widths, $x = \frac{\nu-\nu_0}{\alpha_D} (ln2)^{\frac{1}{2}}$ as the wave number scale in units of the Doppler width and α_D as the Doppler half-width (see. Eq. 2.26).

2.1.4 Relaxation Processes

With respect to the distinct selection rules, the absorption of a photon induces a transition from the ground state into an energetically higher electronic or vibronic state. Due to the change of the electronic structure after excitation of an electron, the electronic potentials are usually shifted as a function of the atomic coordinates. The Born-Oppenheimer-approximation states the acceptance of a separate consideration of the atomic and the electronic wavefunctions, on the basis of the considerably larger mass and therefore, slower velocity of the atoms with respect to the electrons. Based on this approximation, the Franck-Condon-principle, describes the negligence of the atomic movement during electronic excitation, resulting in a perpendicular excitation in the Jablonski-diagram (Fig. 2.3). Consequently, the excitation results in the Franck-Condon-region of the excited state, which usually implies higher vibrationally excited states.

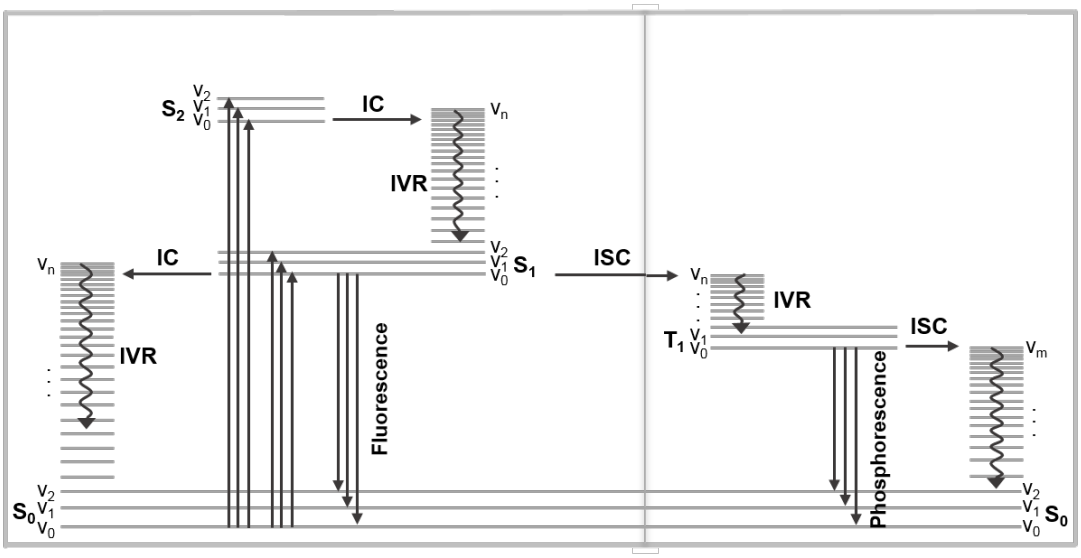

Figure 2.3: Scheme of the Jablonksi-diagram, which displays a variation of possible relaxation pathways.

The consecutive transition into the electronic ground state is coupled to energy release or distribution and can be divided into a radiative and a non-radiative deactivation process.

- Non-radiative deactivation process: In a non-radiative deactivation process, the absorbed photon energy is released without the emission of light, but only due to conversion into e.g. vibrational energy of neighboring atoms or molecules or into heat energy, which is transferred to the coupled bath modes. An additional non-radiative deactivation pathway is the performance of a photo-reaction in terms of conformational changes, like isomerization, or energy transfer or electron transfer reactions.

  After excitation into the Franck-Condon-region, an intramolecular vibrational relaxation (IVR) occurs in the energetically lower vibrational states on the excited electronic potential. During this relaxation, the excess energy, which is absorbed locally by a defined molecular orbital, is distributed intramolecularly to the neighboring atoms until the energy is equilibrated onto the whole molecular structure. After equilibration, the excess energy is released to the solvent molecules via coupled bath modes. In addition, an isoenergetic transition into vibrationally excited states of an energetically lower excited state can occur. These so-called internal conversions (IC) are often enabled due to conical intersections (CI) of two electronic potential surfaces and only possible for a sufficient overlap of the corresponding potentials. The transition of the energetically higher excited states into the first electronically excited state (S_1) is usually an ultrafast process with a lifetime of less than 10^{-12} s.

  Distribution of excess energy to coupled bath modes is also present in the electronic ground state. The energy is transferred to the solvent molecules, which

results in an increased temperature. This so-called vibrational cooling is dependent on the system and can occur on a time scale of a few tens of picoseconds.[14,15]

The excitation of the electronic transition has also an influence on the vibrational transitions, which are coupled to the electronic potential. Due to the different anharmonic potentials, the energy of the excitation of the higher vibrationally excited modes is lower and therefore red-shifted, in case of a higher anharmonic constant for the excited state. During the IVR-process, the Franck-Condon-modes are coupled to the lower vibrationally excited modes or bath modes, which results not only in a change in intensity or shape of the absorption band, but also in a shift in wavenumbers. The more pronounced the difference of the anharmonic potentials of the excited and the ground state is, the larger is the shift of the absorption band of the vibrational transitions.

Interestingly, also a singlet-triplet-transition (or *vice versa*) can occur as a deactivation pathway despite the violation of the conservation of the multiplicity. This *per se* forbidden transition, the so-called inter-system crossing (ISC), is enabled by a spin-flip of an electron. However, the required spin-flip energy needs to be available, for what reason vibrationally excited states are usually implied in these transitions. Moreover, transitions involving the necessary spin-flip of an electron occur on a longer time scale than for transitions with the same multiplicity.

However, the excited and ground states, which are included in a transition via e.g. CI, do not necessarily be assigned to the same molecule or conformation. If the overlap between the electronic potential of two molecules is significant, a photo-reaction can be observed, resulting in, for example, a photo-induced isomerization.

- Radiative deactivation process: The transition from an electronically excited state into the ground state involving the release of excess energy can also be enabled by the emission of a photon. While for singlet-singlet transitions, the fluorescence takes place on the time scale of $10^{-12} - 10^{-9}$ s, the emission of a photon from a triplet into the singlet ground state, so-called phosphorescence, has a lifetime of $10^{-9} - 10^{+2}$ s due to the spin-flip of the electron.

  Due to the fact that the internal conversion in combination with the intramolecular vibrational relaxation into the first electronically excited state occurs in only a few hundred femtoseconds, the radiative transition into the ground state only occurs from the S_1-state, which is described by Kasha's rule.[16] Moreover, also an independence of the excitation-wavelength is stated for the fluorescence and the corresponding quantum yields (Kasha-Vavilov-rule). However, exceptions are known e.g. azobenzene, for which a fluorescence from the S_2-state was observed.[17,18] This is possible e.g. for either a large energy difference between the S_2- and S_1-state, where the relaxation time is increased significantly, or for

a small oscillator strength of the $S_0 \rightarrow S_1$-transition, which however, should be large for the $S_0 \rightarrow S_2$-transition and an additional small energy difference between the S_2- and S_1-state (two-level fluorescence).[19]

The shift of the fluorescence to higher wavelength with respect to the $S_0 \rightarrow S_1$-absorption band is described by the Stokes-shift.

$$\lambda_S = \lambda_{in} - \lambda_{out} \tag{2.28}$$

After absorption of a photon, the dipole moment of the system changes and therefore, the interactions with the surrounding solvent molecules.[20] For an equilibrated system in the excited state, the electronically excited state is preferred and reduced in energy, while the energy of the electronic ground state is increased, since the new equilibrated structure is unpreferable in the ground state. The excess energy is converted into heat or vibrational energy.

2.2 Time-Resolved Pump/Probe Spectroscopy

Chemical reactions are involved in every process in nature, while the lifetime of these reactions can vary from femtoseconds to days. Investigations on the mechanism of processes require a method with a detection, which is faster than the lifetimes of the considered reaction. Fast processes with a lifetime of less than nanoseconds, like photo-induced reactions, electron transfer or early conformational changes, require a technique covering the femto- and picosecond time range for data acquisition. One common example is the pump/probe experiment,[21] which relies on ultrashort laser pulses (see section 2.2.1). The absorbance changes induced by a pump pulse can be detected by a second laser pulse, the probe pulse, at different delay time (see section 2.2.3).

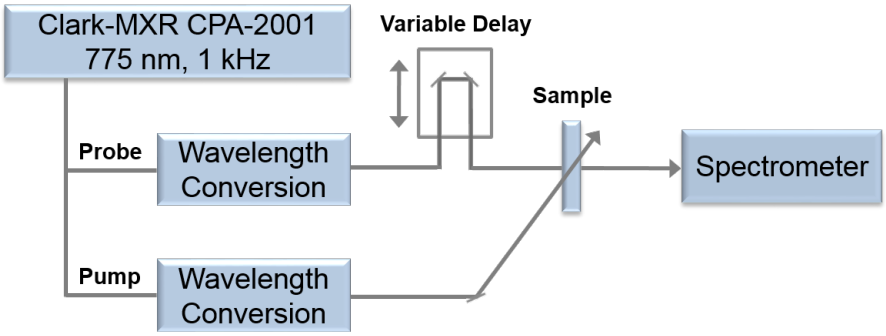

Figure 2.4: Schematic representation of a pump/probe experimental setup.

In this chapter, the generation of ultrashort laser pulses will be explained at the example of the solid-state laser Clark MXR CPA-2001. Moreover, the theoretical background of the frequency-conversion of laser pulses relying on the principles of nonlinear optics will be shortly presented. Examples for wavelength conversion will be given in form of second-harmonic generation, sum and difference frequency generation and a (non-collinear) optical parametric amplifier. The pump/probe experiment will be presented briefly for an excitation in the spectral range of the ultraviolet and visible light and a detection in the spectral range of the visible as well as of the middle infrared light.

2.2.1 Generation of Ultrashort Laser Pulses

Generation of ultrashort laser pulses[5,22] is inalienable for investigations of ultrafast dynamics of processes, like chemical reactions or conformational changes. The temporal resolution is limited to Heisenberg's uncertainty relation (Eq. 2.20). Therefore, the achievement of short laser pulses is only possible for pulses with a larger bandwidth. Consequently, ultrashort laser pulses can only be the result of laser media with a sufficient large emission bandwidth, which is often valid for solid-state lasers. The realization of ultrashort laser pulses with a high intensity can be achieved by amplification of temporally stretched pulses (CPA = Chirped Pulse Amplification[23]), like

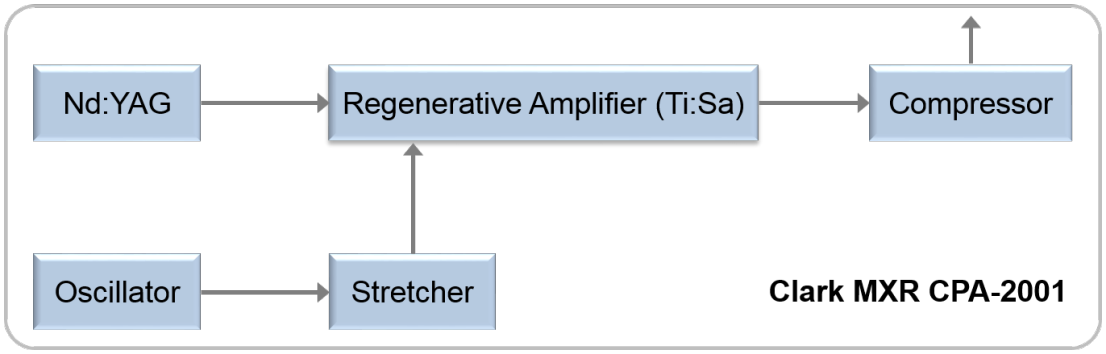

Figure 2.5: Schematic representation of the laser setup of a laser system Clark MXR CPA-2001.

in the laser system Clark MXR CPA-2001. This system is a solid-state laser with a repetition rate of 1 kHz and a power of about 800 mW at a wavelength of 775 nm.

In an Er^{+}-doped fiber oscillator, a laser pulse is generated, by using a laser diode (InGaAs) with a wavelength of 980 nm and a power of ca. 166 mW to pump the fiber oscillator. The resulting emission is located around a wavelength of 1550 nm. A passive mode-coupling of the variety of longitudinal modes of the laser enables laser pulses with a significantly high laser power. For example, an additive pulse mode-coupling can be used, which relies on intensity-dependent non-linear rotation of the polarization. Consequently, only the temporally central part of the laser pulse is amplified.

In a periodically poled Lithium Niobate (PPLN) crystal, the second harmonic frequency of the emission pulse of the oscillator is generated with a wavelength of 775 nm and a distinct repetition rate of 35 MHz.
For reasons of protection of the optical elements, this so-called *seed* pulse is temporally stretched by a factor of about $2 \cdot 10^3$. The resulting pulse exhibits a positive chirp with a pulse length of ca. 200 ps.

For excitation of the laser medium of a Ti-doped sapphire-crystal (Ti:Sa, Ti:Al_2O_3) in the regenerative amplifier, a Nd:YAG laser is used. The Nd:YAG-crystal (neodymium-doped yttrium aluminum garnet, Nd:$Y_3Al_5O_{12}$) is pumped by a flash lamp. This pulse of the Nd:YAG with a wavelength of 1064 nm is frequency-doubled in a KTP-crystal to obtain a wavelength of 532 nm. For short pulses with a high intensity, a Q-switch, here an acousto optical modulator, is used. By modulation, it generates an acoustic wave, which results in a periodic variation of the refractive index. Therefore, the light wave is diffracted and the quality of the laser decreases. If the inversion of the population is achieved, the acousto optical modulator is switched off. The laser quality is increased immediately, resulting in stimulated emission and a short pulse with an intensity of ca. 7 W and a adjustable repetition rate of 1 kHz.

By excitation of the Ti:Sa crystal with a Nd:YAG laser in the regenerative amplifier, the laser medium emits in a wavelength range of 600 to 1100 nm. In combination with the seed pulse, the emission wavelength is predetermined to a wavelength of 775 nm. Due to the excitation of the laser medium, the seed pulse is amplified by a factor of

about 10^6. However, not every pulse is amplified, due to a necessary adaptation with the Nd:YAG laser, which is obtained by a Pockels cell. Here, a current-dependent rotation of the polarization of the transmitted light with a repetition rate of 1 kHz realizes that the seed pulse can only enter the resonator in case of a complete inversion of the population of the laser medium. Then, the full amount of amplification by stimulated emission is achieved via few circulations in the resonator.
Using a compressor, the laser pulse is temporally compressed to a final pulse length of ca. 170 fs.

2.2.2 Non-Linear Optics

In linear optics, the dielectric polarization $\vec{P}$ is proportional to the electric field vector $\vec{E}$

$$\vec{P}\left(\vec{E}\right) = \epsilon_0 \cdot \chi^{(1)} \cdot \vec{E} \tag{2.29}$$

with ϵ_0 as the electric constant and $\chi^{(1)}$ as the first-order susceptibility, which is, in general, a 3x3-matrix. Due to the superposition principle, the amplitudes of two light waves coincide with the sum of the amplitudes of the two individual light waves. Therefore, no distortion or interaction of the two waves occurs.

However, in non-linear media, the dielectric polarization $\vec{P}$ responds to the electric field vector in a non-linear way.[24,25] This behavior can be written in a Taylor-series

$$\vec{P}\left(\vec{E}\right) = \epsilon_0 \left[\left(\chi^{(1)} \cdot \vec{E}\right) + \left(\left(\chi^{(2)} \cdot \vec{E}\right)\vec{E}\right) + \dots \right] \tag{2.30}$$

where $\chi^{(n)}$ describes the susceptibility of a medium as tensor of n-th order. While the frequency-mixing process usually is a second-order non-linearity, the effect of higher order non-linearities can be observed, e.g. the third-order non-linearity for a Kerr effect. Therefore, a second-order non-linearity can be described by

$$\vec{P}^{(2)}\left(\vec{E}\right) = \epsilon_0 \cdot \left(\chi^{(2)} \cdot \vec{E}\right)\vec{E} \tag{2.31}$$

With the electric field vector, composed of two components with the frequencies ω_1 and ω_2 and the propagation directions $\vec{k_1}$ and $\vec{k_2}$,

$$\vec{E} = \vec{E_1} \cdot \cos\left(\omega_1 t + \vec{k_1}\vec{z}\right) + \vec{E_2} \cdot \cos\left(\omega_2 t + \vec{k_2}\vec{z}\right) \tag{2.32}$$

Eq. 2.31 changes to Eq. 2.33

$$\begin{aligned}\vec{P}^{(2)}\left(\vec{E}\right) = \epsilon_0 \cdot \chi^{(2)} \Bigg[&\left(\vec{E_1} \cdot \cos\left(\omega_1 t + \vec{k_1}\vec{z}\right)\right)^2 + \left(\vec{E_2} \cdot \cos\left(\omega_2 t + \vec{k_2}\vec{z}\right)\right)^2 \\ &+ 2\vec{E_1}\vec{E_2} \cdot \cos\left(\omega_1 t + \vec{k_1}\vec{z}\right) \cdot \cos\left(\omega_2 t + \vec{k_2}\vec{z}\right) \Bigg]\end{aligned} \tag{2.33}$$

which can be rewritten using $\cos^2(v) = \frac{1}{2}\Big(1 + \cos(2v)\Big)$ and $\cos(x) \cdot \cos(y) = \frac{1}{2}\Big[\cos(x+y) + \cos(x-y)\Big]$, where $x = \omega_1 t + \vec{k_1}\vec{z}$ and $y = \omega_2 t + \vec{k_2}\vec{z}$:

$$\begin{aligned}\vec{P}^{(2)}\left(\vec{E}\right) = \epsilon_0 \cdot \chi^{(2)} \Bigg[& \frac{1}{2}\vec{E_1}^{\,2} + \frac{1}{2}\vec{E_2}^{\,2} + \frac{1}{2}\vec{E_1}^{\,2} \cdot \cos\left(2\omega_1 t + 2\vec{k_1}\vec{z}\right) \\ & + \frac{1}{2}\vec{E_2}^{\,2} \cdot \cos\left(2\omega_2 t + 2\vec{k_2}\vec{z}\right) \\ & + \vec{E_1}\vec{E_2} \cdot \cos\left[\left(\omega_1 + \omega_2\right) t + \left(\vec{k_1} + \vec{k_2}\right)\vec{z}\right] \\ & + \vec{E_1}\vec{E_2} \cdot \cos\left[\left(\omega_1 - \omega_2\right) t + \left(\vec{k_1} - \vec{k_2}\right)\vec{z}\right]\Bigg]\end{aligned} \tag{2.34}$$

Therefore, the second-order non-linearity can be described by Eq. 2.34, which contains a frequency-independent component, as well as components, which include either only one frequency or a combination of two frequencies.

The electric field vectors are oriented in a three-dimensional space, which is why the dielectric polarization is dependent on the orientations of the electric field vectors in a coordinate system.

$$\vec{P_i} = \epsilon_0 \left[\sum_{k=1}^{3} \chi_{ik}^{(1)} \vec{E_k} + \sum_j \sum_k \chi_{ijk}^{(2)} \vec{E_j}\vec{E_k} + \ldots\right] \tag{2.35}$$

For the first-order term, the dielectric polarization $\vec{P}^{(1)}$ can be described by Eq. 2.36 for the directions x, y and z.

$$\begin{pmatrix} P_x^{(1)} \\ P_y^{(1)} \\ P_z^{(1)} \end{pmatrix} = \epsilon_0 \begin{pmatrix} \chi_{xx}^{(1)} & \chi_{xy}^{(1)} & \chi_{xz}^{(1)} \\ \chi_{yx}^{(1)} & \chi_{yy}^{(1)} & \chi_{yz}^{(1)} \\ \chi_{zx}^{(1)} & \chi_{zy}^{(1)} & \chi_{zz}^{(1)} \end{pmatrix} \cdot \begin{pmatrix} E_x \\ E_y \\ E_z \end{pmatrix} \tag{2.36}$$

By transformation of the main axis, the matrix of the susceptibility is diagonalized.

$$\begin{pmatrix} P_x^{(1)} \\ P_y^{(1)} \\ P_z^{(1)} \end{pmatrix} = \epsilon_0 \begin{pmatrix} \chi_1^{(1)} & 0 & 0 \\ 0 & \chi_2^{(1)} & 0 \\ 0 & 0 & \chi_3^{(1)} \end{pmatrix} \cdot \begin{pmatrix} E_x \\ E_y \\ E_z \end{pmatrix} \tag{2.37}$$

With $\epsilon_i = 1 + \chi_i$ and $\epsilon = n^2$, an index ellipsoid results with radius vectors with a length of $n = \sqrt{\epsilon}$ in the coordinates of the three refractive indices n_i:

$$\frac{1}{\epsilon_\nu}\left(\frac{n_x^2}{\epsilon_1} + \frac{n_y^2}{\epsilon_2} + \frac{n_z^2}{\epsilon_3}\right) = 1 \tag{2.38}$$

For uniaxial crystals, the symmetry axis, also called optical axis, is located in direction of z. Therefore, the two resulting dielectric constants are equal ($\epsilon_1 = \epsilon_2$).

The resulting ellipsoid has a rotational symmetry. For light waves with a propagation direction *k* through the center of the system of coordinates, the plane perpendicular to the propagation direction *k* intersects the rotational ellipsoid again in a geometry of an ellipsoid. This new ellipsoid can be described by the main axes $n_o = n_3$ and $n_e = n_1 = n_2$, where *o* describes the ordinary beam and *e* is the extraordinary beam in a birefringent crystal. While the refractive index n_o is the same for each propagation direction, n_e is highly dependent on direction and therefore, the electromagnetic wave $\left(\vec{E} = \vec{E_0}\cos\left(\omega t + \vec{k}\vec{r}\right)\right)$. The angle-dependent refractive index can be described by

$$\frac{1}{n^2(\Theta)} = \frac{\cos^2\Theta}{n_o^2} + \frac{\sin^2\Theta}{n_e^2} \tag{2.39}$$

The second-order non-linear dielectric polarization $\vec{P}^{(2)}$ for the sum/difference frequency generation (SFG/DFG) is significantly more complicated, especially, when $\omega_1 \neq \omega_2$.

$$\begin{pmatrix} P_x^{(2)}(\omega_1 \pm \omega_2) \\ P_y^{(2)}(\omega_1 \pm \omega_2) \\ P_z^{(2)}(\omega_1 \pm \omega_2) \end{pmatrix} = \epsilon_0 \begin{pmatrix} \chi_{xxx}^{(2)} & \chi_{xxy}^{(2)} & \cdots & \chi_{xzz}^{(2)} \\ \chi_{yxx}^{(2)} & \chi_{yxy}^{(2)} & \cdots & \chi_{yzz}^{(2)} \\ \chi_{zxx}^{(2)} & \chi_{zxy}^{(2)} & \cdots & \chi_{zzz}^{(2)} \end{pmatrix} \cdot \begin{pmatrix} E_x(\omega_1) & \cdot & E_x(\omega_2) \\ E_x(\omega_1) & \cdot & E_y(\omega_2) \\ E_x(\omega_1) & \cdot & E_z(\omega_2) \\ E_y(\omega_1) & \cdot & E_x(\omega_2) \\ & \vdots & \\ E_z(\omega_1) & \cdot & E_z(\omega_2) \end{pmatrix} \tag{2.40}$$

Phase-Matching Condition

The electric field vectors are dependent on the propagation vectors and therefore, on the orientation in a three-dimensional space. For a second-order non-linearity, the sum of two waves with the frequencies ω_1 and ω_2 results in $\omega_3 = \omega_1 + \omega_2$. Therefore, to obtain a wave with the frequency ω_3 with a high intensity, the phase matching condition Eq. 2.41 pursues to $\Delta\vec{k} = 0$. Therefore, a constant phase is required for the generated and the propagating waves.

$$\Delta\vec{k} = \vec{k}(\omega_1 \pm \omega_2) - \left(\vec{k}(\omega_1) \pm \vec{k}(\omega_2)\right) \tag{2.41}$$

Due to the phase velocity, which is defined by Eq. 2.42 and consequently depends on the frequency, however, the generated wave with the frequency ω_3 travels with a different velocity than the generating waves ω_1 and ω_2 through the non-linear crystal. This leads to destructive interference, which are more pronounced for an increasing thickness of the crystal. This phase mismatch ($\Delta\vec{k}$) results in a less efficient frequency mixing process.

$$v = \frac{\omega}{\vec{k}} = \frac{c_0}{n(\omega)} \tag{2.42}$$

Table 2.1: Required polarizations of the three laser pulses participating in a frequency-mixing process of type I and type II for a negative ($n_e < n_o$) and a positive ($n_e > n_o$) uniaxial crystal.

	Type I			Type II		
	ω_1	ω_2	ω_3	ω_1	ω_2	ω_3
negative uniaxial crystal ($n_e < n_o$)	o	o	e	o	e	e
positive uniaxial crystal ($n_e > n_o$)	e	e	o	e	o	e

With increasing angle between the three vectors, the efficiency decreases, due to the smaller overlap of the volume. Therefore, the maximal efficiency can be obtained for collinear propagation. In this case, the phase-matching condition (Eq. 2.41) changes to

$$n_3\left(\omega_3\right)\omega_3 = n_1\left(\omega_1\right)\omega_1 \pm n_2\left(\omega_2\right)\omega_2 \tag{2.43}$$

One way of obtaining this phase-matching condition is the so-called angle tuning. Non-linear crystals are cut with an appropriate orientation. By rotation of the crystal, the angle between the optical angle and propagation direction is changed, and can therefore, fulfill the condition.

Uniaxial crystals, which are the most common crystals for frequency conversion processes, consist of one main axis, which is called the extraordinary (*e*) axis, while the remaining two axes are ordinary (*o*). The properties of the non-linear crystals need to match the properties, like the polarization, of the three included waves. There are two major classes of suitable polarizations; the polarizations of the incident waves are parallel (type I) or perpendicular (type II) to each other (see Tab. 2.1).

The phase matching angles in a negative uniaxial crystal can be calculated by using Eq. 2.44 for a type I frequency generation

$$tan^2\Theta_{pm}^{ooe} = \frac{1 - \frac{\left(\frac{n_{o1}}{\lambda_1} + \frac{n_{o2}}{\lambda_2}\right)^2}{\left(\frac{n_{o3}}{\lambda_3}\right)^2}}{\frac{\left(\frac{n_{o1}}{\lambda_1} + \frac{n_{o2}}{\lambda_2}\right)^2}{\left(\frac{n_{e3}}{\lambda_3}\right)^2} - 1} \tag{2.44}$$

and Eq. 2.45 for a type II generation.[26]

$$tan^2\Theta_{pm}^{oee} = \frac{1 - \frac{\left(\frac{n_{o1}}{\lambda_1} + \frac{n_{o2}}{\lambda_2}\right)^2}{\left(\frac{n_{o3}}{\lambda_3}\right)^2}}{\frac{\left(\frac{n_{o1}}{\lambda_1} + \frac{n_{o2}}{\lambda_2}\right)^2}{\left(\frac{n_{e3}}{\lambda_3}\right)^2} - \frac{\left(\frac{n_{o1}}{\lambda_1} + \frac{n_{o2}}{\lambda_2}\right)^2}{\left(\frac{n_{o1}}{\lambda_1} + \frac{n_{e2}}{\lambda_2}\right)^2}} \tag{2.45}$$

By using the Sellmeier equation (Eq. 2.46) and the empirical coefficients (Tab. 2.2), the wavelength-dependent refractive indices can be obtained.

$$n = \sqrt{A + \frac{B}{\lambda^2 - C} - D \cdot \lambda^2} \tag{2.46}$$

Table 2.2: Sellmeier coefficients for a negative uniaxial crystal (BBO, beta-barium borate) for Eq. 2.46 with wavelength in μm.[27]

	ordinary (o)	extraordinary (e)
A	2.7405	2.3730
B	0.0184	0.0128
C	0.0179	0.0156
D	0.0155	0.0044

Group Velocity and Group Velocity Dispersion

Regarding the frequency conversion in a non-linear crystal, the interacting waves do not only need to fulfill the phase-matching conditions, but also the group velocity needs to be taken into account for a frequency conversion with a high intensity. The group velocity of a wave refers to the velocity of the wave package, which travels through a medium, and is described by the first derivative of the wave vector

$$v_g = \frac{\partial \omega}{\partial \vec{k}} \tag{2.47}$$

with ω as the angular frequency and $\vec{k}$ as the wave vector.

Since the signal implies different frequencies, the signal travels with different group velocities, depending on the frequency. Therefore, the components of the laser pulse disperse over time. The group velocity dispersion (GVD) describes the frequency-dependent delay of the different spectral components of a laser pulse and is defined as the first derivative of the inverse group velocity v_g (Eq. 2.48).

$$GVD\left(\omega_0\right) = \frac{\partial}{\partial \omega}\left(\frac{1}{v_g\left(\omega\right)}\right) = \frac{\partial}{\partial \omega}\left(\frac{\partial \vec{k}}{\partial \omega}\right) = \frac{\partial^2 \vec{k}}{\partial \omega^2} \tag{2.48}$$

In a normally dispersive medium, the components with the higher frequencies travel slower than the components with the lower frequencies, which results in a positively chirped pulse.

Frequency Mixing Processes

The commonly used laser systems provide a laser pulse with a distinct wavelength, which are not spectrally variable in their laser output. This is also true for the used Clark MXR CPA-2001, which has a wavelength of 775 nm. In the most experimental approaches, like in pump/probe spectroscopy, however, a variety of different wavelengths is inalienable. Therefore, wavelengths are generated from the fundamental laser pulse in different non-linear processes. The non-linear optical processes within a non-linear crystal as well as the conditions for an interaction of two laser pulses in a non-linear crystal have already been discussed in section 2.2.2.

In general, frequency mixing process in an uniaxial crystal can be performed in two different ways. While in the first case, the polarizations of the two laser pulses with the lower frequencies are parallel (type I) to each other, in the second way, these polarizations are perpendicular (type II).
A third-order non-linear process is used to generate a spectrally broad pulse from one pulse with a distinct wavelength to achieve different wavelength from the laser output. However, since $\chi^{(3)}$-processes do not deliver high intensities, the supercontinuum generation is not applicable for the generation of pump pulses. Consequently, the broadband pulses are combined with a frequency mixing process in a tunable (non-collinear) optical parametric amplifier to achieve intense pulses with a variable wavelength.

Supercontinuum Generation: The generation of white-light, or a supercontinuum, with a laser pulse with a narrow bandwidth in a medium is a very complex process. The high intensity of the ultrashort laser pulse induces a change in the refractive index of the isotropic medium ($\chi^{(2)} = 0$), which relies on the Kerr-effect (Eq. 2.51) as a third-order non-linear process.[28]

$$\begin{aligned}\vec{P}\left[\vec{E}(\omega)\right] &= \vec{P}^{(1)}\left[\vec{E}(\omega)\right] + \vec{P}^{(3)}\left[\vec{E}(\omega)\right] \\ &= \epsilon_0\left[\chi^{(1)}\cdot\vec{E}(\omega) + \chi^{(3)}\cdot\vec{E}(\omega)\cdot\vec{E}(\omega)\cdot\vec{E}(\omega)\right] \\ &= \epsilon_0\Big[\underbrace{\left(\chi^{(1)} + \chi^{(3)}\cdot\left|\vec{E}(\omega)\right|^2\right)}_{\chi_{eff}}\cdot\vec{E}(\omega)\Big]\end{aligned} \tag{2.49}$$

This resulting effective susceptibility χ_{eff} can be rewritten as an expression for the refractive index

$$n = \sqrt{1 + \chi^{(1)} + \chi^{(3)}\cdot\left|\vec{E}(\omega)\right|^2} \tag{2.50}$$

since the relative permittivity is described as $\epsilon_r = \frac{\epsilon}{\epsilon_0} = 1 + \chi^{(1)} + \chi^{(3)} \cdot \left|\vec{E}(\omega)\right|^2$ and due to the relation $n = \sqrt{\epsilon}$. After several steps with $n_0^2 = 1 + \chi^{(1)}$ and $I = \frac{1}{2}\epsilon_0 c n_0 \left|\vec{E}(\omega)\right|^2$, an expression for the refractive index results, which implies an intensity-dependent refractive index n_2 in addition to the linear refractive index n_0

$$n(t) = n_0 + n_2 I(t) \tag{2.51}$$

with $I(t)$ as the time-dependent intensity of the laser pulse, n_0 and n_2 as the refractive indices of zeroth and second order, respectively and $n(t)$ describes the intensity- and therefore also time-dependent refractive index. This change in the refractive index has not only an effect on the phase of the pulse, which is why it is called self-phase modulation (SPM), but also on the frequency. While the front part of the laser pulse shows a shift to lower frequencies with respect to the original frequency, the opposite site is shifted to higher frequencies. These additional frequencies lead to a broadening of the spectrum around the original frequency of the laser pulse. Also, the self-steepening as a consequence of the intensity-dependence of the GVD, can change the shape of a pulse. Moreover, an important aspect is the self-focusing (SF) due to the intensity-dependent refractive index, which acts as a positive lense. The self-trapping effect acts as an opposite force to the SF and defocuses and therefore prevents the beam from collapsing. The reason for the effect of self-trapping is the generation of free electrons via multi-photon excitation (MPE) in the non-linear medium, which results in a negative change of the refractive index (Eq. 2.52). In an equilibrated system, a constant beam diameter is the result

$$\Delta n_e = -\frac{2\pi e^2 N_e}{n_0 m_e \omega^2} \tag{2.52}$$

with N_e as the free-electron density and ω as the frequency of the laser and Δn_e as the change of the refractive index due to the self-trapping effect.

Sum-Frequency Generation: The interaction of two photons in a non-linear crystal with $\omega = \omega_1 = \omega_2$ leads to a resulting photon, which is the second harmonic of the incident photons and obtains a frequency of 2ω. Therefore, this process is called second-harmonic generation (SHG). Here, the two photons can be provided by either two light waves or even only one light wave. Resulting from Eq. 2.41, the phase-matching condition for this non-linear process can be described by

$$\vec{k}(2\omega) = 2\vec{k}(\omega) \tag{2.53}$$

with $\vec{k}$ as the wave vector. This condition is fulfilled only for a distinct wavelength and angle Θ between the propagation direction and the optical angle when

$$n_e(2\omega) = n_o(\omega) \tag{2.54}$$

with n_o and n_e as the refractive indices of the ordinary and the extraordinary beam (Fig. 2.6).

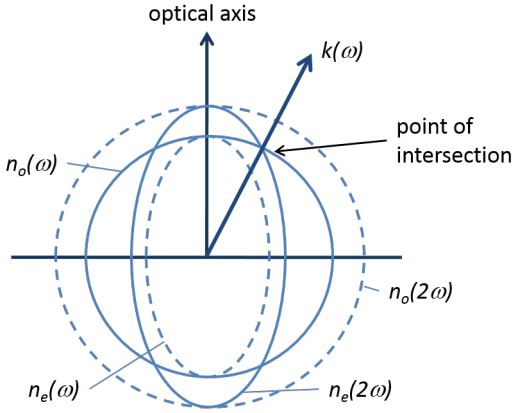

Figure 2.6: Schematic representation of the phase-matching condition for a sum-frequency generation.

However, the two incident photons can also differ in their frequency ω. Consequently, this process is then called sum-frequency generation (SFG). Here, the sum-frequency ω_s, is a combination of two photons with a different frequency $\omega_1 \neq \omega_2$.

$$\omega_s = \omega_1 + \omega_2 \tag{2.55}$$

$$\frac{c}{\lambda_s} = \frac{c}{\lambda_1} + \frac{c}{\lambda_2} \tag{2.56}$$

A non-linear interaction of two photons with a different frequency is also possible by subtracting corresponding frequencies. This difference-frequency generation (DFG) is highly important for the generation of laser pulses with a spectral range in the infrared region.

$$\omega_d = \omega_1 - \omega_2 \qquad \text{with} \qquad \omega_1 > \omega_2 \tag{2.57}$$

Optical Parametric Amplifier: For a flexible generation of wavelengths, an optical parametric amplifier (OPA) is a very common technique.[29] Here, an intense pump pulse is lead into a non-linear crystal. Referring to Eq. 2.56, the frequency of the pump pulse ω_p can be split in an infinite number of combinations of two smaller frequencies. This variety of possible frequencies can be seen as the parametric fluorescence or superfluorescence behind the non-linear crystal. By using a supercontinuum, a distinct frequency is chosen as a seed pulse to overlap spatially and temporally with the pump pulse. Like that, the high number of possibilities of frequencies decreases to only possibility. The pump pulse with the frequency ω_p is split into two pulses with lower frequencies, which travel collinearly; the signal with a frequency ω_s, which correspond to an amplified seed pulse, and the idler with the lower frequency ω_i.

$$\omega_p = \omega_s + \omega_i \tag{2.58}$$

However, a simultaneous matching of the three different group velocities of the three laser pulses cannot be assured, resulting in a propagation with differing speed. Therefore, the resulting signal and idler pulses often show a pulse length of hundreds of femtoseconds. To guarantee shorter laser pulses, a variation of the optical parametric amplifier can be used, in which the pump and the seed pulse do not travel collinearly anymore. In cases of a non-collinear optical parametric amplifier (NOPA),[30] the pump pulse enters the non-linear crystal in a certain angle. Still a signal and an idler pulse are generated due to the spatial and temporal overlap of the pump pulse with a distinct wavelength of the seed pulse. However, due to the angle of the incident pulse, the signal and the idler pulse do not travel collinearly anymore, but with a distinct angle in between. In approaches using a NOPA, only one of the resulting pulses, usually the signal pulse, is used. By angle torsion of the non-linear crystal and temporal correction of the chirped white-light, a wide spectral range from ca. 450 to 1200 nm can obtained.

2.2.3 The Pump/Probe Experiment

Investigations on fast molecular dynamics require an experimental setup with an even faster data acquisition. One common spectroscopic technique is the pump/probe experiment. This method relies on intense ultrashort laser pulses, which are generated by a solid-state laser system e.g. Clark MXR CPA-2001 (see section 2.2.1). The laser beam with a wavelength of 775 nm, a repetition rate of 1 kHz and a power of ca. 800 mW is separated into two laser beams; the pump pulse and the probe pulse. The pump pulse excites the studied sample at a distinct wavelength of an absorbance band, while the probe pulse detects the absorbance changes upon photo-excitation. Therefore, absorbance differences between the excited and the non-excited sample are measured. Technically, this is achieved by exciting the sample only with every second pump pulse. A chopper, rotating with a frequency of 500 Hz, which is half of the repetition rate of the laser system, is blocking every second pump pulse, which enables a measurement of the non-excited sample. The probe pulse is temporally delayed with respect to the pump pulse for measurements of the temporal evolution of the absorbance changes. The temporal delay is generated by an additional optical path length via a variable delay stage.

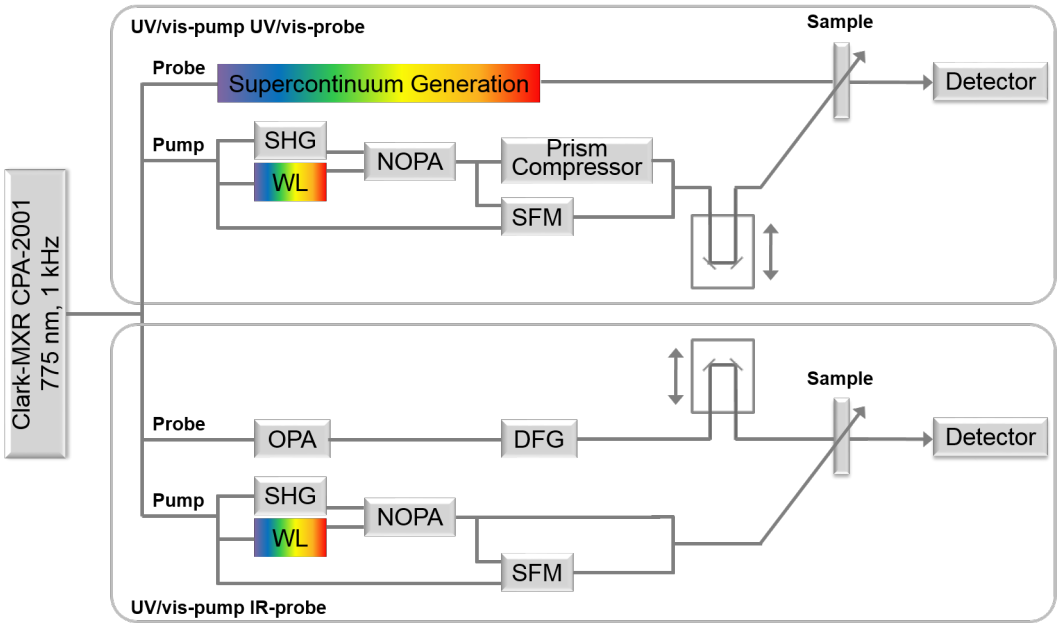

Figure 2.7: Schematic representation of an UV/vis-pump UV/vis-probe and an UV/vis-pump IR-probe setup.

The pump pulse is used to excite the investigated sample. Therefore, an intense and spectrally and temporally narrow pump pulse is inalienable. The wavelength of the pump pulse is obliged to be tunable in a spectral range between 280 and 800 nm for a distinct excitation of one electronic transition of the component. A common technique to obtain pulses with a wavelength between ca. 450 and 1200 nm, is the non-collinear parametric amplifier (NOPA) (see subsection 2.2.2). For that the fundamental laser pulse is separated into the pump and the seed pulse for the NOPA process. For

the seed pulse, a supercontinuum is generated in a sapphire crystal (WL = white-light), then leading into a BBO-crystal ($\theta = 28.5°$). The pump pulse is generated by a second-harmonic generation (SHG) in a BBO-crystal ($\theta = 30.2°$), resulting in a wavelength of 387.5 nm. With an angle between the pump and the seed pulse of about 5°, both pulses overlap spatially in the crystal. In dependence on the resulting wavelength, the seed pulse is temporally delayed to achieve a temporal overlap with the pump pulse and the component of the white-light with the desired wavelength to be amplified.

For an excitation of the studied sample in a spectral range between 280 and 450 nm, a subsequent sum-frequency mixing (SFM) with the NOPA pulse and a part of the fundamental pulse is performed (type I). For a significant overlap of both pulses in the BBO-crystal ($26° \leq \theta \leq 43°$; dependent on the resulting wavelength), a small angle between the two pulses is worthwhile. The correct wavelength is obtained by angle tuning and a temporal delay of the fundamental pulse.
For a short laser pulse with a pulse length of less than 100 fs, a prism compressor can be used for correction of the chirp of the pulse after the frequency conversion. However, a prism compressor for pulses with a wavelength in the ultraviolet range is not trivial.

For detection of the absorbance changes in the visible region upon photo-excitation, a supercontinuum is generated either in a sapphire (Al_2O_3) crystal or in a calcium fluoride (CaF_2) window. The advantage of a sapphire crystal is that it is more stable than a calcium fluoride window regarding damages by the laser pulse, which is why the CaF_2-window must be moved in the *x*,*y*-plane constantly. This is also the reason for a more stable white-light by the usage of a sapphire. However, the spectral range of a white-light produced by a sapphire crystal is limited to about 450 to 1200 nm, while with a CaF_2-window, wavelengths down to 340 nm can be obtained. For the non-trivial generation of a probe pulse in the ultraviolet range, LiF-windows[31] or a supercontinuum generation by using the second harmonic of the fundamental wavelength can be used.

A probe pulse for the detection of absorbance changes in the infrared region can be generated by using a two-step OPA with a subsequent DFG process. Here, a pump pulse with a wavelength of 775 nm collinearly interacts with a seed pulse in a BBO-crystal ($\theta = 27°$, $\phi = 30°$), which corresponds to wavelengths greater than 680 nm of a white-light pulse. In a frequency conversion (type II), a signal and an idler pulse are generated. The signal pulse can be varied in a spectral range between 1.2 and 1.45 μm and is amplified in a second OPA step as a seed pulse, which is pumped by a second part of the fundamental pulse. The resulting intense signal and idler pulses travel collinearly into a silver thiogallate ($AgGaS_2$) crystal ($\theta = 40°$, $\phi = 45°$), where a difference-frequency generation is performed (type I), resulting in a probe pulse in the mid-IR between 3 and 10 μm.
For the detection of the IR-pulses, a spectrometer and a nitrogen-cooled mercury cadmium telluride (MCT) detector are used.

Data Acquisition

The absorbance of the sample is defined by the Lambert-Beer's Law (Eq. 2.7) as the negative decadic logarithm of the ratio of the transmitted intensity and the incident intensity of light. Therefore, the absorbance of the non-excited ($A(\tilde{\nu})$) and the excited ($A^*(\tilde{\nu}, t)$) sample can be described by Eq. 2.59 and 2.60, respectively.[21]

$$A(\tilde{\nu}) = -\log_{10}\left(\frac{I(\tilde{\nu})}{I_0(\tilde{\nu})}\right) \tag{2.59}$$

$$A^*(\tilde{\nu}, t) = -\log_{10}\left(\frac{I^*(\tilde{\nu}, t)}{I_0^*(\tilde{\nu}, t)}\right) \tag{2.60}$$

In a pump/probe experiment, however, only the absorbance differences between the excited and the non-excited sample are detected. Therefore, the absorbance differences can be written as Eq. 2.61. While the intensity of the non-excited case can be detected by blocking the pump pulse, the intensities of the incident pulse can be detected by using an alternative optical path leading past the sample position.

$$\begin{aligned}\Delta A(\tilde{\nu}, t) &= A^*(\tilde{\nu}, t) - A(\tilde{\nu}) \\ &= -\log_{10}\left(\frac{I^*(\tilde{\nu}, t)}{I_0^*(\tilde{\nu}, t)}\right) + \log_{10}\left(\frac{I(\tilde{\nu})}{I_0(\tilde{\nu})}\right) \\ &= -\log_{10}\left(\frac{I^*(\tilde{\nu}, t) \cdot I_0(\tilde{\nu})}{I_0^*(\tilde{\nu}, t) \cdot I(\tilde{\nu})}\right)\end{aligned} \tag{2.61}$$

Although, no differences of the intensities of the incident pulses for the excited and the non-excited case should be expected ($I_0^*(\tilde{\nu}, t) = I_0(\tilde{\nu})$), which simplifies Eq. 2.61 to

$$\Delta A(\tilde{\nu}, t) = -\log_{10}\left(\frac{I^*(\tilde{\nu}, t)}{I(\tilde{\nu})}\right) \tag{2.62}$$

due to e.g. variations in the shot-to-shot stability of the laser, this approximation cannot be applied at any time.

The high amount of measured data is analyzed by a global lifetime analysis (GLA) technique.[32]

Coherent Artifacts

In a pump/probe experiment, several artifacts can be observed around the delay time of 0 ps, at which the pump and the probe pulse overlap temporally at the sample position.[33]

- Coherent artifact: A coherent artifact can be observed around the temporal zero point due to three major aspects – the cross phase modulation (XPM), impulsive-stimulated Raman-scattering (ISRS) and Raman contributions.[34] In cases of simultaneous and aligned propagation of two laser pulses, the phases can be affected by each other. Relying on the optical Kerr-effect, which describes the change of the refractive index in a medium, which is usually the solvent of the sample, due to the high intensity of the laser pulse (Eq. 2.51). The coherent artifact contains no information about the sample and can therefore, be corrected by the coherent artifact resulting from measurement of the solvent without sample. However, due to absorbance of the sample, the intensity of the artifacts of the two measurements can differ significantly.

- Perturbed free induction decay (PFID): For delay times before the temporal zero point, the probe pulse arrives earlier at the sample position than the pump pulse. The probe pulse can induce a polarization in the sample, which decays with a lifetime T_2

$$T_2 = \frac{1}{\pi c \Delta\nu} \tag{2.63}$$

  with $\Delta\nu$ as the bandwidth of the spectral line. Due to the large bandwidth of absorbance bands in the visible range, the lifetime T_2 is smaller than the temporal resolution. In the infrared spectral range, however, this lifetime is in a range of picoseconds due to the narrow absorbance bands. The subsequent arriving at the sample of the pump pulse perturbs this free induction decay, which results in a variation of the measured intensity.

2.3 Quantum Mechanics and *Ab Initio* Approaches

Quantum mechanics and corresponding *ab initio* approaches, like the Hartree-Fock approach or the density functional theory, are important tools for the understanding of molecular systems. The performance of e.g. geometry optimizations of the examined molecule results in a equilibrated molecular structure and can give information not only about structural properties, e.g. torsion angles or possible hydrogen bonds, but also about stable structural isomers or the structure of e.g. transition states for the electronic ground state as well as for excited states. Frequency analysis of these structures is an important supporting technique for interpretation of experimentally obtained frequency spectra. Also, transitions between electronic states can be characterized, which can help to understand and interpret experimental UV/vis-absorption spectra. Moreover, the resulting energy differences of, for example, two isomers can give a hint on the ratio of the molecules under study in consideration of the accuracy of the different approaches. However, for a correct description of the ratio, a calculation of the energetic barrier between two energy minima is necessary by choosing an appropriate reaction coordinate between the two studied structures. These calculations of reaction pathways is also a common way to study photo-chemical reactions involving excited states. The resulting potential energy curves are a powerful tool for determining possible pathways for reaction mechanisms, especially in combination with experimental results.

2.3.1 Schrödinger Equation

The time-dependent Schrödinger equation is the most important equation of the non-relativistic quantum mechanics and describes the undisturbed temporal evolution of a system (Eq. 2.64), which is influenced by its energy in form of an operator, the Hamilton operator. Using the exact wave function, the spatial and temporal evolution of a system can be described by

$$i\hbar\frac{\partial}{\partial t}\left|\Phi\left(r,t\right)\right\rangle = \overbrace{\left(-\frac{\hbar^2}{2m}\nabla^2 + V\left(r,t\right)\right)}^{\hat{H}}\left|\Phi\left(r,t\right)\right\rangle \tag{2.64}$$

with i as the imaginary unit, $\hbar$ as the angular momentum, m as the mass of the particle, $\nabla = \left(\frac{\partial}{\partial r_1}, \ldots, \frac{\partial}{\partial r_n}\right)$ as the Nabla operator and $\hat{H}$ as the Hamilton operator and r and t as the place and the time, respectively. By separation of the variables r and t, the time-independent Schrödinger equation (Eq. 2.65) can be derived.

$$\hat{H}\left|\Phi\right\rangle = E\left|\Phi\right\rangle \tag{2.65}$$

If the exact wave function and the corresponding Hamiltonian are known for a system, the Schrödinger equation can be solved exactly. However, due to the many-particle problem, the exact description is a challenge and therefore, approximations

are used to overcome this limitation. Wave functions describing the system can be constructed using a linear combination of a distinct number of basis sets for each atom. Although, molecular orbitals can be described by a Slater-function, a wide range of different basis sets can be used, which are usually combinations of Gaussian-type orbitals (GTO), which are mathematically easier to handle. This approximation is possible due to the similar shape of the two functions in a defined range and is compensated by the use of a set of Gaussian-functions.

The minimal basis set contains a single basis function for each orbital on the atoms, e.g. STO-3G[35] (Slater-type orbital with three Gaussian functions as the basis set). In general, these, however, can be expanded by an infinite number of functions. Moreover, polarization functions (*,** , . . .) can be used to include additional functions with an additional node or diffuse functions $(+, ++, \ldots)$ for Pople-type basis sets and *aug(-mented)* for Dunning-type basis sets can be added for the long-range part of the atomic orbitals for better description. Two major groups of basis sets should be noted here: the split-valence, or Pople, basis sets, e.g. $6-31G$,[36] and the correlation-consistent, or Dunning, basis sets,[37] e.g. $cc-PVDZ$.

The Hamilton operator is the sum of the kinetic and the potential energy ($\hat{H} = \hat{T} + \hat{V}$) with the kinetic energy described as $\hat{T} = -\frac{\hbar^2}{2m}\frac{\partial^2}{\partial r^2}$ and the potential energy as a combination of Coulomb attraction and repulsion.[38] The Hamilton operator describes the properties of a system containing nuclei and electrons. It consists of the different distances as well as interactions between M nuclei and N electrons and among themselves.

$$\hat{H} = -\sum_{i=1}^{N}\frac{1}{2}\nabla_i^2 - \sum_{A=1}^{M}\frac{1}{2M_A}\nabla_A^2 - \sum_{i=1}^{N}\sum_{A=1}^{M}\frac{Z_A}{r_{iA}} + \sum_{i=1}^{N}\sum_{j=1}^{N}\frac{1}{r_{ij}} + \sum_{A=1}^{M}\sum_{B=1}^{M}\frac{Z_A Z_B}{R_{AB}} \quad (2.66)$$

where $M_A = \frac{m_A}{m_e}$ is the ratio between the mass of the nuclei and the electron, Z_A is the atomic number of the nuclei A and the distance between an electron i and a nucleus A is defined as $r_{iA} = |r_i - R_A|$, between the electron i and j as $r_{ij} = |r_i - r_j|$ and between the nuclei A and B as $R_{AB} = |R_A - R_B|$. While the first and the second terms correspond to the kinetic energy of the electrons and the nuclei, respectively, the third term is the Coulomb attraction between the electrons and the nuclei. The fourth and fifth term describe the repulsion between the electrons and the nuclei, respectively.

2.3.2 Born-Oppenheimer Approximation

One of the most important approximations in quantum chemistry is the Born-Oppenheimer approximations. The Born-Oppenheimer approximation states that due to the significantly higher mass of the nuclei with respect to the mass of the electron, the velocity of the nuclei is severely lower than the the speed of the electrons. Consequently, the electrons can be regarded as moving in the field of fixed nuclei. Therefore, the kinetic energy of the nuclei is negligible ($\hat{T}_{nuc} \approx 0$) and the repulsion between the nuclei can be regarded as constant. The Hamiltonian can be simplified to an electronic Hamiltonian

$$\hat{H}_{el} = -\sum_{i=1}^{N} \frac{1}{2}\nabla_i^2 - \sum_{i=1}^{N}\sum_{A=1}^{M} \frac{Z_A}{r_{iA}} + \sum_{i=1}^{N}\sum_{j=1}^{N} \frac{1}{r_{ij}} \tag{2.67}$$

with the Schrödinger equation describing the electronic wave functions $|\Phi_{el}(r;R)\rangle$, which explicitly depend on the coordinates of the electrons and only parametrically on the coordinates of the nuclei.

$$\hat{H}_{el}\,|\Phi_{el}\rangle = E_{el}\,|\Phi_{el}\rangle \tag{2.68}$$

Descriptions of the degrees of freedom – vibration, rotation and translation –, however, require nuclear wave function $|\Phi_{nuc}(R)\rangle$ and the nuclear Hamiltonian

$$\hat{H}_{nuc} = -\sum_{A=1}^{M} \frac{1}{2M_A}\nabla_A^2 + E_{tot} \tag{2.69}$$

with $E_{tot} = E_{el} + \sum_{A=1}^{M}\sum_{B=1}^{M} \frac{Z_A Z_B}{R_{AB}}$ as total energy of the system, which is composed by the energy resulting from the electronic Schrödinger equation and the repulsion of the nuclei.

The entire wave function of the system including electrons and nuclei

$$|\Phi_{tot}(r;R)\rangle = |\Phi_{el}(r;R)\rangle \cdot |\Phi_{nuc}(R)\rangle \tag{2.70}$$

can be described by the product of the electronic $|\Phi_{el}(r;R)\rangle$ and the nuclear wave function $|\Phi_{nuc}(R)\rangle$.

2.3.3 Hartree-Fock Approximation

One way of finding an approximated solution to the Schrödinger equation is the Hartree-Fock approximation. It enables a rough determination of an electronic structure and is often a starting point for more precise methods. The Hartree-Fock theory relies on the Born-Oppenheimer approximation and therefore, uses the electronic Schrödinger equation. By separation of the multiple-particle wave function into one-particle wave functions, the Hartree-Fock approximation can be described as a one-particle theory. By using variations of spin orbitals, the Hartree-Fock equation can be described as

$$f(i)\,\chi(x_i) = \epsilon\chi(x_i) \tag{2.71}$$

where $f(i)$ describes the effective one-particle operator, the so-called Fock-operator.

$$f(i) = -\frac{1}{2}\nabla_i^2 - \sum_{A=1}^{M}\frac{Z_A}{r_{iA}} + v^{HF}(i) \tag{2.72}$$

The Hartree-Fock potential $v^{HF}(i)$ describes the potential, in which the i-th electron moves and is therefore dependent on the coordinates of the other electrons (see Eq. 2.67), which complicates the solution of the HF equation 2.71.

$$E_{HF} = \sum_{i=1}^{N} h_i + \frac{1}{2}\sum_{i,j=1}^{N}(J_{ij} - K_{ij}) \tag{2.73}$$

where $\sum_{i=1}^{N} h_i = \sum_{i=1}^{N}(T_{e,i} + V_{ne,i}) = T_e + V_{ne}$ and

$$h_i = \int \Psi_i^*(\vec{x})\left[-\frac{1}{2}\nabla_i^2 - V_{ext}(\vec{x})\right]\Psi_i(\vec{x})\,d\vec{x} \tag{2.74}$$

describes the kinetic energy of the electrons as well as the electron-nucleus attraction.

$$J_{ij} = \iint \Psi_i(\vec{x}_1)\,\Psi_i^*(\vec{x}_1)\,\frac{1}{r_{12}}\Psi_j^*(\vec{x}_2)\,\Psi_j(\vec{x}_2)\,d\vec{x}_1 d\vec{x}_2 \tag{2.75}$$

Eq. 2.75 is the Coulomb integral, which describes the repulsion of the electron i at the distinct position $\vec{x}_1$ and j at position $\vec{x}_2$.

The Exchange integral (Eq. 2.76) describes the interaction between two identical electrons i and j and is a non-classical correction term for the Coulomb integral, which overestimates the Coulomb repulsion by neglecting the antisymmetrization of the electronic density.

$$K_{ij} = \iint \Psi_i^*(\vec{x}_1)\,\Psi_j(\vec{x}_1)\,\frac{1}{r_{12}}\Psi_i(\vec{x}_2)\,\Psi_j^*(\vec{x}_2)\,d\vec{x}_1 d\vec{x}_2 \tag{2.76}$$

Therefore, the Hartree-Fock operator can be described by

$$\hat{f}^{HF} = -\frac{1}{2}\nabla_i^2 + V_{ext} + J_{ij} - K_{ij} \tag{2.77}$$

Using an initial guess for the wave function, the HF potential can be calculated based on a self-consistent field (SCF) scheme and the variational principle to further calculate the eigenvalues of a new set of spin orbitals. This iterative cycle ends when the self-consistency is reached.

The variational principle is an important concept, which states that best solution of the Schrödinger equation, meaning the best wave function, which describes the system accurately within the limits of a one-particle approximation, results in the lowest ground state energy of the system.[39] Consequently, for improving the description, the initially guessed wave function $\left|\tilde{\Psi}\right\rangle$ is incrementally varied until the lowest energy $\tilde{E}$ is reached, which however, is always larger than the exact energy E_{exact}.

$$\frac{\left\langle\tilde{\Psi}\right|\hat{H}\left|\tilde{\Psi}\right\rangle}{\left\langle\tilde{\Psi}\right|\left.\tilde{\Psi}\right\rangle} = \tilde{E} \geq E_{exact} \tag{2.78}$$

2.3.4 Density Functional Theory

The density functional theory (DFT) is a technique, which solves the Schrödinger equation by describing the multi-electron system as a function of the electron density.[40] Like that, the number of variables decreases drastically from $3N$ from the description of each particle by a wave function to only 3 spatial variables x, y and z.
DFT is based on the Hohenberg-Kohn theorems, which were stated by Pierre Hohenberg and Walter Kohn in 1964. The first Hohenberg-Kohn-theorem states that the Hamilton operator and consequently all contained properties can be determined by the electronic density ρ.[41]

Therefore, the energy of a system E can be displayed by the electron-nucleus attraction E_{ne}, the kinetic energy T and the electronic repulsion E_{ee}.

$$E[\rho] = E_{ne}[\rho] + \overbrace{T[\rho] + E_{ee}[\rho]}^{F_{HK}} \tag{2.79}$$

with F_{HK} as the Hohenberg-Kohn operator.

The second Hohenberg-Kohn-theorem refers to the variational principle, which states that $F_{HK}[\rho]$ delivers only the lowest ground state energy, if the electron density $\tilde{\rho}$ is the true density of the system ($E_{exact} \leq E[\tilde{\rho}]$).
The time-dependent density functional theory (TDDFT) relies on the Kohn-Sham approach, which were stated by Walter Kohn and Lu Jeu Sham. They suggested that the electron density of the complete interacting system can be approximated by the

electron density of the non-interacting system.[42]

$$\rho_s(\vec{r}) = \sum_i^N \sum_s |\Psi_i(\vec{r}, s)|^2 = \rho(\vec{r}) \tag{2.80}$$

The method of using the electron density can be used for the description of the energy of the system, which can be, in principle, calculated exactly, since the deviation of the electron density of the non-interacting system from the interacting system is considered in the exchange-correlation energy $E_{xc}[\rho]$.

$$E[\rho] = E_{ne}[\rho] + T_s[\rho] + J[\rho] + E_{xc}[\rho] \tag{2.81}$$

The exchange-correlation potential is the only unknown term and depends actually on the electron density at each position of the system, which makes it difficult to solve exactly.

Consequently, approximations to calculate this potential are generally used. The local density approximation (LDA) neglects the dependency of the electron density on each position of the system, but only considers it at one point, while the generalized gradient approximation (GGA) not only uses the density, but also the derivative of the density of the position. A high number of different methods, or so-called functionals, are known using this approximation, which can be divided in the exchange functionals, e.g. S (Slater exchange[43] or local spin density approximation (LSDA)), PBE[44,45] (Perdew, Burke and Ernzerhof) or B88[46,47] (Becke 1988), and in the correlation functionals, e.g. LYP[48] (Lee, Yang and Parr), PW91[44,49] (Perdew and Wang, 1991) and VWN[50] (Vosko, Wilk and Nusair). Exchange and correlation functions can also be combined, like in the B-LYP functional (Becke and Lee, Yang, Parr). A very common technique is the combination of Hartree-Fock exchange and DFT exchange-correlation functionals, the so-called hybrid functionals. Well-known examples are the "Becke Three Parameter Hybrid Functionals", e.g. B3PW91 (Eq. 2.82) or B3LYP, which were devised by Becke in 1993[47] or the *half-and-half*-functionals, e.g. BHLYP.[51]

$$E_{EX} = E_{XC}^{LSDA} + a_0 \cdot \left(E_X^{exact} - E_X^{LSDA}\right) + a_X \cdot \Delta E_X^{B88} + a_C \cdot \Delta E_C^{PW91} \tag{2.82}$$

with $a_0 = 0.20$, $a_X = 0.72$ and $a_C = 0.81$ as constants found by fitting procedures.

However, it should be noted, that the variational principle is not valid for the approximations of the exchange-correlation potential. Therefore, ground state energies, which were obtained by using TDDFT methods, can be even lower than the exact ground state energy.

2.4 *Ab Initio* Calculation Setup

In this work, quantum-mechanical calculations were performed to support the characterization of experimental vibrational spectra as well as for the assessment of possible structural isomers with respect to their ground state energies. Due to the system size, the used theoretical approach for each calculation was density functional theory, using the B3LYP functional and the Dunning basis set cc-PVDZ.

For the calculation of the optimal molecular structure, an initial molecular structure was pre-optimized using the program Avogadro[52] and the implemented UFF force field approach (universal force field[53]). Force field methods rely on Newton's law of motion and describe the molecular properties in a classical sense, using e.g. the harmonic oscillator. Force field methods are an inexpensive alternative for quantum-mechanical calculations, but, however, deliver a significantly worse description of the molecular properties. Therefore, based on the so pre-optimized structure, a TDDFT geometry optimization was performed using the *steepest decent* approach until a defined threshold value is reached (e.g. change in total energy or gradient).

The performed frequency calculations are based on a Hesse matrix. The calculation of the second derivative of the Hesse-matrix corresponding to the geometry-optimized structure delivers the force constants k and frequencies ν of the vibrations. These are not only important for the interpretation of experimentally obtained vibrational spectra, but also for the distinction between an optimized structure in a local/global energy minimum or at an energy maximum, a so-called transition state, where the corresponding force constant is negative, and the frequency is imaginary. Due to the approximations of the used methods and the limited description of the system by the basis sets, calculated frequencies need to be scaled with a distinct constant factor, which either comes from the comparison with experimental data or is a precalculated vibrational scaling factor known from the literature referring to one pair of functional and basis set (in case of B3LYP/cc-PVDZ: scaling factor of 0.97[54]).

In general, quantum-mechanical calculations are performed for molecules in vacuum. For a better description of the molecular system, also the interactions to the surrounding bath, the solvent molecules, should be considered. An explicit description of the solvent molecules as point charges, using e.g. TIP3P or SPC, considers the interactions explicitly and therefore, give reliable results. However, these calculations usually require a prior molecular dynamics (MD) simulation for correct positions of the solvent molecules and even the quantum-mechanical calculation using an explicit model is extremely expensive. A good alternative is the implicit description of the solvent molecules, using a polarizable continuum model (PCM) by Tomasi,[55] which creates a solute cavity and therefore, describes the electrostatic potential of the solvent. Here, the solvent is mainly characterized by the dielectric constant ϵ (e.g. $\epsilon_{H_2O} = 78.3553$ and $\epsilon_{MeCN} = 35.688$). The performed quantum chemical calculations using the described setup help to understand and interpret the experimental results including an implicit description of solvents effects.

Chapter 3

Photo-Chromic Compounds: Photoswitches

Small organic molecules, which can be interconverted reversibly between at least two isomeric forms by the use of light, are called *photoswitches*.[56] There is a variety of different photo-chromic compounds and the photo-induced change in properties is highly dependent on the class of photoswitches.

In general, photoswitches can be divided in two major classes, which distinguish in their introduction of the back reaction. For molecules with a low energy barrier between the two isomeric structures, the back reaction is enabled by temperature. Consequently, these photoswitches show a photo-chromism of *type T* (thermally). Photoswitches of *type P* (photo-chemically) can only be converted back in the original, more stable, form by excitation at a defined wavelength.[57] Interestingly, substances are known, which show a back reaction, that can be introduced thermally and photochemically.

Two major groups of chemical processes can be found, which are involved in the interconversion of the two isomeric forms (Fig. 3.1a). The first group is characterized by the conformational change upon photo-induced *cis*/*trans*-isomerization (Fig. 3.1b). These include the important classes of azobenzenes[58] and stilbenes.[59] By photoexcitation with UV-light, the energetically favored *trans*-conformation is converted into a less stable *cis*-isomer. Therefore, a change of not only the electronical structure, but also of the conformation results from this isomerization. Especially, the change of the end-to-end distance, which is about 2.6 Å for azobenzene, should be noted. The *cis*-to-*trans*-isomerization of the azobenzene can either be induced thermally or by photo-activation with visible light.

The second major group of photoswitches with the same chemical processes is characterized by a ring-opening/ -closure reaction and contains important examples like fulgides[60]/ fulgimides,[61] dithienylethenes (DTE)[62,63] and spiropyrans.[64–69] Upon photo-excitation, the initial conformational change after electrocyclization leads to a massive change in the electronic structure. Usually, the ring-closure reaction is usually obtained by excitation with UV light and the corresponding reverse ring-opening reaction can be initiated by absorption of visible light. As important exception, the photoswitch spiropyran/ merocyanine should be noted, which shows a contrary behavior. During the ring-opening and -closure reactions, a change between a

planar and electronically delocalized structure and a structure with aromatic rings, which is twisted or even perpendicular, in case of the spiropyran, to each other, can be observed. Moreover, a massive change in photo-physical properties is the result due to the planarization and the π-electron delocalization.

By incorporation of these small molecules into larger systems, like biomolecules or polymeric materials, this distance change of the photoswitch can easily induce a conformational change on a larger scale. Like that, photo-responsive polymers and crystals are obtained, which enable the development of photoswitchable materials for data or energy storage.[70,71] Moreover, also the conformation of the secondary and tertiary biomolecular structures can be controlled spatially and temporally by using photoswitches. Interestingly, even processes of biomacromolecules, like the opening and closure of potassium ion channels, can be regulated by photo-activation of one azobenzene molecule.[72,73] Moreover, also the changes in the electronic structure can be used, like it was shown for a DTE-BODIPY-[74] or DTE-CdSe quantum dot-systems,[75] where a FRET-process could be controlled by photo-induced ring-opening and -closure reactions.

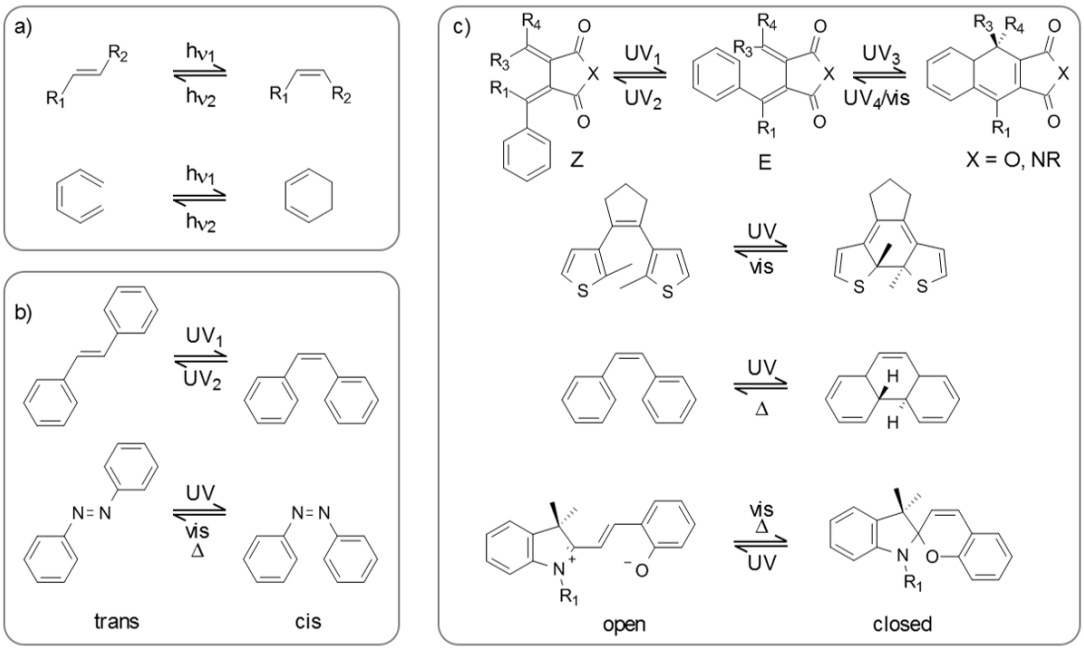

Figure 3.1: a) General principles of photoswitches relying on photo-isomerization and of ring-opening and -closure reactions. b) Chemical structure of *trans*- and *cis*-stilbene and -azobenzene as example for photoswitches relying on photo-isomerization. c) Chemical structure of fulgides (*X=O*), fulgimides (*X=NR*), dithienylethene (DTE), stilbene/Dihydrophenanthrene and Merocyanine/Spiropyran as example for photoswitches relying on ring-opening and -closure reactions.

Using light as an invasive tool for the control over conformations is a very important field in research. The overall aim of these studies is the transfer of the changed photo-chemical properties, which result from the photo-induced isomerization, onto larger systems, like biomolecules or materials. Therefore, a suitable incorporation

of photoswitches into these macromolecules enables not only an important research field due to a spatio-temporal control over changes in conformation and consequential function, but also in medicine and pharmacology as a new therapy relying on e.g. a photo-responsive gene expression. Also, in material science, photoswitches play an important role. Due to the spatio-temporal control of the isomerization process and the resulting change in (photo-)physical properties, photoswitches can be used as new materials for energy or data storage or even transfer.

3.1 Azobenzene

The most prominent photoswitch is azobenzene, which has already been studied in 1937,[76] where the photo-chromic behavior of azobenzene was observed at the first time.

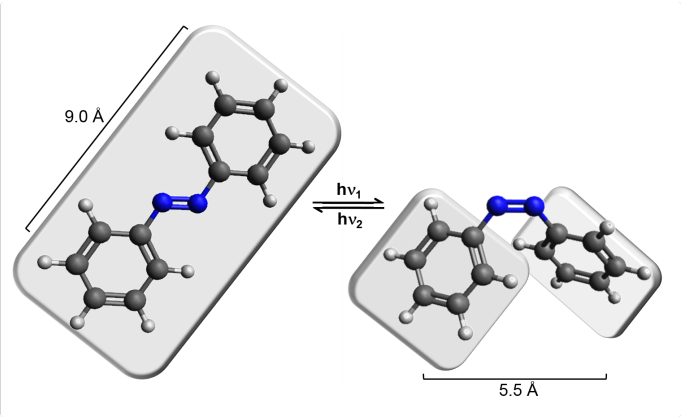

Figure 3.2: Chemical structure of *trans*- and *cis*-azobenzene. Clamps indicate the end-to-end-distances of 9.0 Å and 5.5 Å, respectively.[77]

Azobenzene consists of an azo-group with two phenyl rings on each nitrogen, which is a variation of the photoswitch stilbene. Depending on the conformation of the two phenyl rings with respect to the azo-group, a *trans*- and a *cis*-isomer, also known as E- and Z-isomers, are feasible (Fig. 3.2). The *trans*-isomer is present in a planar conformation, which can be described by a C_{2h} point group, with a torsional angle CNNC of 180°. The end-to-end distance between the carbon atoms, each in *para*-position to the azo-group, is 9.0 Å.[77] The *cis*-azobenzene is energetically unfavorable with respect to the *trans*-isomer ($\Delta E(trans - cis) = 0.66\ eV$[78]) and shows a torsional angle CNNC of about 10° and a twist of about 50° of the one phenyl ring with respect to the NNC-plane, which is caused due to sterical hindrance and which is highly dependent on the substituents.[78,79] The structure of the *cis*-isomer is described by a C_2-symmetry and the distance between the phenyl rings decreases by about 3.5 Å to a final value of 5.5 Å.[77]

The nitrogens of the azo-group are sp^2-hybridized (Fig. 3.3a). Therefore, three hybrid orbitals, arranged in a triangular form, can interact with atomic orbitals of neighboring atoms (Fig. 3.3b). While one one the hybridized orbitals is responsible for

the formation of the bond to a carbon of the phenyl group, a second hybridized orbital forms the N-N-σ-bond (Fig. 3.3c). The third hybrid orbital contains two electrons, building a free electron pair. By overlap of the two p_z-orbitals of the two nitrogens, a π-bond is formed (Fig. 3.3c).

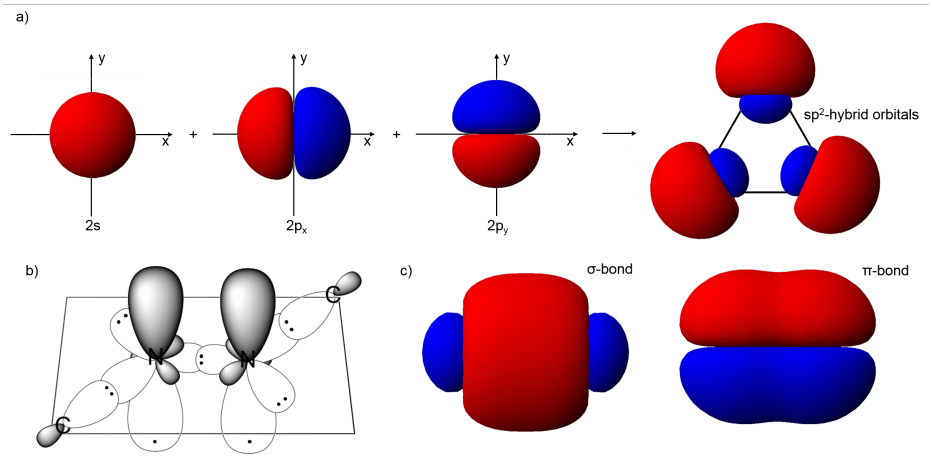

Figure 3.3: a) Combination of $2s$-, $2sp_x$- and $2sp_y$-atomic orbitals, which is representing the sp^2-hybrid orbitals of the nitrogens of the azo-group. b) Schematic representation of the atomic orbitals, which participate in the bond formation of the azo-group including the carbon substituents, which are part of the phenyl rings. c) Molecular orbitals, forming the σ- and the π-bond of the azo-group.

In a molecular orbital (MO) scheme, the interactions of the atomic orbitals of the two nitrogens with the same symmetry can be seen, which are forming the molecular orbitals of the azo-group (Fig. 3.4b). While the two non-bonding orbitals are splitted into a n_+- and a n_--molecular orbital, the interaction of the two P_z-atomic orbitals result in a bonding (π) and an anti-bonding (π^*) molecular orbital.[80] While the n_+-MO, is the highest occupied molecular orbital (HOMO), the π^*-MO is the lowest unoccupied molecular orbitals (LUMO). Electronic transitions between these two states can occur by absorption of light, which is of equal energy as the energy difference between the two states ($\Delta E = h\nu$). The $n_{(+)}\pi^*$-transition in azobenzene can usually be achieved by light with a wavelength of 430 nm and is often referred to the excitation of the S_1-state. This transition can be seen in an UV/vis-absorbance spectrum as an absorbance band around 430 nm for the *trans*- as well as for the *cis*-azobenzene (Fig. 3.4a). While for the *trans*-isomer this $n\pi^*$-transition is forbidden due to symmetry reasons, only a weak absorbance is detectable, which is enabled, because of vibronic coupling. Due to the non-planarity of the *cis*-isomer, the $n\pi^*$-transition of the *cis*-isomer is an allowed transition. Also an electronic transition from the HOMO-1 into the LUMO of the *trans*-isomer ($\pi\pi^*$-transition, S_2-state) is possible in a spectral range around 330 nm. This very intense absorption band can be seen between 270 and 370 nm. For the *cis*-isomer, this transition is less pronounced and blue-shifted to a wavelength of 280 nm.

Excitation within the absorbance bands of the *trans*-isomer can induce a *trans*-to-*cis*-isomerization. However, due to the overlap of the absorbance spectra of both iso-

Table 3.1: Extinction coefficients of the $n\pi^*$- and the $\pi\pi^*$-band of *trans*- and *cis*-azobenzene in acetonitrile.[81] Also the quantum yields Φ in acetonitrile are given for the isomerization after excitation within the corresponding absorption band. The quantum yield Φ for the *trans*-azobenzene corresponds to the value of the isomerization from *trans*- to *cis*-isomer (Φ_c).[82]

	$\pi\pi^*$			$n\pi^*$		
	λ_{max} nm	$\epsilon_{\lambda_{max}}$ $L/(mol \cdot cm)$	$\Phi_{\pi\pi^*}$ %	λ_{max} nm	$\epsilon_{\lambda_{max}}$ $L/(mol \cdot cm)$	$\Phi_{n\pi^*}$ %
trans-azobenzene	316	21000	15	445	550	31
cis-azobenzene	279	4300	21	428	1200	46

mers, no pure *cis*-isomer can be achieved by excitation at 330 nm. Therefore, the photochemically equilibrated state, which contains the maximal-achievable *cis*-amount for a defined excitation wavelength, is called the photo-stationary state (PSS). Since there is an overlap of the $n\pi^*$-bands of both isomers aswell, a PSS can also be found for the state after excitation at 430 nm. The amount of *trans*-azobenzene is usually slightly lower than in the thermal-equilibrium, which is about 100%. However, due to the small extinction coefficient of the $n\pi^*$-transition of *trans*-azobenzene, the amount of the *trans*-isomer in the PSS is usually >90% (Tab. 3.1). Therefore, the photo-stationary state results from a combination of the *trans*- and the *cis*-isomer (Eq. 3.1).

$$A_{exp} = x \cdot A_{cis} + y \cdot A_{trans} \tag{3.1}$$

with *x* and *y* as weighting factors, A_{trans} and A_{cis} as the absorbance values at a defined wavelength of the spectrum of the pure *trans*-isomer and *cis*-isomer, respectively, and A_{exp} as the absorbance value at the same wavelength of the measured spectrum, e.g. the photo-stationary state.

On the condition that no side reactions occur, like degradation or photolysis, then one has $y = 1 - x$, which simplifies Eq. 3.1 to

$$A_{exp} = x \cdot A_{cis} + (1 - x) \cdot A_{trans} \tag{3.2}$$

Therefore, for known pure spectra of the *trans*- and the *cis*-isomer, the exact ratio between both isomers can be determined for each experimentally obtained spectrum by using Eq. 3.3.

$$x = \frac{A_{exp} - A_{trans}}{A_{cis} - A_{trans}} \tag{3.3}$$

The isomerization can be visualized by the absorbance difference spectrum of the spectra of *trans*-azobenzene and the PSS (Fig. 3.4a). Here, an intense negative signal should be detected around 330 nm as well as two positive signals below 270 nm and between 370 and 470 nm.

The isomerization of azobenzenes is proposed to proceed via four possible mechanisms, which are still under debate in literature. The mechanism highly depends on

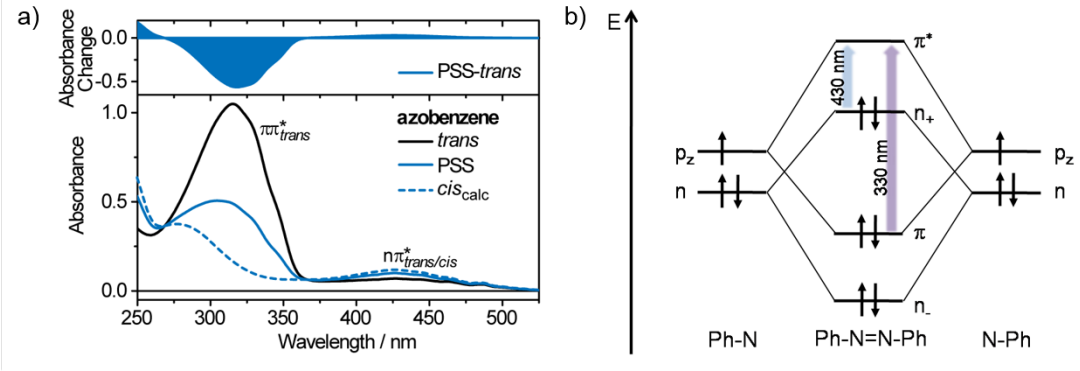

Figure 3.4: a) UV/vis-absorbance spectrum of *trans*-azobenzene and of the photostationary state (PSS) after excitation at 430 nm in methanol. Also, a calculated pure *cis*-spectrum is shown. The isomerization is visualized by the absorbance difference spectrum (PSS-*trans*) (top). b) Schematic representation of the energetic scheme of the formation of the molecular orbital of the azo-group of azobenzene, showing only the two highest occupied and the two lowest unoccupied molecular orbitals, modified after ref. [83]. Energies are not reproduced in facsimile. Arrows indicate the excitation wavelength of the $n\pi^*$- and the $\pi\pi^*$-transitions.

the excitation wavelength and the structure of the azobenzene. Thus, the isomerization mechanism and the corresponding lifetimes differ for pure azobenzene in contrast to cyclic azobenzene[84,85] or azobenzenes with rigid or space-demanding substituents.[86]

- *Inversion*: For the isomerization e.g. from *trans*- to *cis*-azobenzene via inversion, one phenyl ring is moving in plane. Here, the angle ∠NNC changes from ca. 115.3° to ca. 124.2°.[87] After the actual isomerization, a reorganisation of the two phenyl rings occur due to steric hindrance, which is reflected in a torsion around the C-N bond of one phenyl ring of about 52°.[79] The isomerization via inversion is the proposed mechanism with an activation barrier of about 1.10 eV[78,79] for the thermal reaction from the *cis*- to the *trans*-azobenzene.[88,89]

- *Torsion*: The torsional mechanism proceeds via a torsion around the azo-bond with one rotating phenyl ring with a constant NNC-angle. The CNNC dihedral angle changes from 180° for *trans*-azobenzene to 20° for the *cis*-isomer.

  Since a high structural flexibility of the phenyl rings is necessary for the torsional pathway, this reaction coordinate is usually not found for cyclic or very rigidly fixed azobenzenes.[86]

- *Concerted inversion*: This pathway is comparable to the already proposed mechanism via inversion. However, for this mechanism both phenyl ring move coincidentally in plane in contrary directions. Like that, the overall movement is reduced.

- *Hula-twist*: The isomerization via hula-twist is the newest concept of the presented possible mechanisms.[90] It describes an isomerization, which is astonishingly little space-demanding. Both nitrogens are involved in the, mostly, out-of-plane movement. By moving in different directions, the corresponding isomer is built, which is completed by a slight correction of the position of one phenyl ring.

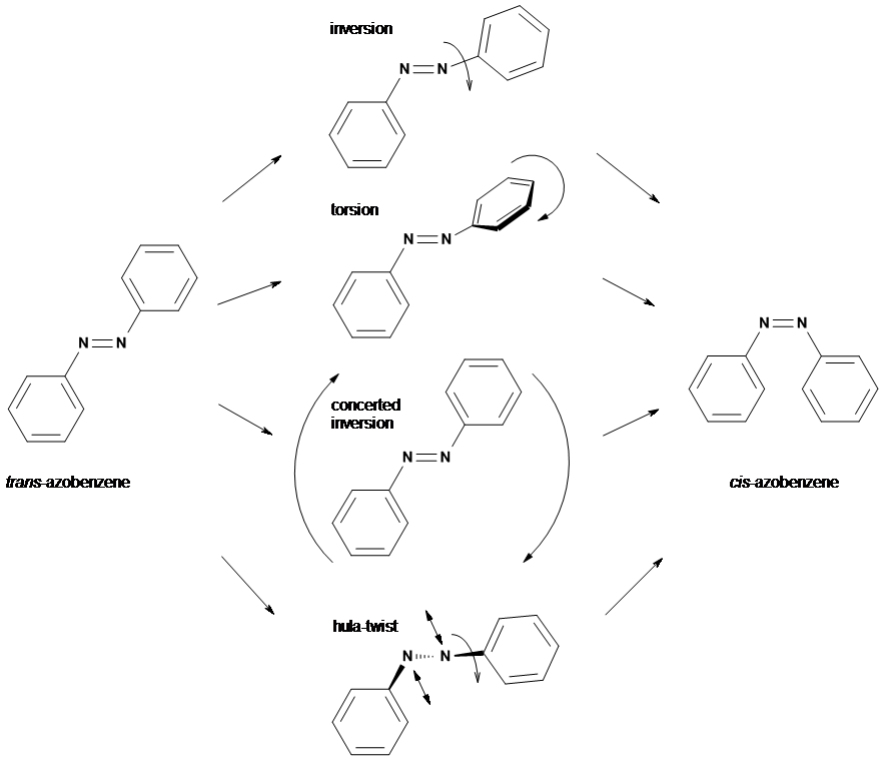

Figure 3.5: Possible reaction pathways for the mechanism of the *trans*-to-*cis*- and the *cis*-to-*trans*-isomerization of azobenzene. (Concerted) inversion of the phenyl rings, torsion around the azo-bond and hula-twist.

The isomerization mechanism of azobenzenes is highly under debate in literature. In 1982, Monti *et al.* suggested an isomerization of the *trans*- to the *cis*-isomer after S_2-excitation, which shows a relaxation via an internal conversion in the S_1-state via a rotational pathway. The isomerization occurs on the S_1-state, which relaxes into the ground state of the *trans*- and the *cis*-isomer via an inversion pathway.[79] This is also in agreement with results from Raman experiments, which indicate the existence of an inversion pathway.[91] The combination of inversion and rotation have been supported by experimental results in the last decades.[92,93] In later quantum chemical calculations, however, an inversion pathway in the S_1-state was rated as an unfavorable isomerization pathway due to a large energy gap between the S_0- and the S_1-state.[94] A conical intersection was observed for the torsional pathway,[94–96] which enables a torsion on the first excited state, while for the S_2-state, this reaction coordinate is energetically unfavorable.[86] In ref. [89, 94], an additional isomerization mechanism via a concerted inversion was suggested for the S_1-state. Due to a small barrier on the

first excited potential energy curve, the conical intersection between the S_0- and the S_1-state becomes accessible after S_2-excitation. In recent studies, the *Hula-twist* isomerization mechanism, a pedal-like motion,[97] which is known for the isomerization of stilbenes,[90] is also suggested for azobenzenes.[98] Also the consideration of higher excited states,[99] triplet states[100–102] or so-called *phantom states*[96] for the isomerization can be found in literature. The effect of substituents, especially cyclic azobenzene[103,104] or bisazobenzenes,[105,106] as well as of solvents[107] on the isomerization mechanism and dynamics cannot be neglected.

In time-resolved studies, the isomerization process from the *trans*- to the *cis*-isomer is usually described by four exponential functions.[108] For S_2-excitation, a fast relaxation from the S_2- into the S_1-state occurs within a few hundred femtoseconds (110 to 300 fs). The interpretation of the second and third lifetime (0.4 ps and 0.5 - 3.0 ps), however, is under debate. One possible explanation is the movement out of the Franck-Condon region (τ_2) with a subsequent $S_1 \rightarrow S_0$-transition via a conical intersection (τ_3).[18,92,109,110] Another interpretation is a biexponential transition from the first excited into the ground state via different paths on the potential energy surface.[111] Afterwards a vibrational cooling can be observed in the range of more than 10 ps. Similar dynamics for the relaxation of the S_1-state can be observed after a S_1-excitation.[93]

The isomerization of the *cis*- to the *trans*-isomer proceeds via a rotational pathway independent of the excitation wavelength.[96,112] The experimentally observed lifetimes of 0.17 ps and 2.0 ps are slightly faster than for the exitation of the *trans*-isomer, due to the steeper potential energy curve of the *cis*-azobenzene.[93]

The quantum yields of the isomerization are not only depending on the solvent,[82,108] but also highly dependent on the excitation wavelength, which is a violation of Kasha's rule.[16] While an excitation of the $n\pi^*$-transition of the *trans*-isomer, which is a forbidden transition and has an extinction coefficient of only 550 $L \cdot mol^{-1} \cdot cm^{-1}$, yields an *cis*-azobenzene of 31 $\%$, isomerization after excitation of the intense $\pi\pi^*$-transition shows a quantum yield of only 15 $\%$ (Tab. 3.1). Different explanations have been proposed for the quenching of the isomerization reaction, yet, however, studying the reason for this violation is still a part of research. Possible reasons include a deformation of the molecular structure of azobenzene in the S_2-state or even in the $S_{3,4}$-state along the torsional pathways or an additional relaxation pathways for high vibrational states of the S_1-state after a fast $S_2 \rightarrow S_1$-transition.[113]

While large substituents can have an influence on the isomerization mechanism, because of sterical hindrance, changes in the substituents have an enormous effect on the electronic structure of the photoswitch. In general, substitution can be divided into four groups.

- *Inactive substituents*: Substituents with neglectable electron donating or withdrawing character, like hydrogen, show only slight influences on the absorption spectrum nor on the thermal reaction rates. Also, substituents, which exhibit these features, are called inactive, for a single-substitution in *meta*-position to the azo-group. However, every substitution on the azobenzene scaffold results

in a small bathochromic shift of the absorption spectrum. While a substitution in *ortho*-position often reduces the extinction coefficient of the $\pi\pi^*$-band, an increase can be observed by a substitution in *para*-position.

- *Push-substituents*: Substituents with a positive mesomeric effect (+M), which act as an electron donor, like amino (NH_2) or methoxy (OMe) groups, show a slightly lower activation barrier (less than 0.1 eV) for a monosubstitution with respect to azobenzene.[78] This is the reason for a slightly accelerated thermal reaction rate for the *cis*- to *trans*-isomerization, which is even more pronounced for the *para*-position.[114] In case of disubstitution on both rings, the activation energy can even be slightly higher than for the pure azobenzene.[78]

  This electron donating feature in *ortho*-position with respect to the azo-group induces an intense bathochromic shift of the $\pi\pi^*$-band of the *trans*-isomer. This effect is even more pronounced for a *para*-substitution, which is often accompanied by a slight hypsochromic shift of the $n\pi^*$-band. Moreover, hyperchromicity can be observed here.[115] The absorption spectrum of azobenzenes with electron-donating substituents also shows a solvent-dependence.

  During photo-induced isomerization, the polar transition state of the rotational pathway is stabilized by the electron donating substituent. Consequently, azobenzenes with push-substituents tend to isomerize via a torsional reaction coordinate.[116,117] The rough classification in different groups of isomerization mechanisms is enabled by using the Hammett-parameter[118] of each substituent.

  Moreover, by using push-substituents, the fluorescence quantum yield of *cis*-azobenzene can be increased.[119]

- *Pull-substituents*: Electron acceptors, like nitro (NO_2) or cyanide (CN) groups, have a negligible effect on the absorption spectrum and show no solvent-dependence.

  However, these substituents, especially in *para*-position, have a high influence on the activation barrier of the thermal isomerization reaction. Due to the mesomeric structures of the *ortho*- and *para*-position, the energy barrier is reduced up to 0.3 eV for nitro-substitution,[78] which results in a faster thermal reaction from the *cis*- to the *trans*-isomer with respect to the pure azobenzene.[114] This electron withdrawing character is stabilizing the linear transition state during an isomerization via an inversion mechanism. Therefore, azobenzenes with substituents with a pull-character usually isomerize via an inversion.[116,117]

- *Push-pull-substituents*: Azobenzenes, which consist of an electron-donating substituent in *ortho*- or *para*-position on one side of the azo-group and an additional electron-withdrawing group on the second part of the azobenzene, are usually called push-pull-azobenzenes. This class is characterized by an enormous effect

on the energy of the electronic transitions. Usually the $\pi\pi^*$-band of the *trans*-isomer is drastically shifted bathochromically.[107] In severe cases, the π molecular orbital is energetically raised even over the non-bonding molecular orbital, which then results in a $\pi\pi^*$-transition as the excitation of the S_1-state. While push-pull-azobenzenes show a large absolute dipole moment, in constrast to pure azobenzenes,[78] the difference of the dipole moments between *trans*- and *cis*-isomer ist often still smaller than for the pure azobenzene.

The thermal *cis*-to-*trans*-isomerization of azobenzenes highly depends on the choice of substituents[120,121] and solvents[114,122] but it is known to be a first-order kinetic in frequent solvents.[123,124] The thermal relaxation of the *cis*-isomer of unsubstituted azobenzene occurs at room temperature with a half-life of days,[108] e.g. 119 h in benzene.[125] The isomerization rate $\frac{dc_x}{dt}$ is dependent on the concentration of the unreacted *cis*-isomer c_x (Eq. 3.4).

$$\frac{dc_x}{dt} = -k \cdot c_x \tag{3.4}$$

with k as the rate constant of the reaction. Therefore, an exponential connectivity results for the concentration of the participating substances and the reaction time (Eq. 3.5).

$$c_x = e^{-k \cdot t} \tag{3.5}$$

However, deviations from this first-order kinetics are common for azobenzene-containing matrices or polymers.[126,127] In diluted solutions in polymer matrices, for example, a stretched exponential behavior[128,129] was observed.[130] Here, with increasing *cis*-to-*trans* conversion, the isomerization rate decreases. Therefore, a time-independent parameter α is added to the exponential connectivity of a first-order kinetic (Eq. 3.6)

$$c_x = e^{-(\kappa \cdot t)^{\alpha}} \tag{3.6}$$

with $0 < \alpha \leq 1$ and κ displays the effective rate constant. Also the converse case of an increasing reaction rate is known in literature, which is described as a "squeezed exponential" kinetic.[131] In cases of azobenzenes at air-water or glass-water interfaces, also second-order kinetics have been observed for the thermal isomerization from the *cis*- to the *trans*-isomer.[132,133]

The rate of a reaction, and therefore, the rate constant k, are highly dependent on the supplied energy in form of temperature. This temperature-dependence is usually described by the Arrhenius-equation (Eq. 3.7)

$$k\,(T) = A \cdot e^{-\frac{E_A}{RT}} \tag{3.7}$$

with A as the elastic collision frequency or the maximal rate constant for a defined reaction at infinitly high temperature and E_A as the activation energy barrier of the process, here the thermal isomerization reaction. R describes the ideal gas constant. While the empirical Arrhenius-equation is neglecting the temperature-dependence of the pre-exponential factor, a complete description of the temperature-dependence of the rate constant is given by the Eyring theory,[134] which is the result of the transition state theory (Eq. 3.9)

$$k\left(T\right) = \frac{k_B T}{h} \cdot e^{-\frac{\Delta G^{\ddagger}}{RT}} \tag{3.8}$$

$$k\left(T\right) = \frac{k_B T}{h} \cdot e^{-\frac{\Delta H^{\ddagger}}{RT}} \cdot e^{-\frac{\Delta S^{\ddagger}}{R}} \tag{3.9}$$

where k_B is the Boltzmann constant, h is Planck's constant and $\Delta G^{\ddagger}$ describes the Gibbs energy of activation. Due to the connectivity $\Delta G^{\ddagger} = \Delta H^{\ddagger} - T \cdot \Delta S^{\ddagger}$, inferences can be drawn about the enthalpy and entropy of activation, $\Delta H^{\ddagger}$ and $\Delta S^{\ddagger}$, respectively, of a defined reaction.

The use of light as a stimulus for the isomerization of azobenzene is not only a tool, which is easy to handle, but also enables a spatio-temporal control of the isomerization process. Implementation of the azobenzene in larger molecular system enables a conformational transport from the photoswitch to the macromolecule. Therefore, photoswitches, and especially azobenzenes, can be found in a wide range of applications from material science[133] to biological system.[135–137]

The incorporation of azobenzene in polymers[77,138–140] enables not only an intervention in the physical properties of the azobenzene, resulting e.g. in a non-linear optical material,[141–143] but also the development of new kinds of molecular machines[144] or photo-mobile polymers,[145,146] which have the ability of translate the molecular motion onto the macroscopic scale. Moreover, due to the functionalization of carbon-nanotubes with azobenzenes, investigations on the storage of solar energy are rendered possible.[70,71] Also, a photo-responsive release of small molecules from a polymeric nanocapsule is enabled by the implementation of azobenzene,[147] which can also be applicable for biological utilization, like photo-controllable DNA capsules.[148] The usage of light as an external stimulus is also practicable for biological system, however, the wavelength used for the photo-isomerization should not interact with the biomolecules.[149] The application of photoswitches in biomolecules ranges from the photo-control of smaller peptides[150–152] and proteins[153–155] to DNA[156–160] or even RNA dehybridization[161,162] to large macromolecules, e.g. ion channels.[72,73]

Part II

Experimental Methods

Chapter 4

Materials and Experimental Methods

While the theoretical background of optical spectroscopy as well as steady-state and time-resolved spectroscopic methods were introduced in part I, in this part first of all the materials, like compounds and solvents, which were used in this work are presented. Moreover, general procedures for the concentration adjustment of RNA solutions and the exchange to deuterated buffered solutions are briefly explained. Furthermore, experimental methods relying on the optical spectroscopy are explained more in detail, regarding the measurements performed in this work.

4.1 Materials

Azobenzene Compounds

Most of the azobenzene derivatives, which are presented in chapter 5 and section 6.2, were synthesized in the research group of Prof. A. Heckel by T. Halbritter. Here, only the derivatives Sulfasalazine (Fig. 5.2c), 1-(2-Pyridylazo)-2-naphthol (Fig. 5.1b) as well as Ponceau Xylidine (Fig. 5.2b) were obtained by Sigma-Aldrich.
Moreover, the azobenzene compounds, which are linked to a desoxyribose, that are presented first in Fig. 5.3b and discussed in detail in section 6.1, were synthesized by T. Goldau from the research group of Prof. A. Heckel.

The photoswitchable foldamer $\mathbf{10_5}$ as well as its azobenzene monomer were prepared by Dr. Z. Yu from the research group of Prof. S. Hecht (Humboldt University of Berlin).

Solvents

The organic solvents, which were used in chapter 5 (DMSO) and in chapter 7 (Acetonitrile), were obtained in an anhydrous state by Carl Roth (ROTIPURAN, $\geq 99.8\%$, p.a.) and Sigma-Aldrich ($\geq 99.8\%$, p.a., in Sure/Seal bottles), respectively.

The phosphate buffered solution (PBS) was prepared in the research group of Prof. A. Heckel (Tab. 4.1). The different Lysis-buffers as well as the SELEX buffer were obtained by the research group of Prof. B. Suess (TU Darmstadt).

Table 4.1: Composition of the buffered solutions used in this work.

			Lysis buffer			
	PBS	SELEX	**1**	**2**	**3**	**4**
pH	7.4	8.0	8.0	8.0	7.6	7.6
KH_2PO_4	1.4 mM	—	—	—	—	—
Na_2HPO_4	10 mM	—	—	—	—	—
Tris-HCl	—	50 mM	25 mM	25 mM	25 mM	25 mM
NaCl	137 mM	250 mM	150 mM	150 mM	150 mM	150 mM
KCl	2.7 mM	—	—	—	—	—
$MgCl_2$	—	5 mM	—	—	—	—
TritonX100	—	—	1%	—	—	—
SDS	—	—	—	1%	—	—
IGEPAL	–	—	—	—	1%	1%
EDTA	—	—	—	—	1 mM	1 mM
Benzamidin	—	—	—	—	1 mM	1 mM
DTT	—	—	—	—	—	10 mM

Preparation of RNA Solutions

The RNA aptamer was folded before each experiment to ensure the desired conformation. Here, the RNA, dissolved in milliQ-water, was heated to 95°C for 5 minutes. Afterwards, it was stored for 5 minutes on ice and then equilibrated for 15 minutes. Subsequently, the required salts for the buffer as well as the ligand was added.

Investigations on the RNA as well as on the RNA-ligand-complexes were performed in the buffer, which was used for the SELEX process (Tab. 4.1).

Precipitation of Nucleic Acids with Ammonium Acetate

For IR-experiments, a high concentration in the mM-range is required. This can be a challenge, especially for biological system, like RNA solutions. To achieve a mM-concentration of the complex of the photoswitchable ligand **CAP** and the RNA aptamer 42_{trunc}, the routine precipitation using ammonium acetate was used.

Here, 0.5 Vol.% ammonium acetate (7.5 M) and 2.5 Vol% ethanol were added to the solution of the RNA in milliQ-water with a concentration of 600 μM. After 10 minutes on ice, the solution was centrifugated for 15 minutes with 12400 rpm. The precipitation was washed using 200 μL ethanol solution (70%) four times, which was removed by centrifugation of the solution each round. In the end, the solution was removed and the pellet was dried.

Preparation of Compounds in Deuterated Solvents

Due to the intense absorption of water in the range between 1550 and 1700 cm^{-1}, which is also an interesting range for biological system, water (H_2O) as solvent is often exchanged against deuterated water (D_2O). If the sample was originally dissolved in pure water, the solvent can be easily exchanged either by removing the water from the

sample and then dissolve it in D_2O or by directly dissolve the compound in D_2O. The H/D-exchange in aqueous buffered solutions, however, is more critical.

A deuterated buffered solution can be in general prepared directly by addition of the required salts to D_2O. However, due to the small amount, which is needed for an IR-experiment (about 35 μL), a distinct volume of the usually already prepared aqueous buffered solution is lyophilized and the same amount of D_2O is added to the salt, which was kindly performed by Dr. C. Grünewald. Here, however, it should be noted, that small variations in the pH-value can be obtained for H_2O and D_2O.

4.2 Illumination Procedure

For photo-induced isomerization, light with a defined wavelength is used for a distinct excitation of only one of the isomers of the photoswitch. Therefore, either light-emitting diodes (LED) can be used or the required wavelength is selected from a light source with a variety of wavelengths by using optical filters.

In this work, both possible illumination procedures have been performed. For the illumination with LEDs, a Thorlabs LED driver DC4100 and DC4100-HUB was used in combination with mounted LEDs (Thorlabs M365L2 and M420L3). For the *trans*-to-*cis*-isomerization, the *trans*-isomer was illuminated within the $\pi\pi^*$-band using a LED with a central wavelength of 365 nm and a bandwidth (FWHM) of 9 nm (Fig. 4.1). In case of a *cis*-to-*trans*-isomerization, the *cis*-isomer was excited within the $n\pi^*$-band using a LED with a central wavelength of 420 nm with a bandwidth (FWHM) of 15 nm. Independent of the wavelength, for collimation of the beam an aspheric condenser lens with diffuser (ACL2520U-DG6-A) and an adjustable lens tube was used.

For illumination within a steady-state UV/vis-spectrometer SPECORD® S100 or S600 (Analytik Jena), the lens tube was adjusted to a cuvette holder (Thorlabs CVH100) on the second optical axis, while the first optical axis was put in the light beam of the spectrometer. The round holes in the second optical axis show a diameter of 9 mm, which is the size of the beam for illumination of the sample in a 10x10 mm-cuvette. For a uniform distribution within the sample, a small stir bar with a length of about 7 mm was added to the cuvette, which was stirred using a magnetic stirrer (Variomag, H+P Labortechnik GmbH), which was placed below the cuvette holder. For investigation with longer durations in a time range of hours, the cuvette holder (CVH100) was replaced by a comparable self-built cuvette holder with a connection to attach a thermostat (Haake F3-K) for temperature control during the measurement.

For measurements, in which this cuvette holder could not be used – FTIR- or CD-experiments, UV/vis-studies in a 1x10 mm-cuvette as well as time-resolved studies – an alternative illumination procedure was performed. Here, the LEDs were placed in a housing, where the light beam was focused on an optical fiber bundle with a diameter of about 1 cm. This optical fiber was then placed in the spectrometer or the optical setup in a way that the light beam overlaps with the measuring beam in the cuvette.

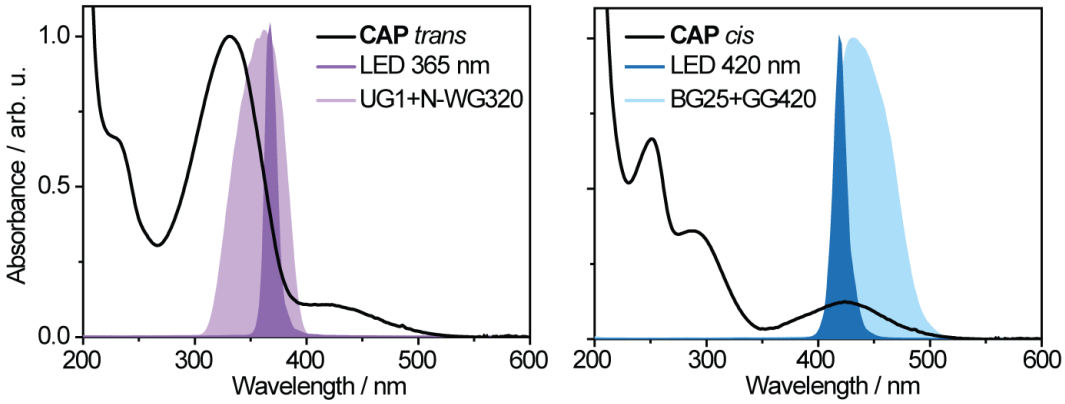

Figure 4.1: LEDs and filters (in combination with lamps) used for illumination. For *trans*-to-*cis*-isomerization, the *trans*-azobenzene, here exemplarily for **CAP**, was excited within the $\pi\pi^*$-band with a high-power LED with a wavelength of 365 nm or with a mercury-xenon lamp combined with the Schott band pass filter UG1 and the long pass filter N-WG320 (left). For *cis*-to-*trans*-isomerization, the *cis*-azobenzene was excited within the $n\pi^*$-band with a high-power LED with a wavelength of 420 nm or with a lamp in the visible range and a band pass filter BG25 and a long pass filter GG420 (right).

For the second illumination procedure, light sources, here Hamamatsu LIGHTNINGCURE Spot light source LC8 L9588, were used for the UV- (type -01) and the visible (type -04) range. A defined wavelength range was selected from the lamp spectrum using a combination of glass filters (Schott). While for the *trans*-to-*cis*-isomerization the band pass filter UG1 and the long pass filter N-WG320 were combined, which results in a central wavelength of 360 nm with a half width of about 60 nm. The *cis*-to-*trans*-isomerization was induced by using a band pass filter BG25 and a long pass filter GG420. This results in a central wavelength of 440 nm and a half width of about 40 nm.

The light is directed via an optical fiber in a small enclosed optical setup, as it was described before. The glass filters are put in a small filter holder cabinet behind the fiber, which is filled with distilled water to preserve the filter against heat damages.

The compounds were illuminated until a photo-stationary state was reached and therefore no changes in the ratio between the absorbance spectra of the *trans*- and the *cis*-isomer were detected by periodically measured UV/vis-spectra. Since the composition of the photo-stationary state is dependent on the wavelength, which was used for illumination, this central wavelength is used as an index in the following (e.g. $PSS_{365\,nm}$).

4.3 Steady-State Investigations

UV/vis-Measurements

UV/vis-spectra were measured using the simultaneous high-performance diode array spectrophotometer SPECORD® S100 or S600 (Analytik Jena). The integration time was selected in a range between 70 and 100 ms, which is dependent on the model as well as on the stability of the lamps, and the accumulation was chosen to be in a range between 5 and 20, which is dependent on the time intervals for cyclic measurements.

The sample was prepared in a way that the absorbance maximum of the absorbance bands under examination shows an optical density in a range between 0.6 and 1.0. Here, for azobenzenes usually the $\pi\pi^*$-band of the *trans*-isomer around 330 nm was used. The measurements were usually performed in a 10x10 mm quartz glass fluorescence cuvette (Hellma Analytics) to enable the illumination from the side during the measurements.

The determination of thermal reaction rates for the *cis*-to-*trans*-isomerization was performed either using the SPECORD® S100 with an external thermostat (Haake) or with the SPECORD® S600 and a Peltier cooled cell holder with external heat exchanging. In the latter case, the sample was originally tempered to the desired temperature within the cell holder, then illuminated externally using an external temperature insulation until the photo-stationary state was reached and consequently placed back into the cell holder to perform the desired temperature-dependent measurements. The small variations in temperature due to the external illumination are negligible due to the usually short illumination time. Studies on e.g. the thermal relaxation of the *cis*- to the *trans*-isomer were usually performed with varying time intervals of e.g. 10, 20 and 30 s between the detection pulses, so the optimal time interval for the measurement could be obtained.

Investigations on the fatigue resistance of azobenzenes were performed by cyclic measurements with simultaneous illumination with alternating LEDs in the UV- and the visible range. The illumination time of the two LEDs was chosen to nearly achieve a photo-stationary state. While the spectrometer recorded a full UV/vis-spectrum, which enables a correction of the baseline afterwards, with a distinct time interval, the LEDs were operated in an alternating way by a routine, which was self-programed in LabVIEW.

CD-Measurements

Investigations on the secondary or tertiary structure of compounds were performed using a CD-spectropolarimeter (Jasco J-810), which was purged with gaseous nitrogen. The measurements were performed in a spectral width between 210 and 450 nm with a scan speed of 50 nm/min and a band width of 1 nm.

For the CD-measurements, a 1x10 mm quartz glass cuvette was used. Since the spectrometer does not enable a simultaneous illumination during the recording of the

data, the samples were illuminated directly before the measurement. This, however, is only feasible for significantly long lifetimes for the *cis*-to-*trans*-isomerization.

FTIR-Measurements

For investigations on the vibrational structure of the compounds, IR-spectra were recorded using a FTIR-spectrometer (Bruker Vector 22 and Vertex 80). The sample chamber of the FTIR-spectrometer was purged using dry air or gaseous nitrogen to eliminate vibrational contributions of the IR-active components of air, especially gaseous water. After opening of the sample chamber or changing the sample, a waiting time of 45 minutes was complied until the next measurement was started to guarantee a comparable background signal.

The sample was placed in between two calcium fluoride windows with a Teflon® spacer with a thickness of 50 μm. For fixation of the teflon spacer and for closure of the two windows, PTFE paste (Carl Roth) was used. The concentration of the compound was in the mM-range. In case of an aqueous solution, deuterated buffered solutions were prepared.

Illumination of the sample was performed within the sample chamber by using optical fibers, which are guided through an isolated hole in the lid. The illumination wavelength can be changed on the outside of the spectrometer. Therefore, an opening of the sample chamber can be avoided. The IR-measurements are usually performed in an absolute manner with air used as background, which was also performed for the pure solvent. Like that, the solvent spectrum can be subtracted from the IR-spectrum of the sample afterwards. More often, however, difference spectra were obtained by measuring the IR-spectra of one photo-isomer as the background of the other photo-isomer. This enables often a better comparison of the samples due to the subsequent measurement of the spectra. However, only IR-bands, which changes upon irradiation, can be observed.

4.4 Time-Resolved Investigations

For all time-resolved experiments, UV/vis-spectra were recorded before and after the measurement to exclude photo-induced damages, degradation or changes in the composition of the sample, regarding photo-isomers.

Flash-Photolysis Experiments

The determination of kinetics in the time range between nanosecond and seconds was achieved by performing flash photolysis experiments in the UV/vis-range.

For excitation, a Nd:YAG-laser was used (Spitfire 600 Innolas Laser GmbH) with a central wavelength of 1064 nm and a pulse width of 10 ns. After second-harmonic generation (SHG) of the laser beam (532 nm), an optical parametric oscillator (OPO, GWU-Lasertechnik Vertriebsges. mbH) is used to generate the desired excitation wavelength. For excitation in the UV-range, an additional second-harmonic generation (SHG) is performed. Here, a pump pulse with a wavelength of 320 nm and a pulse energy of about 0.7 mJ with a spot size of about 1 cm^2 was obtained. The frequency of the pump pulse, which is 10 Hz, can be reduced by using an external optical shutter (Thorlabs), which is placed behind the pump pulse generation.

For detection of the absorbance changes in the UV/vis-range, a xenon flash lamp (Hamamatsu) is used for pulsed detection beams with a wavelength range between 300 and 650 nm. For broadband detection, a charge-coupled device (CCD) camera (PI-MAX3, Princeton Instruments) and a spectrograph (Acton SP2150, Princeton Instruments) were used.

To obtain information on the light-induced absorbance changes, the probe pulse was used to detect the intensity of the transmitted light of the sample before excitation and a second time after a distinct time delay with respect to the pump pulse. Like that, a broadband detection is obtained for the ns-to-s time range with a temporal resolution of about 100 ns, which is set due to the pulse width of the laser, the instrument response function (IRF) and the electronic jitter.

A quartz glass fluorescence cuvette (10x4 mm) was used for the measurements, while the 10 mm pathway was used for the detection pulse and the 4 mm pathway for the excitation in a perpendicular manner.

UV/vis-pump UV/vis-probe Experiments

For investigations on the kinetics in the fs/ps-range a Clark-MXR CPA 2001 laser system is used, which generates laser pulses with a central wavelength of 775 nm, a repetition rate of 1 kHz, a laser power of about 800 mW and a pulse width of about 150 fs.

In this work, only pump pulses with a distinct wavelength in the UV range (290, 320 and 435 nm) were generated (Tab. 4.2). Here, a combination of a NOPA process and a subsequent sum frequency mixing was used (see subsubsection 2.2.2). For pulses with a wavelength of 290 nm, a NOPA pulse with a wavelength of 460 nm

Table 4.2: Sum-frequency generation for UV-pump pulses used in this work.

λ_{SFM}	λ_{NOPA}	BBO
290 nm	460 nm	$\Theta = 39°$, d = 0.5 mm
320 nm	545 nm	$\Theta = 36°$, d = 0.1 mm
435 nm	990 nm	$\Theta = 26°$, d = 0.1 mm

was used, which was further spatially and temporally overlapped with a part of the fundamental pulse of 775 nm (about 120 μJ) in a BBO-crystal with a cut-angle of 39° (d = 0.5 mm) in a sum-frequency mixing (SFM) process (type-I). The angle between the NOPA and the fundamental pulse is about 5°. While for the NOPA pulse a focusing mirror is used, the fundamental laser pulse is focused about 1 cm behind the BBO-crystal by using a lense with a focal length of 300 mm.

The generation of pump pulses in the UV range with a wavelengths of 320 nm and 435 nm was performed in an equivalent manner by using NOPA pulses and BBO crystals with properties defined by Tab. 4.2. For a facilitation of the adjustment of the spatial overlap of the NOPA pulse with a wavelength of 990 nm with the fundamental laser pulse, a second harmonic generation (SHG) was performed for the NOPA pulse between the setup of the NOPA and the SFM by using a BBO-crystal ($\Theta = 30.2°$). This results in a wavelength of 495 nm, which enables a better adjustment of the spatial overlap. The resulting pump pulses showed a pulse width of about 200 fs and an energy of about 25 nJ.

The probe pulse was generated by a performance of a supercontinuum generation, in which the fundamental laser pulse is focused slightly in front of a calcium fluoride window. To prevent this window from damages, it is moved in the *x*,*y*-plane continuously. Light with a wavelength range from 340 to 650 nm was obtained.

Both pulses are focused in the same spot within the sample, while the spot size of the pump pulse is slightly larger with a size of about 200 μm than the probe pulse (100 μm) to ensure that the detected signal contains only signals of an excited sample. A quartz cuvette with a path length of 1 mm was used, which is moved constantly in the *x*,*y*-plane to ensure a fresh sample for each measurement. All measurements have been captured under magic angle polarization geometry.

For excitation of the *trans*-isomer at 320 nm, the concentration was chosen, so that the $\pi\pi^*$-band of the *trans*-isomer shows an absorbance band with an optical density of about 0.8. For the excitation of the *cis*-isomer at 450 nm, the concentration of the sample was chosen, that the $n\pi^*$-band of the *cis*-isomer in the photo-stationary state ($PSS_{365\,nm}$) shows an optical density of about 0.3. To guarantee a comparable photostationary composition of the sample during the experiment, the sample was irradiated constantly with a wavelength of 420 and 365 nm, respectively, as described in section 4.2.

UV/vis-pump IR-probe Experiments

For investigations on the vibrational changes in the fs/ps-time range upon excitation with UV-light, the generation of the pump pulse with a wavelength of 320 nm is equivalent to the UV/vis-pump UV/vis-probe setup. However, the excitation energy is slightly higher with a power of about 40 nJ, although the energy of the fundamental laser pulse for the SFM process is less intense with about 100 μJ.

In this work, the probe pulse for the detection of absorbance changes covers a general wavelength range of 5.6 to 8.5 μm.

The generation of the IR-probe pulse uses a two-step OPA and a subsequent DFG process (section 2.2.3).[163] The wavelengths, which were used for the generation of the mid-IR pulses can be found in Tab. 4.3. The wavelength of the mid-IR-pulse, which is generated by a DFG process, as well as the wavelength of the idler pulse can be calculated in dependence of λ_{signal} by using the equations 4.1.

$$\lambda_{DFG} = \frac{\lambda_{signal} \cdot 0.775\mu m}{1.55\mu m - \lambda_{signal}} \qquad \lambda_{idler} = \frac{1}{\frac{1}{0.775\mu m} - \frac{1}{\lambda_{signal}}} \tag{4.1}$$

For calibration of the wavelength range, channel 11 (of 32) was used. A grating with a blaze wavelength of 6 μm and a ruling of 150 lines/mm was used, which has a resolution of 11.3 nm per channel. The pump and the probe pulse overlap spatially in the sample with a spot size of 300 μm for the pump pulse and 250 μm for the probe pulse. The time-resolution was estimated by the coherent artifacts around the temporal zero point to a value of about 0.3 ps.

The sample is placed between two calcium fluoride windows with a diameter of one inch with a teflon spacer of 50 μm thickness, like for the FTIR-measurements. This window is rotated in a plane perpendicular to the pump and probe pulse and additionally moved in this perpendicular *x*-direction.

Table 4.3: Wavelength ranges for the IR-probe pulses used in this work.

probe range				
$[cm^{-1}]$	$[\mu m]$	λ_{DFG} $[\mu m]$	λ_{signal} $[\mu m]$	λ_{idler} $[\mu m]$
1790-1684	5.587-5.937	5.700	1.365	1.794
1687-1593	5.927-6.277	6.040	1.374	1.778
1629-1541	6.137-6.487	6.250	1.379	1.769
1598-1513	6.257-6.607	6.370	1.382	1.764
1520-1444	6.577-6.927	6.690	1.389	1.753
1325-1266	7.547-7.897	7.660	1.408	1.725
1274-1220	7.847-8.197	7.960	1.413	1.717
1230-1180	8.127-8.477	8.240	1.417	1.711

Part III

Results

Chapter 5

Water-Soluble Photoswitches for Biological Use

The incorporation of photoswitches in biological molecules is a well-established field in research.[164] The use of photo-chromic compounds enables the spatial and temporal control of conformational changes of biomacromolecules, which allows investigations on structural and dynamical properties of the biological system for the understanding of biological mechanisms. Moreover, due to the direct coupling of structure and function in nature, this structural rearrangement entails an influence on the biological function, which can be consequently, controlled by using light as an external trigger.

This concept was successfully implemented by introducing photoswitches in biological systems for the photo-control of folding events in, e.g. a collagen triple helix,[153,154] the photo-regulation of DNA transcription[156–158] or even RNA dehybridization.[161,162] Astonishingly, the photo-isomerization of e.g. azobenzene can also be used to regulate ion channels,[72,73] glutamate receptor[165–167] or inhibitors of human carbonic anhydrase II.[168] An application of photoswitches *in vivo* was successfully proved by e.g. Wachtveitl *et al.*.[169,170]

The photoswitches, e.g. azobenzene, can be introduced in the macromolecule either via covalent bonds by using e.g. small photoswitchable peptides[103,150,171] or via non-covalent interactions between the photoswitch and the biomolecule. A variety of examples for photoswitches in aqueous media are known,[172] however, often this application is only possible due to the covalent coupling of the photoswitch to the water-soluble biomolecule, since the most prominent candidates - azobenzenes and spiropyrans - are usually highly insoluble in water. Thus, incorporation of these insoluble compounds into biological systems via non-covalent interactions would be impossible. However, due to the high synthetical effort of introducing photoswitches covalently into the biomolecule, the binding via interactions is an attractive alternative. Therefore, the water-solubility of photoswitches is a major task. Another challenge is the fact that photo-chromic compounds often show undesirable properties in aqueous media, like hydrolysis or accelerated rate constants for thermal back reactions. Moreover, due to the sensibility of biomolecules against UV-light, the used wavelength for the photo-induced reaction of the photoswitch should be in a spectral range, where nucleic acids etc. do not absorb.[149,165,170]

In this chapter, the challenge of finding water-soluble azobenzenes with reasonable photo-physical properties will be discussed in section 5.1. Moreover, the isomerization behavior of water-soluble hydroxy-substituted azobenzenes is shown in section 5.2.

5.1 Water-Soluble Azobenzenes

Due to the highly hydrophobic structure of azobenzenes, only a poor solubility in water is observed. Therefore, the choice of substituents is very important, if a photoswitch is supposed to be used in aqueous solution.

Consequently, to achieve a better solubility, it is necessary to change either the backbone structure into a better soluble version or hydrophilic substituents can be added to the existing azobenzene structure. By changing the aromatic structure of the azobenzene scaffold into, e.g. heterocyclic aromatics (Fig. 5.1b), the water solubility is supposed to increase. By using nitrogen-containing aromatics, for example, an additional electron donating group is included in the structure, which has also the ability to perform interactions, like hydrogen bonds, with biological systems, e.g. RNA. This is highly important, if the photoswitch is supposed to be used as a non-covalently bound ligand, which interacts with macromolecules.

Therefore, it is beneficial, if the hydrophilic side groups, which can be attached to the phenyl rings, have the ability to perform interactions. One possibility is the use of primary amine-, amide- (Fig. 5.1a) or hydroxy-groups (Fig. 5.2), which show, in general, a good solubility in water. Moreover, functional groups, which are known for a good water solubility, are sulfonamides (Fig. 5.2c and Fig. 5.3d). Therefore, these groups can often be found in therapeutics. Another concept for an increase of hydrophilicity of azobenzene derivatives is the addition of amino acids on both sides of the phenyl rings. Here, the small amino acids glycine and alanine (Fig. 5.1c), as well as proline were studied (Fig. 5.3c).

Amine- or amide-groups in *para*-position were added to the aromatic rings of the azobenzene, also in terms of amino acids, like glycine and alanine.

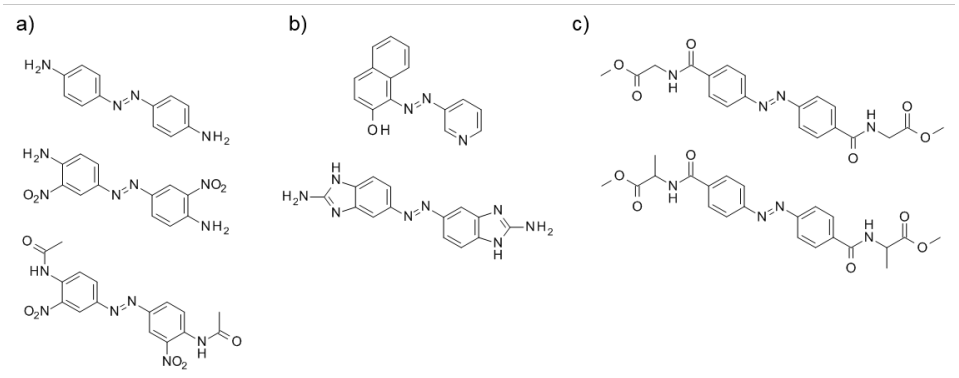

Figure 5.1: Chemical structures of azobenzene derivatives, which show insufficient solubility in aqueous solution. Chemical structures contain amino-groups (a) or heterocyclic aromatics (b) or rely on a peptidyl structure, which contain amino acids (glycine or alanine) as substituents (c).

However, the solubility in aqueous solution could not be increased sufficiently. Consequently, only concentrations less than the μ-molar range could be achieved in aqueous buffered solution (Fig. 5.1). Moreover, also changes within the aromatic structure from a homocyclic into a nitrogen-containing heterocyclic aromatic could not compensate the hydrophobic interactions of the carbon scaffold (Fig. 5.1 b), resulting in a still insoluble component. Although hydrophilic substitutions have been performed, the hydrophobic properties of the azobenzene scaffold still dominate the properties of the photoswitch in a variety of examples (Fig. 5.1). Interestingly, by increasing the number of amine-groups from a diamino-azobenzene into, e.g. a tetraamino-azobenzene, the component shows sufficient water solubility (Fig. 5.2a). Also the choice of hydroxy-groups was more promising regarding the solubility in contrast to amine-groups.

Moreover, therapeutics were studied with structures, which are based on an azobenzene scaffold and contain sulfonamides (Fig. 5.2c). The use of known therapeutics has two advantages. While no complicated synthesis of the substance is necessary, also some chemical properties are already known. Indeed, sulfonamides as additional functional groups show a good solubility in water of the azobenzene. Consequently, a variety of hydroxy-substituted azobenzenes as well as bicyclic azobenzenes, some in addition with sulfonamide groups, could be studied in aqueous solution by UV/vis-spectroscopy (Fig. 5.2).

Each of the components shown in Fig. 5.2 show a *trans*-to-*cis*-isomerization, which could be induced by illumination with UV-light (365 nm) in dry DMSO. The *cis*-isomer could be reversibly converted into the *trans*-azobenzene by the use of visible light (420 nm). The UV/vis-absorbance spectra revealed sufficient switching amplitudes.

However, in an aqueous solution, for none of these compounds, the *cis*-isomer could be accumulated by excitation of the *trans*-isomer on a time scale larger than seconds. One characteristic, they all have in common, is a hydroxy-group in either a *para*- or an *ortho*-position with respect to the azo-group. Consequently, this functional group has an influence on the isomerization behavior of the azobenzene derivatives in water.

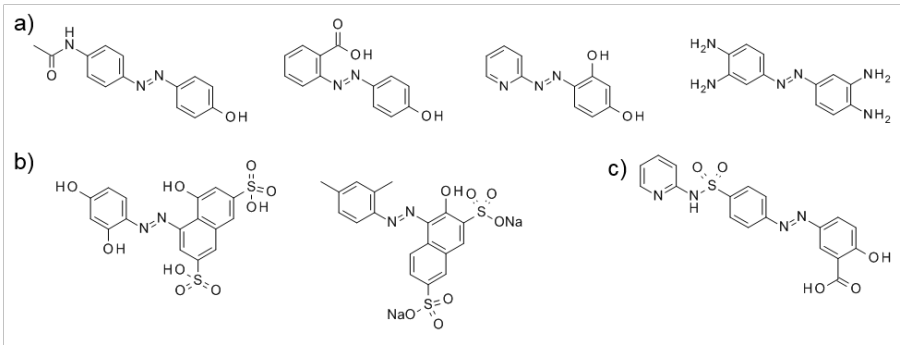

Figure 5.2: Chemical structures of azobenzene derivatives, for which no *cis*-isomer could be accumulated in aqueous solution by excitation of the *trans*-isomer. Chemical structures contain hydroxy- and amino-groups (a) and bicyclic aromatics (b) or rely on a sulfonamide structure (c).

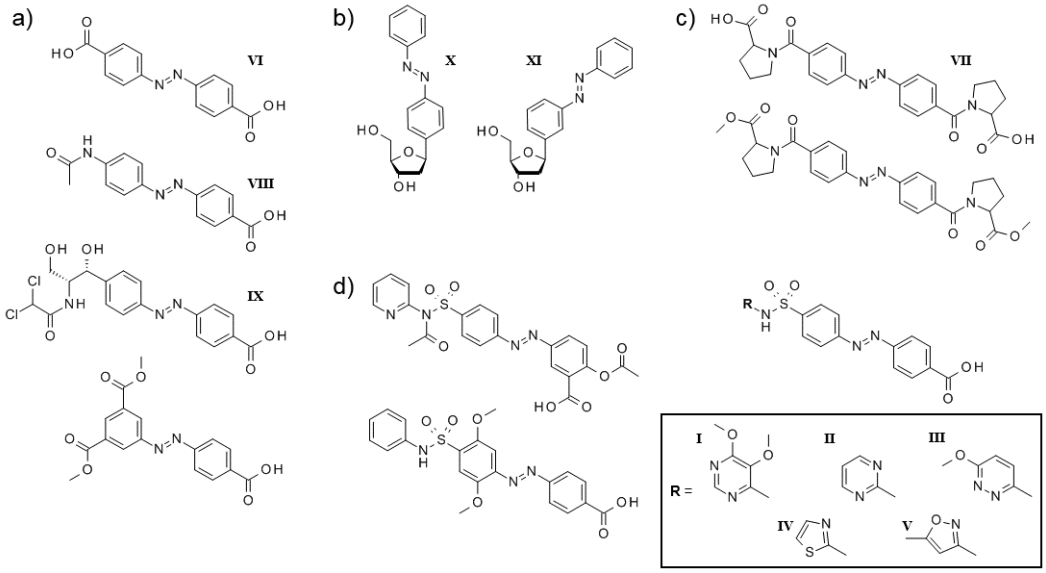

Figure 5.3: Chemical structures of azobenzene derivatives, which show an isomerization behavior in aqueous solution. Chemical structures contain carbon acid- (a) or desoxyribose-groups (b) or rely on a peptidyl structure, which contain amino acids (proline) as substituents (c) or on a sulfonamide structure (d).

A detailed study on the influence of hydroxy-groups on the electronic structure and the isomerization behavior can be found in section 5.2.

By avoiding hydroxy-groups in *ortho*- and *para*-position or by acetylation of this group (Fig. 5.3d), not only a sufficient solubility in water, but also a significant isomerization behavior could be observed for a number of derivatives, e.g. containing sulfonamides. However, the variation of the aromatic rings, connected to the azobenzene via a sulfonamide bridge, from a phenyl ring to a pyridine, pyrimidine and pyridazine or thiazole and an isoxazole has only a small effect on the solubility. The UV/vis-spectra of the different derivatives show a very similar absorption behavior (Fig. 5.4a). In general, the $\pi\pi^*$-bands of the *trans*-isomer of these compounds are located at about 330 nm and the corresponding $n\pi^*$-bands at about 425 nm. No significant shift by variation of the side chain can be observed. Only by addition of a thiazole to the sulfonamide (compound **IV**), the absorption spectrum of the *cis*-isomer is slightly shifted hypsochromically, which can be seen by comparison of the isosbestic points of each compound as well as in the absorbance difference spectrum. This can be explained by the less pronounced positive mesomeric effect (+M) of the sulfur with respect to the oxygen, causing a less pronounced red-shift of the spectrum.

Regarding the comparison of the absorbance bands and also the switching amplitudes of the derivatives, also the absorbance bands of the additional heterocyclic rings should be taken into account. While thiazoles and isoxazoles show only an absorption band below 230 nm (thiazole: band A at 233 nm and band B at 205 nm; isoxazole: 211 nm),[173,174] pyrimidines show an absorption band around 240 nm and an additional band at 270 nm, which can reach to about 310 nm.[175] For compound **I**, this absorption band can be seen at about 270 nm in Fig. 5.4a. The absorption band of

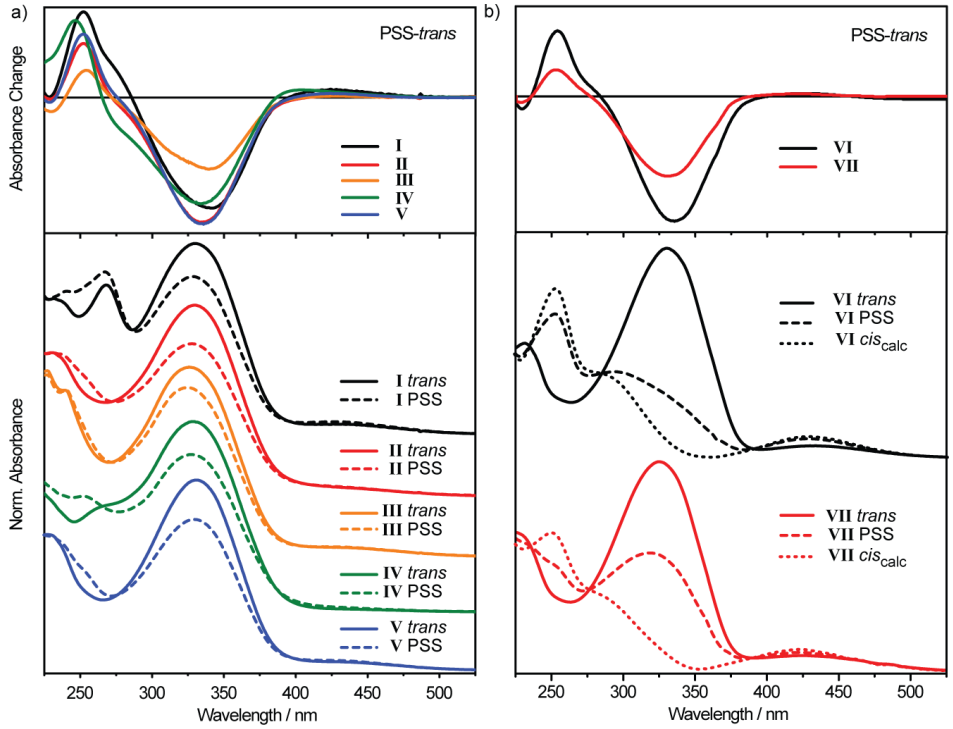

Figure 5.4: UV/vis-spectra of the *trans*-isomer and the photo-stationary state (PSS_{365nm}) of the photoswitchable azobenzene derivatives consisting a variation of heteroaromatics (a, I to V) and dicarboxy-azobenzene (b, IV) and proline-azobenzene-proline (b, VII) in aqueous solution; for chemical structures, see Fig. 5.3. Absorbance changes during photo-isomerization are indicated by the absorbance differences (top). Spectra are normalized on the absorption maximum of the $\pi\pi^*$-band of the *trans*-isomers around 330 nm. In panel b, also the calculated pure *cis*-spectra of compound VI and VII can be seen.

pyridazines at 300 nm can even be seen until 340 nm.

Consequently, the absorption bands of the heterocyclics overlap with the absorption bands of the azobenzene varyingly strong for the different compounds. This is the reason for the less pronounced absorption difference spectrum of the compound (compound **III**). However, for each of these compounds the switching amplitude is relatively small with an amount of the *cis*-isomer in the photo-stationary state of only slightly more than 20%, which can be estimated by the calculation of a pure *cis*-spectrum from the *trans*-spectrum and the corresponding absorbance changes during isomerization (see section 3.1).

A significantly increased switching amplitude can be found for dicarboxy-azobenzene, compound **VI**. The photo-stationary state contains about 76% *cis*-isomer, which is even slightly more than for the unsubstituted azobenzene (Fig. 3.4). The thermal reaction rate for the *cis*-to-*trans*-isomerization is $k = 1.4 \cdot 10^{-4}$ s^{-1} at room temperature. Moreover, compound **VI** shows a high fatigue resistance with no indication of degradation or photolysis. This compound shows good (photo-)chemical properties. So far, however, it was not pursued for a further biological use.

The azobenzene-derivative with a symmetrical substitution with the amino acid pro-

line, compound **VII**, shows a less promising switching amplitude with a photo-stationary state containing a *cis*-amount of 50%. In the UV/vis-measurements on the thermal reaction from the *cis*- to the *trans*-isomer and the fatigue resistance, fluctuations in absorbance were observed, which are larger than the signal-to-noise ratio of the measurement. This can be explained by the *cis*-*trans*-isomerization of the amino acid proline. Due to that, different conformations can be present depending on the conformation of the prolines, which have a slight influence on the electronic structure of the azobenzene. Consequently, because of this conformational change within the backbone structure of this derivative, a biological use, especially as a rigid photo-responsive ligand, is not feasible.

The derivatives **VIII** and **XI** will be characterized in section 6.2 for the use as a photoswitchable ligand, interacting with a RNA aptamer. The spectral characterization of the compound **X** and **XI** will be found in section 6.1, which will be discussed as a suitable photoswitch for a covalent incorporation into RNA structures.

5.2 Photo-Isomerization of Hydroxy-Substituted Azobenzenes in Water

For applications of azobenzenes in water, substitutions on the highly hydrophobic framework with water-soluble side chains are indispensable, especially for the use as non-covalently binding ligands. Depending on the intended purpose, the choice of substituents should be digested thoroughly. While sterically demanding substituents can disturb the binding of the azobenzene and the biomolecule, too small derivatives are either not recognized by the macromolecules or it may bind unspecifically. Moreover, to be applicable, the synthesis should not be unnecessarily challenging.

Functional groups, which are often used as substituents, are hydroxy-groups. These groups are not only small, easy for synthesis and highly soluble in water, but have in addition the ability to build hydrogen-bonds outstandingly. Due to these reasons, hydroxy-substituted azobenzenes are frequently used in pharmaceutical applications as drugs, e.g. antibiotics. One of the examples, which should be noted here, is the azobenzene Sulfasalazine, which belongs to the disease-modifying antirheumatic drugs (DMARDs). It is used in the treatment of inflammatory diseases, e.g. arthritis. In this application, the characteristics of the photoswitch, more precisely the ability of photo-isomerization, are irrelevant. For investigations on water-soluble azobenzenes, however, a listed drug with an azobenzene-scaffold appears reasonable.

In the following sections, the photo-switchability of Sulfasalazine in an aqueous buffered solution will be discussed (subsection 5.2.1).[176] Moreover, a detailed study on the influence of hydroxy-substitution on the photo-isomerization mechanism of azobenzenes and its position-dependence is shown (Subsection 5.2.2).

5.2.1 Photo-Isomerization of Sulfasalazine

The commonly used Sulfasalazine (**SSZ**) (2-hydroxy-5-[(E)-2-(4-[(pyridin-2-yl)sulfamoyl]phenyl)diazen-1-yl]benzoic acid) consists of an azobenzene scaffold with a hydroxy-group in *para*-position relative to the azo-group and a neighboring carboxylic acid. This structure is coupled to a pyridine via a sulfonamide (Fig. 5.5a). Sulfasalazine is highly soluble in water – in this study a phosphate-buffered solution (PBS) with a pH-value of 7.4 was used to simulate physiological conditions.

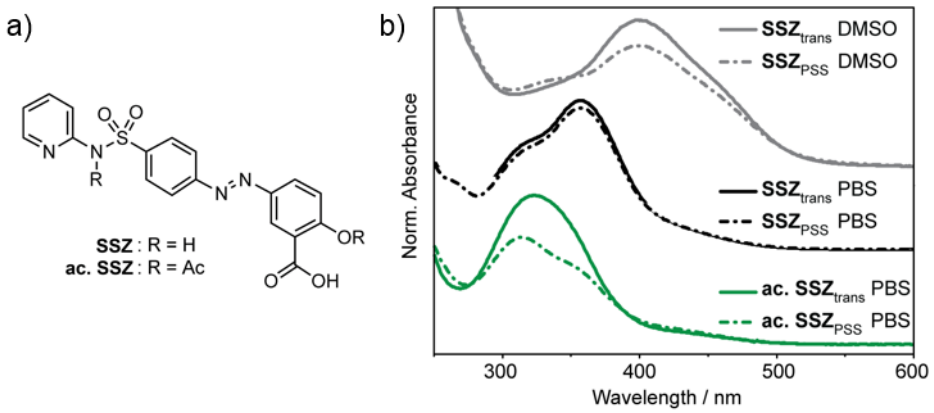

Figure 5.5: a) Chemical structures of Sulfasalazine (**SSZ**) and acetylated Sulfasalazine (**ac. SSZ**). b) Steady-state UV/vis-absorption spectra of the *trans*-isomer and of the photo-stationary state (PSS = PSS_{365nm}) of Sulfasalazine in DMSO and PBS and acetylated Sulfasalazine in PBS.

In Fig. 5.5b, the UV/vis-absorption spectrum of Sulfasalazine in PBS-solution is shown for the *trans*-isomer. A structured $\pi\pi^*$-absorption band from 280 to 400 nm can be seen with two absorption maxima at 320 nm and 360 nm. Moreover, contributions of an $n\pi^*$-band can be seen between 400 and 500 nm, which overlaps with the $\pi\pi^*$-band. Illumination within the $\pi\pi^*$-band of the *trans*-isomer with light with a wavelength of 365 nm results in the spectrum of the photo-stationary state (PSS_{365nm}), which differs only slightly from the spectrum of the *trans*-isomer. Therefore, neither a decrease of the absorbance bands of the *trans*-isomer, nor an increase of the absorbance band of the *cis*-isomer can be observed. Consequently, no photo-isomerization can be detected in the steady-state spectrum for **SSZ** in PBS.

Although changes within UV/vis-absorption spectra in different solvents are not unusual, the absorption spectrum of **SSZ** in dry DMSO, however, looks significantly different. The absorbance maximum at 360 nm in aqueous solution is red-shifted to 400 nm. Moreover, the $\pi\pi^*$-band of the *trans*-isomer is broadened significantly with an additional contribution at 450 nm. The $n\pi^*$-band is located above 500 nm. After illumination with light with a wavelength of 365 nm, two clear isosbestic points can be detected at 350 nm and at 500 nm. While the absorption of the $\pi\pi^*$-band of the *trans*-isomer decreases between 350 and 500 nm, the $\pi\pi^*$-band of the *cis*-isomer at 327 nm and the $n\pi^*$-band of the *cis*-isomer at 536 nm increase. Therefore, in contrast to aqueous solution, a photo-isomerization of **SSZ** can be observed in dry DMSO.

However, the addition of already a few μL of water to the dry DMSO solution shifts the absorption maximum of the $\pi\pi^*$-band of the *trans*-isomer about 40 nm to lower wavelength. Interestingly, this addition of water also results in a loss of switchability on the steady-state time range.

Consequently, **SSZ** shows an isomerization behavior in dry DMSO, which cannot be observed in the second to minute time range by addition of water. Therefore, the water molecules have a strong influence on the isomerization mechanism of **SSZ**. Investigations on this drastic change of the photo-physical properties of the azobenzene, the substitution pattern of **SSZ** was regarded. Since no accumulation of *cis*-azobenzene was observed for a variety of other azobenzene derivatives, which contain a hydroxy-group in either *para*- or *ortho*-position (Fig. 5.2), the hydroxy-group of **SSZ** was acetylated to find out whether it has an influence on the isomerization. For reasons of synthesis, also the sulfonamide was acetylated. Comparing the absorption spectrum of the acetylated and the original Sulfasalazine (Fig. 5.5), a clear blue-shift of the $\pi\pi^*$-band of the *trans*-isomer of the acetylated Sulfasalazine (**ac. SSZ**) to 328 nm is observed, which is accompanied by the loss of structure within the absorbance band. More importantly, however, a significant photo-isomerization can be detected after excitation at 365 nm. A decrease in the absorption spectrum of the *trans*-isomer and an increase of the $n\pi^*$-band of the *cis*-isomer at about 420 nm are visible, which is a typical azobenzene-like absorption difference. Consequently, acetylation of the hydroxy-group of the azobenzene leads to a recovery of the photo-isomerization of **SSZ** in water.

The fact that no isomerization of **SSZ** in aqueous solution in the second to minute range can be detected can be explained by two possible reasons. One possibility is, that an excitation of the *trans*-isomer leads only to an excited *trans*-isomer, which further relaxes back into the ground state of the *trans*-isomer. In that case, no photo-isomerization would occur. The second possible explanation is a fast thermal reaction from the formed *cis*- to the *trans*-isomer on the μs- to ms-time scale, so no absorbance changes can be detected in the second to minute time range. Therefore, investigations on the *trans*-to-*cis*-isomerization mechanism of **SSZ** and **ac. SSZ** in PBS were performed in the ps-range by UV/vis-pump UV/vis-probe experiments.

Instantaneously after excitation at 320 nm, two excited state absorption bands (ESA) between 400 and 500 nm (ESA_1) and between 500 and 600 nm (ESA_2) can be observed for **SSZ**. Moreover, a strong ground-state bleach (GSB) is located below 400 nm. The relaxation processes after excitation can be described by four exponential functions with sufficient accuracy (Tab. 5.1). In Fig. 5.6, an increase of the absorbance difference of the two ESA-bands can be seen, while positive bands at 400 and above 450 nm slightly decrease. This decay is described by the lifetime τ_1 of 400 fs. Since no absorbance change can be observed for the GSB at that delay time, this process is assigned to an excited states dynamic – the fast $S_2 \rightarrow S_1$-transition.

The decay of the S_1-state is described by the two additional time constants τ_2 and τ_3. While the decay-associated spectra (DAS) of lifetime τ_2 show a broad contribution

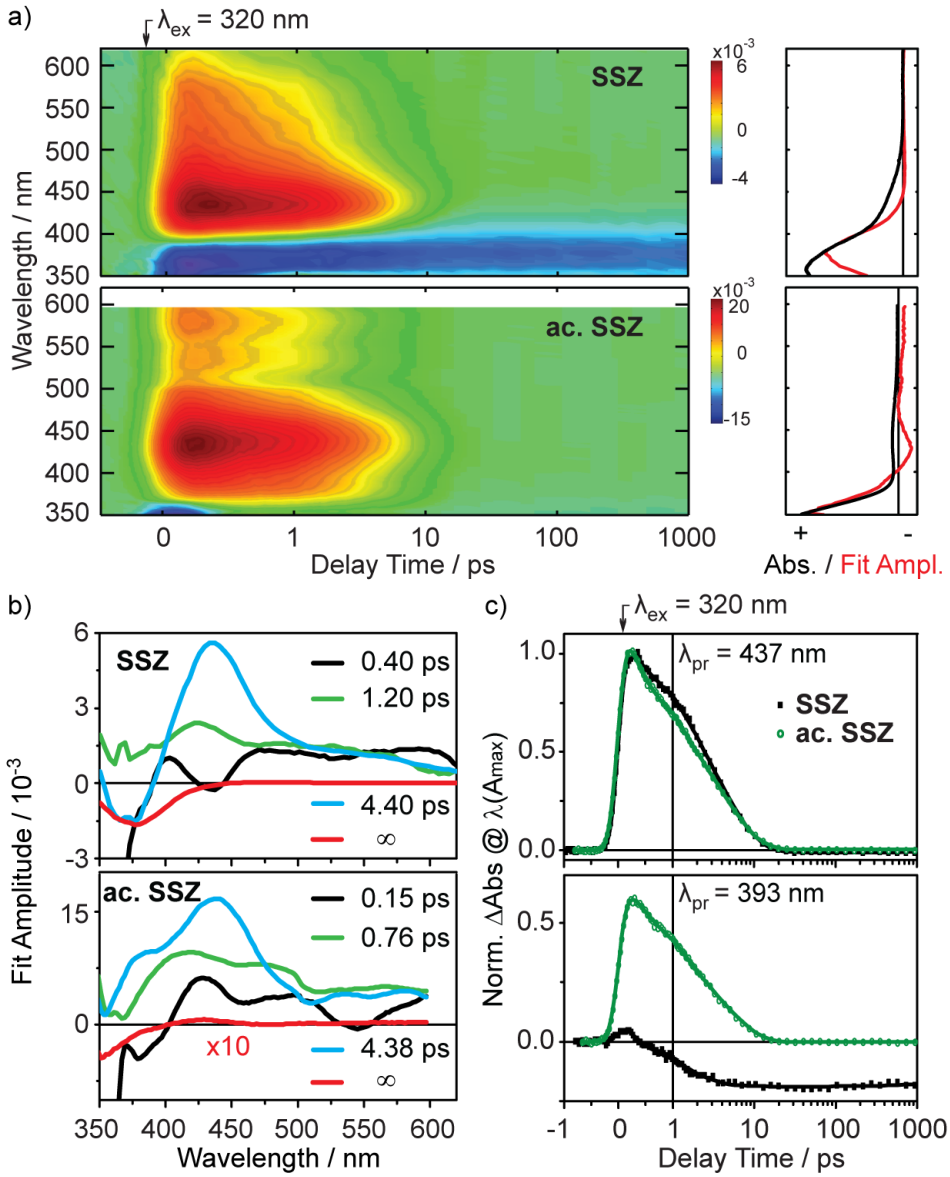

Figure 5.6: a) Transient absorption difference spectra of Sulfasalazine (top) and acetylated Sulfasalazine (bottom) in PBS (with addition of 10 % DMSO). Comparison of absorption spectra before excitation (black) and the inverse decay-associated spectra of the longest lifetime (red) can be found. b) Decay-associated spectra of Sulfasalazine and acetylated Sulfasalazine. c) Transients at 393 and 437 nm of both samples are compared by normalization at the absorption maxima of both samples around 435 nm.

Table 5.1: Lifetimes, resulting from global lifetime analysis, describing the relaxation processes during *trans*-to-*cis*-isomerization of Sulfasalazine **SSZ** and acetylated Sulfasalazine **ac. SSZ** after excitation at 320 nm in PBS in a UV/vis-pump UV/vis-probe experiment.

Lifetime [ps]	**SSZ**	**ac. SSZ**
τ_1	0.40	0.15
τ_2	1.20	0.76
τ_3	4.40	4.38
τ_4	∞	∞

over the whole spectral range, the time constant τ_3 describes mostly the decay of the ESA_1-band at 440 nm and of the GSB at 360 nm. These two lifetimes are assigned not only to the relaxation of the *trans*-isomer back into the *trans*-ground-state, but also the transition from the excited *trans*-isomer into the ground-state of the photo-product *cis*-**SSZ**. The product absorption (PA) of the *cis*-isomer can be slightly seen between 450 and 500 nm after about 20 ps. At that time, the system is completely relaxed to the ground state and the ground states of the *trans*- and the *cis*-isomer are (re-)populated. Although vibrational cooling may contribute, no separate lifetime was necessary to describe the data. At later delay times, the GSB is still observable due to the formation of a photo-product and consequently a loss of initial sample. An infinite lifetime τ_4 is used to display the absorbance difference at the longest delay time of about 1.8 ns.

Comparing the inverse DAS of the infinite lifetime τ_4 with the steady-state spectrum before excitation (Fig. 5.6), in general, there is quite a good agreement: However, the maximum of the absorption difference of the inverse DAS around 370 nm does not coincide with the maximum of the steady-state spectrum at about 360 nm, which could indicate a slow conversion reaction beyond the 1 ns time scale.

Comparing these results of **SSZ** to the transient absorption spectrum of **ac. SSZ** in PBS, the spectral as well as the dynamical behavior are quite similar. While the lifetimes of **ac. SSZ** are only slightly shorter, the corresponding DAS spectra coincide quite well with the spectrum of **SSZ**. The only significant difference can be found in the spectral range below 400 nm. While **SSZ** shows an intense GSB, for **ac. SSZ**, an ESA-band can be detected at 393 nm. Due to the intense blue-shift of the $S_0 \rightarrow S_2$-transition of **ac. SSZ** of 32 nm with respect to **SSZ**, this ESA-band is not overlapped by the GSB of **ac. SSZ**. A clear product absorption is observed at about 440 nm after a delay time of about 20 ps. The comparison of the inverse DAS of the infinite lifetime τ_4 with the steady-state spectrum of **ac. SSZ** perfectly coincides in the $\pi\pi^*$-band.

Comparing the transients at 393 nm of both samples (Fig. 5.6c), the same dynamics can be clearly seen for both samples at 437 nm. However, also at a wavelength of 393 nm, a very similar dynamical behavior of **SSZ** and **ac. SSZ** is detected, which is only changed by a negative offset in case of **SSZ**. This is caused by the intense overlap of the ESA-band with the GSB. Consequently, this ESA-band at 393 nm, found for **ac. SSZ** is also present for **SSZ**.

In summary, only slight differences of the transient absorption spectra of **SSZ** and

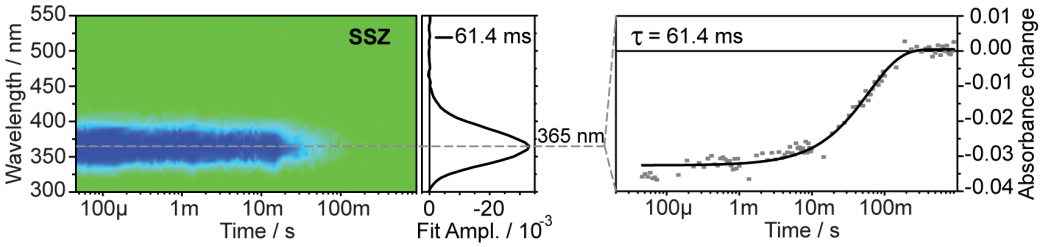

Figure 5.7: Transient absorption difference spectrum of Sulfasalazine in PBS in the μs-ms-range (left), the corresponding decay-associated spectrum (middle) and the transient at 365 nm (right).

ac. SSZ can be detected, which refer to the ground-state behavior, more precisely to the $S_0 \rightarrow S_2$-transition. The energetic as well as dynamical behavior of the excited states of the two compounds are very similar to each other. As a result, a *trans*-to-*cis*-isomerization after excitation of the *trans*-isomer occurs for acetylated as well as for the pure Sulfasalazine in PBS on a picosecond time scale.

Due to the fact, that a photo-isomerization is detectable for **SSZ** in the ps-range, which, however, is not observable in the steady-state spectrum anymore, a fast reaction from the *cis*- to the *trans*-isomer is assumed. Therefore, flash photolysis measurements were performed for **SSZ** in PBS with an excitation wavelength of 320 nm and a broadband detection between 300 and 550 nm (Fig. 5.7). An intense GSB can be detected between 340 and 400 nm with a central wavelength of 365 nm, which decays mono-exponentially with a lifetime of 61.4 ms. Unfortunately, no positive feature of the $n\pi^*$-band of the *cis*-isomer is obtained above 400 nm. After 300 ms, no absorption difference can be detected anymore. Therefore, the thermal reaction from the *cis*- to the *trans*-isomer of **SSZ** in PBS occurs with 61.4 ms, which explains the missing enrichment of the *cis*-isomer in the second to minute time range. This is in good agreement to earlier studies on *para*-substituted hydroxy-azobenzenes.[177,178]

5.2.2 Position-Dependent Influence of Hydroxy-Substituents on the Isomerization Mechanism of Azobenzenes

In earlier studies, a variety of experiments were reported regarding the fast thermal reactions from the *cis*- to the *trans*-isomer of hydroxy-substituted azobenzenes depending on the substitution pattern and derivatives[178] as well as on physical properties like the pH-value.[179] This fast thermal reaction is only observed in the case of *ortho*- and *para*-substituted hydroxy-azobenzenes. While for *ortho*-substitution, the lifetime of this reaction is independent of the solvent, for *para*-hydroxy-azobenzenes the lifetime decelerates in aprotic solvent, like dry DMSO, where isomerization can still be detected in the time regime of seconds (see section 5.2.1). In case of *meta*-substitution, however, an accumulation of the *cis*-isomer is possible on a time scale longer than minutes. Therefore, the lifetime of the *cis*-to-*trans*-isomerization is highly position-dependent. This effect is often explained by the keto-enol-tautomerism of the hydroxy-group (Fig. 5.8). A proton transfer is assumed to happen from the hydroxy- to the azo-group resulting in a hydrazone structure. For *para*-substitution, a formation of an azobenzene dimer is often discussed,[180] while the general idea includes a water-chain between the two groups of the same molecule resulting in an intermolecular proton transfer via water molecules.[176] Since the mesomeric structure is highly unfavorable for the *meta*-position, a typical azobenzene-like behavior is observed for this substitution-pattern (Fig. 5.8).

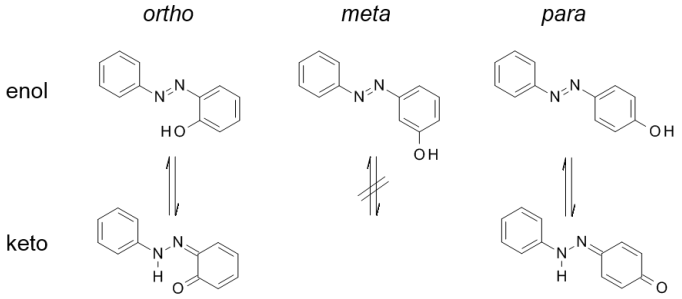

Figure 5.8: Chemical structures of *ortho*-, *meta*- and *para*-substituted hydroxy-azobenzene (top) and the stable keto-isomers of *ortho*- and *para*-substituted hydrazone structure (bottom).

So far, little is known about the ultrafast dynamics of hydroxy-substituted azobenzenes. Neither the dynamics of the isomerization nor the influence of the keto-enol-isomerization was studies on the ps-time scale. Therefore, a detailed study of the isomerization behavior of *ortho*- (furthermore called only ***ortho***), *meta*- (***meta***) and *para*- (***para***) substituted hydroxy-azobenzenes was performed in aqueous media.

Steady-state UV/vis-spectra were recorded for the three azobenzenes in aqueous solution (PBS, pH=7.4), while an addition of 10% DMSO was necessary due to the highly hydrophobic structure of these samples (Fig. 5.9). The spectrum of the *trans*-isomer of ***ortho*** shows a dominant absorption band at 330 nm, while a second band appears at 380 nm. Moreover, a broad absorption band can be seen up to 500 nm. After

illumination with light of a wavelength of 365 nm, no absorbance change is detected in the time range of seconds. In contrast to that, ***meta*** shows a typical azobenzene absorption spectrum with an intense $\pi\pi^*$-band of the *trans*-isomer at 310 nm and a weak band at 420 nm. With 365 nm-excitation, a *trans*→*cis*-isomerization occurs, resulting in a decrease of the $\pi\pi^*$-band at 310 nm and an increase of the absorption bands of the *cis*-isomer at 280 nm ($\pi\pi^*$) and 430 nm ($n\pi^*$). For the ***para***-isomer, no *cis*-azobenzene is observed after excitation, similar to ***ortho***. While the $\pi\pi^*$-band of the *trans*-isomer is located at 351 nm, slightly red-shifted with respect to ***ortho*** or ***meta***, the steady-state spectrum differs significantly over 400 nm.

At 433 nm, a strong absorption band can be seen with a third of the intensity of the $\pi\pi^*$-band at room temperature ($A_{\frac{351nm}{433nm}} = 3.3$). Upon temperature increase, the ratio between the two absorption bands changes to the benefit of the band at 433 nm (Fig. 5.9b). While at 4°C, the ratio is $A_{\frac{351nm}{433nm}} = 3.7$, the ratio decreases drastically to $A_{\frac{351nm}{433nm}} = 1.8$ at higher temperatures (80°C). This usually indicates a rearrangement of the *trans*/*cis*-equilibrium. However, the $\pi\pi^*$-band of the *trans*-isomer only decreases and shows no hypsochromic shift, which usually results from the emerging $\pi\pi^*$-band of the *cis*-isomer at lower wavelength. Moreover, the absorbance change is significantly more pronounced than a typical $n\pi^*$-band of the *cis*-isomer.

Consequently, a rearrangement occurs after temperature increase, however, no *trans*-to-*cis*-isomerization takes place. Here, a different energetically unfavorable structure benefits of the energy input by temperature - the keto species of ***para***, which was already suggested in earlier studies. Therefore, a keto-enol-tautomerism occurs in aqueous media for ***para*** already in the ground state. The ratio between the two species can be temperature-controlled. By extrapolation of the temperature-dependent change in absorption, the pure spectrum of the enol-species of the *trans*-isomer at 351 nm as well as of the keto-species at 433 nm can be calculated.

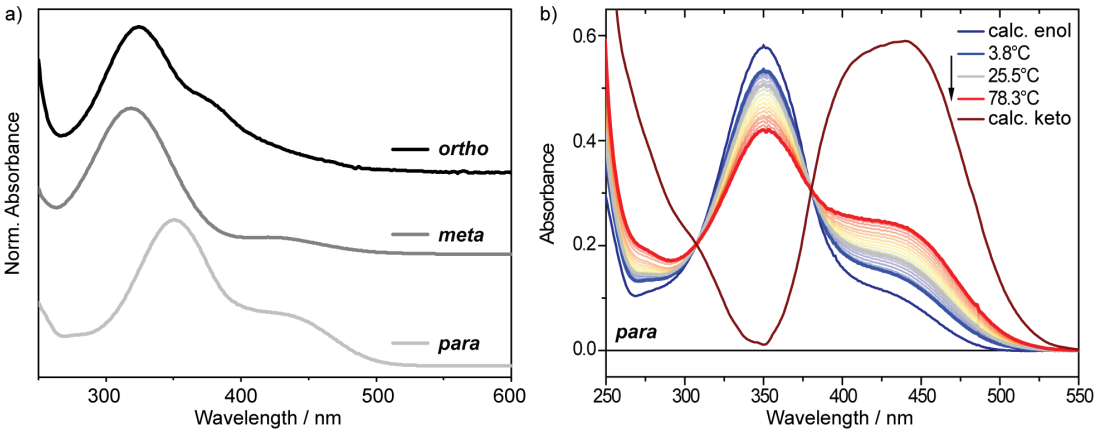

Figure 5.9: a) Steady-state UV/vis-absorption spectra of the *trans*-isomer of *ortho*-, *meta*- and *para*-substituted hydroxy-azobenzenes in PBS (with addition of 10% DMSO). b) Temperature-dependent steady-state UV/vis-spectrum of *para*-substituted hydroxy-azobenzene in PBS. Extrapolation results in a spectrum of the pure enol- and the pure keto-species.

The fast recovery of the *trans*-isomer of ***ortho*** (3.2 ms, determined by flash-photolysis measurement) and ***para*** (approx. 30 μs) suggests an involvement of the keto-species. Therefore, quantum-mechanical calculations were performed to classify the energy differences between different isomers of the hydroxy-substituted compounds. Note, that no energy barriers between the isomers were calculated. Therefore, due to these calculations, no absolute prediction can be made about the probability of processes. It is only useful for a general comparison of the relative energies. Here, initial structures of the *trans*-enol- and -keto- as well as *cis*-enol- and -keto-isomers of ***ortho***, ***meta*** and ***para*** were created and pre-optimized using the UFF force field (see subsection 2.4). Further, a geometry-optimization was performed using the program Gaussian09[181] using the steepest-decent approach. As *ab initio* method, the density functional theory was used with the B3LYP[51] functional and the basis-set cc-PVDZ.[37] For a better description of the system, an implicit water model, a polarized continuum model (PCM), was used with $\epsilon = 78.3553$.

For ***meta***, the most stable isomer is the *trans*-enol species with an azo-bond length of $r_1 = 1.258\ \mathring{A}$ and a CNNC-dihedral angle Θ of 180.0° (Fig. 5.10). The planar structure shows no torsion of the phenyl rings (NNCC-dihedral angle Φ: -0.1°) with a C-C bond length, which is comparable for both phenyl rings. Isomerization of the azo-group of the enol-species leads to an energy difference between *trans*-enol and *cis*-enol of 0.64 eV, which is comparable to the energy difference of pure azobenzene.[78]

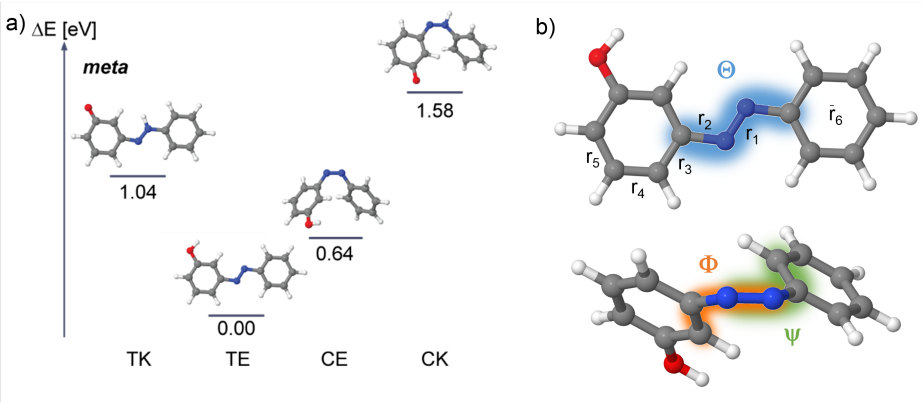

Figure 5.10: a) Ground-state optimized structures and relative ground-state energies of *meta*-substituted hydroxy-azobenzenes in enol- (E) and keto- (K) species as *trans*- (T) and *cis*- (C) isomer; energies are relative to the most stable *trans*-enol isomer. Theoretical calculations have been performed using DFT/B3LYP/cc-PVDZ and an implicit water model with the Gaussian 09 program package. b) Ground-state structure of ***meta*** with general notation of distances and dihedral angle.

While the bond length of the azo-group is only slightly smaller than for the *trans*-isomer, the CNNC-dihedral angle Θ shows only a value of 9.6° and the torsion of the phenyl rings is characterized by the NNCC-dihedral angle Φ of 52.8°. The energy of the *trans*-keto-species is significantly higher than the energy of the *trans*-enol. The reason for that is the unfavorable mesomeric structure of the *meta*-substitution. While the bond length r_1 is increased with respect to the *trans*-enol-structure, the dihedral an-

Table 5.2: Structural properties of ***ortho*** (***o***), ***meta*** (***m***) and ***para*** (***p***) resulting from quantum-mechanical geometry-optimization (B3LYP/cc-PVDZ, PCM=water), referring to the general notation of Fig. 5.10b.

		r_1 [Å]	r_2 [Å]	r_3 [Å]	r_4 [Å]	r_5 [Å]	$\bar{r}_6$ [Å]	Θ [°]	Φ [°]	Ψ [°]
o	TE	1.269	1.397	1.412	1.387	1.407	1.402	180.0	0.0	0.0
	CE	1.254	1.439	1.405	1.393	1.402	1.401	8.7	57.3	46.8
	TK	1.296	1.346	1.434	1.369	1.433	1.400	180.0	0.0	0.0
	CK	1.310	1.334	1.446	1.364	1.439	1.400	30.5	18.3	17.0
m	TE	1.258	1.420	1.402	1.399	1.394	1.401	180.0	-0.1	0.1
	CE	1.248	1.438	1.402	1.398	1.396	1.401	9.6	52.8	50.7
	TK	1.275	1.377	1.424	1.395	1.391	1.399	180.0	0.0	0.0
	CK	1.280	1.376	1.430	1.393	1.392	1.398	13.5	12.2	49.7
p	TE	1.261	1.411	1.410	1.388	1.409	1.401	180.0	0.0	0.0
	CE	1.252	1.431	1.407	1.390	1.405	1.400	10.3	40.0	56.2
	TK	1.306	1.327	1.447	1.359	1.466	1.400	180.0	0.0	0.0
	CK	1.313	1.328	1.452	1.358	1.465	1.400	18.7	6.2	51.5

gles Θ and Φ are comparable with 180° and 0°, respectively. However, aromaticity can only be observed for the unsubstituted phenyl ring. Here, an averaged bond length $\bar{r}_6$ of 1.399 $\mathring{A}$ can be observed, while for the hydroxy-substituted ring, a variation of the distances between 1.391 and 1.424 $\mathring{A}$ can be seen, which are not alternating. Therefore, two shorter distances r_4 and r_5 are next to each other, indicating a double-bond character for neighbored atoms, while on the opposite of the six membered ring, two neighbored single bonds are obtained. Consequently, an energetically unfavorable electron distribution is the result of the *trans*-keto-structure. Similar electronic properties can be found for the *cis*-keto-form of ***meta***. The bond length of the azo-group is even further increased to $r_1 = 1.280$ $\mathring{A}$, and the dihedral angle Φ is significantly lower than the *cis*-enol-structure (12.2°). Although, no energy barriers were calculated, it can clearly be seen, that the formation of the keto-species is highly unfavorable for a *meta*-substitution.

Calculations for ***ortho*** and ***para*** also reveal the *trans*-enol-species as the most stable isomer (Fig. 5.11). The energy of the *cis*-enol-isomer of ***ortho*** is significantly higher than the equivalent energy of ***para***, which could indicate a less pronounced isomerization for ***ortho***. It can clearly be seen that the energies of the keto-species of the compounds ***ortho*** and ***para*** are significantly lower than for ***meta***, which could indicate a population of the keto-species. Moreover, the energies of the isomeric forms *trans* and *cis* of both species enol and keto for these two compounds are very comparable with only small energy differences of less than 0.04 eV for *cis* and 0.16 eV for *trans*. Only by comparison of these comparable energies of the *cis*-enol- and *cis*-keto-tautomer, the resulting photo-product of the *trans*-to-*cis*-isomerization, the *cis*-enol-***ortho***, could perform a proton transfer to the *cis*-keto-tautomer in the ground state. Without calculations on the energy barrier of this pathway, however, this process cannot be ensured. Via a torsion around the N=N-single bond of the hydrazone structure,

the *cis*-keto-species results in the *trans*-keto-isomer. Due to the small energy difference of less than 0.16 eV between the *trans*-enol and -keto-species, the keto-species could easily convert back into the enol-form, which could be the reason for the fast recovery of the *trans*-isomer.

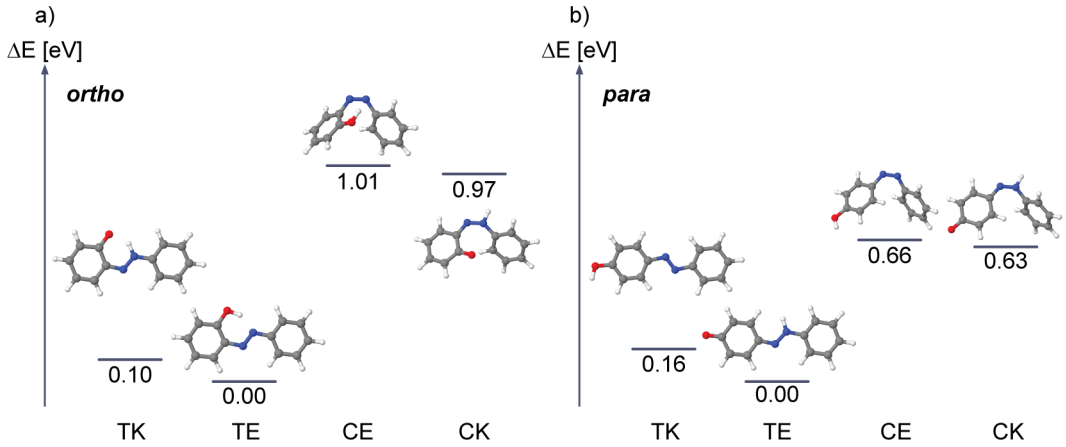

Figure 5.11: Ground-state optimized structures and relative ground-state energies of *ortho*- (a) and *para*- (b) substituted hydroxy-azobenzenes in enol- (E) and keto- (K) species as *trans*- (T) and *cis*- (C) isomer; energies are relative to the most stable isomers *trans*-enol. Theoretical calculations have been performed using DFT/B3LYP/cc-PVDZ and an implicit water model with the Gaussian 09 program package.

In general, by comparison of the calculated structures, it can be seen that for each substitution pattern, the bond length of the azo-group r_1 is enlarged going from *trans*-enol to *trans*-keto, which is due to a less pronounced double-bond character. While this distance is shortened during a *trans*-to-*cis*-isomerization of the enol-species, it becomes slightly longer for the same isomerization of the keto-species. Moreover, the C-N bond length r_2 also increases from the enol to the keto species, which results from an increased double-bond character. While the bond lengths of the unsubstituted phenyl ring $\bar{r}_6$ is completely independent of the position of substitution as well as the corresponding species, significant changes can be seen for the substituted phenyl ring. For the keto-species of ***ortho*** and ***para***, the single- and double-bond character of the alternating C-C bonds is amplified. Therefore, the distances r_3 and r_5 are slightly longer, while the bond length r_4 is shorted by a similar amount. However, this cannot be observed for ***meta***, since it shows no mesomeric structure. Here, in the substituted ring, two single bonds as well as two double bonds (r_4 and r_5) are observed at neighboring positions. The dihedral angles Θ, Φ and Ψ for the *trans*-isomers are absolutely unaffected by the enol and keto species. However, for the *cis*-isomers tremendous changes can be seen, first of all, for the CNNC-dihedral angle Θ, which increases slightly for ***meta*** going from *cis*-enol to *cis*-keto, even more for ***para*** and strongly for ***ortho***. Due to this increase of Θ, the structural hindrance of the two phenyl rings is avoided. Therefore, a smaller torsion of the two phenyl rings is observed for ***ortho*** for both dihedral angles Φ and Ψ and for ***meta*** and ***para*** only for Φ.

Trans-to-*Cis*-Isomerization of Hydroxy-Azobenzenes

On the behalf of time-resolved UV/vis-pump UV/vis-probe experiments, the influence of the keto-species on the isomerization mechanism in aqueous solution was studied for the different positions of hydroxy-substitution.

After excitation of ***meta*** at 320 nm, two ESA-bands arise instantaneously with a maximum at 400 nm (ESA_1) and at 550 nm (ESA_2) (Fig. 5.12). While ESA_1 is spectrally narrow, ESA_2 ranges from 430 to 600 nm. In general, the dynamics after excitation can be described by four exponential function accurately. A slight increase of the the two ESA-bands is characterized by lifetime τ_1, which is in the range of the experimental time resolution. Since the excitation wavelength of 320 nm addresses the $\pi\pi^*$-band (S_2-state), the lifetime τ_1 describes the ultrafast $S_2 \rightarrow S_1$-transition. The decay of the S_1-state and therefore of the two ESA-bands is described by the two exponential functions τ_2 and τ_3. The system does not only relax back into the ground state of the *trans*-isomer, but also into the ground state of the *cis*-isomer via a conical intersection. Therefore, after 5 ps, the ESA_1-band decreased enough to detect the GSB below 400 nm as well as the product absorption band of the *cis*-isomer with a maximum at 420 nm. The inverse DAS of the infinite lifetime τ_4 is in good agreement with the steady-state spectrum (Fig. 5.12).
Consequently, the isomerization of the ***meta*** is completed before 1 ns, which is in good agreement with earlier studies showing an azobenzene-like isomerization behavior.[93,111]

Comparing these results to the ultrafast dynamics after excitation at 320 nm of the ***para*** at room temperature, the transient absorption difference spectrum shows significant similarities (Fig. 5.12). While the ESA_2-band is very similar for both samples, the ESA_1-band looks slightly narrower for ***para***.
However, this is mostly due to the intense GSB below 400 nm, which is about 70 nm red-shifted with respect to the ***meta*** and therefore, overlaps with the ESA_1-band. The lifetimes describing the decay of the S_1-state are only slightly shorter for the ***para***. The corresponding DAS of the lifetimes τ_1 to τ_4 show a typical isomerization of azobenzene resulting in a product absorption, the $n\pi^*$-band of the *cis*-isomer, at 430 nm. The comparison of the inverse DAS of lifetime τ_4 with the steady-state spectrum shows only a slight red-shift of the GSB of about 10 nm, which could indicate slow conversion reactions beyond 1 ns (Fig. 5.12, see also **SSZ** in Fig. 5.6).

Table 5.3: Lifetimes, resulting from global lifetime analysis, describing the relaxation processes during *trans*-to-*cis*-isomerization of ***ortho***, ***meta*** and ***para*** after excitation at 320 nm in PBS in a UV/vis-pump UV/vis-probe experiment.

Lifetime [ps]	***ortho***	***meta***	***para***
τ_1	0.25	0.24	0.33
τ_2	1.30	1.00	1.85
τ_3	3.90	4.27	5.03
τ_4	∞	∞	∞

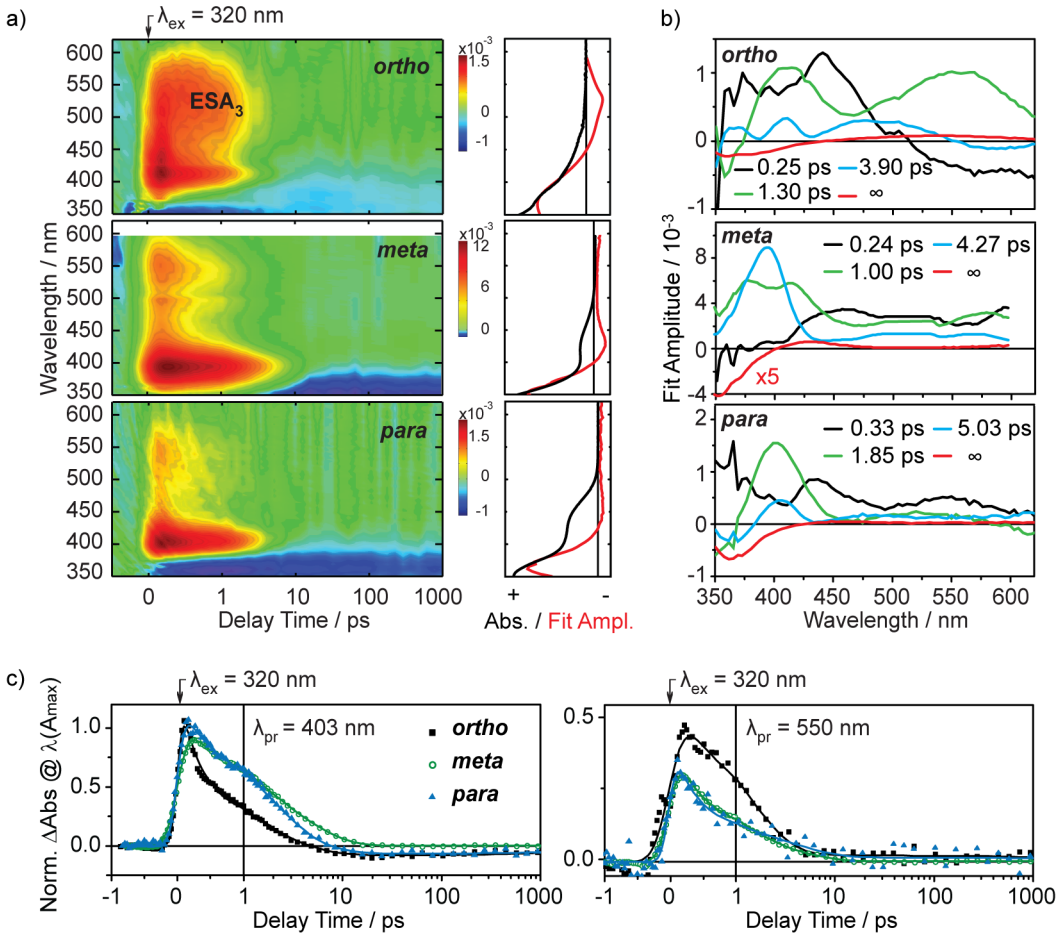

Figure 5.12: a) Transient absorption difference spectra of ***ortho***- (top), ***meta***- (middle) and ***para***- (bottom) substituted hydroxy-azobenzenes in PBS (with addition of 10% DMSO). Comparison of absorption spectra before excitation (black) and the inverse decay-associated spectra of the longest lifetime (red) are shown with the corresponding color codes. b) Decay-associated spectra of ***ortho***, ***meta*** and ***para***. c) Transients at 403 and 550 nm of all samples are compared by normalization at the absorption maxima of both samples around 400 nm.

Consequently, the *trans*-enol-isomer of ***para*** can be exclusively excited at 320 nm leading to a typical isomerization process without contribution of the keto-species.

The transient absorption difference spectrum of ***ortho*** in aqueous media shows contributions, which can also be seen in the measurements of the other two samples (Fig. 5.12). An ESA_1-band is located at 400 nm and a weak ESA_2-band can be seen at 550 nm instantaneously after excitation. These ESA-bands decay biexponentially with the lifetimes τ_2 and τ_3 into the ground state of the *trans*-isomer as well as in the ground state of the *cis*-product. Therefore, an isomerization process can be detected after excitation at 320 nm. However, this *trans*-to-*cis*-isomerization is subordinate for ***ortho***. A intense new ESA-band arises with the lifetime τ_1 of 0.25 ps at 550 nm (ESA_3), which can be seen in the transients at 550 nm in Fig. 5.12. While the transient at 403 nm of ***ortho*** is significantly smaller than the transients of the two other samples, the absorption changes at 550 nm of this sample are extremely high. Observing the

DAS of this lifetime τ_1, a decrease of the ESA_1 can be detected at 400 nm, while the new ESA_3-band increases. This ESA_3 is assigned to the keto-species of ***ortho***.

Consequently, an excited state intramolecular proton transfer (ESIPT) occurs with 0.25 ps from the excited *trans*-enol-isomer to the S_1-state of the keto-species. The decay of this S_1-state is also described by the lifetime τ_2 of 1.30 ps into the ground state of the keto-species. Since the relaxation time of the enol and the keto species are obviously very similar, in the global lifetime analysis, no additional lifetime was found, but a combined lifetime for both processes. The ESA-bands completely relax to the ground states after about 20 ps; the inverse DAS of the infinite lifetime matches the steady-state spectrum quite well in the range below 400 nm. Nevertheless, in the range between 400 and 600 nm, in contrast to the steady-state spectrum, a broad positive absorption band can be seen until a delay time of 1 ns. Since this absorption band cannot be seen in flash photolysis measurements in the time range between 45 μs to 1 s, a faster process occurs resulting in the loss of this absorption band. This band could either be assigned to a triplet state contribution of the keto-species or to a different keto-species, like a *cis*-keto-species (Fig. 5.11, CK).

As a result, excitation of ***ortho*** at 320 nm leads to two simultaneous processes. The first process is the photo-isomerization from the *trans*- to the *cis*-isomer. However, for this compound, the structural conversion is subordinate and proceeds only to a small percentage. The even more pronounced process is the excited states intramolecular proton transfer from the enol- to the keto-species of ***ortho***.

Theoretical calculations on the deactivation pathways of ***ortho*** after S_2-excitation, performed by D. Rastädter and Dr. J. M. Ortiz-Sánchez (research group Prof. I. Burghardt), are in good agreement with the experimental results from the time-resolved UV/vis-measurements, indicating the same two possible processes after excitation of the *trans*-isomer.[176]

The first possible pathway after excitation of the *trans*-enol ***ortho*** is the *trans*-to-*cis*-isomerization. After a fast transition from the S_2-state into the S_1-state via a variation of e.g. the OH-distance, the ground state of either the *trans*-enol- or the *cis*-enol-***ortho*** can be reached via a conical intersection between the S_1-state and the ground state. This pathway is completely barrier-less, showing only minor energy gaps of partially less than 0.1 eV between the different states. The more prominent pathway to happen starting in the S_2-state of the *trans*-enol ***ortho*** is the ESIPT from the S_2-state of the *trans*-enol tautomer into the S_1-state of the *trans*-keto-species. This pathway involves only a small energy gap of less than 0.1 eV between the two states. Via a CNNC and/or NNCC torsion, the keto-species can relax into the ground state of either a *trans*- or a *cis*-keto-species.

Keto-Species of *Para*-Hydroxy-Azobenzene

Regarding Fig. 5.9, the steady-state UV/vis-spectrum of ***para*** in PBS shows clearly two separate intense absorption bands. While the absorption band at 330 nm response to the $\pi\pi^*$-band of the *trans*-enol-isomer, the absorption band at 430 nm is assigned to the *trans*-keto-species. The energy difference between the ground state of the *trans*-enol- and -keto-species is 0.16 eV based on theoretical calculations using an implicit water model (Fig. 5.11) and 0.1 eV for an explicit water chain connecting the azo- with the hydroxy-group.[176] Referring to theoretical calculations,[176] the energy barrier between the two ground states is supposed to be overcome by an interplay of vibrational modes of the azo- and hydroxy-group and the involved water molecules of the first solvent shell.

This could explain the interconversion of the enol- and the keto-species already in the ground state, which is highly affected by temperature changes (Fig. 5.9). Already at room temperature an intense keto-absorption band can be detected at 430 nm, allowing excitation within this band and performing time-resolved UV/vis-experiments with an excitation wavelength of 440 nm.

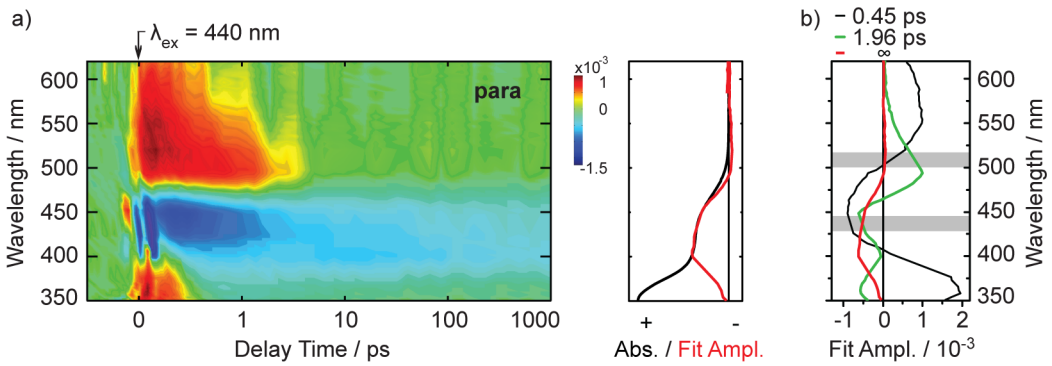

Figure 5.13: Transient absorption difference spectra (a) and corresponding decay-associated spectra resulting from global lifetime analysis (b) of *para*-substituted hydroxy-azobenzenes in PBS (with addition of 10% DMSO). Comparison of absorption difference spectra before excitation (black) and the inverse decay-associated spectra of the longest lifetime (red).

After excitation at 440 nm of ***para***, a GSB can be detected between 400 and 470 nm, which corresponds clearly to the keto-species seen in the steady-state spectrum (Fig. 5.13). Moreover, after excitation, three ESA-bands arise instantaneously at 383 nm (ESA_1), an intense band at 510 nm (ESA_2) and a less pronounced at 570 nm (ESA_3). The relaxation processes can be described by three exponential functions. The lifetime $\tau_1 = 0.45$ ps describes the decay of the ESA_1 and ESA_3 as well as a partial decay of the GSB at 452 nm. ESA_2 as well as the GSB decay on a longer time scale, which is described by the lifetime $\tau_2 = 1.96$ ps. After 10 ps, the ground state of the initial sample and of the photo-product are (re-)populated, which can be seen at a positive remaining absorption difference at 510 nm and the remaining GSB between 350 and 490 nm.

Since neither the GSB at 452 nm nor the resulting dynamics can be assigned to a *trans*- or *cis*-enol-***ortho***-excitation, a different species has to be responsible. Therefore, an excitation of the keto-species can be observed after excitation with 440 nm. However, the absorption bands ESA_1 and ESA_2 can hardly be explained by the keto-species. An additional minor excitation of the *trans*-enol-***ortho*** within the $n\pi^*$-band is responsible for the less dominant dynamics. Due to this *trans*-to-*cis*-isomerization, a *cis*-isomer can be seen as the photo-product at 510 nm. Nevertheless, this product absorption band is too intense compared to the GSB of the *trans*-enol seen at 358 nm. In the DAS of the infinite lifetime τ_3, the ratio between the absorption of the product at 520 nm to the GSB at 361 nm is 0.47; in case of excitation with 320 nm, this ratio is significantly smaller (0.03). Therefore, the photo-product absorption band at 510 nm referring to the *cis*-species is not only formed by an isomerization of the enol-species, but also of the keto-species. Whether a *cis*-enol- or a *cis*-keto-tautomer arises, cannot be seen in these results due to the intense overlap of the containing absorption bands.

5.3 Conclusion

In this chapter, the immense challenge of designing a water-soluble azobenzene with beneficial photo-physical properties was highlighted. Due to the highly hydrophobic structure of the azobenzene scaffold, variations in the structure are inalienable. Therefore, a number of hydrophilic functional groups needs to be added to the phenyl rings of the photoswitch. A variety of small substituents was found to reduce the hydrophobicity. Here, amine- and amide-groups should be noted, although only a higher number of substituents lead to a soluble derivative. Moreover, the use of sulfonamides as well as hydroxy-groups showed a significant change in the water-solubility. However, variations of the azobenzene structure always influence the photo-chemical properties of the photoswitch. Therefore, the spectral position of absorbance bands as well as the switching amplitude from one isomer to the other can be changed. A more drastic influence is the acceleration of the thermal reaction of the reformation of the *trans*-isomer in aqueous solution to a time scale of milliseconds. Consequently, no *cis*-isomer can be accumulated on a reasonable time scale of seconds to minutes, which was observed in aqueous solution for the hydroxy-substitution in *ortho*- or *para*-position with respect to the azo-group (section 5.2). Here, beside the model systems *para*- and *ortho*-hydroxy-azobenzene, also a therapeutic, based on an azobenzene scaffold, Sulfasalazine **SSZ** was investigated. It could be shown that by acetylation of **SSZ** the thermal reaction is significantly decelerated to the time range of minutes. For investigations on the isomerization behavior of **SSZ** and the influence on the isomerization process of the position of the hydroxy-group with respect to the azo-group, time-resolved UV/vis-experiments have been performed. It could be revealed, that independent of the position of hydroxy-substitution, a *trans*-to-*cis*-isomerization occurs after excitation of the *trans*-enol-isomer (Fig. 5.14). The lifetimes of the isomerization process are in the range of 0.76 - 1.85 ps and 3.90 - 5.03 ps for the hydroxy-azobenzenes **ortho**, **meta**

and **para** as well as for the therapeutic **SSZ** and its acetylated derivative **ac. SSZ**. Therefore, the dynamics of this process are only slightly affected by the substitution position. However, significant differences could be observed in the contribution to this relaxation pathway. While for *meta*- and *para*-substitution as well as for both Sulfasalazine derivatives, an azobenzene-like isomerization mechanism is obtained, the photo-isomerization of ***ortho*** is subordinate after excitation of the *trans*-enol-isomer. For *ortho*-hydroxy-substituted azobenzenes in aqueous solution, an excited state intramolecular proton transfer (ESIPT) is observed from the excited state of the *trans*-enol-isomer to the excited state of the keto-species within 0.25 ps. Afterwards, a subsequent relaxation of the keto-species into the ground state of the keto-species as well as into another species can be seen, which cannot be characterized further due the immense overlap of absorbance spectra. Here, either a triplet state or a sterical isomer of the keto-species can be involved. These results are supported by theoretical calculations, which show a close proximity of the potential energy curves of the S_2 - and S_1-state along the proton transfer coordinate.[176]

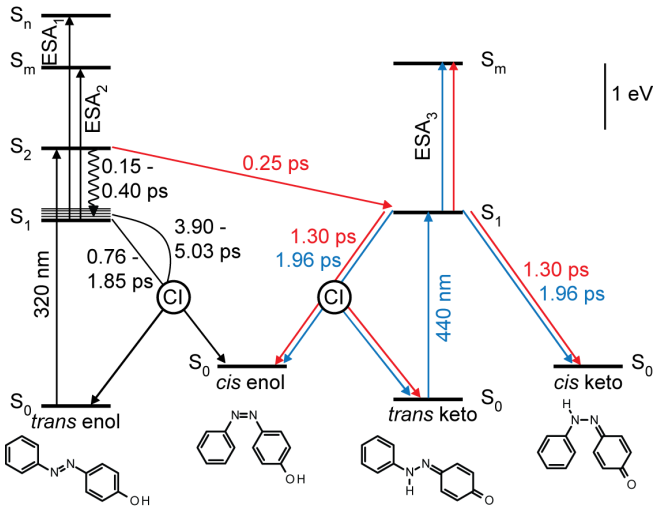

Figure 5.14: Reaction scheme of hydroxy-substituted azobenzenes in aqueous solution in a simplified potential energy scheme. Black arrows indicate the isomerization mechanism for **SSZ**, **ac. SSZ** as well as the the three hydroxy-azobenzenes **ortho**, **meta** and **para**. Colored arrows indicate an additional pathway for **ortho** (red) and **para** (blue). Chemical structures of the respective species are exemplarily shown for **para**.

Consequently, a transition from the enol- to the keto-species is obtained for ***ortho*** in the excited state. For ***para***, however, this keto/enol-tautomerism can already be seen in the ground state. The ratio of the enol- and the keto-species of **para** is highly affected by temperature. In time-resolved UV/vis-studies, it could be shown, that the two species can be addressed specifically. While a *trans*-to-*cis*-isomerization can be obtained by excitation of the enol-species at 320 nm, the keto-species can be excited specifically at 440 nm, which relaxes not only back into the *trans*-keto-species with a lifetime of about 2 ps, but also a formation of a *cis*-isomer of the enol- or the keto-species is observed.

Unless, a fast reaction of the *cis*- to the *trans*-isomer is preferred for a specific application, the use of hydroxy-substitution of azobenzenes, at least in *ortho*- or *para*-position, should be avoided for water-soluble photoswitches. Although the solubility in water is increased, a lower quantum yield of the photo-isomerization as well as side reactions of the keto-species can be the result, which is unfavorable in biological applications.

Chapter 6

Photo-Control of Structure and Function of Ribonucleic Acids

Nowadays, the classical understanding of the three major biological groups of desoxyribonucleic acid (DNA), ribonucleic acid (RNA) and proteins with a fixed task in biological systems is overcome. It is known that the processes and the relationship between the macromolecules are far more complex and difficult to categorize generally. Certainly, the long-known processes of the transcription of the DNA to gather the gene information in RNA and the translation of the RNA into proteins remain valid. However, the high diversity especially of ribonucleic acids ranges from the messenger of genetic information (mRNA), an important component in the protein biosynthesis (tRNA and rRNA) to genetic material of viruses and is continuously extended in a wide field in research.[182]

This variety of functions can be explained by the high structural flexibility of RNA in contrast to DNA. While DNA molecules are mostly present in a helical structure, RNA is usually present as a single strand. However, RNA can also form high variety of secondary structures, e.g. an A-form helix conformation,[183] which are stabilized by hydrogen-bonds between the nucleic bases of opposite strands. While for DNA, usually only two combinations can be found – adenosine and thymine as well as guanine and cytosine –, which are known as *Watson-Crick base pairs*, in RNA, a high variety of non-canonic base pairs are possible. Here, the base pairing can be observed as *Watson-Crick* base pairs, *Wobble-* or *Hoogsteen-* base pairs, in either a normal or an inverse way.[184] Due to this flexibility, RNA molecules can be present in different secondary structures, like hairpins, loops, bulges or junctions, leading to tertiary structures ranging from interactions of helices, pseudoknots or kissing-complexes.

One important example of short single stranded nucleic acids are aptamers, which have the ability to bind ligands via electrostatic interactions and hydrogen bonds between the ligand and the aptamer.[185] A variety of ligands, which are bound to an aptamer, are literature known ranging from metal ions, small biological molecules, e.g. amino acids or proteins.[186] During the binding process, the ligand can either be encapsulated by the aptamer or it can bind sideways to a specific binding site on the structure of the RNA. This specific interaction between the aptamer and the ligand is known for its high binding affinity within the nano- and picomolar range and its high selectivity[187] or even enantioselectivity.[188] Due to this specific binding and

the inelaborate *in vitro*-selection with respect to the production of e.g. antibodies, aptamers are often used in field of pharmacology or oncology as transporter for small molecules, like antibiotics, or for inhibition of pathogenic proteins. Moreover, the *in vitro*-selection enables an adaptation of the binding affinity on the conditions regarding pH-values, temperature or concentrations of ions.

Using the conformational change of the RNA structure upon ligand binding, aptamers are found as a receptor component in biosensors, e.g. *aptasensor*, or in the further discussed riboswitches. Riboswitches are structured RNA elements with a flexible three-dimensional structure for the binding of specific ligands. Due to the division of the riboswitch into a sensor- and a regulation platform,[189] the aptamer serves as a binding domain and regulates the expression platform of the riboswitch. Therefore, aptamers as a part of the riboswitch can be regarded as keyfactors for controlling the gene expression, which is the reason for the high interest in synthetic riboswitches.

Riboswitches can be found in the untranslated region at the 5'-end (5'UTR) of messenger RNA (mRNA). Ligand-binding of aptamers can have significant influences on the stability of the secondary structure of the binding region and therefore the aptamer structure. It is preferable that the free aptamer structure exhibits no distinct secondary structures, so after ligand binding, the conformational change is as pronounced as possible. Therefore, in many cases, the free and the bound state of the aptamer are present in a different tertiary structure. The expression platform reacts on the change in conformation and causes, dependent on the class of riboswitch, either a termination of the transcription or translation. While for transcription riboswitches, like the guanine riboswitch, the transcription is terminated by conformational rearrangements into a stable hairpin structure of the expression platform by binding of guanine (or hypoxanthine), which leads to a formation of a transcription terminator and therefore, to a stop of the polymerase. In case of translation riboswitches of prokaryotes, e.g. SAM riboswitch type II, controlling of the translation results from the inaccessibility of the Shine-Dalgarno (SD) sequence and the start codon (Fig. 6.1a). This can be either achieved by including the SD-sequence in a double-stranded conformation or only by sterical hindrance of this sequence, so that the ribosome-binding is prevented. In case of translation riboswitches of eukaryotes, the ribosomal scanning of the ribosome on the messenger-RNA (mRNA) is disturbed due to the stable aptamer structure, which binds the ligand (OFF state). If no ligand can be bound, the aptamer structure can be passed (ON state) (Fig. 6.1b). Riboswitches can act as ON- or as OFF-switches, depending on the fact whether the ligand-binding activates (ON) or inactivates (OFF) the gene expression.

While in nature, this regulation is enabled by concentration gradients of the ligand, external intervention regarding medical treatment is hardly achievable. Therefore, a photo-responsible starting and termination of the gene expression with spatial and temporal control is desirable and of high interest in research. So far, however, only few photo-responsive aptamers are known.[190,191]

A regulation by light requires a photo-active molecule, which reacts on the photo-

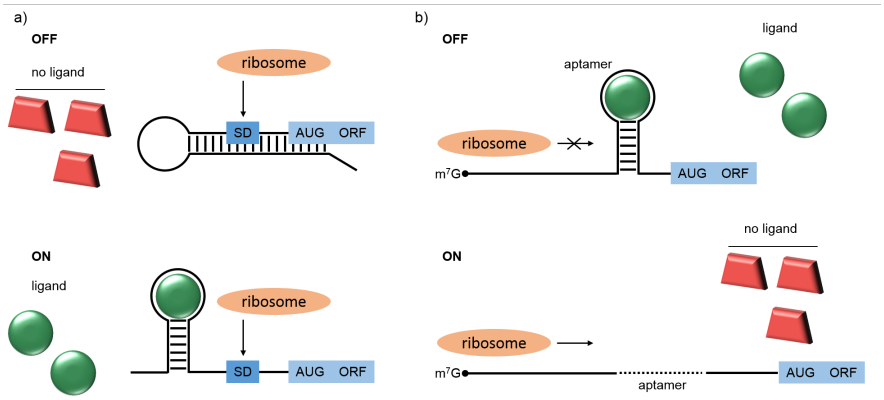

Figure 6.1: a) Scheme of the control of gene expression in prokaryotes via riboswitches. In the OFF state (top), the Shine-Dalgarno (SD) sequence is included in a double-stranded conformation and cannot be bound by the ribosome. By specific binding of a ligand to the aptamer sequence, the SD sequence is accessible for the ribosomal complex (bottom). b) Scheme of the control of the ribosomal scanning in eukaryotes. By ligand-binding of the aptamer domain, the ribosomal scanning is disturbed (top) and can be restored by releasing the ligand molecules (bottom).

excitation by e.g. a conformational change, that influences the secondary and tertiary structure of the binding domain. By that, the ribosomal scanning is either more likely (ON state) or unlikely (OFF state). One example of a small photo-active molecule is the photoswitch azobenzene, which can be switched between a planar *trans*-isomer and an energetically unfavorable *cis*-isomer by using a defined wavelength (see chapter 3 and 5).

In general, there are two possibilities to use photoswitches for the conformation control of aptamers. The first possibility is a covalent incorporation of the photoswitch in the backbone of the RNA. Due to the planar conformation of the *trans*-azobenzene, it can be used as an artificial base, which can interact with the nucleic bases dependent on the substituents of the photoswitch and can be introduced in double-stranded structure, like a helix or a stem structure of an aptamer. After photo-isomerization into the *cis*-isomer, the interactions of the neighboring base pairs are disrupted due to the non-planar conformation. Dependent on the number of incorporated photoswitches within the strand and the corresponding positions, a *photo-responsive RNA-dehybridization* can be achieved (see section 6.1).

The second possibility is the incorporation of the photoswitch via non-covalent interaction (see section 6.2). In that case, the photoswitch acts as a ligand and binds specifically in the binding domain. Therefore, an aptamer sequence needs to be found in a SELEX process (section 6.2.1), which binds, however, only one photo-isomer of the photoswitch specifically and with a high affinity. Like this, an OFF-state can be generated e.g. for the *trans*-isomer, which binds to the aptamer resulting in a stable tertiary structure, which prevents a ribosomal scanning. After isomerization, the *cis*-isomer shows no binding affinity to the binding domain (ON-state). Due to that, the RNA structure is not stabilized by the ligand anymore and a translation can occur.

6.1 Photo-Responsive RNA-Dehybridization

Although single-stranded RNA is quite common in nature, a high amount of this single strand is folded into secondary structures, like stem-loops, in which a double-stranded part is built within the single-stranded structure. By incorporation of a photoswitch, like azobenzene, covalently bound into the RNA sequence within this double-stranded part of the RNA, a spatial and temporal control over the conformation of RNA can be enabled. While the planar *trans*-azobenzene can intercalate between the neighboring base pairs, the stabilizing hydrogen bonds of the base pairs within the duplex structure are disrupted by the non-planar *cis*-azobenzene. Consequently, the conformation of the secondary structure is changed or can even unfold.

Stem-loops and hairpin-structures are very common conformations of aptamers, e.g. in riboswitches. An OFF-state could be generated by a stable aptamer conformation with one or even several *trans*-azobenzenes within its stem structure, which results in a blocking of the ribosomal scanning (eukaryotes) or a double-stranded conformation including the SD sequence (prokaryotes). By photo-isomerization of the azobenzene into its *cis*-isomer, a photo-responsive dehybridization occurs leading to a different secondary/tertiary structure, which enables the translation again (ON-state). To obtain this to a high amount, the choice of the photoswitch as well as the incorporation of the azobenzenes into the RNA structure is essential for the success. In addition to the photoswitch with good (photo-)chemical properties, the appropriate position within the stem structure is of high interest to guarantee not only a destabilizing effect, but a dehybridization of the duplex. A photo-regulation of the hybridization of DNA structures with the photoswitch azobenzene is well-known in literature.[192,193] A variety of incorporation methods to introduce the azobenzene in the backbone of the DNA can be found. One promising approach is the D-threoninol linker (tAzo) presented by Asanuma, which showed a photo-responsive effect for the transcription by T7-RNA polymerase by introducing azobenzenes into the T7 promoter at specific positions.[156,158]

However, a high amount of photo-isomerization of the azobenzene could only be observed within the DNA above about 70°C. Changes in the chemical structure of the linker, which results in a less rigid bond, would enable a higher degree of freedom of azobenzene and therefore, leads to an isomerization already at lower temperatures. Nevertheless, the flexibility of the linker should not be too high, so that the azobenzene should still be kept within the duplex structure of the DNA and is not able to spin out into the major groove.

Besides the incorporation of the azobenzene via the D-threoninol linker into RNA, which showed a photo-responsive hybridization only at high temperatures close to the melting point of the double-helix, only little is known about the photo-control of the hybridization of RNA. Therefore, a new linker was designed in the group of Prof. A. Heckel, which is based on desoxyribose and is coupled to the azobenzene as the β-anomer either in the *meta*- (**mAzo**) or the *para*-position (**pAzo**) relative to the

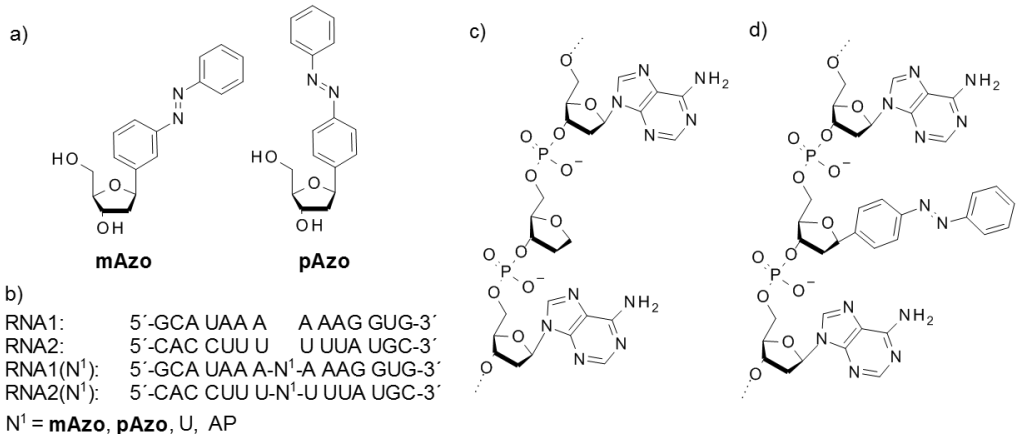

Figure 6.2: a) Chemical structures of **mAzo** and **pAzo**. b) RNA model sequences of the 14-mer RNA1 and RNA2 and of the 15-mer with an additional nucleotide N^1 (uridine, **mAzo**, **pAzo** or an abasic (apurinic/ apyrimidinic (AP)) site). c) RNA single-strand of RNA1-AP. d) RNA single-strand of RNA1-**pAzo**.

azo-group (Fig. 6.2). Since the *trans*-isomer is present in a planar conformation, the azobenzene should intercalate in the RNA duplex structure, while the *cis*-azobenzene should interact negatively with the neighboring base pairs.

6.1.1 Isomerization Behavior of Sugar-Linked Azobenzenes within Single-Stranded RNA Sequences

For characterization of the isomerization behavior of the azobenzene derivatives **mAzo** and **pAzo**, the compounds were spectroscopically characterized regarding their switching amplitudes as well as their kinetics of the *cis*-to-*trans*-isomerization. Moreover, the fatigue resistance of the azobenzene derivatives upon isomerization was studied. Furthermore, comparable investigations were performed on short model RNA strands with incorporated azobenzenes at the central position of the RNA sequence (Fig. 6.2). To simulate the physiological conditions, each of the spectroscopic characterizations on **mAzo** and **pAzo** have been performed in a phosphate-buffered solution (PBS) at a pH value of 7.4. The monomers show good solubility in PBS of 0.4 mg/mL for **mAzo** and 0.6 mg/mL for **pAzo**, which is unusual in contrast to azobenzene.

Comparing the steady-state UV/vis-spectra of the *trans*-isomer of **mAzo** and **pAzo**, a small hypsochromic shift of about 6 nm for **mAzo** can be detected for the $\pi\pi^*$-band at 320 nm, while the $n\pi^*$-band for both samples are located at 434 nm. Excitation with light with a wavelength of 365 nm induces a photo-isomerization from the *trans*- to the *cis*-isomer, resulting in the UV/vis-spectrum of the photo-stationary state (PSS_{365nm}). An increase of the absorption band ($n\pi^*$-band) at 428 nm for **pAzo** and at 426 nm for **mAzo** can be detected as well as an increase for both samples at about 290 nm, which corresponds to the $\pi\pi^*$-band of the *cis*-isomer. Two clear isosbestic points can be seen at about 270 and 370 nm. The amounts of the *cis*-isomer of **mAzo** and **pAzo** in the photo-stationary state were determined by pure spectra obtained by RP-HPLC and achieve 91% for **pAzo** and 88% for **mAzo**. This lower *cis*-amount for

compound **mAzo** can clearly be seen in the less pronounced absorbance change in the $\pi\pi^*$-band of the *trans*-isomer with respect to **pAzo** (Fig. 6.3).

Alternating excitation with light of a wavelength of 365 nm and 420 nm leads to a perfectly reversible isomerization behavior of the monomers **mAzo** and **pAzo** in aqueous solution. During 25 cycles, changes were observed neither in the absorption spectrum nor in the switching amplitudes. Therefore, degradation due to hydrolysis and photo-oxidation can be excluded. Consequently, a high fatigue resistance of these two photoswitches can be seen in Fig. 6.3.

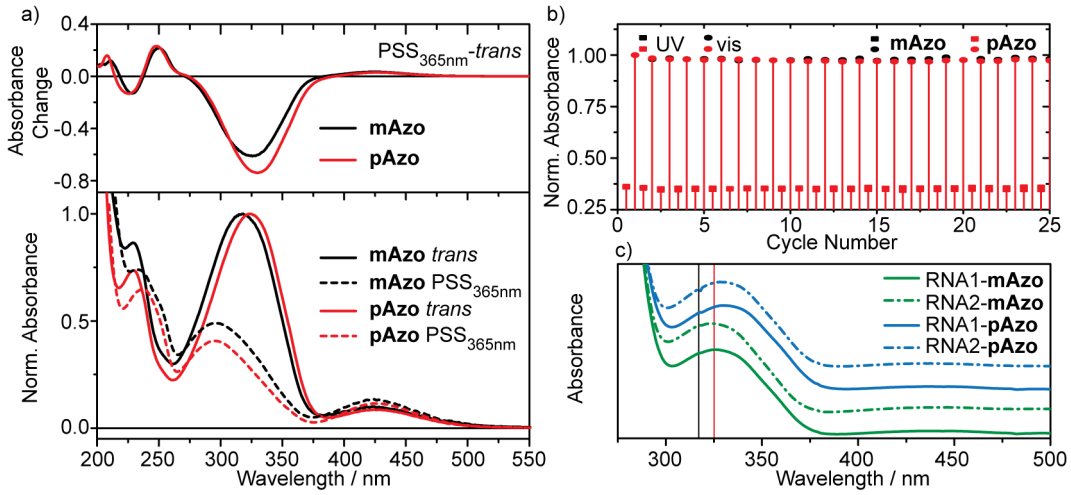

Figure 6.3: a) UV/vis-spectrum of the *trans*-isomer (solid line) and the photo-stationary state (PSS_{365nm}, dashed line) of **mAzo** and **pAzo** in PBS (bottom). Difference UV/vis-spectra (top) indicate the absorbance changes during isomerization (PSS_{365nm}-*trans*). b) Normalized absorption at the absorption maximum of the $\pi\pi^*$-band of the *trans*-isomer at 320 nm after alternating excitation at 365 and 420 nm for **mAzo** and **pAzo**. c) UV/vis-spectra of the *trans*-isomers of RNA1-**mAzo**, RNA2-**mAzo**, RNA1-**pAzo** and RNA2-**pAzo** in PBS. Black and red vertical solid lines indicate the absorption maximum of the $\pi\pi^*$-band of the *trans*-isomer of **mAzo** and **pAzo**, respectively.

The influence of the photo-isomerization of the azobenzene compound on the RNA-structure is not only depending on the degree of isomerization, but also on the thermal stability of the energetically unfavorable *cis*-isomer. Since the time for a reaction of the RNA on the spatial disruption due to the non-planar isomer should be sufficiently long, a slow thermal reaction from the *cis*- to the *trans*-isomer is needed. Therefore, it is important to study the thermal reaction rates as well as the energy barrier between the two isomers in the electronic ground state. The temperature-dependent isomerization rates for the monomer **mAzo** and **pAzo** can be seen in Tab. 6.1. By using the Arrhenius-equation Eq. 6.1, the activation energy of the thermal reaction process from *cis*- to the *trans*-isomer can be determined (see section 3.1).

$$k = A \cdot e^{-\frac{E_A}{RT}} \tag{6.1}$$

The thermal rates at $37°C$ for the *cis*-to-*trans*-isomerization of the two monomers **mAzo** and **pAzo** of about 1.7 to $2.0 \cdot 10^{-6}$ s^{-1} are very similar to each other. Moreover,

Table 6.1: Energy barrier of the thermal *cis*→*trans*-isomerization and the corresponding relaxation rates for **mAzo** (**m**) and **pAzo** (**p**) in PBS.

	$(k \pm \Delta k)$ $[10^{-6} \cdot s^{-1}]$				E_A
	37°C	42°C	50°C	70°C	$[kJ/mol]$
m	1.703 ± 0.010	2.722 ± 0.014	4.742 ± 0.006	17.942 ± 0.013	62.3 ± 1.7
p	1.986 ± 0.011	—	6.73 ± 0.05	44.82 ± 0.17	84 ± 4

they are comparable to the reaction rate of the unsubstituted azobenzene. However, at higher temperatures, clear differences are observed for the two compounds. For example, **pAzo** shows at $70°C$ a thermal reaction rate of $k_{70°C}$ (**pAzo**) $= 4.48 \cdot 10^{-5}$ s^{-1}, which is more than twice the value than for **mAzo** with $k_{70°C}$ (**mAzo**) $= 1.79 \cdot 10^{-5}$ s^{-1}. Due to the smaller activation energy of E_A(**mAzo**) $= 62.3\ kJ/mol$ for the thermal reaction from the *cis*- to the *trans*-isomer of **mAzo**, the temperature increase has a smaller influence on the relaxation rates. However, both monomers are still quite similar and with a half-life of $t_{1/2}$ (**mAzo**) $= 113$ h and $t_{1/2}$ (**pAzo**) $= 97$ h at 37°C suitable for the biological use.

For the investigation on the photo-isomerization of the azobenzene derivatives, which are incorporated into a RNA strand as well as its influence on the stability of the RNA, the two azobenzene monomers **mAzo** and **pAzo** were introduced into small RNA model strands with a length of only 15 nucleotides. The size and the sequence of the model RNA was chosen to not interact with itself. For comparison to a RNA strand without a photoswitch, also two oligonucleotides with a length of 14 monomer units have been studied (Fig. 6.2), which are complementary to each other. In general, also the effects of the incorporation of an additional base on the stability were investigated by studying an abasic site as well as uridine instead of azobenzene.

In general, the UV/vis-spectra of both RNA single strands RNA1 and RNA2, which contain **mAzo** and **pAzo**, show comparable absorption bands with a $\pi\pi^*$-band of the *trans*-isomer around 330 nm and a $n\pi^*$-band at about 440 nm (Fig. 6.3). After excitation at 365 nm, an increasing $n\pi^*$-band of the *cis*-isomer can be observed at 430 nm. An additional very intense absorption band can be detected at 260 nm, which corresponds to the nucleobases of the RNA.

However, two important features should be noted. Firstly, incorporation of the azobenzene derivatives into the RNA model strands leads to a red-shift of absorbance spectra of the *trans*-isomers. While the $\pi\pi^*$-band of the *trans*-isomers in the RNA1-strand shows a bathochromic shift of about 5 nm with respect to the monomers, for the RNA2-strand this red-shift is slightly increased to 7 nm. These small changes in absorbance in the two different strands can be explained by the different interactions of the RNA with the azobenzene due to the complementary character. Secondly, the observed red-shift of the **pAzo** monomer with respect to the **mAzo** monomer is still observable after incorporation into the RNA strands.

The *cis*-amount of the photo-stationary state was estimated by using the pure spectra of the single strands by HPLC.[161] Suitable scaling on the isosbestic point at 270 nm

enables the determination of a *cis*-amount of 80-90% for **mAzo** and 87-98% for **pAzo** within the different oligonucleotides already at room temperature. Consequently, an extraordinary switching amplitude results for the azobenzene compounds within the RNA strand, especially regarding that a comparable *cis*-amount for other azobenzene linkers, like D-threoninol, could only be obtained at about 70°C.

Intense absorbance changes are obtained for the absorbance bands of RNA at about 260 nm at different temperatures, resulting from the changes in interactions between the nucleotides. Therefore, the determination of the *cis*-amount of the photo-stationary state by using the isosbestic point within the RNA-absorption band was not performed for different temperatures. Although, the isosbestic point at 390 nm does not overlap with the RNA-absorption band and would therefore be clearer, due to limited concentrations, the absorption at 390 nm is lower than 0.01 and therefore contains high errors.

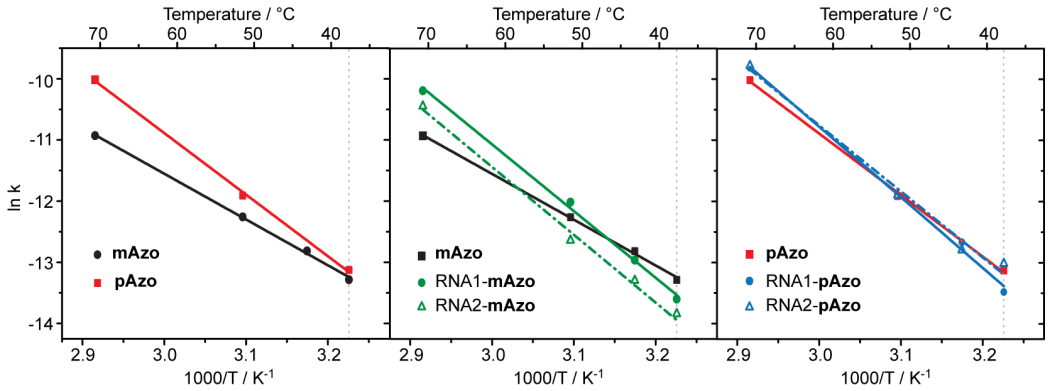

Figure 6.4: Temperature-dependence of **mAzo** and **pAzo**, free as well as incorporated in the RNA single strands RNA1 and RNA2.

Comparing the thermal reaction rates for the *cis*-to-*trans*-isomerization of the azobenzene monomers as well as of the azobenzene compounds incorporated in RNA oligonucleotides (Tab. 6.1 and 6.2), no significant differences can be seen at 37°C. Therefore, the introduction of the compounds **pAzo** and **mAzo** and the interactions with the neighboring base pairs leads to no further destabilization of the *cis*-isomers at this temperature. However, the temperature-dependence of the azobenzenes within the single strands is more pronounced with respect to the free monomer due to a higher activation energy of 91 kJ/mol for both RNA-strands containing **mAzo** and 90-96 kJ/mol for **pAzo** (Fig. 6.4). Consequently, the energy barrier in the electronic ground state is either increased or the energy of the *cis*-isomer is lower for azobenzenes within RNA strands.

To summarize the results for the azobenzene monomers **mAzo** and **pAzo** as well as for the two oligonucleotides RNA1 and RNA2 containing one of the azobenzenes, respectively, good chemical and photo-chemical properties could be found. Comparison to the unsubstituted azobenzene, a high *cis*-amount of 90% could be generated for the azobenzene monomers **mAzo** and **pAzo**. Moreover, realization of such a high *cis*-amount at room temperature for a RNA 15-mer is extraordinary. In addition to

Table 6.2: Energy barrier of the thermal *cis*→*trans*-isomerization and the corresponding relaxation rates for the two different oligonucleotides RNA1 and RNA2 including **mAzo** ($\mathbf{1}_m$ and $\mathbf{2}_m$) and **pAzo** ($\mathbf{1}_p$ and $\mathbf{2}_p$), respectively, in PBS.

	$(k \pm \Delta k)$ $[10^{-6} \cdot s^{-1}]$				E_A
	37°C	42°C	50°C	70°C	$[kJ/mol]$
$\mathbf{1}_m$	1.24 ± 0.05	2.353 ± 0.007	6.06 ± 0.05	37.45 ± 0.06	91 ± 4
$\mathbf{1}_p$	1.40 ± 0.03	3.163 ± 0.006	6.823 ± 0.015	54.6 ± 0.3	96 ± 5
$\mathbf{2}_m$	0.981 ± 0.014	1.69 ± 0.03	3.253 ± 0.012	29.23 ± 0.06	91 ± 5
$\mathbf{2}_p$	2.24 ± 0.03	2.794 ± 0.007	6.869 ± 0.015	56.76 ± 0.13	90 ± 7

that, at 37°C, the thermal relaxation of the *cis*-isomer to the *trans*-isomer is observed with a half-life of at least 86 h in case of RNA2-**pAzo**, allowing the RNA to react on the conformation change of the azobenzene.

6.1.2 Photo-Responsive Dehybridization

Investigations on the stability of the RNA structure and on the destabilizing effects due to photo-isomerization of the photoswitches within the RNA strands were done by performing melting point studies of the RNA duplex structure in the spectral range of UV-light. By increasing the temperature, the hydrogen bonds between the nucleobases between the two single strands are weakened until a dehybridization of the double strand can be observed. Due to the lower interactions at higher temperature, an increase of the absorption band at 260 nm can be seen. The temperature at which 50% of the double strand is separated, is called melting point temperature T_m. The following melting point studies have been performed in the group of Prof. A. Heckel.[161]

In this study, a RNA oligomer with 14 nucleotides was used, which was chosen not to interact with itself (Fig. 6.2b). An additional base or the azobenzene derivative **mAzo** or **pAzo** were introduced at the central position (N^1) of the RNA sequence of the strand RNA1 or of the complementary strand RNA2. The duplex structure containing only the 14-mer without additional bases, which is further called the *unmodified* double strand, shows a melting temperature of 55.4°C. Incorporation of *trans*-**pAzo** in the RNA1-strand is virtually independent of the choice of bases on the opposite site. Here, the influence of e.g. the incorporation of an abasic site (apurinic/apyrimidinic (AP)) and of a missing nucleotide in the complementary strand were studied, which contains only the ribose with no attached base or which leads to a kink in the double strand. While no nucleotide in the RNA2-strand shows a melting point temperature of 48.7°C, an abasic site leads to 49.6°C and an additional e.g. uridine to 47.2°C. Therefore, the *trans*-isomer already destabilizes the duplex structure, which results in a decrease of the melting point of about 5.8 to 8.2°C. After photo-isomerization from the *trans*- to the *cis*-isomer, the double strand destabilizes even further by about 3.8°C in the presence of a 15-mer as the opposite strand.

Interestingly, the incorporation of the *trans*-**pAzo** in the RNA2-strand shows less destabilization effects with a melting point temperature of 52.7°C for an abasic site on

the opposite site. The melting point of $N^1 = AP$ and $N^2 = cis - \mathbf{pAzo}$ is quite comparable to the melting temperature for $N^1 = cis - \mathbf{pAzo}$ and $N^2 = AP$, but the photo-responsive destabilization of the latter double strand is higher with $\Delta T = 5.7°C$. Moreover, the same trend can be observed for the incorporation of **mAzo**. Interestingly, the combination of the *trans*-isomers of both azobenzenes in opposite strands shows comparable or even less destabilizing effects of the duplex structure with respect to e.g. an abasic site. However, no significant improvement on the photo-responsive destabilization of the helical conformation is observed after isomerization from the *trans*- to the *cis*-isomer. Incorporation of two azobenzenes in the RNA strands at different positions, however, is expected to increase the destabilization effect on the double strand.

The melting point studies are supported by MM/MD calculations, performed in the group of Prof. I. Burghardt. Here, the calculation of the B-factor values, which display the root mean square fluctuations of the molecules, can deliver information on the stability of the double strand of the studied RNA strands $N^1 = \mathbf{pAzo}/N^2 = U$ and $N^1 = \mathbf{pAzo}/N^2 = AP$. For the first double helix, a destabilization of the helical conformation is observed already for the *trans*-isomer of **pAzo**, which is in agreement with the earlier melting point studies. Due to the sterical hindrance of the azobenzene and the uridine at the opposite position in RNA2, the photoswitch can hardly intercalate and therefore fluctuates in and out of the double strand. A photo-isomerization from the *trans*- to the *cis*-isomer leads to complete movement out of the helical conformation. Therefore, no significant destabilization effect due to the photo-isomerization can be observed for this double strand. By using an abasic site for the opposite site to the photoswitch in strand RNA2, intercalation between the neighboring base pairs is now possible for the *trans*-isomer of **pAzo**. Like that, the destabilization is decreased for the double strands. The *cis*-isomer of this construct is now able to stay within the duplex structure and induces a destabilizing effect on the whole structure by disrupting the neighboring hydrogen bonds.

Consequently, for a perfect system for a photo-responsive dehybridization, the *trans*-azobenzene should not influence the stability of the double strand significantly, which can be enabled by creating enough space for intercalation between the base pairs. The destabilization effect of the *cis*-azobenzene, however, should be as large as possible, which is only feasible for no fluctuation out of the helical conformation. Therefore, the linker should not be too flexible to allow too much freedom of movement of the azobenzene. So far, solely a destabilization effect due to photo-isomerization could be observed. To generate a photo-responsive dehybridization of the whole double strand, the number of azobenzenes within the single strands needs to be increased. Moreover, the position of the corresponding azobenzenes has to be well-considered to guarantee the photo-control to a maximum extent.

6.1.3 Conclusion

In this section, the influence of covalent incorporation of azobenzenes in a sequence of a ribonucleic acid by using the newly designed linker, which relies on a desoxyribose structure, on the photo-chemical properties of the photoswitch as well as on the stability of the helical conformation of the RNA model oligonucleotides was studied.

It could be shown, that the free azobenzene derivative **mAzo** and **pAzo** show excellent chemical as well as photo-chemical properties in an aqueous phosphate-buffered solution (pH=7.4). Beside a good water-solubility for both derivatives, significant switching amplitudes are observed with a *cis*-amount of around 90% in the photo-stationary state. Due to small reaction rates for the *cis*-to-*trans*-isomerization of both compounds, the *cis*-azobenzene is stable for days with a lifetime of about 100 hours at 37°C.

The covalent introduction of azobenzene in model RNA 15-mers via the desoxyribose linker revealed very comparable photo-physical properties of the photoswitch. An extraordinary amount of the *cis*-isomer in the photo-stationary state of 80-90% for **mAzo** and even 87-98% for **pAzo** can be observed at low temperatures of 37°C. This result is astonishing, since in earlier studies,[192] a comparable amount of a *cis*-isomer could only be observed at high temperatures of about 70°C, which is not feasible for biological systems.

The thermal reaction of the *cis*- to the *trans*-isomer in RNA is similar to the monomers **mAzo** and **pAzo**. Consequently, the *cis*-state can be obtained independent of the composition of the RNA single strands for days. In a RNA duplex structure with a photoswitch at least in one strand, the RNA double helix can react on the conformational change of the photoswitch to the *cis*-azobenzene by loosening or even opening of the helical structure.

In melting point studies as well as by MM/MD calculations, the influence of the both isomeric azobenzene structures on the RNA conformation was studied. As shown, the stability of the helical conformation is highly dependent on the composition of the RNA strand itself. Here, for example, differences in stability were obtained for the *trans*-azobenzene in a RNA strand and in the antiparallel strand. Moreover, the choice of the nucleic base on the complementary RNA strand at the opposite position to the photoswitch is highly important. For nucleic bases, like an uridine, the helical structure is already destabilized in case of the *trans*-isomer due to sterical hindrance. By using abasic sites, the conformation of the RNA is not significantly affected, but a placement of the photoswitch between the neighboring base pairs is enabled. A destabilization of the secondary structure due to photo-isomerization from the *trans*- to the *cis*-isomer can be observed independent of the composition of the RNA. However, the amount of destabilization due to photo-isomerization is highly dependent on the environment of the photoswitch. Consequently, a high amount of photo-responsive disturbance of the helical structure is observed for little influence of the *trans*-isomer and high influence of the *cis*-azobenzene. This can be achieved by creating space within the helix for the *trans*-azobenzene by omitting the nucleotide on

the opposite position, leaving an abasic site, for example. For a rigid incorporation of the planar *trans*-isomer between the neighboring base pairs, the conversion in the non-planar *cis*-isomer has strong influence on the structure.

So far, only the influence of one photoswitch, which is built in a RNA model strand, on the stability of the secondary structure was studied. In further experiments, the effect of two or even a higher number of azobenzenes incorporated in one RNA strand should be studied. For a complete photo-responsive dehybridization, investigations on not only the number of photoswitches, but also the relevant positions within the strand are inalienable.

6.2 Development of a Photo-Responsive Riboswitch

An alternative way for the conformational control of RNA structures is the attachment of an azobenzene to the RNA strand by strong non-covalent interactions between the ligand molecule and the RNA-strand. Therefore, a small photo-active molecule with a variety of functional groups is inalienable for the binding with high affinity, while especially hydrogen-bonds are aspired. The idea of the photo-control reveals that the photoswitchable ligand is supposed to bind to the aptamer only in one of the two photo-isomer structures. A number of aptamer structures are known, which bind small molecules, like Tetracyclin,[194] Neomycin[195] or Chloramphenicol,[196] however, only few photochrome-binding aptamers are obtained.[190,191]

Though, the idea of a photo-responsive aptamer relies on the idea of the non-covalent binding of one isomer to the RNA strand, which induces a conformational change of the tertiary structure of the aptamer. Photo-isomerization of the ligand into the second isomer results in a release of the photoswitch from the RNA and a consequent conformational change in the previous tertiary structure. Although, aptamers are known, which do not react on the binding of the ligand by a structural change, but only on the stabilization of the structure, a high structural difference between the two states is preferred for further application. Since aptamers are an important part of the sensor domain of a riboswitch, the concept of a photo-responsive riboswitch for the photo-control of the gene expression is an interesting field in research.

The binding of the photoswitch to the RNA aptamer structure induces a structural change, which has an influence on, for example, the accessibility of the SD-sequence. If this sequence is unattainable after binding, because it is implemented in the e.g. stem structure of the aptamer or due to sterical reasons, the translation of the genetic information is terminated (OFF-riboswitch). Depending on the desired function to control, the system can be designed either as an OFF- or ON-riboswitch.

The success of the development of a photo-responsive riboswitch depends on a variety of factors, starting with the optimization of the photoswitch. The molecule should be highly soluble in water due to the use as a non-covalent ligand. Moreover, the stability, not only in aqueous solution but more importantly in cells, is inalienable. The photo-responsive molecules as well as potential decomposition products need to be nontoxic for the living cell. To guarantee a good interaction with the biomolecule, there should be a high number of substituents with the ability to develop interactions, like hydrogen bonds. As significant as the chemical properties are the photo-chemical properties of the photoswitch. Therefore, a high switching amplitude with ideally nearly pure states of the photo-isomers and a high fatigue resistance are desirable. Moreover, an excitation wavelength of lower-energy than UV-light should be used for excitation of the photoswitch to exclude damages of the biomolecules.

Since the RNA strand needs to bind the ligand, it is important to find an RNA aptamer with a high binding affinity to one of the photo-isomers of the ligand. By using a SELEX process,[197] a suitable RNA sequence can be found (see subsection 6.2.1).

However, the success of this process hinges on the choice of the proper SELEX routine, which depends on the properties and the size of the ligand. Moreover, the stability of the aptamer structure should be high enough to result in stable ON- and OFF-states. However, it should not be too stable, because no conformational change would be observed after photo-isomerization.

A photo-responsive aptamer, however, does not result necessarily in a photo-responsive riboswitch. Therefore, the choice of the RNA sequence for the regulator function in addition to the aptamer domain is a very critical step.

6.2.1 Systematic Evolution of Ligands by Exponetial Enrichment (SELEX)

For the realization of the high affinity and specificity of the binding of a ligand to a DNA or RNA structure, an aptamer sequence needs to be found in a selection process called SELEX (Systematic Evolution of Ligands by EXponential enrichment), which in general, implies each *in vitro*- and amplification techniques (Fig. 6.5).

During this systematic process, a, usually chemically synthesized, DNA library is used to provide a high diversity of sequences, typically containing less than about 100 nucleotides. In case of a fully randomized DNA pool, this results in 4^{100} different DNA sequences, while the amount of used DNA sequences is usually limited to about 10^{13} to 10^{15} different DNA strands. However, this smaller variety has no effect on the success rate of finding an aptamer sequence, since not every nucleotide is included in the ligand binding. Therefore, these position show a high variability in their choice of nucleotides.

A different approach is the use of a partially structured DNA pool. Here, only a central part of the DNA sequence is randomized, while the outer part is composed of a fixed sequence. In this structured part of the DNA, defined secondary structure, like stable loops, can be predetermined to achieve stable aptamer structures.

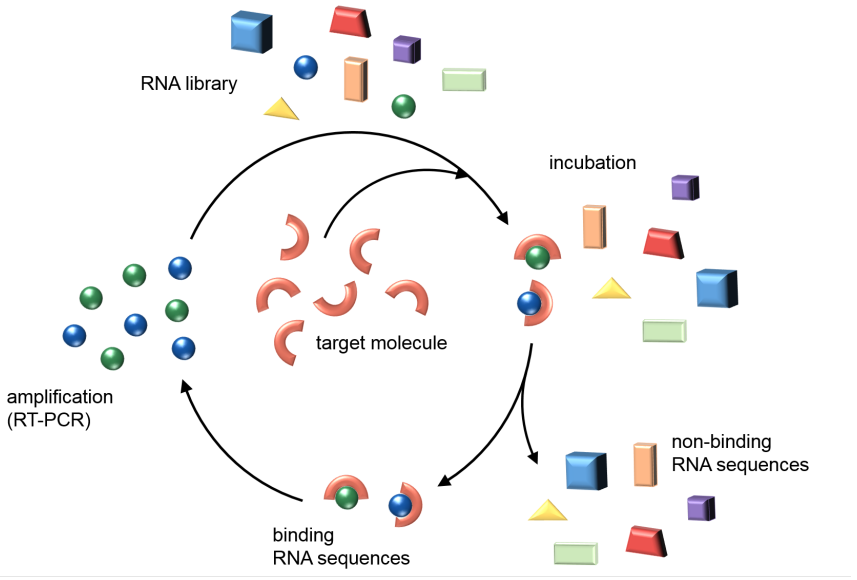

Figure 6.5: Schematic representation of a SELEX-routine.

This DNA library can be transcribed into a RNA library by using a polymerase chain reaction (PCR) and a subsequent *in vitro*-transcription. The first selection round usually implies a negative selection, which excludes the RNA sequences, which bind to the matrix material. Afterwards, the RNA pool is incubated with the target molecule, which results in a separation of the non-binding RNA sequences from the binding aptamers. The elution of the binding RNA-aptamers is dependent on the properties and can therefore proceed unspecifically (thermally) or specifically by using an affinity selection with the free target molecule or by setting up a salt concentration gradient. These RNA sequences are then amplified by a RT-PCR (reverse transcription polymerase chain reaction). These enriched sequences are again incubated in a number of rounds until one aptamer sequence is found that binds the target molecule specifically with a high affinity. If the affinity cannot be increased, the SELEX process is finished. The resulting RNA sequences are further compared and analyzed regarding not only their primary but also their secondary structure. The binding constant of the RNA aptamer and the target molecule can be determined by e.g. affinity electrophoresis in case of larger target molecules like proteins. For small molecules, one common technique is the fluorescence titration, which uses the concentration-dependence of the fluorescence of the ligand in the presence of RNA. However, for non-fluorescent molecules, a technique called isothermal titration calorimetry (ITC) is used for the determination of dissociation constants, which uses the effect of temperature changes as a result of the Gibbs-Helmholtz-equation.

In case of photoswitches used as the target molecule, usually a *photo*-SELEX is performed, in which an additional step is included, in which the ligand is illuminated with a defined wavelength resulting in the second photo-isomer, which should not bind to the aptamer. Therefore, every aptamer sequence binding to both photo-isomers will be excluded by washing steps.

In a SELEX process, the target molecules are usually immobilized to separate binding and non-binding RNA sequences. A variety of different techniques are known, which are highly depending on the structure and properties of the ligand. One very common method of performing a SELEX makes use of magnetic beads, which are superparamagnetic particles with a size in the μm-range. These magnetic beads can be controlled by magnets during the SELEX process. To connect the target molecules with the particles, the magnetic beads are loaded with the protein streptavidin. Due to the high affinity of streptavidin to biotin with a dissociation constant of $K_d = 4 \cdot 10^{-14}\ M$, it is possible to fix the target molecule to the beads, only by biotinylation of the ligand. By adding the linker of the biotin to the target molecule, however, one functional substituent of the ligand, which has the ability to interact with the RNA sequences, needs to be exchanged. So, a high number of functional groups of the target needs to be present. The linker between the target and the biotin is flexible and of arbitrary length. It should be, however, long enough to guarantee the ligand contact to the RNA sequences within the column. Since the streptavidin is quite space demanding, this method is usually only used for large target molecules of comparable size.

A second possible method of fixing the target molecule to the column material is the use of N-hydroxysuccinimidyl (NHS)-activated agarose beads. Due to the linker between the NHS-group and the agarose beads, it is possible to use smaller target molecules due to less sterical hindrance. For coupling, the target molecule needs a primary amine as a substituent, which further reacts covalently with the NHS-ester.

Consequently, in those two methods the target molecule is fixed to the column, while the variety of RNA sequences pass through it. In the washing steps, only the non-binding RNA sequences are washed out, while the binding strands are held on the column due to the interactions with the target molecules. These binding RNA sequences can then be extracted from the column and can further be amplified and studied.

Another important method is the capillary electrophoresis-SELEX (CE-SELEX), which was first published in 2004.[198] It shows a variety of advantages in contrast to other methods. First of all, using CE-SELEX less selection rounds are necessary for finding aptamers with high binding affinity. In contrast to other methods, where the number of rounds can increase to 20, aptamers could be found in one to four selection rounds using CE-SELEX. Moreover, the capture of one part of the molecules is not necessary, since the selection proceeds via the different electrophoretic mobilities of the bound complex and the unbound molecules. Therefore, the free target and the free RNA sequences are injected into the capillary, while the electroosmotic flow pushes the molecules to the cathode. Depending on their mass and charge, they differ in their mobility and can be separated by collecting the consecutive bathes. Therefore, this method can also be used for smaller target molecules. The size of the ligand is limited indirectly by the effect on the electrophoretic mobility of the RNA sequences, which is often only slightly changed.

6.2.2 Photoswitchable Ligands for Photo-Responsive Aptamers

In search of feasible photoswitches for biological use, a variety of azobenzene derivatives was synthesized by T. Halbritter in the group of Prof. A. Heckel and studied, in cooperation, regarding chemical as well as photo-chemical properties. Different approaches were pursued to achieve not only suitable properties of the photoswitch but also interactions with RNA strands (see chapter 5).

For a starting point for the initial guess of a ligand structure, it is often helpful to look for ideas in nature or pharmaceutics. By making use of e.g. antibiotics, the tolerance of the molecule is often already given and challenges of water-solubility and non-toxicity can be skipped. One noticeable example is shown in this subsection 6.2.2 for chloramphenicol-azobenzene (**CAP**).

A different approach is the addition of a variety of functional groups to the azobenzene scaffold to enable a number of interactions with the RNA. The used substituents should have the ability to interact or build hydrogen bonds, but should not affect the properties of the switching process negatively. Therefore, hydroxy- as well as nitro-groups were not used in this study, since it was shown (for hydroxy-groups in

section 5.2) that the thermal back reaction from the *cis*-isomer to the thermally stable *trans*-isomer is highly accelerated by substitution of hydrogens in *ortho*- or *para*-position to the azo-group against hydroxy-groups. In a detailed study, a number of functional groups were attached in different positions on the azobenzene. As a result, the quite small azobenzene derivative 4-[(E)-(4-acetamidophenyl)azo]benzoic acid (**AAPAB**) was designed, which boasts only two functional groups - one acetamide and one carboxy group. This molecules shows, however, suitable properties and was therefore, used for a further search of a specific binding RNA aptamer.

4-[(E)-(4-Acetamidophenyl)Azo]Benzoic Acid (AAPAB)

The azobenzene derivative 4-[(E)-(4-acetamidophenyl)azo]benzoic acid (**AAPAB**), which was derived from a detailed search of a biologically usable photoswitch (see chapter 5), shows a water-solubility of 2.0 mmol/L in PBS at a pH-value of 7.4 (Fig. 6.6).

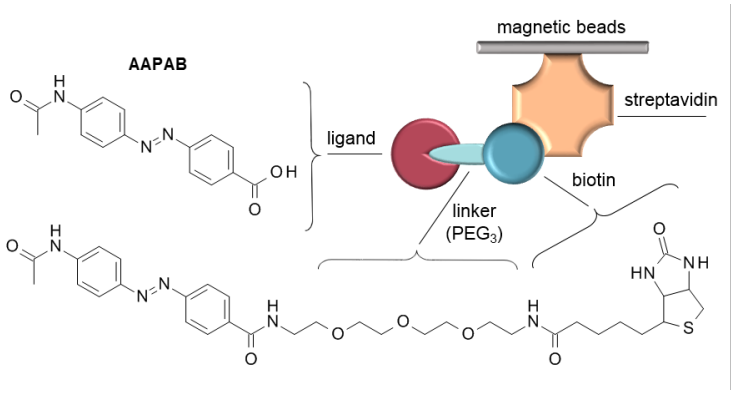

Figure 6.6: Chemical structure of 4-[(E)-(4-acetamidophenyl)azo]benzoic acid (**AAPAB**) and the **AAPAB**-benzamide-derivative, which is coupled via a PEG_3-linker to biotin. The scheme illustrates the fixation of the target molecule to the column during the SELEX procedure via streptavidin magnetic beads.

The UV/vis-spectrum of the *trans*-isomer of **AAPAB** in PBS shows an intense absorption band with a maximum at 350 nm, which corresponds to the $\pi\pi^*$-band (Fig. 6.7a). Moreover, a contribution of the $n\pi^*$-band of the *trans*-isomer can be seen between 400 and 520 nm as well as higher excited states below 270 nm. After excitation with light of a wavelength of 365 nm, the $\pi\pi^*$-band of the *trans*-isomer decreases, while the $n\pi^*$-band of the *cis*-isomer at 440 nm increases with respect to the *trans*-isomer. There is also an increase in the absorption bands between 240 and 300 nm, which is partially due to higher excited states, but also due to the $\pi\pi^*$-band of the *cis*-isomer. In the difference spectrum (Fig. 6.7a, top), a decrease can be observed at about 350 nm and an increase at ca. 450 nm, which is a typical absorption change due to an azobenzene-like isomerization behavior.

A repeatable switching process of the photoswitch is very important, especially for the use within the cells, to exclude the necessity of a constant exchange of ligand. Therefore, an illumination study was performed to determine the fatigue resistance of the azobenzene-derivative in PBS. The sample **AAPAB** was excited at 365 and 420 nm

in an alternating manner for 24 cycles (Fig. 6.7b). By observing the absorption within the $\pi\pi^*$-band of the *trans*-isomer at 350 nm, changes can be observed neither at the absorption intensity nor in the absorption spectra before and after the 24 cycles. Consequently, **AAPAB** shows a high fatigue resistance in PBS.

Moreover, the reaction rate from the *cis*-isomer to the *trans*-**AAPAB** at room temperature was determined to be $k = (2.38 \pm 0.02) \cdot 10^{-4}\ \mathrm{s}^{-1}$. Therefore, the lifetime of this reaction is smaller than of the lifetimes known for the unsubstituted azobenzene. However, the half-life of the *cis*-isomer is still slightly less than one hour, which is stable enough to impact the conformation of the RNA aptamer.

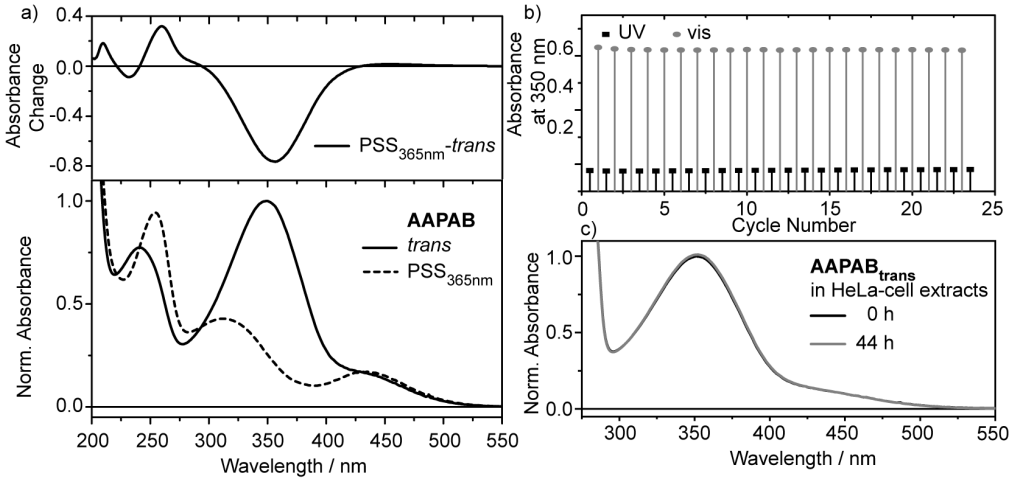

Figure 6.7: a) UV/vis-spectrum of the *trans*-isomer (solid line) and the photo-stationary state (PSS_{365nm}, dashed line) of **AAPAB** in PBS (bottom). Difference UV/vis-spectra (top) indicate the absorbance changes during isomerization (PSS_{365nm}-*trans*). b) Fatigue resistance study on **AAPAB**, showing the absorption at 350 nm after alternating excitation at 365 and 420 nm. c) UV/vis-spectra of the *trans*-isomer of **AAPAB** in HeLa-cell extract before illumination (0 h). The ligand was excited at 365 nm to generate the *cis*-isomer, which is more susceptible to hydrolysis than the *trans*-isomer. After excitation at 420 nm, the *trans*-**AAPAB** is obtained (44 h) with no indication of degradation.

Since the aim is the use in biological systems, it is not enough to guarantee stability of the photoswitch in PBS. Therefore, the system **AAPAB** was studied in HeLa-cell extracts. These cell extracts were added in different lysis-buffers, which differ in additional detergents (see chapter II). The switching behavior as well as the stability of **AAPAB**, however, show no significant differences for the different lysis-buffers. The spectra in Fig. 6.7c) were recorded in lysis buffer Nr. 1. The absorption spectrum of the *trans*-isomer of **AAPAB** can be seen, which is comparable to the spectrum recorded in PBS. Below 300 nm, the absorption band of the components of the HeLa-cell extract can be seen. While this sample was stored in absence of light, UV/vis-spectra show no changes over a time range of days. However, due to the non-planarity of the *cis*-isomer, this isomeric form is supposed to be more exposed to the decomposition due to cell components. Therefore, **AAPAB** was excited at 365 nm to obtain the energetically less stable *cis*-isomer and was then stored again in absence of light. Due to the half-life

of the *cis*-isomer of about 0.8 h, a repeated illumination at 365 nm was necessary. After nearly two days, the sample was excited at 420 nm to obtain the *trans*-isomer again. The resulting UV/vis-spectrum of *trans*-**AAPAB** shows nearly no changes in comparison to the spectrum recorded in the beginning of the study. Consequently, a use of the photoswitch **AAPAB** is feasible also in cells.

Since good (photo-)chemical properties are given for **AAPAB**, an aptamer, which binds specifically one isomer of the photoswitch, needs to be found. Therefore, a SELEX process was performed in the group of Prof. B. Suess. The well-known procedure using magnetic beads as matrix to immobilize the target molecule during the SELEX cycles was used (see subsection 6.2.1). Here, a streptavidin, which is coupled to the beads, binds biotin with a high affinity and specificity. By biotinylation of the target molecule, the ligand can be fixed to the column. By addition of a biotin to the ligand, one functional group, here a carboxy group, is changed into an amide bond (Fig. 6.6). To enable interactions of the photoswitch with the RNA sequences, an additional linker between the biotin and **AAPAB** is used. The very common polyethylene glycol (PEG) linker was introduced with a length of three units (PEG_3).

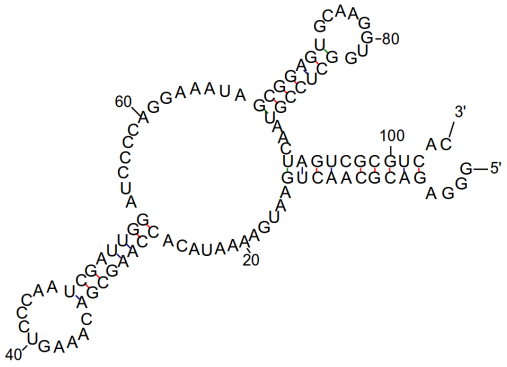

Figure 6.8: RNA sequence (F10), which was revealed from a SELEX process, binding *trans*-**AAPAB**. The secondary structure was proposed by the program mfold.[199]

A SELEX process was performed using a partially structured DNA pool with a fixed structure of 20 nucleotides on the 5'- as well as on the 3'-end of the sequence. In the central part of the RNA sequence, 64 nucleotides are randomized. In this SELEX, a variety of aptamer sequences could be selected, which show high similarity in their primary structure. One of these sequences (F10) is shown in Fig. 6.8 in a proposed secondary structure.

A binding of the *trans*-**AAPAB** was observed already during the SELEX process, while after excitation of the target molecule at 365 nm a significantly less pronounced binding of the RNA sequence to the photoswitch in the *cis*-form reveals. This higher binding affinity of the *trans*-isomer to the RNA sequence can be obtained again after excitation at 420 nm. Consequently, a photo-responsive binding of a RNA aptamer to a photoswitch **AAPAB** is accomplished.

The determination of the binding constants of both isomers to this RNA sequence was performed by ITC-measurements. Here, free **AAPAB** was added to a defined RNA concentration. However, no binding could be observed independent of the concentration of the ligand- neither for the *trans*- nor for the *cis*-isomer. Not even the addition of the biotinylated **AAPAB** showed a binding to the RNA. Therefore, ITC-measurements of the whole ligand/biotin/streptavidin complex have been performed, which indeed show a binding to the *trans*-isomer. This binding can also be affected negatively by excitation of the ligand at 365 nm. Therefore, a binding can only be observed to only one of the isomers. However, there is an additional essential binding of the RNA to the streptavidin. A variation of the length of the linker, which can have an arbitrary length, could help achieving only an interaction between the RNA and the photoswitch. Also, the use of a different SELEX method without the utilization of streptavidin, like CE-SELEX, could result in a photoswitchable RNA aptamer, which only binds the azobenzene ligand. A further investigation, however, has not been performed, yet.

In summary, a photo-responsive binding of a target molecule to a RNA sequence was achieved. The binding could be influenced by light and restored again. Since, however, the ligand is not only the photoswitch, but a combination of a biotinylated azobenzene with a streptavidin, this aptamer is not feasible for application for a photo-responsive riboswitch. However, most of the requirement have been fulfilled, so in cases where no limitation to sizes exist, an application could be feasible.

Chloramphenciol-Azobenzene (CAP)

A broad-spectrum antibiotic, which is not only used for the critical diseases, like typhoid fever or malaria, but also for eye diseases, like styes, is chloramphenicol. It is blocking the building of peptide bonds by binding to the ribosome during the translation process. Since an RNA aptamer is known,[196] which binds chloramphenicol, this molecular structure is an ideal starting structure for designing a photoswitchable ligand. By exchanging the nitro-group into an azo-group with an attached phenyl-ring, a chloramphenicol-azobenzene is generated, which is well-soluble in water with 0.3 mmol/L.

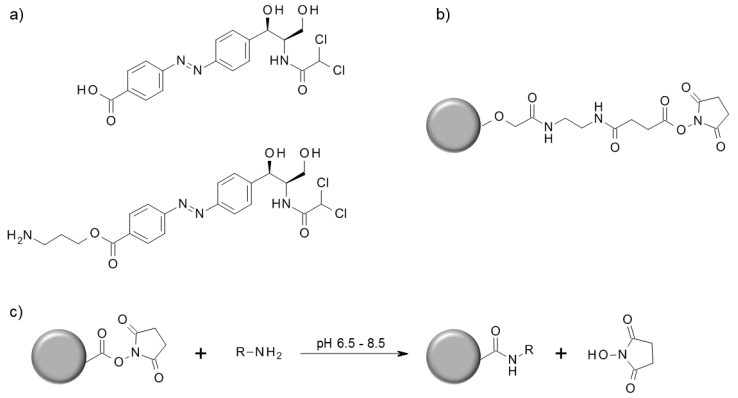

Figure 6.9: a) Chemical structure of chloramphenicol-azobenzene (**CAP**) as well as the **CAP**-derivative with a free primary amino group for coupling to the agarose beads. b) Chemical structure of the N-hydroxysuccinimide (NHS) ester of an agarose derivative with a 10-atom spacer arm. c) Coupling reaction of the agarose beads with the target molecule, which contains a free primary amino group.

Regarding the UV/vis-spectrum of chlorampenicol-azobenzene (**CAP**) in PBS (Fig. 6.10), a clear absorption maximum at 330 nm can be observed, which responds to the $\pi\pi^*$-band of the *trans*-isomer. Moreover, a contribution of the $n\pi^*$-band can be observed between 380 and 500 nm. By excitation with light of a wavelength of 365 nm, the $\pi\pi^*$-band of the *trans*-isomer decreases due to photo-isomerization to the *cis*-isomer, which can be detected at the increase of an absorption band at 280 nm as well as a small band at 435 nm, which can be explained by the $\pi\pi^*$- and the $n\pi^*$-band of the *cis*-isomer, respectively. By extrapolation of the pure *cis*-spectrum, the amount of the *cis*-**CAP** after excitation at 420 nm of 4.6% ($PSS_{420\,nm}$) and at 365 nm of about 80% ($PSS_{365\,nm}$) was estimated. The thermal stability of the *cis*-isomer at room temperature in a buffered solution (pH=7.4) is suitable with a rate of $k_{therm} = 2.9 \cdot 10^{-7}$ s^{-1}, which is even more stable than the unsubstituted azobenzene.[124]

Consequently, with a lifetime of the *cis*-isomer of about 27 days at room temperature, this isomer has an enormous stability. Relying on the Arrhenius-equation (Eq. 3.7), an energy barrier for the thermal relaxation of *cis*-**CAP** to its *trans*-isomer is determined to be $E_A = (109 \pm 7)\ kJ/mol$.

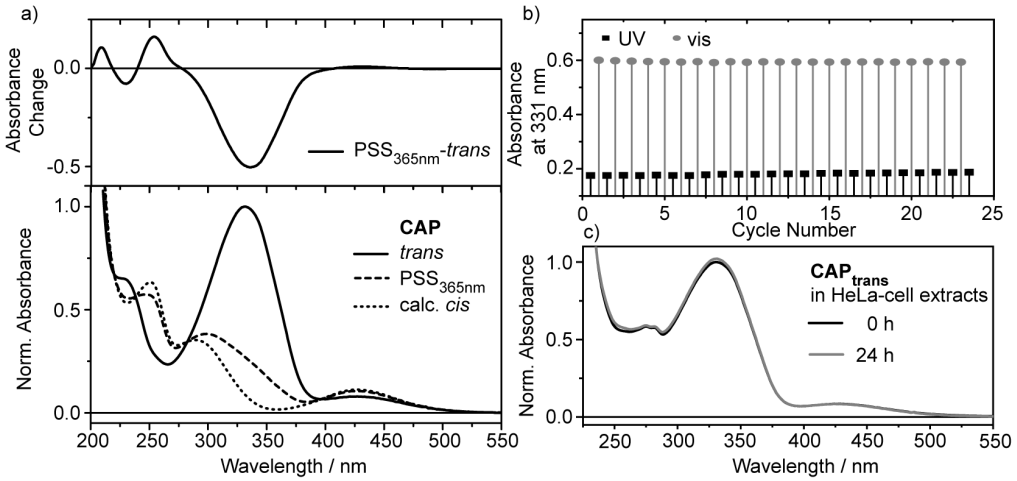

Figure 6.10: a) UV/vis-spectrum of the *trans*-isomer (solid line) and the photo-stationary state (PSS_{365nm}, dashed line) of **CAP** in PBS (bottom). Difference UV/vis-spectra (top) indicate the absorbance changes during isomerization (PSS_{365nm}-*trans*). b) Fatigue resistance study on **CAP**, showing the absorption at 331 nm after alternating excitation at 365 and 420 nm. c) UV/vis-spectra of the *trans*-isomer of **CAP** in HeLa-cell extract before illumination (0 h). The ligand was excited at 365 nm to generate the *cis*-isomer, which is more susceptible to hydrolysis than the *trans*-isomer. After excitation at 420 nm, the *trans*-**CAP** is obtained (24 h) with only slight changes, which can mainly be ascribed to changes in the isomerization grade.

The UV/vis-spectra after alternating excitation at 365 and 420 nm can be seen in Fig. 6.10. Since the absorption at 330 nm can be restored to the same amplitude after alternating UV- and vis-excitation and no additional product bands can be detected in the UV/vis-spectra, a high fatigue resistance can be observed even after 25 cycles.
To ensure a stability against hydrolysis and degradation within the cell, UV/vis-spectra were recorded for **CAP** in HeLa-cell extracts over a time range of hours. It can be clearly seen (Fig. 6.10), that for 24 h nearly no changes in the absorption spectrum of the *trans*-isomer can be observed. Therefore, **CAP** can be used for days without decomposition.

Consequently, the photoswitch **CAP** shows excellent chemical and photo-chemical properties, regarding its solubility and stability in water and cell-extracts as well as its switching amplitudes, the fatigue resistance and the thermal stability of the *cis*-isomer. Therefore, **CAP** was chosen to act as a photoswitchable ligand for binding to an RNA aptamer, which was selected in a SELEX process.

Since the SELEX process of small ligands is very difficult, especially performing a selection with streptavidin-coupled magnetic beads, a different matrix was used to immobilize the chloramphenicol-azobenzene during the selection process. In this case, N-hydroxysuccinimide (NHS) ester-coupled agarose with a 10-atom linker was used (Fig. 6.9b). In this process the target molecule is covalently bound to the agarose (Fig. 6.9c). To ensure a coupling, a free primary amino group at the ligand is necessary. Therefore, the carboxy group of **CAP** is modified to an amino group (Fig. 6.9a, bottom). Moreover, a partially structured DNA pool was used to generate a stable

RNA secondary structure of the aptamer. Therefore, a small sequence, which forms a very stable stem-loop structure, was chosen to be a part of the initial RNA pool and added to the randomized part. These stabilizing effects of this loop have been shown in earlier studies (personal communication with research group of Prof. B. Suess).

Using this procedure, a RNA sequence of 104 nucleotides was selected (aptamer 42), which binds specifically only the *trans*-**CAP** and not the *cis*-**CAP**. It was possible to shorten the selected RNA sequence to a 42-mer without loosing its good qualities (aptamer 42_{trunc}). It is suggested to consist of a stem-loop structure with two loops; the first loop with 12 nucleotides (loop A), which is the initially added RNA sequence, and the second loop with 8 (loop B) nucleotides (Fig. 6.11a).

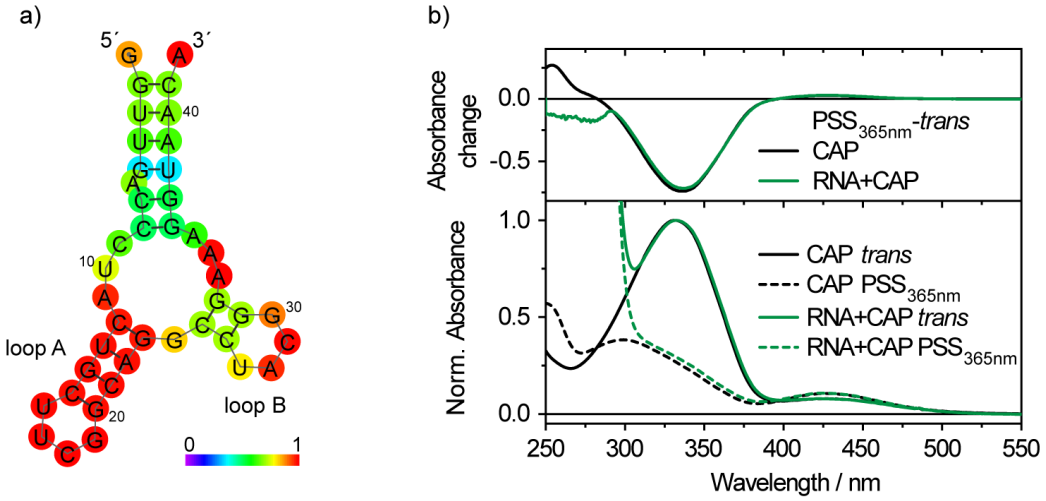

Figure 6.11: a) RNA sequence of the aptamer 42_{trunc}, which binds specifically the *trans*-isomer of **CAP**. The secondary structure was predicted by RNAfold[200] using the minimum free-energy prediction, resulting in a free minimum energy of -9.2 kcal/mol. The color-code gives the base pair probability and in case of unpaired regions, the probability of being unpaired. b) UV/vis-spectra of the *trans*- (solid line) and the photo-stationary state after excitation at 365 nm (dashed line) of the ligand **CAP** and the RNA-aptamer with **CAP**. The isomerization behavior is illustrated by the difference of absorbance changes of the spectra of the *trans*- and the photo-stationary state (top). Spectra were normalized on the absorption maximum of *trans*-**CAP** in both samples at 332 nm. **CAP** and RNA were measured in a ratio 1:1 with a concentration of 200 μM.

For determination of the dissociation constant, ITC-measurements were performed, in which a K_d-value of 820 nM was found for the modified *trans*-amino-**CAP**, while for the *cis*-isomer no binding could be observed. The affinity of the original *trans*-**CAP** with the carboxy group is slightly lower with a value of 3.55 μM, which is comprehensible, since this is not the molecule that was selected for.

Consequently, a very high affinity and selectivity of the RNA aptamer 42_{trunc} is given for *trans*-**CAP**. Moreover, it was shown that there is no binding affinity to the pure chloramphenicol without the additive azobenzene. A binding of **CAP** to the chloramphenicol binding site in the loop of ribosomal RNA of bacterial ribosomes,

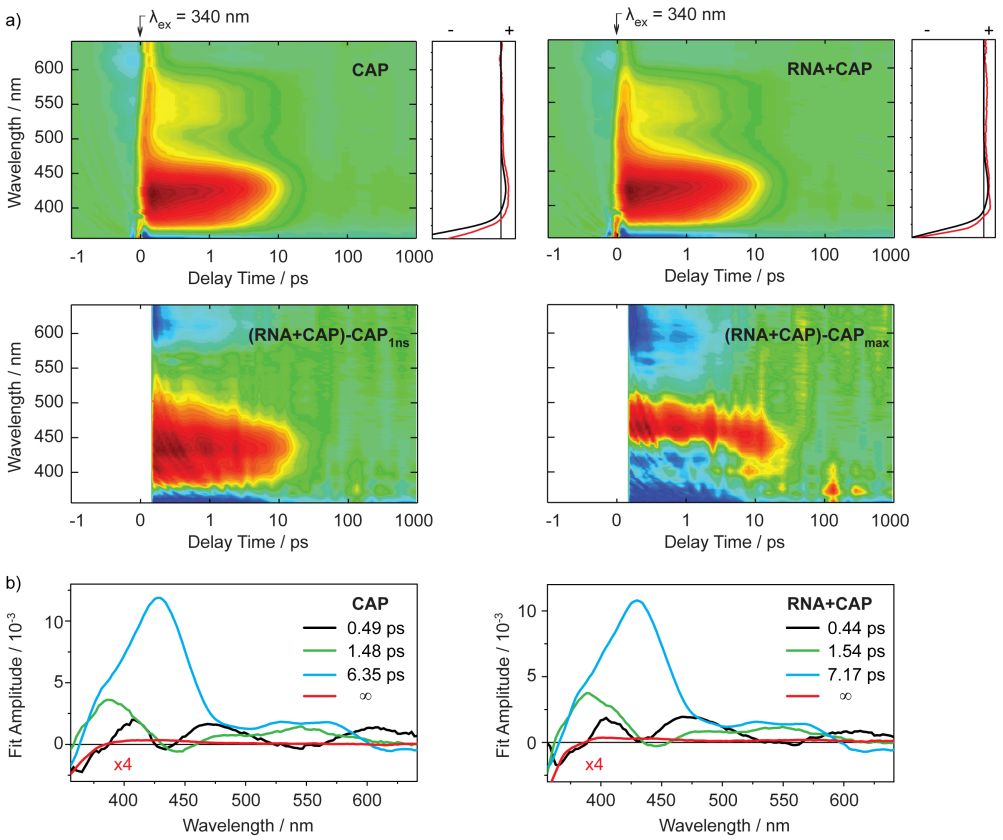

Figure 6.12: a) Transient absorption difference spectra of **CAP** (left, top) and the complex **RNA+CAP** (right, top) in SELEX buffer. A comparison of the infinite lifetime (red) and the steady-state difference spectrum (black) is shown. Subtraction of the measurements, which were normalized on the absorption difference spectra at a delay time of 1 ns (left, bottom) and normalized on the absorption maximum at 420 nm at a delay time of 200 fs (right, bottom); for reasons of visualization only shown after about 200 fs. b) Decay-associated spectra of the transient absorption difference spectra of **CAP** and the complex **RNA+CAP**.

which results in inhibition of the peptide bond formation in case of chloramphenicol, has not been studied yet. Comparison of the UV/vis-spectra of the ligand **CAP** and the complex of RNA aptamer 42_{trunc} and *trans*-**CAP** in a ratio 1:1 (200 μM) in SELEX buffer shows, that there is nearly no influence of the RNA on the steady-state absorption spectrum of the azobenzene-ligand upon binding (Fig. 6.11b). Neither the absorption maxima of the *trans*- and the *cis*-isomer shift significantly with respect to the pure **CAP** (bathochromic shift of **RNA+CAP** of 1 nm), nor the switching amplitude is influenced (Fig. 6.11b, top). Below 310 nm, the absorption band of the RNA can be detected.

A fast switching process of the photoswitch is desired to not temporally overlap with the change in conformational or subsequent function of the biological system. Therefore, it is necessary to study the dynamics of the isomerization process and the following changes of not only the **CAP**-photoswitch but also in combination with the RNA-aptamer. Due to the interactions of the azobenzene with the RNA sequence, the isomerization behavior of the photoswitch could be affected. Therefore, ultrafast

Table 6.3: Lifetimes of time-resolved UV-pump UV/vis-probe experiments on **CAP** and the complex of **CAP** and the RNA aptamer 42_{trunc}.

	τ_1 [ps]	τ_2 [ps]	τ_3 [ps]	τ_4 [ps]
CAP	0.49	1.48	6.35	∞
CAP+RNA	0.44	1.54	7.17	∞

time-resolved UV-pump UV/vis-probe experiments have been performed for both substances in SELEX-buffer. An excitation wavelength of 340 nm was used with a low pump energy of 30 nJ to prevent RNA damages.

For the pure **CAP**, after excitation within the absorbance band of the $\pi\pi^*$-band of the *trans*-isomer of **CAP**, two ESA-bands arise in a broad spectral range between 380 and 600 nm (Fig. 6.12). ESA_1 is located at 420 nm, while ESA_2 can be found at 550 nm with lower intensity. Both ESA-bands correspond to a transition from the first excited state in different higher excited states *m* and *n* ($S_1 \rightarrow S_{m,n}$). The temporal evolution of the absorption behavior can be described by four exponential functions. The first lifetime τ_1 describes mostly the increase of the absorption bands of ESA_1 and ESA_2 with a simultaneous decrease at 410 and 470 nm (Tab. 6.3). This can be explained by a $S_2 \rightarrow S_1$-transition and a movement out of the Franck-Condon-region, which can be seen in the sinusoidal shape of the corresponding DAS. The lifetimes τ_2 and τ_3 describe the decay of the S_1-state. The lifetimes τ_2 mainly simulates the decay of the part of the absorption difference band of ESA_1, which corresponds to the energetically higher energy difference, as well as of the general ESA_2-band. The relaxation of the contribution of the ESA_1-band of transitions with lower energy differences and the ESA_2-band can be described by the lifetime τ_3. While τ_2 can be regarded as the lifetime of the direct $S_1 \rightarrow S_0$-transition via a conical intersection (CI) into the ground state of the *trans*-state as well as in the ground state of the photo-product *cis*-**CAP**, the lifetime τ_3 describes an additional pathway into these two ground states, remaining slightly longer on the potential energy surface of the S_1-state of the *trans*-isomer. An additional lifetime for the vibrational cooling effect of the ground state could not be observed. This may slightly contribute to the lifetime τ_3. After about 30 ps, the ground state of the *trans*- as well as of the *cis*-isomer are completely (re-)populated. This can be seen in the weak product absorption (PA) band of the *cis*-isomer between 400 and 460 nm. The absorption difference spectrum at the longest delay time of about 2 ns is described by an infinite lifetime τ_4, which coincides quite well with the steady-state difference spectrum. Therefore, an isomerization of **CAP** can be detected before 30 ps, which is completely finished within this time scale, with typical azobenzene isomerization dynamics.

Comparing the transient absorption difference spectra of **CAP** and the complex of **CAP** and the RNA aptamer 42_{trunc}, the overall structure is quite comparable. There are two ESA-bands located at about 420 and 550 nm and a GSB below 380 nm. The lifetimes τ_1 and τ_2 of **RNA+CAP** are the same as for the pure ligand **CAP** (Tab. 6.3). The lifetime τ_3, however, is slightly prolonged by a value of about 1 ps. By normalizing

the measurements of the two samples on the PA- and GSB-bands at the longest delay time of about 2 ns, a reasonable comparison can be made due to identical experimental conditions, like concentrations and pulse energy. The resulting transient absorption double difference spectrum after subtraction of the measurement of **CAP** from the spectrum of **RNA+CAP** can be seen in Fig. 6.12a. A positive contribution within the ESA_1-band between 380 and 520 nm as well as a contribution of the GSB below 380 nm remain for the complex. Interestingly, no difference can be seen within the ESA_2-band at 550 nm for both samples. Therefore, a redistribution of the transitions from the S_1-state into higher excited states $S_{n,m}$ occurs in case of interaction of **CAP** with the RNA aptamer. On the supposition that the same amount of photo-product is the result for both samples, transitions $S_1 \rightarrow S_m$ (ESA_1) are more probable after interaction with RNA, while transitions $S_2 \rightarrow S_n$ (ESA_2) are not affected. However, also an increased extinction coefficient for the transition $S_1 \rightarrow S_m$ is feasible for the complex of azobenzene and RNA. Moreover, a lower quantum yield of the *trans*-to-*cis*-isomerization ($QY_{\pi\pi^*}(t \rightarrow c)$) is possible for the azobenzene **CAP** interacting with the RNA. In this case, the PA-band is overestimated resulting in too intense ESA-bands. This, however, does not explain the missing difference within the ESA_2-band.

Consequently, not only the quantum yield of the isomerization of the azobenzene **CAP** is influenced slightly by incorporation within the RNA-structure but also the transition probabilities of the excited states absorption processes.

The assumption of retention of the properties of the ESA-bands leads to the transient absorption double difference spectrum after normalization of both experimental spectra at the absorption maximum of the ESA_1-band of each sample around 420 nm. The subtraction of the spectrum of the ligand **CAP** from the measurement of the complex **RNA+CAP** can be seen in Fig. 6.12 (right, bottom). Firstly, a slight bathochromic shift within the ESA_1-band can be observed for **RNA+CAP** with respect to **CAP**, which emerges from the positive contribution at about 470 nm and the negative part at 420 nm.

Therefore, the energy of the transition $S_1 \rightarrow S_m$ is lower for the azobenzene within the RNA. Interestingly, the energy of the transitions starting from the ground state (e.g. $S_0 \rightarrow S_1$ and $S_0 \rightarrow S_2$) are not affected (Fig. 6.11). Consequently, the interaction between the photoswitch and the RNA influences the electronic structure of the higher excited state m. Moreover, a negative contribution can be seen not only within the ESA_2-band, but also in the PA-band. On this second assumption, the $S_1 \rightarrow S_n$ as well as the product formation is less probable for the complex **RNA+CAP** than for the ligand **CAP**. Furthermore, a positive absorption can be seen within the ESA_1-band after a delay time of about 6 ps. This results from the slightly prolonged decay into the ground state for the RNA-complex, which can also be seen in the lifetime τ_3 (Tab. 6.3).

To summarize, just like the isomerization of the pure ligand **CAP**, the *trans*-to-*cis*-isomerization of the azobenzene incorporated in the RNA occurs within 30 ps via a typical azobenzene-like isomerization mechanism. However, influences of the RNA can be determined not only in the electronic properties of the excited state m, which is

the final state of the transition corresponding to the ESA_1-band, but also presumably in the quantum yield of the isomerization process.

Since in the wavelengths between 360 and 600 nm, only the photoswitch shows an absorption behavior but not the RNA, in these experiments only the influence of the RNA on the azobenzene can be observed. However, even more interesting is the impact of the **CAP** on the RNA-structure. This was studied in CD-experiments in a spectral range from 210 to 450 nm (Fig. 6.13a). In these experiments, the RNA concentration was 10 μM and the ratio **RNA:CAP** was 1:1.

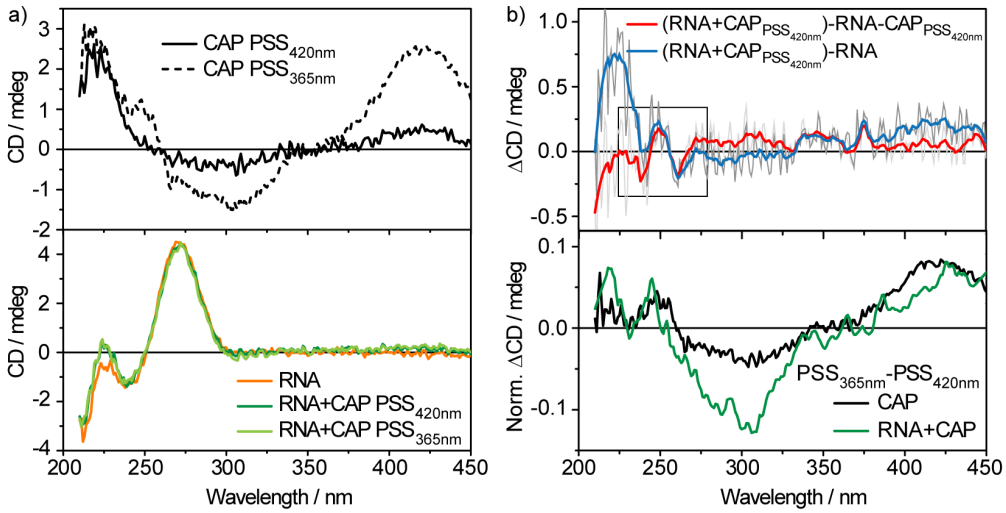

Figure 6.13: a) CD-spectra of the *trans*-isomer (black solid line) and the photo-stationary state (black dashed line) of **CAP** in SELEX buffer (top). CD-spectra of RNA-aptamer 42_{trunc} (10 μM; orange), the RNA-aptamer with the photoswitch **CAP** in its *trans*-isomer (dark green) and its *cis*-isomer (light green) (1:1) (bottom). b) For visualization of the isomerization process of the free ligand (black) and the ligand within the RNA (dark green) (PSS_{365nm}-trans), the difference of the CD-spectra are normalized on the positive CD-difference band of **CAP** at 420 nm (bottom). For investigations on the effect on the structural changes of the RNA and the corresponding CD-spectra upon binding of *trans*-**CAP**, the CD-spectrum of the the pure RNA-aptamer (blue) as well as in combination with the free *trans*-**CAP** (red) was subtracted from the spectrum of *trans*-**RNA+CAP** (top).

The pure ligand **CAP** shows dominant features in the CD-spectrum in the spectral region between 210 and 450 nm. While the CD-signals can already be seen for the *trans*-isomer, these bands intensify after excitation at 365 nm. Therefore, most of the CD-signals are supposed to rely on the *cis*-isomer of **CAP** and can only be seen in the PSS_{420nm}-state due to the small amount of *cis*-**CAP**. An intense positive band can be detected between 360 and 450 nm, which is caused by the *cis*-isomer. Moreover, a negative signal can be seen between 350 and 360 nm and a broad structured band below 250 nm. Thus, the isomerization process can be displayed by the difference of these two measurements (Fig. 6.13 b) bottom), which show two positive difference bands at 250 and 420 nm and a negative signal at about 300 nm.

The CD-spectrum of the pure RNA-aptamer 42_{trunc} ($c = 10\ \mu M$) shows three dominant features below 300 nm. One intense positive CD-signal at 270 nm and two neg-

ative signals at 240 and 210 nm. These CD-signals are comparable to earlier studies on ribonucleic acids and correspond to the characteristics of a RNA hairpin.[201,202] The influence of the *trans*-isomer of the **CAP**-ligand on the CD-spectrum of the RNA aptamer is only slightly moderate. To reveal small differences, the CD-spectrum of the pure RNA aptamer was subtracted from the CD-spectrum of the RNA-aptamer with the bound *trans*-**CAP** (Fig. 6.13b top). Here, a small positive band can be seen between 360 and 450 nm, which results from the *cis*-isomer of **CAP** itself, which is contained to a small amount even after 420 nm excitation. Moreover, a negative band between 260 and 380 nm is observable, which is also due to the pure CD-spectrum of the azobenzene, which shows a negative signal within this region (Fig. 6.13a top). Due to the strong spectral overlap of azobenzene and the RNA aptamer, the CD-spectrum of the *trans*-**CAP** was scaled on the CD change of the latter CD-difference spectrum at 420 nm. Since the CD-spectra of the RNA as well as of the photoswitch were subtracted from the CD-spectrum of the complex of RNA and azobenzene, the resulting differences are consequences from structural changes upon binding of the ligand (Fig. 6.13b). Here, a sinusoidal shape can be detected between 230 and 270 nm, which implies a small shift of the CD-spectrum due to a conformational change within the RNA structure. Changes in the CD-spectrum around 260 nm can be ascribed to changes in the secondary structure of RNA. Therefore, the small obtained differences are supposed to refer to the binding of the *trans*-**CAP** to the RNA aptamer via non-covalent interactions.

The normalized CD-difference-spectrum after photo-isomerization of **CAP** within the RNA-structure is, in general, comparable to the difference-spectrum of the pure photoswitch (Fig. 6.13 b) bottom). However, the negative change between 260 and 380 nm is increased for the measurement with RNA in contrast to the pure ligand. Therefore, the intercalation of the azobenzene with the RNA-aptamer has most probably an effect on the structure of the azobenzene-ligand. In addition to the changes within the CD-signals of azobenzene, the comparison of the CD-spectra referring to the photoswitching event in the free ligand with the complex of RNA and ligand reveals small changes at 220 and 240 nm and between 260 and 290 nm, which coincide with the CD-signals of the RNA. Since a photo-isomerization of the ligand **CAP** should only result in CD-differences in the signals of the photoswitch, unless the RNA aptamer and the ligand interact, a slight photo-responsive change of conformation of the RNA aptamer 42_{trunc} is observed.

Summarizing, there is a weak change in the CD-signal of the RNA by addition of **CAP**, which is not an additional behavior due to the presence, but due to the interaction of **CAP** with the RNA. A very weak hypsochromic shift from 260 to 250 nm can be observed, which cannot be found in the CD-spectrum of the pure ligand. Moreover, a slight change in the RNA signals is obtained by photo-isomerization. Since the aptamer is designed to not interact with the *cis*-isomer, the effect of the *trans*-**CAP** should be reversible by illumination at 365 nm, which should result in the CD-spectrum of the pure RNA with additional, not interacting *cis*-**CAP**. Nevertheless, the CD-spectrum of

the pure RNA-aptamer cannot be restored (Fig. 6.13a bottom). One possible reason could be that the photo-stationary state after excitation at 365 nm still contains 20% *trans*-isomer, which corresponds to a concentration of 2 μM in this experiment. While the K_d-value of the RNA-aptamer 42_{trunc} and *trans*-**CAP** is 3.55 μM, the influence of the *trans*-to-*cis*-isomerization on the CD-spectrum within the RNA-band could be still quite small.

A second possible reason for the very small effect of photo-isomerization of the ligand can be found in the RNA-structure. About 30% of the nucleotides is highly fixed in a hairpin-loop (loop A) with an immense stability (Fig. 6.11a). This stable hairpin-loop was originally requested for a general stability of the aptamer. However, if the stabilizing effect of this loop is too pronounced, no effect of the isomerization on the RNA structure can be observed, since the binding of the ligand does not induces a conformational change of the aptamer-structure.

For additional information on the photo-induced conformational change within the RNA-structure, experiments in the infrared-spectral region have been performed for investigations on the vibrational changes of the ligand **CAP** as well as of the RNA-aptamer 42_{trunc} upon release of the ligand (*trans*-to-*cis*-isomerization). Since the binding of a ligand usually occurs on a longer time scale than nanoseconds (μs to ms), which cannot be detected by the available experimental setups, the *cis*-to-*trans*-isomerization has not been studied.

In the IR-difference spectrum (PSS_{365nm}-*trans*) of **CAP** in a deuterated SELEX-buffer ($c = 5\ mM$), a variety of difference signals can be detected between 1480 and 1650 cm^{-1} (Fig. 6.14a). To get an idea about the vibrations, which are located in this region, (TD)DFT-calculations (B3LYP/cc-PVDZ and PCM(water)) have been performed for the *trans*- and the *cis*-isomer of **CAP**. The results of the ground-state optimization and a subsequent frequency calculation can be seen in Fig. 6.14. The calculated frequencies were broadened with Lorentz-functions with a half-width of 10 cm^{-1} and scaled with the scaling factor corresponding to the functional and basis set (0.97). Comparing the calculated and the experimental difference spectra, the general structure is quite similar. During the isomerization from *trans*- to the *cis*-isomer, the bending vibrations of the phenyl rings of the *trans*-**CAP** disappear at 1608 cm^{-1}, while the bending vibrations of the *cis*-isomer appear at 1597 cm^{-1}. Here, theoretical calculations match the experiment quite well, however, a small shift can be observed. Also the disappearing bending vibrations of the *trans*-isomer at 1393 cm^{-1} as well as the stretching vibration of the azo-bond at 1508 cm^{-1} can be found in the experimental difference spectrum. High intensities were found for the vibration of the amide group in the side chain of the azobenzene at about 1500 cm^{-1} (displacement vectors not shown), which is slightly more pronounced for the *trans*-isomer. However, in the experiment, this difference could not be observed.

While the spectral position of the frequencies of the *trans*-isomer at 1566 cm^{-1} and of the *cis*-isomer at 1566 and 1562 cm^{-1} coincide very well with the measured IR-difference spectrum, the calculated intensities cannot reproduce the negative ab-

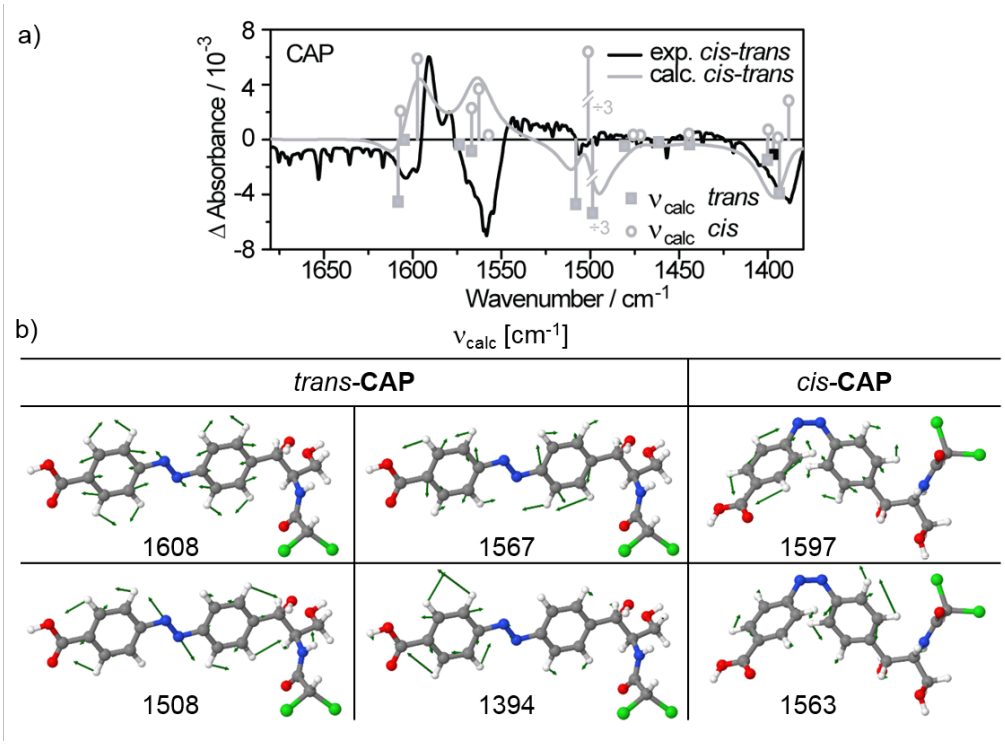

Figure 6.14: a) Experimental IR-difference spectrum (PSS_{365nm}-*trans*) of the photoswitch **CAP** (black) and the difference spectrum of the calculated frequencies (grey) of the *trans*- (squares) and the *cis*-**CAP** (circles) in a polarized continuum model (PCM) describing water (DFT/B3LYP/cc-PVDZ). For calculation of the difference spectrum, the frequencies of both isomeric forms were broadened by a Lorentz-function with a half-width of 10 cm^{-1}. The calculated frequencies were corrected by the method-depending scaling factor 0.97.
b) Calculated frequencies of the *trans*-**CAP** (left) and *cis*-**CAP** (right), which changes upon isomerization.

sorbance change upon photo-isomerization. Therefore, either the frequencies of the *cis*-isomer are overestimated or the vibrations of the *trans*-isomer are underestimated. A possible reason could be interactions of these vibrations to the water molecules, which can influence the corresponding intensities. Since only an implicit water model was used for the calculations, these interactions cannot be obtained in the current theoretical description.

Consequently, besides the vibrations around 1560 cm^{-1}, the theoretical calculations and the experimental IR-difference spectrum are in quite good agreement.
For examination of the vibrations of the complex of the RNA aptamer 42_{trunc} and the ligand **CAP** and for comparison to the vibrations of the free ligand **CAP**, a sample was prepared using the precipitation technique with ammonium acetate. Afterwards, the RNA-pellet was dissolved in a deuterated SELEX-buffer, which contains **CAP** in a concentration of 2.5 mM and was prepared by lyophilization. The resulting clear solution contained an RNA concentration of about 2.5 mM and a ratio of **RNA:CAP** = 1:1. However, about 30 minutes after preparation of the calcium fluoride window for the IR-measurements, small white crystals precipitated from solution, which decreased the RNA concentration in solution. Consequently, the reason for the low RNA con-

centration is supposed to be the result of the precipitation routine, e.g. an insufficient washing of the RNA pellet. Therefore, the remaining ammonium acetate from the precipitation dragged the RNA out of the solution.

Therefore, the resulting ratio of the RNA and the ligand was about 1:10, which leads to very weak contribution of the IR-bands of the RNA in this region. A comparison of the absolute spectra of the ligand and the complex of ligand and RNA, however, reveal a slightly more pronounced band between 1600 and 1660 cm^{-1}, which could refer to interactions between A and U at 1620 cm^{-1} or G and C at 1661 cm^{-1}.[203]

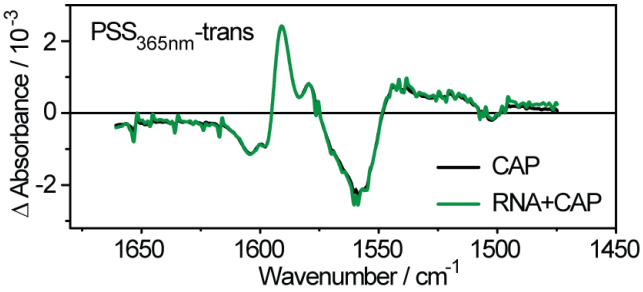

Figure 6.15: IR-difference spectra of the free photoswitch **CAP** in its *trans*- and *cis*-isomer pure (black) and incorporated in the RNA-aptamer 42_{trunc} (green) in deuterated SELEX-buffer.

After photo-isomerization of the ligand **CAP** within a complex with the RNA aptamer, the IR-difference spectrum matches the spectrum of the free ligand **CAP** almost entirely (Fig. 6.15). The positive difference bands of the measurement of **RNA+CAP** around 1580 cm^{-1}, which refers to the *cis*-isomer, are identical to the difference spectrum of the pure **CAP**. However, there are minor differences in the negative bands around 1560 cm^{-1} and between 1600 and 1650 cm^{-1} of the *trans*-isomer. Since only the *trans*-isomer of **CAP** should interact with the RNA, this weak increase of the signals could be ascribed to the interaction. It is, however, unclear whether this band is a small variation upon photo-isomerization within the IR-band of the ligand **CAP** or of the RNA.

To study the origin of these small signals and the dynamics of the release of the ligand, ps-time-resolved UV-pump IR-probe experiments have been performed with an excitation wavelength of 320 nm and an IR-detection range from 1520 to 1680 cm^{-1}.

In the transient absorption difference spectra of the free ligand **CAP** (Fig. 6.16), two GSB can be clearly seen at 1600 cm^{-1} and more intense at 1550 cm^{-1}, which can also be seen in the steady-state IR-difference spectrum (Fig. 6.14). Moreover, positive bands can be obtained at 1620 and 1575 cm^{-1}, which refer to the excited states absorption, which appear due to the anharmonicity of the system. With a time constant of 4 ps, the positive signals slightly shift to higher wavenumbers, which result from a relaxation process. With a time constant of 10 ps, the ground state of the *trans*-isomer is repopulated. Moreover, clear positive absorbance differences can be detected after about 20 ps for the photo-product *cis*-**CAP** at 1540, 1590 and 1630 cm^{-1}, which coincide with the steady-state IR-difference spectrum of **CAP** (Fig. 6.16, right). Moreover,

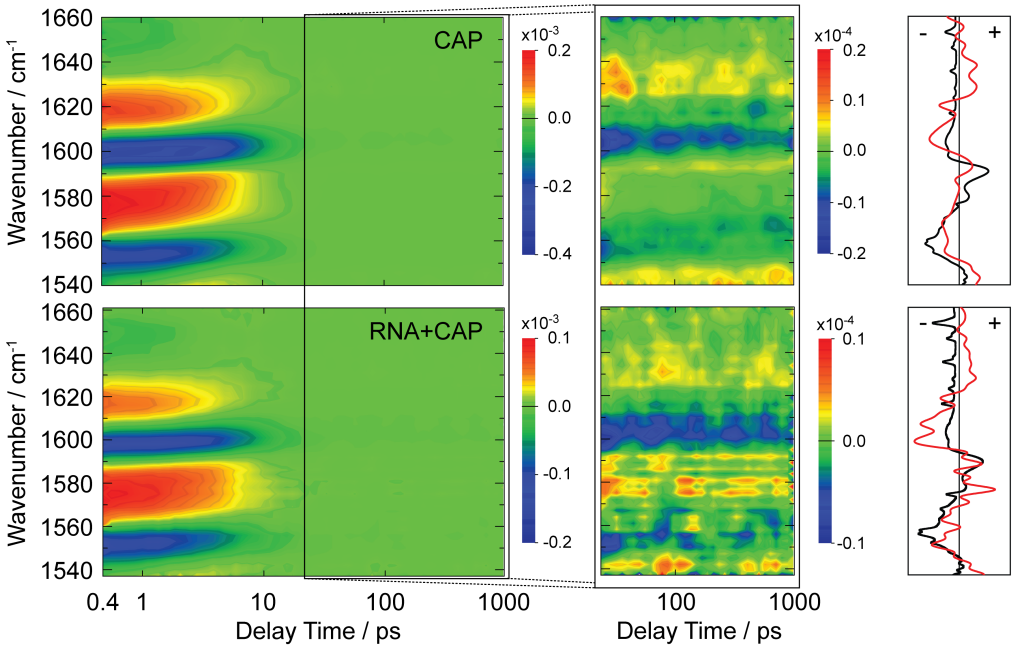

Figure 6.16: Transient IR-difference spectra of **CAP** (top) and the complex of **CAP** and the RNA aptamer 42_{trunc} (bottom) in deuterated SELEX buffer (left). Magnification of the absorbance changes of the compounds between a delay time of 20 ps to 1 ns is shown (middle). Comparison of the DAS referring to the infinite lifetime (red) and the steady-state FTIR-spectra (black) indicates a good agreement (right).

the remaining GSB bands can be observed due to the formation of the *cis*-isomer.

Comparing these data to the results from the transient absorption difference spectra of the complex of the ligand **CAP** and the RNA aptamer 42_{trunc}, no significant difference can be observed. While the IR-transients at 1552 cm^{-1} coincide completely with the transients of the free ligand **CAP**, only slight differences can be observed at 1626 cm^{-1} between a delay time of 8 and 30 ps (Fig. 6.17a). Moreover, while the spectral position of the GSB and the positive bands are very similar, there are slight differences in the PA-bands at 1640 and 1575 cm^{-1} (Fig. 6.17b). The changes due to the addition of RNA can be observed in the transients as well as in the spectral position around 1630 cm^{-1}. These small variations could indicate small conformational changes of the RNA. Consequently, a weak photo-induced conformational change within the RNA could be assumed. However, these changes are unincisive and the conformational changes of the RNA upon photo-isomerization of the ligand are not significant, which coincides with the results, that were obtained by CD-measurements.

To obtain insights into the secondary structure of the RNA aptamer 42_{trunc}, especially regarding a binding site of the ligand, in-line probing experiments[204] were performed in the research group of Prof. B. Suess, which is an often-used method to examine structural changes due to ligand binding. This technique uses the tendency of cleavage of RNA, which is highly dependent on the RNA structure. Therefore, a cleavage can indicate sequences, which are not involved in base pairs. These experiments revealed a high rigidity and stability of loop A as it was already proposed be-

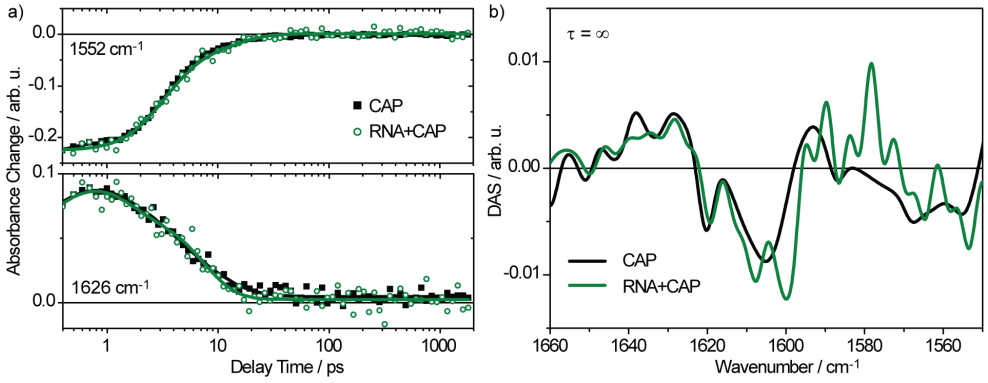

Figure 6.17: a) IR-Transients at 1552 and 1626 cm^{-1} of **CAP** (black) and the complex of **CAP** and the RNA aptamer 42_{trunc} (green) in deuterated SELEX buffer. b) Comparison of DAS, which refer to the infinite lifetime, of the two compounds.

forehand. Moreover, due to the high tendency of cleavage of the sequence $C^{25}CUAC^{29}$ in loop B, a high flexibility could be observed. While this sequence is partially induced in a double-strand, which is proposed by the initial structure of the aptamer 42_{trunc}, a high cleavage is usually observed within single-stranded parts. Consequently, a different aptamer structure is suggested, which is in agreement with these results of the in-line probing experiment (Fig. 6.18).

Furthermore, a cleavage was observed for two adenosines (A^{33} and A^{34}), which is dependent on the state of the photoswitch. While for *trans*-**CAP**, these nucleotides are quite stable, for the *cis*-isomer, they show an increased cleavage behavior. Consequently, this photo-induced changes in the flexibility can be referred to as ligand binding to the RNA, which results in ligand protected nucleotides in the aptamer. Since the only photo-induced changes, which are obtained in the in-line probing experiments, are at the binding site of the ligand, no strongly pronounced conformational transition is supposed upon ligand binding. This is in good agreement with the experiments, which were performed in this work.
Studies on the toxicity of the ligand **CAP** by GFP-induced fluorescence measurements in yeast cells showed no clear evidence for an influence of the azobenzene **CAP** on the fluorescence. Therefore, it is unclear whether the photoswitch is incorporated by the cells or if the azobenzene-derivative shows a critical toxicity.

Investigations on the photo-induced regulation behavior were performed by using the test system GFP-reporter plasmide pWHE601, which has already successfully been approved for the construction of the tetracycline-binding riboswitch.[205] Introduction of the aptamer 42_{trunc} in the 5'-end of the riboswitch sequence leads, however, to a considerable loss of GFP-expression. Consequently, no influence by the photoisomerization of the ligand can be observed. Destabilization of loop A results in an increased GFP-fluorescence, however, a reduction induced by photoswitching could neither be obtained.

Consequently, the RNA aptamer 42_{trunc}, which shows a photo-induced binding of

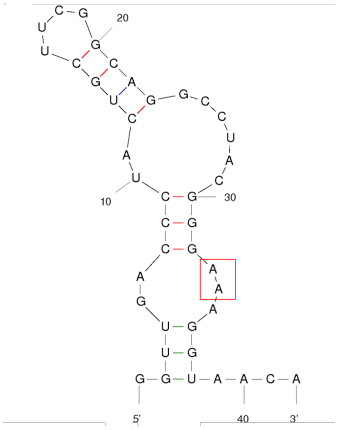

Figure 6.18: New predicted secondary structure of the RNA aptamer 42_{trunc}, which implies the assumptions on the structure, that are obtained by in-line probing experiments. A free-energy prediction was performed by mfold,[199] which results in a free minimum energy of -8.1 kcal/mol. Red rectangle indicates binding site of *trans*-**CAP**.

the ligand **CAP**, results in an insufficient photo-responsive conformational change of the aptamer structure. This leads to a tremendous reduction of the GFP-expression of the riboswitch, which shows no influence of the photo-isomerization of the ligand. Therefore, the use of this aptamer as a sensor domain of a riboswitch is unfortunately not feasible.

6.2.3 Conclusion

In this section, two photo-responsive aptamers were presented, which bind specifically only the *trans*-azobenzene-derivatives.

The first photoswitch, **AAPAB**, showed reasonable chemical properties with a water-solubility of 2 mmol/L as well as photo-chemical properties in aqueous buffered solution. Beside the high switching amplitude, the *cis*-isomer shows a reasonable stability with a half-life of about 48 minutes. Moreover, in fatigue resistance experiments no changes were detected for 25 switching cycles for this azobenzene derivative and and also a high stability against hydrolysis or degradation in aqueous solution as well as in HeLa-cell extracts was shown.

For immobilization of the photoswitchable ligand, the azobenzene structure was modified by biotinylation of the carboxy group. This biotin binds with high affinity and specificity streptavidin, which is coupled to magnetic beads. In a SELEX-process with a partially randomized DNA-pool, a RNA sequence was found, which binds only the *trans*-isomer of the ligand **AAPAB**, but not the *cis*-isomer. However, the RNA aptamer does not solely bind the target molecule, but also the streptavidin, which is significantly larger than the ligand molecule. Consequently, a photoswitchable RNA aptamer was found, which binds specifically one photo-isomer of the target and which allows a reversible binding between the RNA and the ligand. However, since streptavidin is a quite large protein, a further application of this photoswitchable RNA

aptamer as the sensor domain of a photo-responsive riboswitch is not feasible. For application without size restriction, the use of this aptamer cannot be excluded.

For the design of the second photoswitch, the broad-spectrum antibiotic chloramphenicol with a number of functional groups was used as an initial point for the structural design of an azobenzene derivative. The chloramphenicol-azobenzene **CAP** shows a good solubility in water as well as reasonable photo-physical properties. A photo-stationary state with an amount of at least 80% *cis*-isomer can be generated by illumination with light of a wavelength of 365 nm. This *cis*-**CAP** is extraordinary stable at room temperature with a lifetime of about 27 days. Moreover, a high fatigue resistance, which was measured for 25 cycles without detectable changes, as well as stability in HeLa-cell extracts for aver 24 h was observed.

For the search of an aptamer for the ligand **CAP**, a different immobilization strategy was implemented. Here, a primary amino group was substituted to a carboxy group of the azobenzene structure, which is further covalently linked to agarose beads with a 10-atom spacer linker. Using this procedure in combination with a partially structured DNA-pool, which reveals a stable hairpin structure, an RNA aptamer sequence was found, which binds specifically only the *trans*-isomer. After truncation of the RNA (42_{trunc}) without loss of binding affinity, a dissociation constant for the *trans*-isomer of 820 nM and for the original **CAP** with a carboxy group of 3.55 μM was found in ITC measurements, while no binding affinity could be observed neither for the *cis*-isomer nor for the pure chloramphenicol.

In (time-resolved) UV/vis-experiments, no influence of the RNA binding on the ground state properties of the ligand **CAP** could be observed. However, differences were detected for the energy difference between the excited states, which is slightly lower for the addition of RNA, as well as for the probability of different excited state absorptions. Moreover, a lower quantum yield for the *trans*-to-*cis*-isomerization was observed for the complex of RNA and **CAP**. As a result, the binding of the RNA slightly influences the isomerization of the azobenzene-derivative, however, neither the isomerization mechanism nor the corresponding dynamics are affected. The photo-isomerization of the ligand is completely finished within 20 ps for the bound and the free state.

In IR-difference spectra, a variety of vibrational changes were observed for the pure ligand **CAP**. To gain insights into the origin of these vibrations, theoretical calculations of the frequencies were performed. These experimental and the calculated IR-difference spectrum are in quite good agreement.

In CD- as well as in (time-resolved) IR-experiments of the complex **RNA+CAP**, only very small influences of the photoswitchable ligand on the conformation of the RNA aptamer 42_{trunc} could be observed. Due to the very stable hairpin structure, which was originally chosen to stabilize the aptamer structure, the conformation of the RNA aptamer is supposed to be too stable, that no conformational change occurs upon binding of the ligand, but only minor rearrangements.

The results of an in-line probing experiment indicate a specific binding site for

the interaction with *trans*-**CAP**. Here, a stabilization of the cleavage behavior of the nucleotides A^{33} and A^{34} upon addition of the *trans*-**CAP** was observed. Unfortunately, the implementation of the aptamer sequence in a GFP-reporter plasmide results in an almost complete loss of GFP-fluorescence, which neither shows an effect upon photo-isomerization of the ligand.

Consequently, a photoswitchable RNA aptamer 42_{trunc} was found, which binds the photoswitchable ligand **CAP** with high affinity and specificity in its *trans*-state. The photoswitch shows reasonable photo-physical properties in its free as well as in its bound state to the RNA. However, due to the not pronounced conformational change upon binding of a ligand, an application in a photo-responsive riboswitch is hardly feasible. Therefore, the secondary structure of the aptamer will be artificially destabilized slightly, e.g. by removal or changes of the hairpin structure (loop A).

Chapter 7

Photo-Responsive Materials: Photoswitchable Foldamers

Natural biopolymers impress with their extraordinary interplay between their secondary/ tertiary structure and their biological function. The understanding of these biological functions and the connection to the defined biological structures is part of a wide field in research. Moreover, in an equally interesting and great field of science, these stable and defined biological structures are used as models for the design of new materials.

Synthetic oligomers, which are constructed by small monomers, that have the ability to form highly stable secondary structures, like helices or sheets, are called *foldamers*.[206] These ordered structures are only stabilized by non-covalent interactions between the monomer units and are either used to mimic biological oligomers or adopt these properties for the non-biological foldamer, which cannot be found in nature.[207–209]

So far, a high variety of monomer units are known in literature. These ranges from monomers, that remind of biological monomers, like oligoamides, which can be constructed by one monomer unit, e.g. β-amino acids,[210,211] aromatic amino acids[212–215] or even different monomers, like alternating amino acids[216] or 2,6-diaminopyridine and 2,6-pyridinedicarbonyl units.[217] Moreover, as important as the biological monomers are the abiotic monomers, where the choice of the monomer unit is less restricted. The abiotic monomers vary from hydrazides[218] or ethynylpyridine[219] to phenylene-ethynylene.[220,221] Dependent on the monomer unit, the secondary structure is stabilized by individual or even combined[222] interactions, like hydrogen bonds, $\pi\pi$-interactions of aromatic groups[223,224] or solvophobic effects.

Applications of synthetic foldamer range from the use in fundamental research on new probes[225] or exhibition of motions on gold substrates[226] to molecular recognition[227] or encapsulation of small molecules[228–230] to macromolecular helicity memory[231,232] and even for energy storage as an alternative utilization of solar energy.[233]

A well-investigated foldamer structure is the oligo-*meta*-phenylene-ethynylene (O*m*PE),[234–236] which consists of phenyl rings, that are bridged by rigid ethynylene groups. The hydrophobic backbone in combination with polar side chains convert the oligomer in an amphiphilic foldamer, which folds in a stable helical conformation in polar solvents, like acetonitrile, in contrast to a random coil conformation in

apolar solvents, like chloroform.[237] However, the stability of the helical conformation highly depends on the number of monomer units, where more than eight monomers are required for the formation of a helix.[234,238] The formation of the helical structure was studied by different optical methods,[239] like UV/vis-absorption, fluorescence, or CD-spectroscopy,[240,241] which is facilitated by the amplification of the CD-signals by chiral side chains, and even by double-spin EPR[242,243] or atomic force microscopy (AFM).[244]

In this chapter, the further development of this amphiphilic O*m*PE-foldamer into a photoswitchable alternative is discussed, which enables a spatio-temporal control over the conformational change. A spectroscopic characterization of the photoswitchable foldamer $\mathbf{10_5}$ was performed as well as investigations on the photo-induced unfolding of the helical conformation (see section 7.1.1).

7.1 Photo-Induced Conformational Changes of Oligo-*meta*-Phenylene-Ethynylene-Foldamers

Amphiphilic Oligo-*meta*-phenylene-ethynylene (O*m*PE) foldamers can be present in two different secondary conformations – a helical and a random coil conformation –, which is dependent on the polarity of the solvent. Consequently, a change of the solvent induces a conformational change of the foldamer.

The use of light as an external stimulus is an excellent tool, which is precise and non-invasive. Consequently, to achieve a spatial and temporal control over the change in secondary structure of the foldamer, photoswitches, here azobenzenes, are introduced in the backbone structure.[245] The attachment of the *trans*-azobenzene to the ethynylene bridge in the *meta*-position with respect to the azo-group reveals a comparable stable helical conformation as the parent foldamer.[246,247]

Relying on the foldamer structures by Moore,[234] which show an excellent transition from a helical conformation in acetonitrile to a random coil conformation in chloroform, every second ethynylene group is exchanged into an azo-group, which was performed by Dr. Zhilin Yu of the research group of Prof. Stefan Hecht by a Sonogashira-Hagihara coupling.[248] Consequently, the backbone structure is built by azobenzenes, which are bridged by ethynylene groups in *meta*-position with respect to the azo-group. Due to the polar side chains of the azobenzenes and the highly hydrophobic character of the backbone of the oligomer, an amphiphilic photoswitchable O*m*PE-foldamer is obtained. In polar solvents, e.g. acetonitrile, a helical conformation is obtained for *trans*-azobenzene, in which the backbone structure is present in a *cisoidal*-conformation.[235] This helix is stabilized by the $\pi\pi$-interactions of the planar *trans*-azobenzenes within the backbone as well as by the hydrophobic effect and consequently, the polar interactions between the side chains and the solvent. One turn of the helical conformation is composed of three azobenzenes. The smallest unit, which forms a stable helical conformation, is a pentameric azobenzene-oligomer ($\mathbf{10_5}$),

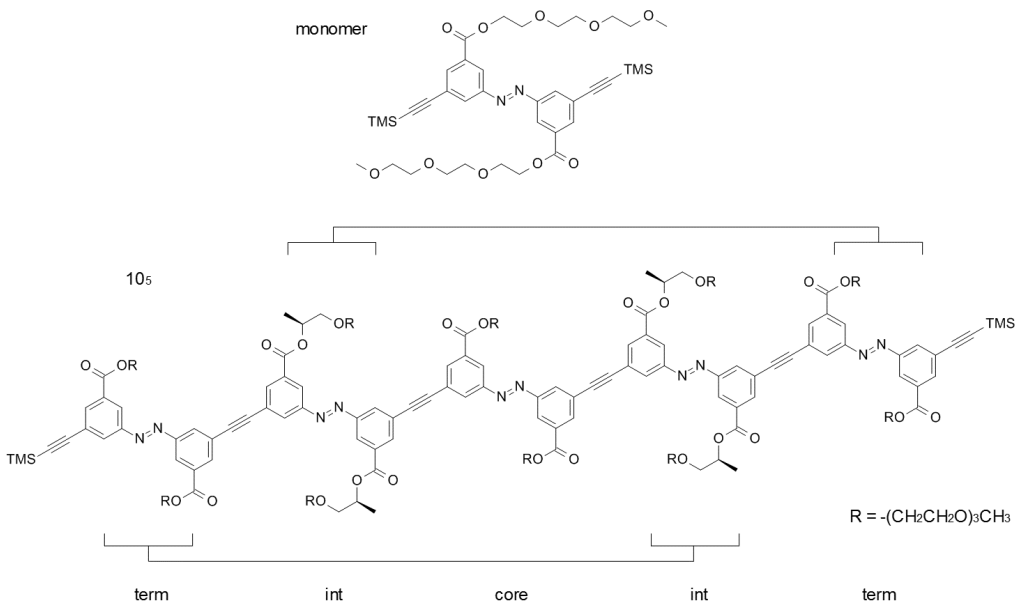

Figure 7.1: Chemical structures of the photoswitchable foldamer $\mathbf{10_5}$ and the corresponding achiral azobenzene monomer unit.

which consists of five azobenzenes and consequently ten phenyl rings (Fig. 7.1). With increasing unit length, the stability of the helical conformation is enlarged.[249]

Only one isomerization process of one azobenzene within the backbone of the smallest photoswitchable foldamer $\mathbf{10_5}$ suffices to unfold the secondary structure into a random coil conformation, while for longer oligomers, e.g. $12_6/14_7/\ldots$, two/three/... isomerization processes are necessary.[249] Due to the non-planarity of the *cis*-isomer of the azobenzene, the $\pi\pi$-interactions, which stabilize the secondary structure, are disrupted that further leads to an unfolding.

In earlier studies, it could be shown, that isomerization of the implemented azobenzenes can be induced by illumination with light of a defined wavelength. By means of ^{1}H-NMR, position-dependent isomerization ratios were obtained for foldamers with $n \geq 6$.[249] It could be shown, that the azobenzenes at the terminal positions within the backbone structure show a more pronounced tendency towards photo-isomerization than azobenzenes at the central position (*core*).

The photo-induced conformational change upon photo-isomerization was detected in earlier studies by means of CD-spectroscopy experiments.[249] Relying on the "sergeants and soldiers"-principle,[250] chiral amplification was achieved by insertion of chiral side chains to the foldamer structure in a non-linear connection between the number of chiral groups and the optical rotation (Fig. 7.1).[251] While for the (all-)*trans*-configuration of the foldamer, a Cotton effect[252] can be observed, which indicates structured conformation, upon photo-isomerization to the *cis*-conformation, this signal decreases and vanishes almost completely for the small foldamers $\mathbf{10_5}$ and 12_6.

7.1.1 Photo-Induced Unfolding of O*m*PE-Foldamers

In this work, the smallest photoswitchable amphiphilic O*m*PE-foldamers $\mathbf{10_5}$, which forms a stable helical structure, as well as the corresponding monomer unit were studied. By means of time-resolved spectroscopy methods, the isomerization behavior of the photoswitch azobenzene was investigated in the free monomeric state and in the structurally restricted foldamer backbone. Moreover, the photo-induced unfolding of the helical conformation of the foldamer $\mathbf{10_5}$ was studied by time-resolved investigation of the vibrational structure.[253] These results were supported by (TD)DFT-calculations on the frequencies of different conformations of the foldamer $\mathbf{10_5}$.

The UV/vis-spectrum of the achiral monomer unit shows typical azobenzene-like absorbance bands for the *trans*-isomer (Fig. 7.2). An intense $\pi\pi^*$-band can be seen at 320 nm, while nearly no contribution of the formally forbidden $S_0 \rightarrow S_1$-transition ($n\pi^*$) is observable above 400 nm. The intense absorbance bands at 250 and 260 nm are $\pi\pi^*$-bands of the phenylene-ethynylene groups. Upon excitation with light of a wavelength of 365 nm, the $\pi\pi^*$-band of the *trans*-isomer decreases at 320 nm, while the $n\pi^*$-band of the *cis*-isomer increases at about 420 nm. Two clear isosbestic points are located at 255 and 380 nm. By extrapolation of a pure *cis*-spectrum, a *cis*-isomer amount of about 67% is obtained for the photo-stationary state.

Due to the spectral overlap with the intense absorbance bands of the phenylene-ethynylene group, the $\pi\pi^*$-band of the *cis*-isomer cannot be seen in the UV/vis-spectrum. In the difference spectrum (PSS-*trans*), however, a contribution of this band is observable at about 280 nm, which leads to a less pronounced negative signal. Compared to the UV/vis-spectrum of the monomer unit, significant differences can be observed for the UV/vis-spectrum of the foldamer $\mathbf{10_5}$. An intense broad absorbance band between 250 and about 350 nm is obtained for the foldamer, which corresponds

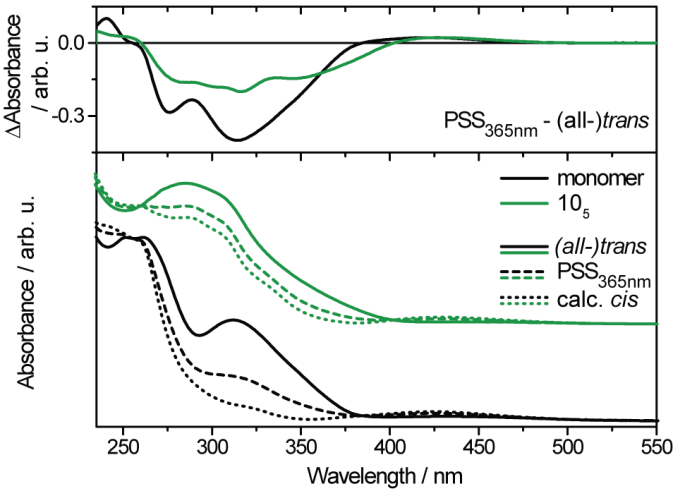

Figure 7.2: UV/vis-absorbance spectra of the *trans*-isomer and the photo-stationary state of the foldamer $\mathbf{10_5}$ and the azobenzene monomer in acetonitrile. The spectra of the *cis*-isomers were calculated from the absorbance differences, represented by the upper panel (PSS-*trans*).

to the absorbance bands of the backbone, more precisely, the phenylene-ethynylene-groups. This broad band overlaps spectrally with the $\pi\pi^*$-band of the (all-)*trans*-configuration of the foldamer. Contributions can be seen between about 350 and 400 nm. Upon excitation at 365 nm, the absorbance decreases between 260 and 400 nm and increases between 400 and 500 nm. While the increase at 430 nm corresponds to the $n\pi^*$-band of the *cis*-isomer, the decrease is ascribed to the less amount of the *trans*-isomer. Two clear isosbestic point are located at about 260 and 400 nm, while the latter is significantly shifted to longer wavelengths with a value of 20 nm with respect to the monomer unit. The amount of the *cis*-isomer is extrapolated to a similar value as for the monomer unit of about 67%. The difference spectrum is highly structured for the foldamer in a spectral range between 270 and 350 nm. This can be explained by the divergence of the amount and especially the position of the *cis*-isomers within the backbone structure. Consequently, the absorbance bands corresponding to the foldamer structure with a *cis*-isomer at the terminal, the internal or the *core* position within the backbone are slightly shifted to each other. Moreover, dependent on the position of the *cis*-isomer as well as the isomerization ratio, different secondary structure are expected, which leads to a difference in the absorbance bands of the *cisoidal* and *transoidal* structures, which can also be found around 300 nm.

In the UV/vis-spectrum of the (all-)*trans*-foldamer $\mathbf{10_5}$, an oscillatory structure can be seen in the intense absorbance band between 250 and 275 nm (Fig. 7.3). Analysis of this oscillation reveals a frequency of 900 cm^{-1}.

For the optimization of the ground state geometry of the helical conformation of the (all-)*trans*-$\mathbf{10_5}$ foldamer and a subsequent frequency analysis, (TD)DFT-calculations were performed using the B3LYP-functional, the Dunning basis-set cc-PVDZ and a implicit solvent model for acetonitrile (PCM). For computational reasons, the side chains of the foldamer were neglected.

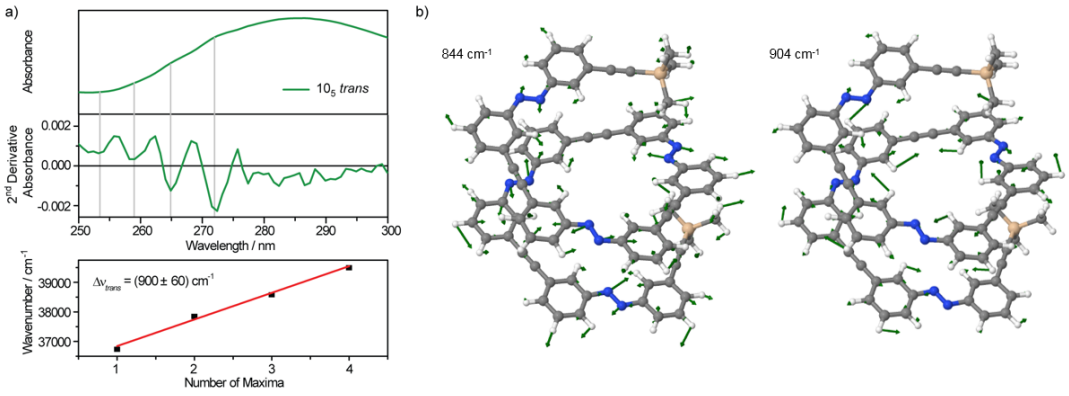

Figure 7.3: a) Magnification of the oscillatory structure on the absorbance spectrum of the *trans*-isomer and the photo-stationary state of the foldamer $\mathbf{10_5}$ and its second derivative (top). The oscillations between 250 and 280 nm correspond to a frequency of $\nu = (900 \pm 60)\ cm^{-1}$ (bottom). b) Frequency analysis revealed two frequencies at $\nu = 844\ cm^{-1}$ and $\nu = 904\ cm^{-1}$ (DFT/B3LYP/cc-PVDZ, PCM=acetonitrile, scaling factor of 0.97[54]). In-plane aromatic vibrations of the general backbone structure are involved for both frequencies.

Table 7.1: Lifetimes of time-resolved UV-pump/ UV/vis-probe experiments on the monomer unit and the foldamer $\mathbf{10_5}$ after excitation at 320 nm.

	τ_1 [ps]	τ_2 [ps]	τ_3 [ps]	τ_4 [ps]	τ_5 [ps]
monomer	<0.20	0.73	2.87	9.09	∞
$\mathbf{10_5}$	<0.20	1.69	5.56	20.5	∞

The optimized structure of the foldamer $\mathbf{10_5}$ can be seen in Fig. 7.3. In the corresponding frequency analysis, a variety of frequencies are located around 900 cm^{-1}, which correspond to the in-plane motions of the backbone structure. In Fig. 7.3, in-plane vibrations of the phenyl rings as well as of the nitrogens of the azo-group are indicated by the displacement vectors, exemplary shown for the frequencies 844 and 900 cm^{-1}, which show contributions in the whole helical structure. Consequently, the vibrations of the *cisoidal* -backbone structure show a contribution on the UV/vis-spectrum of the (all-)*trans*-foldamer.

In time-resolved UV/vis-pump UV/vis-probe experiments, the dynamics of the isomerization of the azobenzene monomer as well as of the azobenzenes within the backbone structure of the foldamer were studied to gain insights in their isomerization mechanism.

Excitation at a wavelength of 320 nm leads to a $S_0 \rightarrow S_2$-transition of the monomer unit. Here, instantaneously arising excited state absorption bands are detected at about 380 nm as well as at about 510 nm, which increase slightly further with a lifetime of less than 0.2 ps with a decrease at about 400 nm at the same time (Fig. 7.4 and Tab. 7.1). This lifetime corresponds to the fast $S_2 \rightarrow S_1$-transition. Below 380 nm, the ground state bleach of the *trans*-isomer can be observed. The relaxation of the S_1-state can be described by three exponential functions, while the lifetime $\tau_4 = 9\ ps$ also describes the vibrational cooling. After a delay time of about 20 ps, the ground states of the *trans*- as well as of the *cis*-azobenzene photo-product are (re-)populated. Here, a product absorption band is observable at 420 nm, which coincides very well with the steady-state absorbance difference spectrum.

A similar behavior can be obtained for a S_2-excitation of one azobenzene within the backbone of the foldamer. However, the spectral behavior is significantly broadened and more structured for the foldamer, which results from the excitation of the three slightly different azobenzenes within the foldamer, one at a time. Consequently, the conformational variety with the isomerization of the different azobenzenes leads to a complex potential energy surface. Moreover, the lifetimes, which describe the relaxation process of the photoswitch as well as the vibrational cooling of the system are significantly longer for the foldamer with a value nearly twice as large as the lifetimes of the monomer. Thus, the ground states of the *trans*- and the *cis*-isomer are completely (re-)populated after a delay time of about 70 ps.

Investigations on the vibrational structure of the monomer unit as well as on the foldamer $\mathbf{10_5}$ were performed in the IR-region. Due to the interest on the photo-induced conformational changes, the vibrational changes upon photo-isomerization

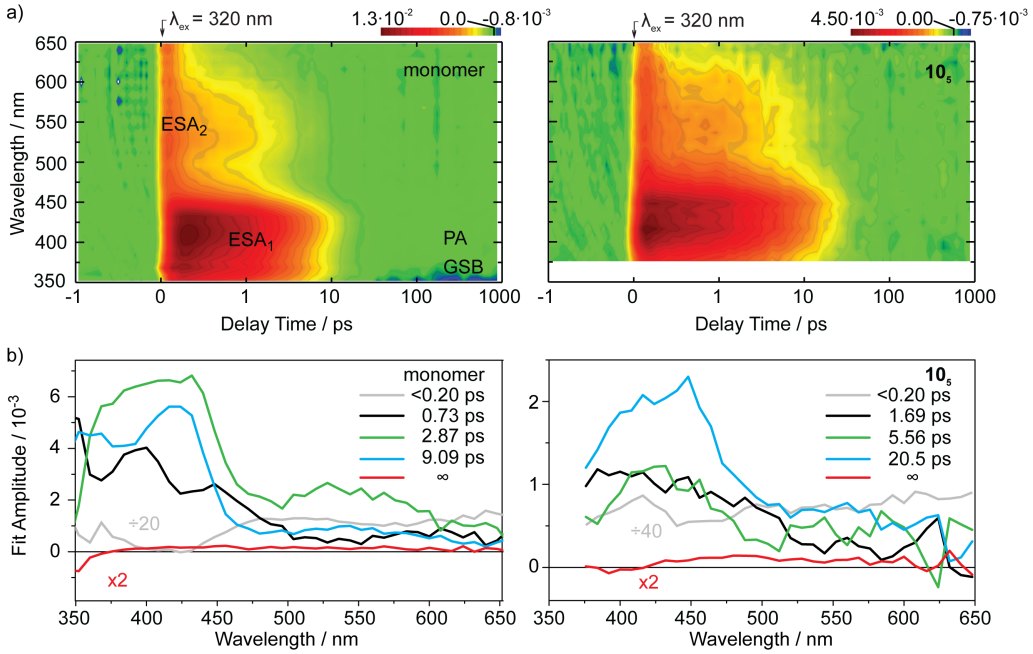

Figure 7.4: a) Transient UV/vis-absorption difference spectra of the foldamer $\mathbf{10_5}$ and the monomer unit after excitation at 320 nm. b) Decay-associated spectra of the monomer unit and the foldamer $\mathbf{10_5}$.

of the azobenzene(s) were studied (Fig. 7.5a). For further analysis of the vibrations, (TD)DFT-calculations were performed for the monomer unit and compared to the experimental spectra (Fig. 7.5b). For distinct vibrations, the corresponding displacement vectors are shown (Fig. 7.5c).

In general, changes in the vibrational structure can be observed in four spectral regions. At about 2150 cm^{-1}, the C≡C-vibration of the alkyne can be seen, which bridges the (terminal) azobenzene with the trimethylsilane (TMS)-group. Upon *trans*-to-*cis*-isomerization (PSS-*trans*), a slight shift can be observed from 2162 to 2150 cm^{-1} for the monomer unit, while for the foldamer, only a slight decrease in intensity is detected. While the calculated frequencies are slightly shifted to higher wavenumbers, the spectral shape is comparable to the FTIR-spectrum. The overall intensities, however, differ significantly over the whole spectral range, which is attributed to the explicit interactions with the solvent molecules, which are not considered in the theoretical calculations.

An interesting photo-induced vibrational change can be observed in the carbonyl vibrations of the side chains at about 1720 cm^{-1}. Here, a negative change is detected for the monomer unit, which refers to a more pronounced vibration in the *trans*-state. This vibrational change is in good agreement to the theoretical calculations. For the foldamer, however, this vibrations intensifies upon *trans*-to-*cis*-isomerization, leading to an intense positive vibrational change at 1725 cm^{-1}. Since the *cis*-isomer leads to an unfolding of the helical conformation and a higher degree of freedom is expected in the random coil structure, this increase of intensity could indicate the unfolding process.

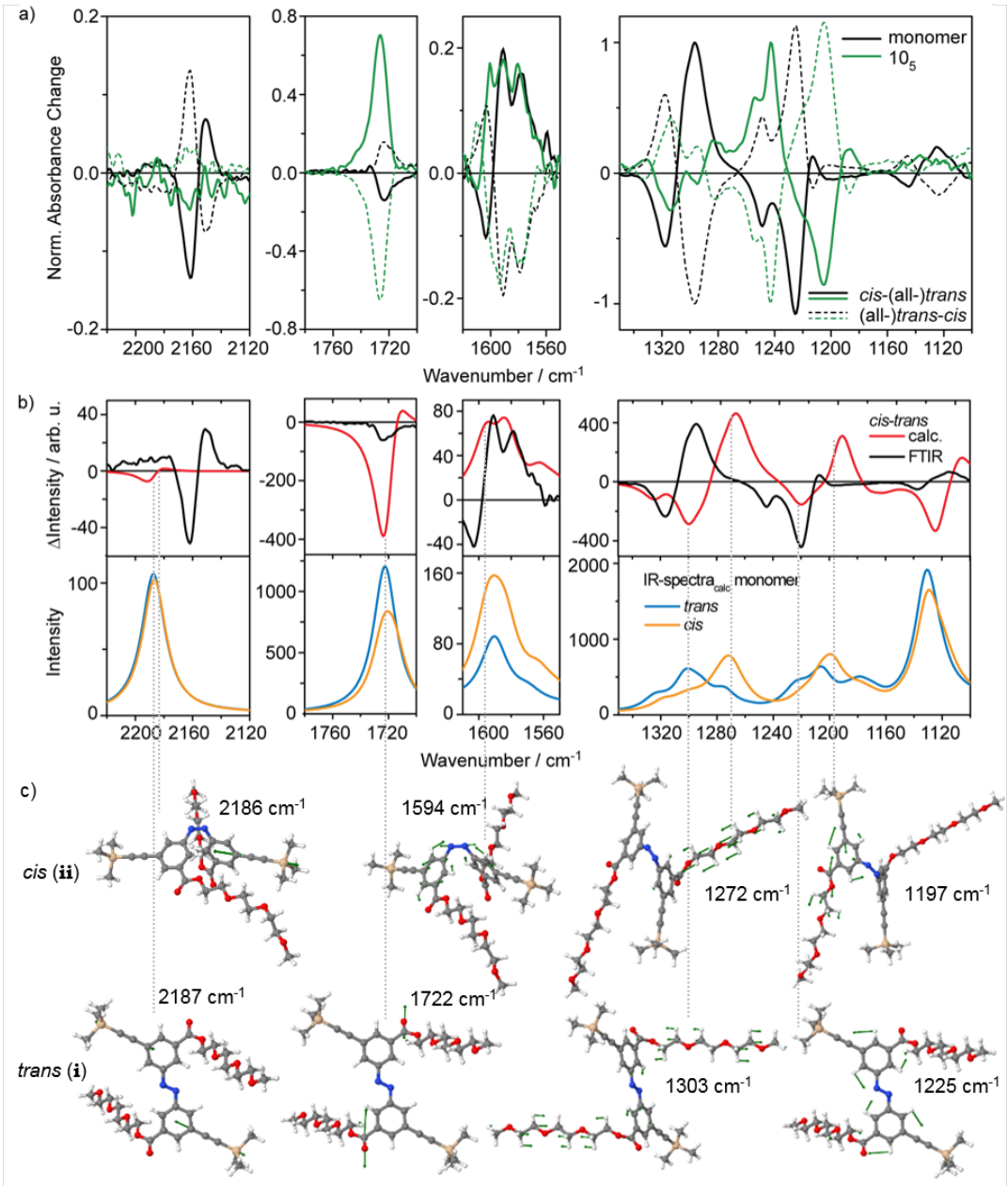

Figure 7.5: a) FTIR-difference spectra of the azobenzene monomer and the foldamer $\mathbf{10_5}$ in acetonitrile after excitation at 320 nm (*cis*-(all-)*trans*) and 420 nm ((all-)*trans-cis*); data are normalized on the maximal absorbance change between 1320 and 1240 cm^{-1}. b) Calculated frequencies of the *trans*- and *cis*-azobenzene monomer (DFT/B3LYP/cc-PVDZ, PCM(acetonitrile); frequencies were broadened with a Lorentz-function with a half-width of 10 cm^{-1}; a scaling factor of 0.97 was used.) (top). Comparison of the calculated difference spectrum with the experimental FTIR-difference spectrum of the monomer (*cis-trans*); spectra are scaled on the aromatic vibrations of the *cis*-isomer at 1594 cm^{-1} (bottom). c) Selected vibrations of the *trans*- and the *cis*-isomer between 2220 and 1110 cm^{-1}, which are indicated by the displacement vectors.

Vibrational changes in the aromatic rings of the azobenzene and therefore also in the backbone of the foldamer can be regarded in the spectral range between 1610 and 1550 cm^{-1}. Here, a small shift can be seen for the monomer unit from 1600 to 1590 cm^{-1} as well as a new vibrational band at about 1580 cm^{-1} for the isomerization to the *cis*-isomer. Beside the small negative contribution of the *trans*-isomer, the vibrational character can also be seen in the calculated frequencies. In case of the foldamer, this spectral shift is less pronounced, but new intense vibrations appear between 1605 and 1560 cm^{-1}. These more structured vibrations for the *cis*-state with respect to the monomer unit refer to the different *cis*-isomers in the photo-stationary state of the foldamer.

Between 1330 and 1120 cm^{-1}, bending vibrations of the aliphatic groups of the side chains as well as of the aromatic rings can be seen, which show a general shift to lower wavenumbers for the monomer unit. Although, a general shift to higher frequencies was observed for the experimental data within this region, this is in quite good agreement with the theoretical calculations. Only minor changes are obtained around 1230 cm^{-1}. For the foldamer, an intense shift of 40 cm^{-1} can be observed from 1242 to 1202 cm^{-1}, which however, can also refer to two different vibrations.

Consequently, the photo-isomerization process is observable in the vibrational spectra for different vibrations for the monomer as well as for the foldamer $\mathbf{10_5}$.

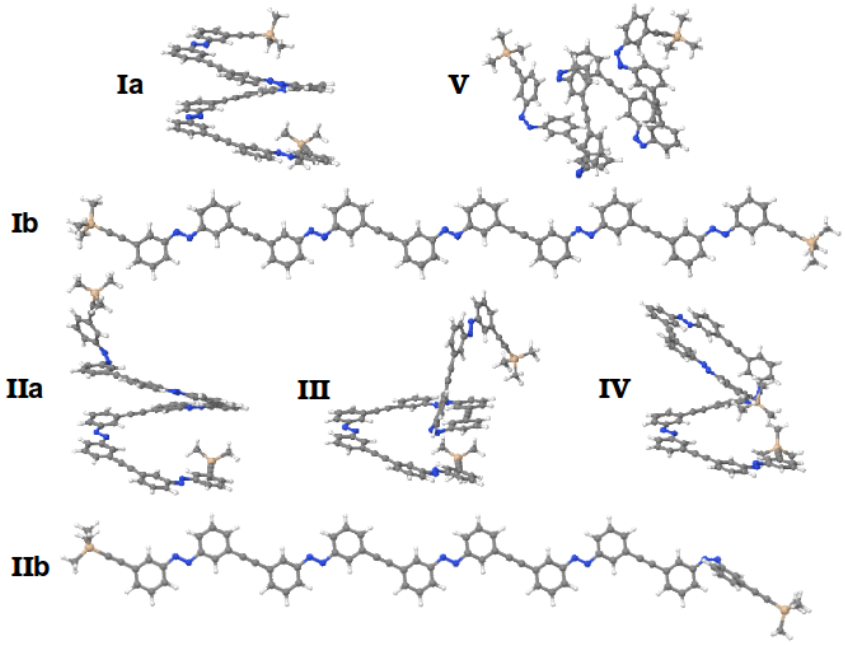

Figure 7.6: Ground-state optimized structures of the foldamer $\mathbf{10_5}$ in all-*trans* in a helical conformation (**Ia**), with one *cis*-isomer in the terminal (**IIa**), the internal (**III**) and the central (**IV**) azobenzene position (DFT/B3LYP/cc-PVDZ, PCM(acetonitrile)). Random-coil structures were calculated for the all-*trans*-conformation (**Ib**) and with one *cis*-isomer in the terminal azobenzene position (**IIb**). Moreover, a structure, containing five *cis*-isomers, in the backbone, was studied (**V**).

Since the vibrational changes in the foldamer upon photo-isomerization could also refer to the photo-induced unfolding of the helical conformation, the vibrational changes of the foldamer can hardly be attributed to only one of the two processes. Due to the high impact of the $\pi\pi$-interactions of the phenyl groups on the stability of the helical conformation, a vibrational change is expected for the aromatic vibrations also during the unfolding process. Therefore, (TD)DFT-calculations were performed on different conformations of the foldamer $\mathbf{10_5}$ with respect to the isomerization ((all-)*trans* vs. *cis*) and/or the secondary structure (helical vs. random coil conformation) (Fig. 7.6). Due to computational reasons, the side chains of the foldamer were neglected, which is feasible, since there is no contribution of the vibration of the side chains in this spectral region.

The helical conformation of the (all-)*trans*-$\mathbf{10_5}$ is nearly isoenergetic to the unfolded (all-)*trans*-$\mathbf{10_5}$, which is due to the missing side chains and the not described stabilizing interactions with the only implicitly described solvent. Isomerization of one azobenzene in the backbone structure, almost independent of the position – terminal (**IIa**), internal (**III**) or core (**IV**) –, leads to an increase of the vibrational bands between 1620 and 1540 cm^{-1}. Consequently, upon photo-isomerization from (all-)*trans* to one *cis*-isomer, a positive vibrational change is observed over the whole spectral range (Fig. 7.7; **IIa-Ia**, **III-Ia** and **IV-Ia**). The three different *cis*-isomers of the foldamer $\mathbf{10_5}$ (**IIa**, **III** and **IV**) are almost isoenergetic and with an energy difference to the (all-)*trans*-isomer of about 0.6 eV comparable to the unsubstituted azobenzene. Moreover, they still show a partially intact helical structure (Fig. 7.6). Photo-isomerization of all five azobenzenes within the backbone structure leads to a random coil structure (**V**).

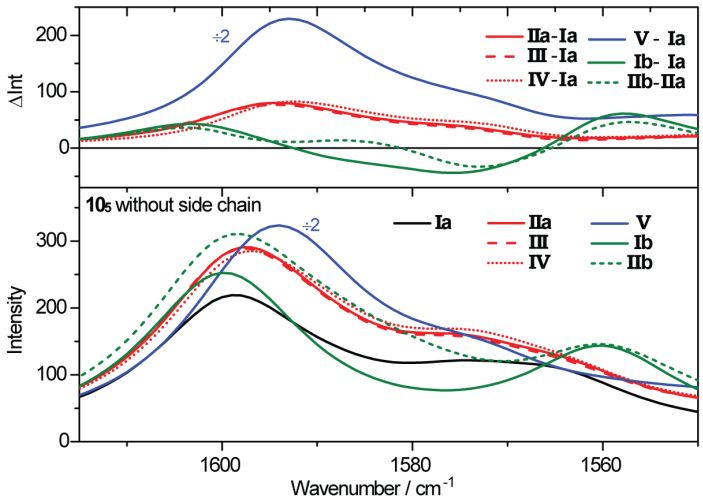

Figure 7.7: Calculated IR-spectra (bottom) for the ground-state optimized structures (Fig. 7.6) and calculated IR-difference spectra (top) for the photo-isomerization (**IIa-Ia**, **III-Ia**, **IV-Ia**, **V-Ia**) and the unfolding (**Ib-Ia**, **IIb-IIa**). The calculated frequencies were broadened with a Lorentz-function with a half-width of 10 cm^{-1}.

The vibrational band of the structure **V** is significantly increased not only with respect to the (all-)*trans*-conformation **Ia**, but also to the structures, which contain already one *cis*-azobenzene. Consequently, also the difference spectrum (**V-Ia**) shows a strong positive signal. Thus, it can be seen, that with increasing number of isomerized azobenzenes the positive signal in the difference spectrum is more pronounced.

Moreover, the difference spectrum of the helical (**Ia**) and the unfolded (**Ib**) conformation, which contain only *trans*-azobenzenes, was calculated and consequently displays the unfolding without influence of photo-isomerization (**Ib-Ia**). This difference spectrum shows a sinusoidal shape and can clearly be distinguished from the spectra after photo-isomerization. More interesting, however, is the spectrum of the photo-induced unfolding, which can be seen in the difference spectrum (**IIb-IIa**) of the partially helical structure and the unfolded conformation, which contain both one *cis*-azobenzene at the terminal position of the backbone. Here, also a sinusoidal shape can be observed with a slightly more positive signal between 1595 and 1573 cm^{-1}.

Consequently, for the photo-induced unfolding of the foldamer $\mathbf{10_5}$, a sequence of the pure photo-isomerization and the subsequent unfolding should be detected in the vibrational bands of the aromatic rings.

For investigations on the dynamics of the photo-induced conformational changes, e.g. the unfolding process of the foldamer, ps-time-resolved UV-pump IR-probe experiments were performed for the monomer as well as for the foldamer $\mathbf{10_5}$ for the *trans*-to-*cis*-isomerization.

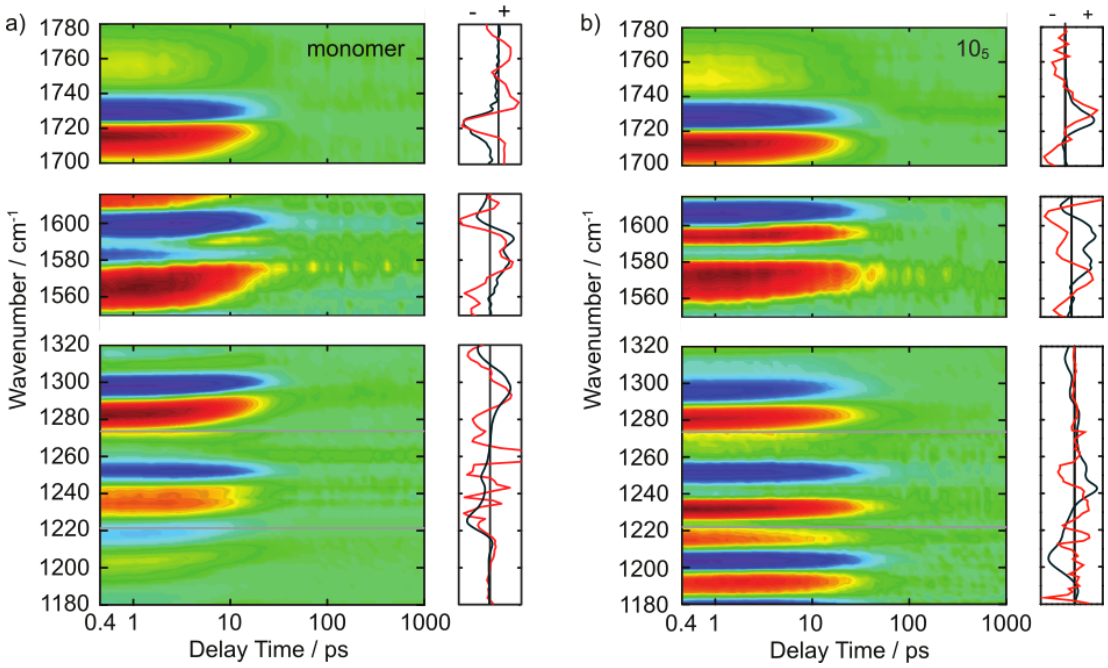

Figure 7.8: Transient absorption difference spectra of the azobenzene monomer (a) and the foldamer $\mathbf{10_5}$ (b) in acetonitrile resulting from time-resolved UV-pump IR-probe experiments after excitation at 320 nm ((all-)*trans* → *cis*); data were offset-corrected. Additionally, a comparison of the time slice after 1 ns (red) and the FTIR-difference spectra (black) is given for both components.

Table 7.2: Lifetimes of time-resolved UV-pump/ IR-probe experiments on the monomer unit and the foldamer $\mathbf{10_5}$ after excitation at 320 nm.

	τ_1 [ps]	τ_2 [ps]	τ_3 [ps]	τ_4 [ps]	τ_5 [ps]	τ_6 [ps]
monomer	1.06	2.80	4.98	11.5	—	∞
$\mathbf{10_5}$	1.61	2.17	8.96	20.6	150	∞

For the monomer, a number of GSB signals can be seen in the different spectral ranges, which coincide quite well with the spectral position of the vibrations of the *trans*-isomer in the steady-state spectrum. Moreover, positive signals can be seen at smaller wavenumbers with respect to the GSB. These signals could be attributed to the transitions between vibrational states of the electronically excited state, which would indicate a higher anharmonicity for the excited state than for the ground state. Moreover, these positive signals can be referred to the photo-product, the *cis*-isomer, which is formed within a few picosecond.

After about 1 ps, a slight shift of the positive signals to higher wavenumbers can be observed, which intensifies significantly after about 8 ps. This indicates the transition from the excited into the ground state. The ground state of the *trans*- as well as of the *cis*-isomer are completely (re-)populated after about 20 ps. The relaxation of the signals of the monomer can be described by five exponential functions (Tab. 7.2). While lifetime τ_1 describes the slight increase of the positive signals, the lifetimes τ_2, τ_3 and τ_4 describe the decay as well as the shift of the signals sufficiently. The lifetime τ_4 contributes to the vibrational cooling.

After 20 ps, absorbance changes can be detected for the monomer, which coincide quite well with the steady-state FTIR-difference spectrum in the spectral region of the carbonylic (1700–1780 cm^{-1}) and the aromatic (1550–1610 cm^{-1}) region (Fig. 7.8).

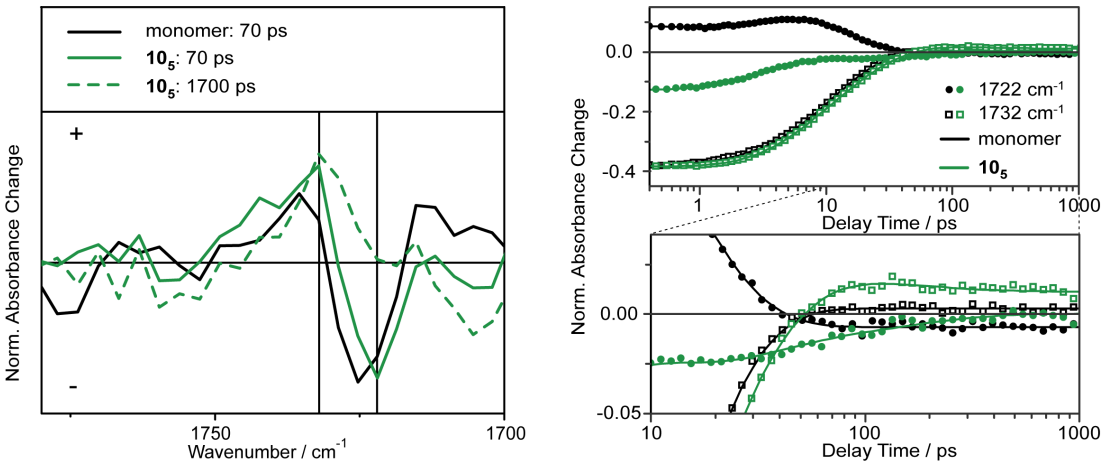

Figure 7.9: a) Comparison of time slices between 1780 and 1700 cm^{-1} of the azobenzene monomer at a delay time of 70 ps and of the foldamer at 70 and 1700 ps.
b) Comparison of IR-transients of the azobenzene monomer and the foldamer at 1722 and 1732 cm^{-1} after excitation at 320 nm. A magnification shows the absorbance changes between a delay time of 10 and 1000 ps. The transients are normalized to the GSB at 400 fs at 1732 cm^1.

However, the time slices after 1 ns of the monomer in the spectral region between 1180 and 1320 cm^{-1} agrees only roughly with the steady-state spectrum. This can be caused by experimental reasons, more precisely an increased signal-to-noise ratio, and moreover, due to spectral overlap of a high variety of different vibrations.

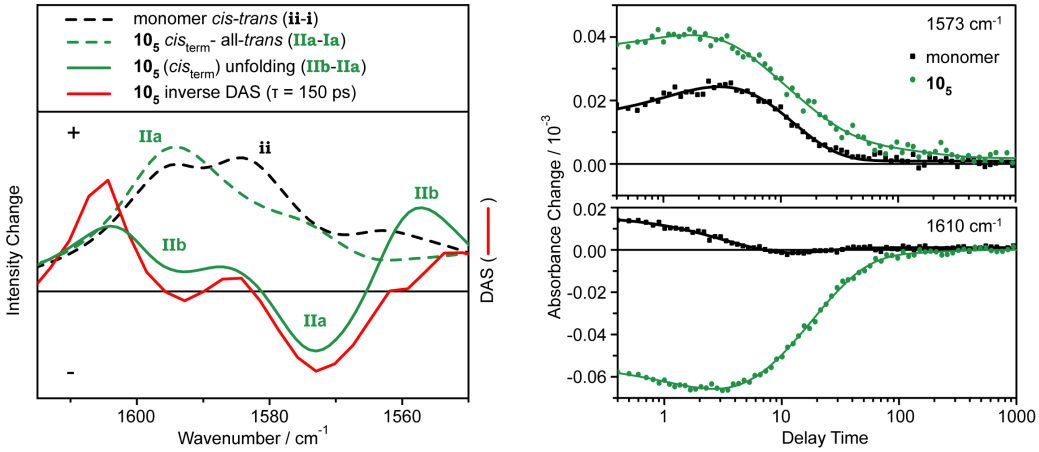

Figure 7.10: Left: Calculated IR-spectra (DFT/B3LYP/cc-PVDZ, PCM(acetonitrile), scaling factor of 0.97, Lorentz-function with a half-width of 10 cm^{-1}) of the *trans*- (**i**) and the *cis*-azobenzene monomer (**ii**), the helical conformation (**Ia**) of the all-*trans*-foldamer and the partially helical conformation of the foldamer containing one *cis*-isomer at the terminal (**IIa**) azobenzene position. Moreover, an IR-spectrum of the unfolded conformation of the foldamer with one *cis*-isomer at the terminal azobenzene position (**IIb**) was calculated. The photo-isomerization is visualized for the azobenzene monomer (**ii-i**) and the azobenzene at the terminal position of the foldamer (**IIa-Ia**). The unfolding of the helical conformation after photo-excitation is indicated by the calculated IR-difference spectrum of the foldamer with one *cis*-isomer at the terminal azobenzene position, exemplarily, in a helical and a random coil conformation (**IIb-IIa**). The similarity of the inverse DAS of the lifetime $\tau = 150$ ps (red) and the calculated difference spectrum of the unfolding demonstrates that this lifetime describes the structural rearrangement of the helical conformation after photo-isomerization. Major contributions in the respective difference spectra are indicated by labels. Right: IR-transients of the azobenzene monomer and the foldamer at two selected wavenumbers after excitation at 320 nm. At longer delay times, the influence of the lifetime $\tau = 150$ ps can be seen for the transients of the foldamer.

Comparing these results of the monomer with the IR transient absorbance spectra of the foldamer, slight spectral shifts can be observed from the GSB as well as from the positive bands, which could already be seen in the steady-state spectra. The relaxation time of the foldamer is prolonged with respect to the monomer. A lifetime of 20 ps is obtained for the cooling process, which coincides with the lifetime of the UV/vis-pump UV/vis-probe experiments. Comparing the time slices of the monomer and the foldamer at a delay time of 70 ps, the spectral behavior is very similar (Fig. 7.9). Consequently, the isomerization process is finished for the monomer as well as for the foldamer at that delay time. However, after this delay time of 70 ps, absorbance changes can still be observed only for the foldamer, which is described by an additional lifetime of 150 ps. This lifetime corresponds to vibrational changes in

the carboxyl group (Fig. 7.9) as well as in the aromatic vibrations of the backbone.

Consequently, a conformational change of the foldamer structure is supposed, which reacts on the photo-isomerization of the azobenzenes.

(TD)DFT-calculations, which were performed to clarify the vibrational behavior of different conformations of the foldamer structure (Fig. 7.7), were compared to the experimental data of the time-resolved IR-experiments to support this assumption (Fig. 7.10).

Regarding the inverse DAS of the lifetime of 150 ps of the foldamer, a sinusoidal shape can be observed, which results in an increase at 1610 cm^{-1} and a decrease in the vibrational band around 1573 cm^{-1}. These absorbance changes can also be seen in the corresponding transients. A comparison of this inverse DAS with the calculated IR-difference spectrum of the unfolding of a helical conformation of the foldamer structure, which contains one *cis*-isomer at the terminal position within the backbone leads to an extraordinary agreement.

Consequently, an early conformational change can be observed with a lifetime of 150 ps, which follows the photo-isomerization of one azobenzene from *trans* to *cis* within the backbone structure. The foldamer structures with one *cis*-azobenzene within the backbone structure at the terminal, internal or at the central (*core*) position do not differ significantly in energy. Therefore, all three structures will lead to a photo-induced unfolding of the helical conformation in the same way.

7.1.2 *Cis*-to-*Trans*-Isomerization of O*m*PE-Foldamers

While the reversible conformational changes of the photoswitchable foldamer $\mathbf{10_5}$ are reported already in literature,[249] the reversibility of the switching event has already been discussed in the section 7.1.1. In this section, however, the isomerization mechanism as well as its dynamics are investigated for the monomer unit as well as for the foldamer after excitation of the *cis*-isomer at 435 nm. It should be noted, that the resulting transient UV/vis-absorbance difference spectra are not corrected by a difference spectrum of a possibly excited *trans*-isomer at 435 nm.

Excitation of the monomer leads to two instantaneously arising ESA-bands at a wavelength of 380 and 550 nm (Fig. 7.11). With a lifetime of 0.4 ps, the decay of these two ESA-bands is described, which relies to the direct transition from the S_1-state into the ground state of the *cis*- as well as of the *trans*-isomer (Tab. 7.3). The product absorption (PA) band of the *trans*-isomer can clearly be seen below 380 nm after a delay time of about 2 ps. The lifetime of 4.47 ps describes a further decay of the positive bands between 350 and 600 nm. The corresponding DAS-spectrum is very broad and flat with an increasing trend to lower wavelengths. While this lifetime is also ascribed to the transition from the first excited into the ground state, this exceeds after a diffusive movement on the potential energy surface of the first excited state, which prolongs this decay time. These lifetimes are very comparable to earlier studies[93,111,254] on the *cis*-to-*trans*-isomerization, however, slightly enlarged. After a delay time of about 20 ps, the ground states of the *cis*- and the *trans*-isomer are completely (re-)populated, which

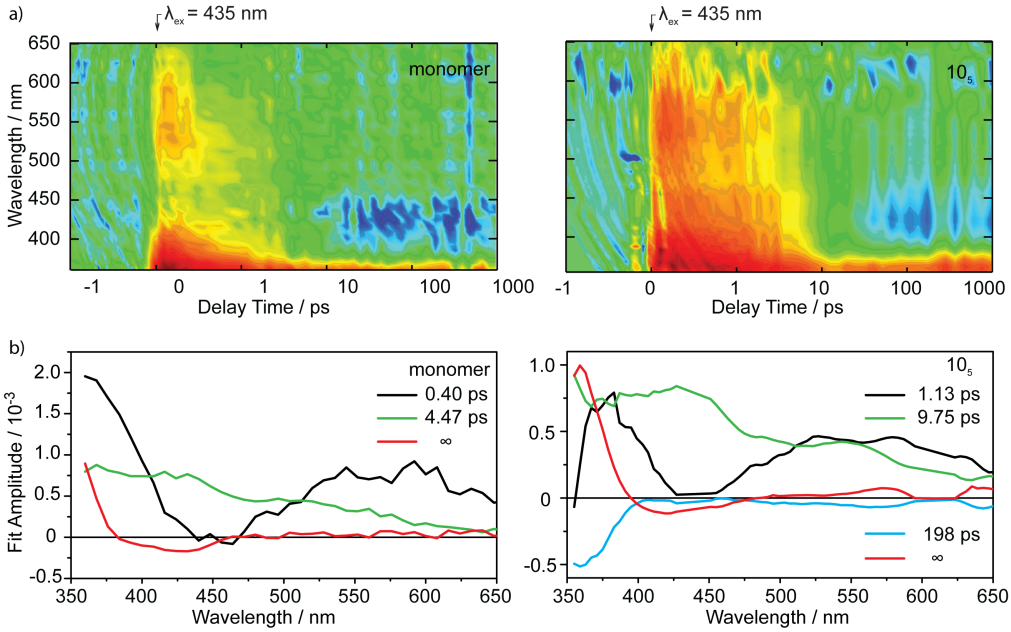

Figure 7.11: a) Transient UV/vis-absorption difference spectra of the *cis*-to-*trans*-isomerization of the monomer unit and the foldamer $\mathbf{10_5}$ after excitation at 435 nm. b) Decay-associated spectra of the monomer unit and the foldamer $\mathbf{10_5}$.

can clearly be seen in the GSB of the *cis*-isomer at 424 nm and the product absorption band of the *trans*-isomer below 380 nm. These absorbance differences are described by an infinite lifetime with a DAS, which coincides quite well with the steady-state absorbance difference (see section 7.1.1, Fig. 7.2).

Regarding the transient UV/vis-absorbance difference spectrum of the foldamer after excitation at 435 nm, ESA-bands can be seen at comparable wavelengths as for the monomer unit at about 380 and 550 nm. However, these positive bands are significantly broadened and show a prolonged lifetime for the decay of these two bands. Both observations result from the highly structured potential energy surface of the foldamer due to great variations in possible isomerization ratios as well as conformations. Although the two obtained lifetimes of 1.13 and 9.75 ps are significantly enlarged with respect to the monomer, the corresponding DAS spectra show the same properties. Consequently, a *cis*-to-*trans*-isomerization occurs within the backbone of the foldamer on a sub-10 ps-time scale. This can also be seen in the product absorption difference band below 400 nm of the *trans*-isomer and in the GSB at about 420 nm of the *cis*-isomer. However, unlike the monomer, the foldamer shows additional dynamics within the product absorbance band below 400 nm with a lifetime of 198 ps

Table 7.3: Lifetimes of time-resolved UV/vis-pump UV/vis-probe experiments on the monomer unit and the foldamer $\mathbf{10_5}$ after excitation at 435 nm.

	τ_1 [ps]	τ_2 [ps]	τ_3 [ps]	τ_4 [ps]
monomer	0.40	4.47	—	∞
$\mathbf{10_5}$	1.13	9.75	198	∞

(Fig. 7.12). In the DAS-spectrum, it can clearly be seen, that this lifetime shows its only contribution in the further increase of the $\pi\pi^*$-band of the *trans*-isomer with no indication of a decrease of another positive bands, like ESA-bands.

Since at this delay time, the ESA bands are already completely relaxed to the ground state, this increase in product absorption cannot be assigned to a formation of the *trans*-isomer from an excited state.

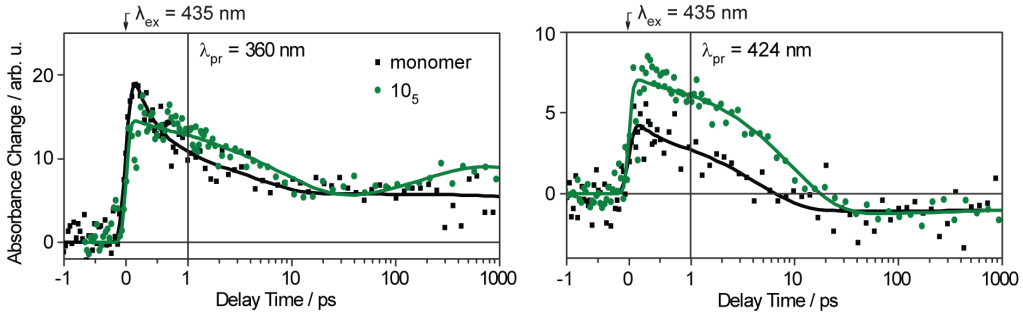

Figure 7.12: Comparison of transients at 360 and 424 nm of the *cis*-to-*trans*-isomerization of the monomer unit and the foldamer $\mathbf{10_5}$ after excitation at 435 nm. Spectra were normalized on the GSB at 424 nm at the longest delay time.

Such a long additional lifetime for the *cis*-to-*trans*-isomerization has already been observed in earlier studies[103] for cyclic azobenzene peptides. In these studies, a shift of the $\pi\pi^*$-band of the *trans*-isomer could be observed in the corresponding DAS, which results in an explanation of this long lifetime of a cooling of the vibrationally excited azobenzene and a subsequent relaxation of the azobenzene and the peptide strand.

In the here observed DAS spectrum of the long lifetime of the foldamer, no contribution of a positive change can be observed, which would indicate a shift of the $\pi\pi^*$-band. However, due to the small expected positive band and the opposite behavior of the lifetimes τ_3 and τ_4 above 470 nm, a sinusoidal structure of the DAS of τ_3 cannot be excluded. In this case, the *trans*-azobenzene is still in a vibrationally excited ground state – not because of heat, but due to structural restraints of the foldamer backbone. Consequently, the lifetime of 198 ps would describe the conformational change of the foldamer backbone from an energetically unfavorable structure into an equilibrated conformation. This leads to a relaxation of the *trans*-azobenzene in the vibrational ground state.

Moreover, a slightly different explanation for the late formation of the product implies the planarization of the azobenzene backbone. This theory still implies a conformational change in the backbone of the foldamer structure, but without a sinusoidal shape of the DAS of τ_3. While the isomerization process is finished after about 40 ps and the azo-group results already in a formed *trans*-conformation, the phenyl rings of the *trans*-azobenzene are still distorted and not correctly oriented due to the longer and rigid foldamer backbone, in which the azobenzene is implemented. The azobenzenes at the terminal position within the backbone structure are less clamped and can therefore form a planar *trans*-isomer structure in the first 40 ps, which results in the

PA band at that delay time. The azobenzenes at the internal or central position of the backbone, however, can align the phenyl rings more difficultly due to the long chain connected to them. Consequently, with a lifetime of 198 ps the phenyl rings of the formed *trans*-azobenzene at the internal or central position of the foldamer backbone are planarized, which results in the typical absorbance band of the $\pi\pi^*$-band of the *trans*-isomer below 400 nm.

As a result, while a typical *cis*-to-*trans*-isomerization is observed for the monomer unit, the azobenzenes within the foldamer structure isomerize clearly slower. Moreover, a conformational change of the foldamer backbone can be indirectly observed with a lifetime of 198 ps via changes in the absorbance band of the $\pi\pi^*$-band of the *trans*-isomer.

7.1.3 Conclusion

The photoswitchable foldamer $\mathbf{10_5}$, which includes five azobenzene derivatives in its backbone structure, can be present in two different secondary structures – a helical and a random coil conformation – in polar solvents dependent on the structure of the photoswitch. The *trans*-isomer enables and even stabilizes via $\pi\pi$-interactions the formation of a helical conformation of the foldamer, which is further stabilized by polar interactions of the side chains with the solvent. The photo-isomerization from the *trans*- into the *cis*-isomer results in a non-planar structure of the azobenzene, which leads to a disruption of the stabilizing interactions between the phenyl rings and consequently to an unfolding of the helical into a random coil conformation. The foldamer $\mathbf{10_5}$ is the smallest oligomer, which can be present in a helical conformation, which shows a complete unfolding after already one isomerization process, while for longer oligomers, e.g. 12_6, at least two isomerization processes are required. This spatial and temporal control over the conformational change of the foldamer allows a wide field of application in the research field of material science regarding data or energy transfer or storage.

Excitation of the *trans*-azobenzene leads to a photo-stationary state, which includes a *cis*-amount of about 66%, which is comparable to the monomer unit. The azobenzene-derivatives of the foldamer are not equivalent due to their different position within the backbone structure. Due to less constriction of the azobenzenes at the terminal position, the isomerization is more probable than for the azobenzene at the central position (values only available for longer oligomers 12_6 and 14_7).[249]

Therefore, the azobenzenes differ slightly in energy and consequently in the energy of their electronic transitions due to their different position within the backbone. Additionally, different isomerization ratios lead to different conformations, which can differ in their ratio of absorbance bands of the *cisoid* and *transoid* structures. These facts result in a highly structured absorbance spectrum of the photo-stationary state.

Time-resolved UV/vis-pump UV/vis-probe studies on the isomerization behavior of the azobenzenes, which are embedded in the foldamer structure, reveal

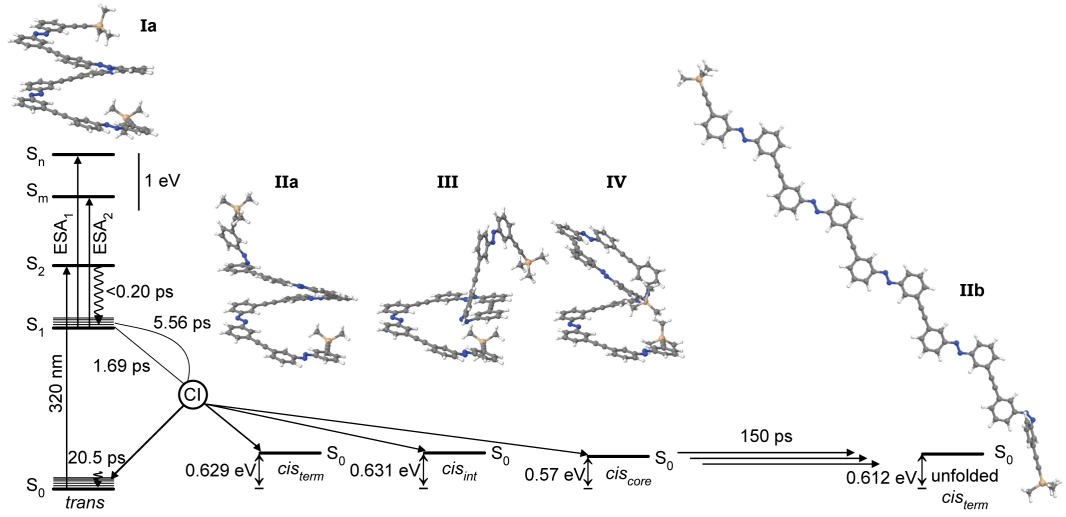

Figure 7.13: Schematic reaction pathway of the foldamer in acetonitrile after excitation at 320 nm. Chemical structures are ground-state optimized (DFT/B3LYP/cc-PVDZ, PCM(acetonitrile)) and their energies are given relative to the folded all-*trans* foldamer. The unfolded conformation is feasible for a *cis*-isomer in each position with the backbone, however, exemplarily, only shown for the *cis*-azobenzene at the terminal position.

comparable dynamics as for the azobenzene monomer unit. The isomerization process from the *trans*- to the *cis*-isomer can be mainly described by two exponential functions with lifetimes of 1.7 and 5.6 ps, which are slightly prolonged with respect to the monomer (Fig. 7.13). Additionally, a lifetime of about 20 ps describes the vibrational cooling of the system, while for the monomer unit the cooling process proceeds with a lifetime of 9 ps. Moreover, the ESA bands of the foldamer are broadened and structured, which refer to the highly structured potential energy surface of the foldamer, which reflect the great variety of different conformations.

Consequently, the photo-isomerization of the embedded azobenzenes proceeds comparable to the monomer, but is completed at a slightly later delay time.

In time-resolved UV/vis-pump IR-probe experiments, the photo-induced conformational change was investigated. Here, the photo-isomerization of the azobenzenes is observed for the monomer as well as for the azobenzenes within the foldamer until a delay time of about 70 ps for the foldamer. Since the dynamics and the spectral shape of the vibrational changes within this time range are comparable for both compounds, solely a photo-isomerization of the azobenzenes can be observed. After 70 ps, however, additional vibrational changes occur only for the foldamer, which can be described by a lifetime of 150 ps. These vibrational changes are supposed to refer to the early conformational changes of the unfolding process upon photo-excitation of the photoswitch. This assumption is supported by (TD)DFT calculations, which show extraordinarily good agreement with the experimental data.

Consequently, in this work, the early photo-induced structural changes of the foldamer $\mathbf{10_5}$ upon *trans*-to-*cis*-isomerization could be observed on a sub-ns-time scale.

Moreover, the *cis*-to-*trans*-isomerization was investigated for the monomer and the foldamer. While the monomer unit reveals a typical azobenzene-type isomerization behavior with only slightly increased relaxation dynamics, the *cis*-to-*trans*-isomerization of the azobenzenes within the foldamer backbone is significantly increased and shows a spectrally broad signature. The reason can be found in the complex potential energy surface of the foldamer, due to a high variability of the isomerization ratio of the five azobenzenes in the backbone as well as the different corresponding conformations. An additional lifetime of 198 ps was observed for the foldamer, which is related to the conformational change of the foldamer structure, more precisely the planarization of the phenyl rings of the backbone, upon *cis*-to-*trans*-isomerization of azobenzene.

It can be summarized, that independent on the direction of isomerization, beside a prolonged isomerization behavior of the azobenzenes in the foldamer structure, early photo-induced conformational changes can be observed in the sub-ns-time range.

7.2 Excitation Energy Transfer in O*m*PE-Foldamers

The photoswitchable O*m*PE-foldamers can be regarded as model systems for longer foldamers, which shall find use in the material science. One desired application of the photoswitchable O*m*PE-foldamers is the ultrafast storage or the transport of data or energy. Consequently, an excitation energy transfer (EET) through the foldamer backbone is preferred.

One possible strategy for achieving an excited energy transfer (EET) within the backbone structure is the implementation of two different azobenzenes to the backbone, in which one of the azobenzenes acts as an energy minimum.[255,256] However, this system consists, more precisely, of three different parts – two different azobenzenes and the phenylene-ethynylene (PE) backbone. Consequently, in this work, only the interactions between the PE units and one type of azobenzenes within the backbone regarding energy transfer are investigated.

Firstly, the compound **3P2E** was studied, which represents a pure PE structure without azobenzenes.

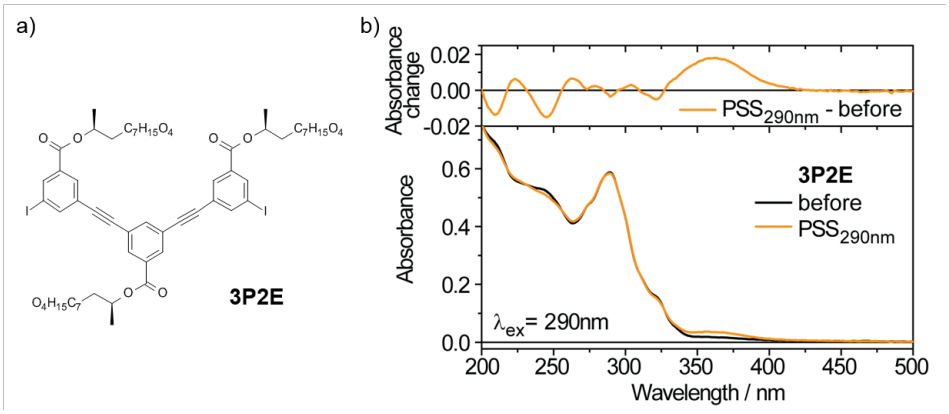

Figure 7.14: a) Chemical structure of the phenylene-ethynylene structure **3P2E**. b) UV/vis-spectra of **3P2E** before and after excitation at 290 nm.

The UV/vis-spectrum of the **3P2E** is characterized by one spectrally narrow absorbance band at 290 nm with small contributions at about 320 nm as well as higher excited states at about 250 nm (Fig. 7.14). After excitation with light of a wavelength of 290 nm, the absorbance band at 290 nm is nearly unaffected, while a shift of about 15 nm can be observed between 200 and 260 nm within the absorbance bands of the higher excited states. More significantly, however, is the increase of a new long-lived absorbance band at 360 nm, which shows a red-shift of about 70 nm with respect to the absorbance band of **3P2E** at 290 nm.

Consequently, by excitation within the phenylene-ethynylene structure **3P2E**, the corresponding excess energy cannot be transferred to the surrounding solvent molecules completely. Instead, a change in the conformation of the structure is induced, which leads to an increased delocalization of the electron density and further to the intense red-shift of the absorbance band. Possible explanations for this red-shift are an increased delocalization due to either a photo-induced accumulation of two **3P2E**

units or by elongation of the **3P2E** strand. Therefore, a photo-reaction of **3P2E** is supposed to occur after excitation at 290 nm. However, so far, it is unclear whether this reaction is reversible or dependent on e.g. concentration or excitation energy. Moreover, also the resulting photo-product is unknown.

In time-resolved UV-pump UV/vis-probe experiments on **3P2E**, the dynamics after excitation at 290 nm are investigated.

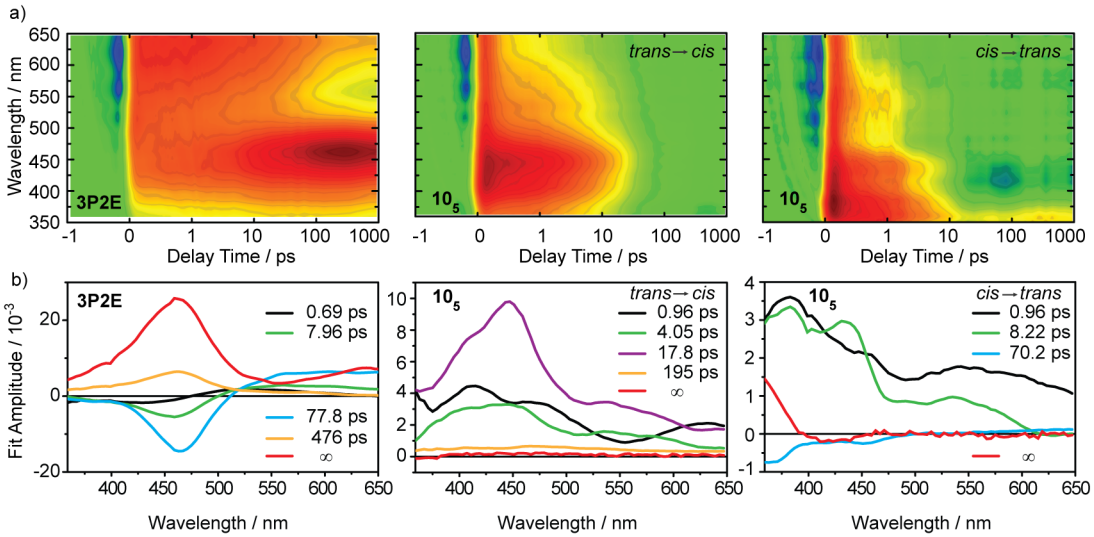

Figure 7.15: a) Transient UV/vis-absorption difference spectra of **3P2E** and the foldamer $\mathbf{10_5}$ in its all-*trans*- and its *cis*-state after excitation at 290 nm. Note that the transient difference spectrum of the *cis*-to-*trans*-isomerization was corrected by the difference spectrum of the *trans*-to-*cis*-isomerization by a factor of 0.3, due to the remaining *trans*-amount in the photo-stationary state ($PSS_{365\ nm}$). b) Decay-associated spectra of **3P2E** and the foldamer $\mathbf{10_5}$ in its all-*trans*- and its *cis*-state.

After excitation of **3P2E** at 290 nm, a broad positive signal arises instantaneously over the whole detection wavelength and especially above 450 nm (Fig. 7.15). A slight decay of the positive contribution at about 520 nm can be described by the lifetime $\tau_1 = 0.69$ ps, which also describes a weak rise 470 nm (Tab. 7.4). While the ESA-band above 550 nm is supposed to correspond to the $S_1 \rightarrow S_m$-transition, the small rising signal below 470 nm is ascribed to a contribution of the stimulated emission at about 350 nm.[257] However, this signal is overlapping with a positive absorbance difference. With the lifetime $\tau_2 = 7.96$ ps and $\tau_4 = 77.8$ ps, the ESA-band above 550 nm decays with a simultaneous increase of an intense ESA-band at 460 nm. These lifetimes are not only referred to the relaxation in the **3P2E** ground state, but also to the formation of an intermediate product, which decays with the lifetime of $\tau_5 = 476$ ps. The contributions at the longest delay time are described by an infinite lifetime τ_6. Here, in the corresponding DAS, the signature of the ESA-band of the $S_1 \rightarrow S_m$-transition can be still observed at 650 nm with the additional positive signal at 460 nm. Comparison of the DAS of lifetime τ_6 and the steady-state difference spectrum leads to the conclusion, that the formation of the product at 360 nm occurs on a time scale of nanoseconds to seconds from the intermediate product, which is

Table 7.4: Lifetimes of time-resolved UV-pump UV/vis-probe experiments on **3P2E** and the foldamer $\mathbf{10_5}$ in its *trans*- and its *cis*-state after excitation at 290 nm.

	τ_1 [ps]	τ_2 [ps]	τ_3 [ps]	τ_4 [ps]	τ_5 [ps]	τ_6 [ps]
3P2E	0.69	7.96	—	77.8	476	∞
all-*trans*-$\mathbf{10_5}$	0.96	4.05	17.8	—	195	∞
***cis*-$\mathbf{10_5}$**	0.96	8.22	—	70.2	—	∞

absorbing at 460 nm. However, a further investigation has not been performed, yet.

Consequently, excitation at 290 nm of **3P2E** leads to a relaxation process into the electronic ground state on the ns-time scale as well as of the formation of an intermediate photo-product with lifetimes of about 8 and 78 ps.

Furthermore, the influence of embedded azobenzenes within the foldamer backbone on the dynamics of the PE backbone unit is studied upon photo-excitation at 290 nm. Therefore, ultrafast time-resolved studies were performed on the foldamer $\mathbf{10_5}$ with azobenzenes in its *trans*- and its *cis*-state (Fig. 7.15). It can clearly be observed, that by excitation of the foldamer $\mathbf{10_5}$ with embedded *trans*-azobenzenes within the backbone, a *trans*-to-*cis*-isomerization is induced, like it was already shown in section 7.1.1 in Fig. 7.4. The decay of the ESA-bands at 420 and 550 nm, which refer to the $S_1 \rightarrow S_m$-transition, can be described by two exponential functions with the lifetimes $\tau_1 = 0.96$ ps and $\tau_2 = 4.05$ ps, while the vibrational cooling of the system occurs with $\tau_3 = 17.8$ ps. These obtained lifetimes are in very good agreement with the earlier studies, which were performed with an excitation wavelength of 320 nm. Here, however, an additional lifetime $\tau_5 = 195$ ps with an only small amplitude was necessary to describe the relaxation sufficiently. This lifetime shows a similar DAS as the lifetime τ_5, which was observed for **3P2E**, although the lifetime is shorter by a factor of about 2.4. Consequently, to a very small extent, the formation of the intermediate photo-product of the PE backbone unit, like it was observed for **3P2E** occurs. The contribution of this reaction to the DAS of the infinite lifetime τ_6 is negligible. Here, mostly the absorbance changes of the photo-product of the *cis*-azobenzene at about 425 nm and the GSB of the all-*trans*-isomer below 380 nm can be seen.

Excitation of the foldamer $\mathbf{10_5}$ in its photo-stationary state ($PSS_{365\ nm}$) at 290 nm shows a clear *cis*-to-*trans*-isomerization of the azobenzenes as it was already observed in section 7.1.2 in Fig. 7.11. The ESA-bands at 380 and 550 nm relax with the lifetimes $\tau_1 = 0.96$ ps and $\tau_2 = 8.22$ ps in the ground state of the *cis*- as well as of the *trans*-isomer. These lifetimes are only slightly shorter than the lifetimes, which were observed for an excitation at 435 nm. After about 30 ps, the GSB of the *cis*-isomer can be observed at 425 nm as well as the formed $\pi\pi^*$-band of the *trans*-isomer below 380 nm. With the lifetime $\tau_4 = 70.2$ ps, the conformational change of the foldamer backbone can be observed, which leads to the late increase of the $\pi\pi^*$-band of the *trans*-isomer, as it was already observed for the $n\pi^*$-excitation at 435 nm. However, comparison of the DAS spectra of this lifetime τ_4 for the two experiments show a clear difference in the range between 400 and 650 nm. Here, the increase of a signal is described at

460 nm with a simultaneous decrease of a positive signal above 520 nm. This specific signature with a comparable lifetime was already observed for the excitation of **3P2E**.

Consequently, independent on the isomeric form of the azobenzenes within the backbone structure of the foldamer $\mathbf{10_5}$, excitation within the absorbance bands of the backbone structure at 290 nm leads almost entirely to an isomerization of the azobenzene. Only a small contribution of the dynamics of the PE backbone unit can be seen as an additional feature. These results lead to two possible explanations. Firstly, excitation with a wavelength of 290 nm leads to a direct excitation within the $\pi\pi^*$-bands of the *trans*- and the *cis*-isomer, which are located within this spectral range, while only a small part of the excitation energy excites the PE unit. However, this contribution of the long-lived S_1-state of the PE unit is subordinate in the time-resolved experiments, while it is not in the steady-state UV/vis-absorbance spectra. Consequently, this leads to the second possible explanation, which involves an ultrafast excitation energy transfer from the PE unit of the backbone to the azobenzenes. The energy transfer in polymers, like PPV, can already be observed on the femtosecond-time scale,[258,259] which is typically faster than the time-resolution of the ultrafast experiments. Therefore, the transfer process cannot be observed directly, but only an instantaneously arising signal of the azobenzene. Here, the azobenzenes within the backbone structure act as an energy minimum. Due to the fact, that the *trans*-isomer is energetically even more favorable than the *cis*-isomer, the energy transfer and consequently the isomerization process is supposed to be even more pronounced for the *trans*-azobenzene.

Whether the excitation at 290 nm leads to a direct excitation of the azobenzenes or to an EET from the PE unit in the backbone to the azobenzenes, it can clearly be seen, that the long-lived dynamics of the PE unit almost entirely disappears by incorporation of an azobenzene in the backbone structure. Consequently, a photo-protection can be obtained by an energetically and kinetically preferred photo-isomerization of azobenzenes.

In further investigations, firstly, the product formation of **3P2E** should be studied, regarding the dynamics of the formation in the time range between nanoseconds and seconds in flash-photolysis measurements. Moreover, a dependence of this formation on the excitation energy as well as on the concentration of the solution should be examined. Furthermore, detection of the ultrafast EET process requires a significantly better time resolution of about 20 fs than the time resolution, which is offered by the experimental setups used in this work. Consequently, optimization of the pump/probe setup would be inalienable, which is non-trivial, especially for pump pulses in the ultraviolet spectral range.

7.2.1 Conclusion

In this section, an excitation energy transfer could be observed from the PE backbone to the azobenzene within the structure of the foldamer $\mathbf{10_5}$. This intramolecular energy transfer is supposed to occur in the early femtosecond-time scale, since the transfer process could not be observed in the time-resolved experiments with a temporal resolution of about 200 fs. The typical azobenzene isomerization behavior can be seen instantaneously after excitation with only a very small amount of initial dynamics of the PE unit of the backbone.

Consequently, the azobenzenes within the foldamer structure serve as energy minima, due to their lower energy states, while the *trans*-isomer is even more preferred. By incorporation of azobenzenes in the PE backbone, the long-lived excited states of PE unit cannot be observed anymore due to kinetic reasons.

Therefore, the implementation of azobenzene within the foldamer strand can be regarded as a photo-protection method, which reduces the lifetime of the excited states from the ns-time scale to about 20 ps. Consequently, the use of azobenzenes, which show an even faster isomerization mechanism or only a fast relaxation back to the *trans*-isomer, like trisazobenzene, could even reduce the lifetime to the early ps- or even sub-ps-time range.

Part IV

Concluding Remarks

Chapter 8

Concluding Remarks and Outlook

The development and improvement of new materials as e.g. energy storage or of synthetic ribonucleic acids for biological use require a detailed understanding of the characteristic properties as well as the dynamics of the corresponding reactions. The incorporation of a small organic chromophore – a photoswitch – into the system of examination enables not only investigations on the specific functions of organic molecules in real time, but also a spatial and temporal control over the respective conformational change as well as chemical or biological reaction.

A photoswitch, here the well-known azobenzene, is a small organic molecule, which can be present in two isomeric forms, which can be interconverted by an excitation with light of a defined wavelength. In case of azobenzene, the planar *trans*-isomer isomerizes into the energetically less preferred *cis*-isomer in its non-planar structure. Due to this ultrafast photo-isomerization, a drastic change in the conformation of the azobenzene occurs, which can be transferred to larger molecules by a linkage of the photoswitch and the macromolecule. Consequently, the well-chosen fixation of e.g. azobenzene to the molecule under investigation in an either covalent or non-covalent manner leads to a conformational change of the large organic molecule, which further influences the corresponding function.

A variety of (photo-)chemical properties are essential for the suitable application of the photoswitch. Here, a good solubility as well as stability in the chosen solvent should be noted. Moreover, the photo-switching event should be ultrafast to not temporally overlap with the actual reaction under investigation. Furthermore, a high switching amplitude as well as a high fatigue resistance is required for a pronounced impact, also in a reversible manner.

Dependent on the desired function of the construct, usually a high thermal stability of the energetically less stable *cis*-isomer is preferred to allow the system to react on the conformational change of the photoswitch. Especially, the use of azobenzenes in biological systems is often challenging, due to the high insolubility of the hydrophobic structure in aqueous solution. Although, a high variety of applications of these photoswitches in biomolecules in water is known in literature, in most cases, this is only achieved by a covalent attachment to the macromolecule. For the use of azobenzene as a non-covalently bound ligand in water or cells, a high solubility of the photoswitch in aqueous media is required.

In this work, a great number of azobenzene derivatives was spectroscopically studied and characterized to receive candidates with good (photo-)chemical properties for biological use (see section 5.1). A variety of azobenzenes was already rejected due to their insolubility in aqueous buffered solution (pH 7.4). Although a number of hydrophilic functional groups, e.g. amino- or amide-groups, was added to phenyl rings, the hydrophobicity of the azobenzene scaffold predominated in many cases. Consequently, the increase of the number of these functional groups as well as substituents, like hydroxy-, sulfate- or sulfonamide-groups show an intense improvement of the solubility in water. However, the use of hydroxy-groups in *ortho*- or *para*-position to the azo-group revealed no accumulation of the *cis*-isomer after excitation of the *trans*-isomer. This photo-isomerization event on a time scale of minutes can be restored by acetylation of the distinct hydroxy-groups.

Consequently, in a detailed study on the influence of the position-dependent hydroxy-substitution of azobenzenes on the photo-isomerization mechanism was performed (see section 5.2). For the hydroxy-substitution of azobenzenes, a keto-enol-tautomerism is discussed.[178] Theoretical calculations ((TD)DFT/B3LYP/cc-PVDZ and PCM=water) on the ground state energies of the keto- and enol-structures of the *trans*- and *cis*-isomeric forms of the three substitution patterns *ortho*, *meta* and *para* were performed for a comparison of the ground state energies of the corresponding structures. It could be shown, that a typical energy difference of the *trans*-enol and *cis*-enol azobenzene of about 0.65 eV is obtained for *meta*- and *para*-substitution, while for *ortho* this difference is increased to about 1 eV. Moreover, a similar energy can be found for the two species enol and keto of *ortho* and *para* in the same isomeric form (less than 0.16 eV for *trans* and 0.04 eV for *cis*), while for **meta**, energy differences of the two species of more than 0.94 eV are shown, which result from the energetically unfavorable structure of the keto-**meta**. In a conformational study of **meta**, the resulting loss of aromaticity and the missing mesomeric form is observed by comparison of bond length of the three compounds.

In time-resolved UV/vis-experiments, a typical azobenzene-like *trans*-to-*cis*-isomerization was observed for *meta*-substitution, which occurs biexponentially with the lifetimes of 1.0 and 4.3 ps. The thermal stability of the resulting *cis*-isomer is in the time regime of hours. For **ortho**, only a subordinate *trans*-to-*cis*-isomerization was observed on a comparable time scale than for **meta**. Interestingly, the preferred deactivation pathway for the *ortho*-substitution after S_2-excitation is an excited states intramolecular proton transfer (ESIPT) from the hydroxy-group to the azo-group with a lifetime of 0.3 ps, resulting in the formation of the keto-species. Afterwards, a relaxation into the keto-ground state proceeds or a further transition in a *cis*-isomer of the keto- or enol-form. Also, a contribution of a triplet state of the keto-species cannot be excluded due to the spectral overlap of the three possible products. The *trans*-enol species is further recovered with a lifetime of 3.2 ms. Hydroxy-substitution in *para*-position in aqueous solution leads already to a keto-enol-tautomerism in the ground state. The ratio between the two species is highly dependent on the temperature,

which leads to the assumption of a low energy barrier between the two energy minima. The two species can be addressed specifically by a defined wavelength, which results in a typical *trans*-to-*cis*-isomerization after excitation of the enol-form. Specific excitation of the keto-species leads to completely different dynamics, which result in the formation of a *cis*-isomer in either the enol- or the keto-form, which can hardly be distinguished due to the spectral overlap.

Consequently, a keto-enol-tautomerism could be detected for **ortho** in the excited state, while for **para**, it can already be observed in the ground state. These experimental results on the keto-enol-tautomerism of **ortho** and **para** could also be supported by theoretical calculations, which were performed in the research group of Prof. I. Burghardt.

This achieved knowledge enables an application of already known molecules with an azobenzene scaffold, like therapeutics, which could not be used for photo-isomerization processes due to the fast thermal relaxation of the *cis*-isomer to the *trans*-form. Acetylation of the hydroxy-group in *para*-position of the therapeutic Sulfasalazine leads to an increase of the lifetime of the relaxation of the *cis*–isomer to the *trans*-isomer from 61 ms to a time regime of minutes (see subsection 5.2.1). Here, it should be noted that no significant change upon acetylation was observed for the isomerization dynamics, which proceed biexponentially with the lifetimes about 1 and 4.4 ps.

A variety of azobenzene derivatives were obtained, which show good (photo-)chemical properties in aqueous buffered solution. Here, for example, dicarboxy-azobenzene should be noted with a sufficient switching amplitude, which results in a photo-stationary state after excitation at 365 nm with a *cis*-amount of 76% (see section 5.1). This *cis*-isomer shows an acceptable thermal stability at room temperature with a relaxation to the *trans*-isomer, which can be described by a half-life of about 1.4 h. Moreover, a high fatigue resistance could be observed.

As seen in chapter 3, the chemical and photo-physical properties of azobenzene are highly dependent on the choice and position of the substituents. A variety of azobenzene derivatives was obtained for an application in aqueous media. Moreover, the influence of hydroxy-substitution of azobenzenes in aqueous solution on the photo-isomerization mechanism was investigated as well as the occurring keto-enol-tautomerism for *ortho*- and *para*-substitution.

Other interesting azobenzene derivatives are azobenzenes, which are coupled to a desoxyribose in *meta*- or *para*-position to the azo-group, **mAzo** and **pAzo**, respectively (see section 6.1). These compounds are designed for the covalent incorporation within a short RNA strand for investigations on the photo-responsive dehybridization of a RNA double helix. Due to the planar structure of the *trans*-azobenzene, an incorporation of the photoswitch between the base pairs of a RNA double helix is supposed to be enabled. The non-planarity of the *cis*-azobenzene, however, should disrupt the stabilizing surrounding base pairs, which leads to a dehybridization of the double helix upon photo-isomerization. One possible application for biological sys-

tems is the destabilization of a RNA stem structure of e.g. a RNA aptamer. By photo-isomerization of the embedded azobenzene, a conformational change of the RNA aptamer results. This could be used for e.g. a photo-responsive riboswitch, which uses the photo-switchable RNA aptamer as sensor domain.

The spectroscopic characterization concentrated on the switching amplitude as well as on the thermal stability of the *cis*-isomer, since in earlier studies,[260] where a different linker was used, a sufficient *cis*-amount could only be achieved at high temperature of about 70°C, which is critical in case of biological systems. In this work on the monomers **mAzo** and **pAzo**, a high *cis*-amount of about 90% already at room temperature could be achieved not for the monomer itself, but also for the azobenzene within RNA single strands. This high switching amplitude is extraordinary for azobenzenes linked to RNA. A high thermal stability of the *cis*-isomer with a half-life of about 100 h as well as a high fatigue resistance could be shown for the monomers **mAzo** and **pAzo**. Also the incorporation of these monomers within RNA 15-mers show a high thermal stability of the *cis*-isomer with a half-life of more than 150 h, which is dependent on the neighboring base pairs within the strand. The melting point studies on the synthetic construct of a short RNA oligomer, which contains one azobenzene derivative in one RNA strand, which were performed in the research group of Prof. A. Heckel, reveals a also high dependence of the choice of the neighboring bases as well as the bases on the opposite site within the complementary strand on the stability of the double helix. Here, already differences were detected for the incorporation of the azobenzene derivatives in the opposite RNA strand.

To achieve a high destabilizing effect on the RNA structure after photo-isomerization from the *trans*- to the *cis*-isomer, the stability of the double helix should not be affected significantly by the *trans*-isomer, but only for the non-planar *cis*-azobenzene. Here, the RNA double strand with an abasic site, which includes only the backbone structure, but without a base, in the opposite strand at the position, which is opposite to the azobenzene **pAzo**, shows sufficiently good results with a destabilization of the helix of $\Delta T = 5.7$°C. These results were supported by MM/MD calculations on the root mean square fluctuations (B-factor) of the helix with the *trans*- and the *cis*-**pAzo** within one strand and an abasic site in the opposite strand, which were performed in the research group of Prof. I. Burghardt. Here, only a minor destabilization of the *trans*-isomer could be observed, while the *cis*-isomer induces a higher fluctuation in the neighboring base pairs, however, without a disruption of the hydrogen bonds.

As seen in section 6.1, extraordinary photo-chemical properties could be observed for the desoxyribose-linked azobenzenes **mAzo** and **pAzo** in the monomeric as well as in the covelantly bound state in the RNA strand. Also a destabilization effect upon photo-isomerization was observed for a RNA double helix.

As an outlook, the number of azobenzenes within the RNA oligomer should be increased to gain insights into a possible complete dehybridization of the RNA double helix. This includes a detailed study on the necessary number of photoswitches as well as the corresponding positions within the RNA strands. Furthermore, the size

of the RNA oligomer could be further increased to obtain information on a possible photo-responsive dehybridization in biological systems.

Another possibility to create a photo-responsive riboswitch is the non-covalent incorporation of an azobenzene in the RNA structure. Here, the azobenzene is used as a photoswitchable ligand, which binds via interactions to the RNA structure, however, specifically only in one of the isomeric forms. Consequently, a stable secondary/ tertiary structure is achieved by specific ligand binding, which results in termination of the gene expression. Upon photo-isomerization, the second isomeric form of the ligand cannot bind to the RNA anymore, which should lead to a conformational change of the RNA aptamer and furthermore to a transcription or translation.

Here, two of the azobenzene derivatives with promising photo-chemical properties in aqueous solution were used as photoswitchable ligands. The first ligand **AAPAB** shows good solubility in water and a reasonable switching amplitude as well as thermal stability of the *cis*-isomer. It has a high fatigue resistance and stability in water as well as in HeLa-cell extracts for about 44 h without an indication of degradation. A SELEX-routine was used for the systematic search for a RNA sequence, which binds specifically only the *trans*-isomer of the ligand. Here, a SELEX procedure was performed by the research group of Prof. B. Suess, which uses streptavidin-coupled magnetic beads for the immobilization of the ligand. Due to the high binding affinity of streptavidin and biotin, the **AAPAB**-ligand was biotinylated and therefore added to the beads non-covalently. Indeed, a RNA sequence was obtained, which binds only the *trans*-, but not the *cis*-isomer of the ligand. However, the RNA sequence results in not only binding the photoswitchable ligand, but also the streptavidin, which is significantly larger than the target molecule.

Consequently, a photoswitchable ligand binding to a RNA aptamer could be obtained, which however, does not bind exclusively the **AAPAB** target molecule.

For another azobenzene-derivative **CAP**, which is an azobenzene coupled to the broad-spectrum antibiotic chloramphenicol and shows satisfying (photo-)chemical properties, a different SELEX-routine was performed. By covalent binding of the target ligand via a primary amino group to an agarose bead, a systematic search for also small ligands is improved. A RNA sequence was obtained, that binds only the *trans*-**CAP** and which could even be shortened to a 42-mer without significant loss of specificity or affinity. A dissociation constant of 0.82 μM for the amino-substituted *trans*-**CAP** and 3.55 μM for the *trans*-**CAP** were found for the aptamer 42_{trunc} without a binding affinity to the corresponding *cis*-isomers or the pure chloramphenicol.

The complex of the RNA aptamer 42_{trunc} and the ligand **CAP** shows a comparable switching behavior as well as spectral characteristics of the ground state as the pure ligand. However, small differences could be observed for the excited state dynamics of the complex. While the free ligand **CAP** shows an isomerization process, which can mainly be described by the lifetimes 1.48 and 6.35 ps, a slightly longer relaxation time of 1.54 and 7.17 ps can be seen for the **RNA+CAP**, which results from the increased

size of the system. Moreover, the energy of the excited state transitions ($S_1 \rightarrow S_m$) is slightly lower for the bound ligand in contrast to the free **CAP**. Also, a change in the intensity of the ESA-bands and PA-bands of the *cis*-isomer are observed. Here, a lower extinction coefficient of the excited state absorption of the S_1-state or a lower quantum yield for the isomerization to the *cis*-isomer are assumed. Beside the small changes, however, a typical isomerization occurs for the free as well as for the bound **CAP**.

In CD- as well as in (time-resolved) IR-experiments only minor photoswitchable conformational changes were observed for the RNA aptamer. Upon addition of the ligand *trans*-**CAP** to the RNA aptamer 42_{trunc} a small spectral change is obtained in CD-spectra, which leads to the assumption of a small structural changes due to the binding to the ligand. However, upon photo-isomerization of **CAP** to its *cis*-isomer, mostly conformational changes, which refer to the ligand itself, were obtained in CD- and IR-spectra.

Consequently, photo-isomerization of **CAP** leads to a stable *cis*-isomer for the free as well as for the complex of ligand and RNA. Since, however, a conformational change of the RNA only occurs for the addition, but not for the photo-isomerization of **CAP**, the secondary structure of the aptamer is supposed to be too stable. The reason for the stable RNA structure is a hairpin within the aptamer, which further leads to a complete termination of gene expression when added to a riboswitch.

Therefore, it is necessary to destabilize the structure of the RNA aptamer by e.g. changes in this loop, which should lead to a secondary structure of the RNA, which changes only upon binding of the *trans*-**CAP**. Also, a new SELEX procedure with a partially structured pool, which does not content the stabilizing loop, but the RNA sequence, that binds to *trans*-**CAP**, could help finding an improved RNA aptamer.

As seen in section 6.2, two photo-responsive RNA aptamers were obtained, which bind specifically only the *trans*-isomer of the azobenzene-ligand. Moreover, the dynamics of the isomerization process of the azobenzene-derivative in a free and a bound state as well as of the photo-induced conformational change were investigated.

In this work, investigations were not only performed on the development of biological systems like a photo-responsive riboswitch, but also of synthetic oligomers, which are used as model systems for material science. Here, the photoswitchable oligo-*meta*-phenylene-ethynylene foldamer $\mathbf{10_5}$, which embeds five azobenzenes in the backbone structure, was spectroscopically studied regarding its photo-induced conformational changes. While, in acetonitrile, for the all-*trans*-conformation a helical structure is obtained, which is stabilized by $\pi\pi$-interactions as well as polar interactions with the side chains, the *cis*-isomer leads to an unfolding of the defined secondary structure.

The variety of different isomerization ratios and conformations of the foldamer $\mathbf{10_5}$ could be observed in the highly structured UV/vis-absorbance spectra not only of the ground, but also of the excited states. A high switching amplitude of about 66% *cis*-isomer was obtained for the monomer unit as well as for the foldamer. The *trans*-

to-*cis*-isomerization proceeds via a conical intersection biexponentially in the ground states of the *trans*- and *cis*-isomers. This relaxation process is generally longer for the foldamer than for the monomer unit with lifetimes of 1.69, 5.56 and 20.5 ps. While the isomerization is completed for the monomer already after about 20 ps, no changes can be obtained for the foldamer after 70 ps in the electronic structure. However, an additional lifetime of 150 ps was obtained solely for the foldamer for the description of the vibrational changes upon photo-excitation. This lifetime is ascribed to an early conformational change of the helical structure of the foldamer upon photo-isomerization of the embedded azobenzenes. This assumption was supported by a detailed theoretical analysis (DFT/B3LYP/cc-PVDZ and the PCM solvent model using acetonitrile) on the vibrational structure of different possible foldamer conformations, which include different isomeric states (*trans* vs. *cis*) and secondary structures (helix vs. random coil). An extraordinary agreement was found for the theoretical and the experimental (DAS of $\tau = 150$ps) vibrational spectra for the unfolding process of the helix, which already includes one *cis*-azobenzene within the backbone structure after a photo-isomerization.

Consequently, an isomerization occurs within the foldamer $\mathbf{10_5}$ via a typical, but slightly prolonged, isomerization mechanism. Afterwards, an early conformational change of the helical conformation upon *trans*-to-*cis*-isomerization of the embedded azobenzenes is obtained on a sub-ns time scale, which further leads to a complete unfolding of the helix.

Also, the *cis*-to-*trans*-isomerization was investigated for the monomer unit and the foldamer $\mathbf{10_5}$. Here, an isomerization proceeds for the foldamer with the lifetimes 1.13 and 9.75 ps, which is significantly longer than for the monomer, but with a similar spectral behavior. After about 20 ps, the GSB of the *cis*-isomer as well as a PA-band of the *trans*-isomer can be observed. However, with an additional lifetime of 198 ps for only the foldamer $\mathbf{10_5}$, this $\pi\pi^*$-band of the *trans*-isomer increases even further.

Consequently, this additional lifetime is ascribed to a conformational change of the foldamer backbone upon photo-isomerization. While after about 20 ps, the isomerization is already complete, the phenyl rings of the azobenzene, especially for azobenzenes at the internal and central position of the foldamer, are not yet planar due to the long foldamer backbone. Therefore, with a lifetime of 198 ps, a conformational change of the foldamer backbone is performed, which leads to a planarization of the azobenzene and further to the formation of the $\pi\pi^*$-band of the *trans*-isomer.

In further studies, investigations on the complete (un-)folding of the foldamer $\mathbf{10_5}$ could be performed in the infrared region. Moreover, the influence of the backbone length of the foldamer on the dynamics of the conformational changes should be studied.

Additionally, the excitation energy transfer from the phenylene-ethynylene (PE) unit in the backbone to the azobenzene was studied. It could be shown, that for the excitation of **3P2E** structure, a long-lived S_1-state can be observed with a lifetime, which is longer than the longest delay time of the experiment. Moreover, the formation of an

intermediate photo-product with the lifetime of about 8 and 78 ps is observed, which relaxes then with a lifetime of 476 ps. When azobenzenes are included in the PE backbone structure, either in the *trans*- or in the *cis*-state, as it is the case for the foldamer $\mathbf{10_5}$, an excitation within the backbone leads to an isomerization of the azobenzene almost entirely. Therefore, the system is relaxed to the ground state after about 40 ps. Consequently, the introduction of azobenzenes in the PE backbone leads to a significant decrease of the lifetime of the excited state, by serving as energy traps. This remarkably effect could be further used for studies on photo-protection of systems. Here, azobenzenes with even shorter isomerization processes could be introduced in the backbone structure to even further decrease the excited states lifetimes to the sub-ps time scale.

For a detailed understanding, however, further investigations are required on the dynamics and the product formation of **3P2E** as well as on its dependence on the excitation energy and on the concentration. Moreover, optimization of the pump/probe setup would be inalienable for the detection of the ultrafast EET process, which is non-trivial, especially for pump pulses in the ultraviolet spectral range.

As seen in chapter 7, the early conformational changes of the short foldamer model system $\mathbf{10_5}$ upon photo-excitation of the embedded azobenzenes were investigated. (Un-)folding dynamics could be observed in the sub-ns-time scale. Moreover, an excitation energy transfer from the backbone to the azobenzenes was observed.

In this thesis, the detailed characterization of a high variety of azobenzene photoswitches was performed by using a number of different (time-resolved) spectroscopic techniques. Interesting influences of the small hydroxy-group as a substituent on the isomerization behavior of azobenzenes were obtained. In cooperation with the research group of Prof. A. Heckel, azobenzene derivatives were optimized regarding their (photo-)chemical properties for biological applications, like the development of a photo-responsive riboswitch. In cooperation with the research group of Prof. B. Suess, RNA aptamers were obtained by a systematic search (SELEX), which bind specifically and with high affinity the *trans*-isomer of azobenzene ligand. The influence of the photo-isomerization on the RNA conformation and the corresponding dynamics were studied by a variety of spectroscopic methods. Unfortunately, due to the size of the system in the first case or the two stable RNA conformations for the seconds aptamer, so far, these RNA aptamers cannot be used for photo-responsive riboswitches. Moreover, the photo-induced early conformational changes of the important model foldamer $\mathbf{10_5}$ could be observed as well as an excitation energy transfer from the backbone to the azobenzenes, which are embedded.

The obtained results allow a better understanding and an improved development of new techniques for biological control of gene expression or the energy transfer of storage in new photo-responsive materials.

Chapter 9

Deutsche Zusammenfassung

Die Erforschung sowie die Weiterentwicklung neuer Materialien für Anwendungen als z.B. Energiespeicher oder synthetischer Ribonukleinsäuren für biologische Nutzung setzen eine fundierte Kenntnis der charakteristischen Eigenschaften sowie der Dynamik der entsprechenden Systeme voraus.

Durch den gezielten Einbau niedermolekularer organischer Chromophore, so genannten Photoschaltern, in das entsprechende System werden nicht nur Untersuchungen spezifischer Funktionen der organischen Moleküle in Echtzeit ermöglicht, sondern auch die örtliche sowie zeitliche Kontrolle über bestimmte Konformationen sowie chemische und biologische Reaktionen.

Bei einem Photoschalter handelt es sich um ein kleines organisches Molekül, welches in mindestens zwei Strukturen vorliegen kann, welche durch gezielte Belichtung mit einer bestimmten Wellenlänge ineinander überführt werden können. In dieser Arbeit wurden Derivate des bekannten Photoschalters Azobenzol untersucht, welches durch UV-Belichtung von seiner planaren *trans*-Struktur in die energetisch ungünstigere nicht-planare *cis*-Form isomerisiert. Auf Grund dieser ultraschnellen Isomerisierung erfolgt eine drastische Änderung der Struktur des Azobenzols, welche, durch eine geeignete Verknüpfung mit Makromolekülen, auf diese übertragen werden kann. Somit ist eine Konformationsänderung eines Moleküls durch eine kovalente oder nicht-kovalente Bindung eines Photoschalters möglich, welche im Weiteren die entsprechende Funktion des Moleküls beeinflusst.

Für eine geeignete Nutzung eines Photoschalters sind eine Vielzahl verschiedener (photo-)chemischer Eigenschaften nötig. Dazu gehören, neben einer guten Löslichkeit sowie Stabilität in dem entsprechenden Lösungsmittel, auch ein gutes Schaltverhalten, welches nicht nur eine hohe Schaltamplitude, sondern auch einen hohen Ermüdungswiderstand berücksichtigt. Zudem ist es notwendig, dass der Prozess der Photoisomerisierung sehr schnell verläuft, sodass eine zeitliche Überlappung mit der eigentlich zu untersuchenden Reaktion verhindert wird.

Insbesondere die Anwendung von Azobenzolen in biologischen Systemen stellt auf Grund der ausgeprägten Unlöslichkeit in wässriger Lösung eine große Herausforderung dar, welche auf das stark hydrophobe Grundgerüst des Azobenzols zurückzuführen ist. Durch die kovalente Einbringung des Photoschalters in das biologische System besteht die Möglichkeit das Problem der Wasserlöslichkeit zu umgehen.

Für die Verwendung des Azobenzols als nicht-kovalent gebundener Ligand in wässriger oder zellulärer Umgebung ist eine zufriedenstellende Löslichkeit sowie eine gutes Schaltverhalten jedoch unumgänglich.

Der erste Teil dieser Arbeit beschreibt die spektroskopische Charakterisierung einer Vielzahl an Azobenzol-Derivaten, um geeignete Kandidaten für eine biologische Anwendung zu finden (Sektion 5.1). Wenige Azobenzole kamen auf Grund ihrer starken Unlöslichkeit in wässrigen gepufferten Lösungen (pH 7.4) für weitere Untersuchungen in Frage. Die Verwendung von hydrophilen funktionellen Gruppen, wie Hydroxygruppen oder Sulfonamiden, ermöglichten Studien in wässrigem Milieu. Hier fiel die fehlende Anreicherung des *cis*-Isomers nach Photoanregung des *trans*-Isomers jedes Azobenzols auf, welches in *ortho*- oder *para*-Position zu der Azogruppe mit einer Hydroxygruppe substituiert war. Bemerkenswerterweise war es möglich, lediglich durch Acetylierung der Hydroxygruppe über den Zeitbereich von Minuten die stabile Photoisomerisierung wiederherzustellen.

Somit wurde eine detaillierte Studie über den Einfluss der positionsabhängigen Hydroxy-Substitution eines Azobenzols auf den Mechanismus der entsprechenden Photoisomerisierung durchgeführt (Sektion 5.2).

Da für die Hydroxy-Substitution von Azobenzolen eine Keto-Enol-Tautomerie diskutiert wird, wurden zunächst quantenmechanische Rechnung für die drei Hydroxy-Azobenzole **ortho**, **meta** und **para** durchgeführt, welche Rückschlüsse auf die energetische Lage der jeweils vier verschiedenen Isomere zulassen. Es konnte gezeigt werden, dass für die Substitution in *meta*-Position eine stabile Keto-Form auf Grund fehlender Aromatizität der Phenylringe nicht vorliegen kann. Zudem konnte eine energetische Nähe der *trans*-Isomere der Keto- und Enol-Form für *ortho*- und *para*-Substitution sowie entsprechend für die *cis*-Isomere bestimmt werden. In zeitaufgelösten UV/vis-Experimenten konnte für **meta** der typische Mechanismus der Photoisomerisierung eines unsubstituierten Azobenzols gefunden werden, welcher mit einer Lebensdauer von 1.0 und 4.3 ps beschrieben werden kann. Auch für **ortho** konnte dieser Isomerisierungspfad, jedoch lediglich als untergeordneter Deaktivierungskanal, detektiert werden. Interessanterweise, verläuft hauptsächlich ein intermolekularer Proton-Transfer im angeregten Zustand (ESIPT) von der Hydroxygruppe der Enol-Form an die Azogruppe der Keto-Form mit einer Lebenszeit von 0.3 ps. Neben der Relaxation in den Grundzustand der *trans*-Keto-Spezies, wird ebenfalls ein *cis*-Isomer des Enols bzw. Ketos besetzt. Auch die Beteiligung von Triplettzuständen kann nicht ausgeschlossen werden.

Während für **ortho** Keto-Enol-Tautomerie im angeregten Zustand beobachtet wurde, findet diese für **para** schon im Grundzustand über eine, die Hydroxy- und Azogruppe verknüpfende, Wasserkette statt. Das Verhältnis von Enol- und Keto-Form ist hierbei stark temperaturabhängig. Diese zwei Spezies können durch geeignete Wahl der Anregungswellenlänge spezifisch adressiert werden und folgen verschiedenen Deaktivierungskanälen. Eine Anregung der Enol-Form resultiert in einer

Photoisomerisierung mit ähnlicher Dynamik wie **meta** und einer Bildung des *cis*-Enol-Isomers. Nach spezifischer Anregung der Keto-Form hingegen relaxiert ein Großteil zurück in die *trans*-Keto-Form, während zu einem kleineren Teil ein *cis*-Isomer gebildet wird. Diese Ergebnisse konnten durch quantenmechanische Rechnung zu den verschiedenen Deaktivierungskanälen nach S_2-Anregung unterstützt werden, welche in der Arbeitsgruppe Burghardt durchgeführt wurden.

Diese erhaltene Kenntnis ermöglicht nun die Verwendung von bereits bekannten Molekülen mit einem Azobenzol-Grundgerüst, wie z.B. das Medikament Sulfasalazin, als Photoschalter. Durch Acetylierung der Hydroxygruppe des Sulfasalazins konnte auf einer Zeitskala von Minuten ein stabiles *cis*-Isomer beobachtet werden ohne den Mechanismus der Photoisomerisierung zu beeinflussen.

Für die Entwicklung eines photoaktivierbaren Riboschalters, welcher eine zeitliche und örtliche Kontrolle der Genexpression ermöglicht, wurden in dieser Arbeit zwei Ansätze verfolgt (Kapitel 6).

Zunächst wurde ein Azobenzol mittels einer Desoxyribose-Verknüpfung kovalent in einen RNA-Strang eingebaut, welcher im Folgenden die Dehybridisierung eines RNA Doppelstrangs lichtinduziert regulieren soll (Sektion 6.1). Auf diese Art wäre eine Konformationsänderung des RNA-Aptamers in der Sensordomäne eines Riboschalters durch Photoisomerisierung eines Azobenzols in der Stammstruktur des Aptamers möglich. Die entsprechend untersuchten Monomere **mAzo** und **pAzo** zeigen bemerkenswerte Eigenschaften mit einem *cis*-Gehalt im photostationären Zustand von etwa 90% und einer thermischen Stabilität von etwa 100 Stunden. Ein solch hoher *cis*-Gehalt bei Raumtemperatur sowie diese ausgeprägte Stabilität konnten zudem für die Azobenzole in einem RNA-Einzelstrang erreicht werden. Entsprechend hohe Schaltamplituden in einer RNA bei Raumtemperatur sind in der Literatur bisher unbekannt. In Schmelzpunktstudien der Arbeitsgruppe Heckel sowie MM/MD-Rechnungen der Arbeitsgruppe Burghardt wurde der positionsabhängige Einfluss der Photoisomerisierung des Azobenzols auf die Stabilität des RNA Doppelstrangs untersucht. Hierbei ist eine geringe Störung des Systems auf Grund des *trans*-Isomers und eine entsprechend große Auswirkung des *cis*-Azobenzols wünschenswert. Eine Destabilisierung des Doppelstrangs von $\Delta T = 5.7°\mathrm{C}$ konnte z.B. durch den Einbau von **pAzo** in ein 15-mer mit einer fehlenden Base an der komplementären Position des Gegenstranges erreicht werden.

In einem weiteren Ansatz für die Entwicklung eines photoschaltbaren Riboschalters wurde die nicht-kovalente Nutzung des Azobenzols als photoschaltbarer Ligand für ein RNA-Aptamer verfolgt (Sektion 6.2). Hierzu wurde für zwei Azobenzol-Derivate mit ausgezeichneten (photo-)chemischen Eigenschaften, eine RNA-Sequenz mittels des SELEX-Verfahrens systematisch gesucht, welche spezifisch und mit hoher Affinität lediglich das *trans*-Isomer und nicht das *cis*-Azobenzol bindet.

Für den ersten photoschaltbaren Liganden **AAPAB** wurde in der Arbeitsgruppe Süß ein SELEX-Ansatz gewählt, bei welchem der Ligand biotinyliert und an magne-

tische Kügelchen (Beads), welche an Streptavidin gekoppelt sind, immobilisiert wird. Hierbei wurde ein RNA-Aptamer gefunden, welches spezifisch nur den Liganden in seiner *trans*-Form bindet. Jedoch wurde auch eine zusätzliche Bindung der RNA an das Streptavidin beobachtet. Somit handelt es sich hierbei um ein photoschaltbares RNA-Aptamer, für welches allerdings die Bindung eines, für die meisten Anwendungen, zu großen Liganden – Streptavidin und Azobenzol – notwendig ist.

Für den zweiten photoschaltbaren Liganden **CAP**, bei welchem das Azobenzol an das Breitbandantibiotikum Chloramphenicol gekoppelt wurde, wurde ein SELEX-Ansatz gewählt, bei welchem das Azobenzol über ein primäres Amin kovalent an Agarose Kügelchen gebunden wird. Es wurde ein RNA-Aptamer gefunden, welches spezifisch und mit hoher Affinität an das *trans*-**CAP** bindet ($K_d = 0.82\ \mu M$). Durch die Kürzung des Aptamers auf ein 42-mer wurden die guten Eigenschaften der Ligandenbindung nicht wesentlich beeinflusst. Auch der Ligand **CAP** ohne die zusätzliche Amino-Gruppe zeigt gute Bindungsaffinität zu dem RNA-Aptamer 42_{trunc} mit einer Dissoziationskonstanten von 3.55 μM. Der freie Ligand wie auch der Ligand im Komplex mit der RNA zeigen gute photochemische Eigenschaften. So kann für den freien Liganden ein *cis*-Gehalt von etwa 80% erreicht werden. Zudem zeigt **CAP** auch nach 24 Stunden keine Anzeichen für eine Zersetzung in HeLa-Zellextrakten.

Ein Photoisomerisierung konnte sowohl für den freien als auch für den gebundenen Liganden mittels zeitaufgelöster UV/vis-Experimente beobachtet werden, welche mit den Zeitkonstanten 1.54 und 7.17 ps für den Komplex beschrieben werden kann. Hierbei ist lediglich eine leichte Verlängerung der Dynamik für den Komplex zu beobachten. Interessanterweise ist das Verhalten der beiden Proben im Grundzustand sehr ähnlich, während die $S_1 \rightarrow S_n$-Übergänge für den Komplex **RNA+CAP** einen leicht geringeren Energieunterschied aufweisen als im freien **CAP**. Auch eine etwas kleinere Quantenausbeute für **RNA+CAP** wird beobachtet.

Eine geringe Änderung in den CD-Signalen der RNA bei Zugabe des *trans*-Liganden lässt auf eine Konformationsänderung des RNA-Aptamers 42_{trunc} schließen, welche jedoch nicht stark ausgeprägt zu sein scheint. Photoisomerisierung des Liganden zeigt sich in den CD- sowie in (zeitaufgelösten) IR-Spektren lediglich in der Konformationsänderung des Photoschalters. Nur sehr schwache zusätzlich Signale lassen sich erahnen, welche von der RNA herrühren können, jedoch nahezu vernachlässigbar klein sind.

Dementsprechend weist die Konformation, welche durch Zugabe des *trans*-Azobenzols angenommen wurde, eine sehr hohe Stabilität auf, welche auch nach Photoisomerisierung bestehen bleibt. Diese Struktur wird besonders durch eine Haarnadelstruktur in der RNA-Sequenz stabilisiert. Durch Kombination des RNA-Aptamers mit einem Riboschalter konnte bisher jedoch lediglich eine nahezu vollständige Terminierung der Genexpression beobachtet werden.

Somit konnten in dieser Arbeit RNA-Aptamere in Kooperation entwickelt werden, welche spezifisch und mit hoher Affinität das *trans*-Isomer der Azobenzol-Derivate **AAPAB** und **CAP** binden, die durch ausgezeichnete photochemische Eigenschaften

überzeugt haben. Für die weitere Anwendung als Bestandteil eines photoschaltbaren Riboschalters sind diese Aptamere derzeitig jedoch noch nicht zu verwenden und es bedarf noch weiterer Entwicklungsarbeit.

Der zweite Teil dieser Arbeit beinhaltet die photo-induzierten Konformationsänderungen eines O*m*PE-Foldamers $\mathbf{10_5}$, welches aus fünf, durch Ethinyl-Gruppen verbrückten, Azobenzolen besteht und in einer helikalen sowie einer entfalteten Struktur vorliegen kann (Kapitel 7). Abiotische Foldamere finden Anwendung z.B. in den Materialwissenschaften als Energiespeicher.

Eine Vielzahl an verschiedenen Isomerisierungsverhältnissen sowie unterschiedlicher daraus resultierender Strukturen für das Foldamer $\mathbf{10_5}$ konnten durch die stark strukturierten UV/vis-Absorptionsbanden beobachtet werden. Eine *trans*- nach *cis*-Isomerisierung wurde für die Azobenzole in dem Foldamer detektiert, dessen Dauer nur etwas länger sind als die des entsprechenden Monomers. Die Relaxation des Systems nach Photoisomerisierung erfolgt nach etwa 70 ps. Allerdings ist lediglich für das Foldamer eine deutliche spätere Änderung in der Schwingungsstruktur zu erkennen, welche mit einer Zeitkonstanten von 150 ps beschrieben wird. Diese Dynamik wird der photo-induzierten frühen Konformationsänderung der helikalen Struktur des Foldamers zugeschrieben, welche sich im Weiteren vollständig entfaltet.

Diese These wurde durch eine detaillierte theoretische Studie bestätigt, welche die Frequenzanalyse verschiedener Strukturen und Isomerisierungsgrade durch quantenmechanische Rechnungen betrachtete. Hierbei wurden außerordentliche Übereinstimmungen des theoretisch berechneten IR-Differenzspektrums des Foldamers mit einem *cis*-Azobenzol, welches die Entfaltung beschreibt, sowie dem experimentellen zerfallsassoziierten Spektrum der 150 ps-Zeitkonstanten ermittelt.

Auch für die *cis*- nach *trans*-Isomerisierung der Azobenzole des Foldamers wurde ein leicht verlängerter Isomerisierungsprozess detektiert. Während dieser Prozess nach bereits 20 ps abgeschlossen ist, wird mit einer Zeitkonstanten von 198 ps auch hier eine frühe Konformationsänderung beobachtet. Durch die längere Kette des Foldamers kommt es erst spät zu einer Planarisierung der Phenylringe des Azobenzols, wodurch erst mit dieser Zeit die charakteristische $\pi\pi^*$-Bande des *trans*-Isomers entsteht.

Zudem wurde in dieser Arbeit ein Anregungsenergietransfer von dem PE-Rückgrat auf die, sich im Rückgrat befindenden, Azobenzole beobachtet. Während die Anregung des reinen **3P2E** zu einem langlebigen S_1-Zustand sowie zu der photoinduzierten Bildung eines Übergangszustands führt, wird die Lebensdauer des angeregten Zustands durch Einführung von Azobenzolen drastisch verkürzt. Unabhängig vom Azobenzol-Isomer findet nach Anregung des Rückgrats eine nahezu instantan beginnende Photoisomerisierung statt, sodass die Azobenzole als Akzeptor des Anregungsenergietransfers wirken.

Zusammenfassend wurde in dieser Arbeit eine detaillierte Charakterisierung einer großen Anzahl an Azobenzol-Photoschaltern mit einer Vielzahl an (zeitaufgelösten) spektroskopischen Methoden durchgeführt. So wurde der Einfluss der Hydroxygruppe als Substituent des Photoschalters auf das Isomerisierungsverhalten des Azobenzols untersucht. Zudem wurden in Kooperation mit der Arbeitsgruppe von Prof. Heckel Azobenzolderivate entsprechend ihrer (photo-)chemischen Eigenschaften für biologische Anwendungen, wie die Entwicklung eines photoschaltbaren Riboschalters, optimiert. In Kooperation mit der Arbeitsgruppe von. Prof. Süß wurden RNA Aptamere durch systematische Suche (SELEX) entwickelt, welche spezifisch und mit hoher Affinität das *trans*-Isomer der Azobenzol-Liganden binden. Der Einfluss der Photoisomerisierung auf die Konformation der RNA und die entsprechenden Dynamiken wurde mittels verschiedener spektroskopischer Techniken untersucht. Hierbei stellte sich jedoch heraus, dass die gefundenen Aptamere noch nicht geeignet sind, um als photoaktivierbarer Riboschalter zu dienen. Des Weiteren wurde die frühe lichtinduzierte Konformationsänderung des wichtigen Modellsystems, des Foldamers $\mathbf{10_5}$, im Zeitbereich von sub-Nanosekunden ermittelt und mittels quantenmechanischer Rechnung unterstützt. Darüber hinaus, konnte der Anregungsenergietransfer vom Foldamerrückgrat auf die, sich im Rückgrat befindenden, Azobenzole bestimmt werden.

Diese erhaltenen Ergebnisse ermöglichen ein besseres Verständnis sowie eine verbesserte Entwicklung neuer Materialien für z.B. die biologische Kontrolle der Genexpression oder der Speicherung oder Weiterleitung von Energie in neuen photoaktivierbaren Materialien.

Bibliography

[1] C. Housecroft, A. G. Sharpe, *Anorganische Chemie*, Pearson Studium - Chemie, **2006**.

[2] G. L. Miessler, P. J. Fischer, D. A. Tarr, *Inorganic Chemistry*, Pearson, **2013**.

[3] O. Laporte, W. F. Meggers, *J. Opt. Soc. Am.* **1925**, *11*, 459–463.

[4] P. W. Atkins, R. S. Friedman, *Molecular Quantum Mechanics*, Oxford University Press, **2010**.

[5] W. Demtröder, *Laserspektroskopie: Grundlagen und Techniken*, Springer Berlin Heidelberg, **2007**.

[6] R. Winter, F. Noll, *Methoden der Biophysikalischen Chemie*, Springer Verlag, **2013**.

[7] Circular Dichroism (CD) Spectroscopy, `https://www.photophysics.com`.

[8] W. Hoppe, W. Lohmann, H. Markl, H. Ziegler, *Biophysik*, Springer Verlag, **2013**.

[9] P. W. Atkins, J. de Paula, *Physikalische Chemie*, Wiley-VCH Verlag, **2006**.

[10] W. Heisenberg, *Z. Phys.* **1927**, *3*, 172–198.

[11] H. M. Foley, *Phys. Rev.* **1946**, *69*, 616–628.

[12] C. Doppler in *Abhandlung der königl. böhm. Gesellschaft der Wissenschaften*, **1903**, pp. 465–482.

[13] B. H. Armstrong, *J. Quant. Spectrosc. Ra.* **1967**, *7*, 61–88.

[14] P. Hamm, S. M. Ohline, W. Zinth, *J. Chem. Phys.* **1997**, *106*, 519–529.

[15] P. Hamm, M. Zurek, T. Röschinger, H. Patzelt, D. Oesterhelt, W. Zinth, *Chem. Phys. Lett.* **1997**, *268*, 180–186.

[16] M. Kasha, *Discuss. Faraday Soc.* **1950**, 14–19.

[17] C. Morgante, W. Struve, *Chem. Phys. Lett.* **1979**, *68*, 267–271.

[18] T. Fujino, S. Y. Arzhantsev, T. Tahara, *J. Phys. Chem. A* **2001**, *105*, 8123–8129.

[19] P. Klán, J. Wirz, *Photochemistry of Organic Compounds: From Concepts to Practice*, Wiley-Blackwell, **2009**.

[20] J. R. Lakowicz, *Topics in Fluorescence Spectroscopy Volume 1*, Kluwer Academic Publisher, **1999**.

[21] R. Berera, R. van Grondelle, J. T. M. Kennis, *Photosynth. Res.* **2009**, *101*, 105–118.

[22] P. M. W. French, *Rep. Prog. Phys.* **1995**, *58*, 169–262.

[23] P. Maine, D. Strickland, P. Bado, M. Pessot, G. Mourou, *IEEE J. Quantum. Electron.* **1988**, *24*, 398–403.

[24] Y. R. Shen, *Principles of Nonlinear Optics*, Wiley-VCH Verlag, **1984**.

[25] R. W. Boyd, *Nonlinear Optics*, Academic Press, **2003**.

[26] V. G. Dmitriev, G. G. Gurzadyan, D. N. Nikogosyan, *Handbook of Nonlinear Optical Crystals*, Springer Verlag, **2013**.

[27] D. N. Nikogosyan, *Appl. Phys. A* **1991**, *52*, 359–368.

[28] S. Uhlig, *Self-Organized Surface Structures with Ultrafast White-Light*, Springer Verlag, **2015**.

[29] M. K. Reed, M. K. Steinershepard, M. S. Armas, D. K. Negus, *J. Opt. Soc. Am. B* **1995**, *12*, 2229–2236.

[30] R. Huber, H. Satzger, W. Zinth, J. Wachtveitl, *Opt. Commun.* **2001**, *194*, 443–448.

[31] J. Kohl-Landgraf, J.-E. Nimsch, J. Wachtveitl, *Opt. Express* **2013**, *21*, 17060–17065.

[32] I. H. M. van Stokkum, D. S. Larsen, R. van Grondelle, *Biochim. Biophys. Acta* **2004**, *1657*, 82–104.

[33] P. Hamm, *Chem. Phys.* **1995**, *200*, 415–429.

[34] S. A. Kovalenko, A. L. Dobryakov, J. Ruthmann, N. P. Ernsting, *Phys. Rev. A* **1999**, *59*, 2369–2384.

[35] W. J. Hehre, R. F. Stewart, J. A. Pople, *J. Chem. Phys.* **1969**, *51*, 2657–2664.

[36] R. Ditchfield, W. J. Hehre, J. A. Pople, *J. Chem. Phys.* **1971**, *54*, 724–728.

[37] T. H. J. Dunning, *J. Chem. Phys.* **1989**, *90*, 1007–1023.

[38] A. Szabo, N. S. Ostlund, *Modern Quantum Chemistry: Introduction to Advanced Electronic Structure Theory*, Dover Publications Inc., Mineola, New York, **1996**.

[39] W. Kutzelnigg, *Einführung in die Theoretische Chemie, Band 1: Quantenmechanische Grundlagen*, Verlag Chemie, GmbH, Weinheim, **1975**.

[40] R. G. Parr, W. Yang, *Density-functional theory of atoms and molecules*, Oxford University Press, **1989**.

[41] P. Hohenberg, W. Kohn, *Phys. Rev.* **1964**, B864–B871.

[42] W. Kohn, L. J. Sham, *Phys. Rev.* **1965**, *140*, A1133–A1138.

[43] J. C. Slater, *Quantum Theory of Molecular and Solids, Vol. 4: The Self-Consistent Field for Molecular and Solids*, McGraw-Hill, New York, **1974**.

[44] J. P. Perdew, K. Burke, M. Ernzerhof, *Phys. Rev. Lett.* **1996**, *77*, 3865–3868.

[45] J. P. Perdew, K. Burke, M. Ernzerhof, *Phys. Rev. Lett.* **1997**, *78*, 1396–1396.

[46] A. D. Becke, *Phys. Rev. A* **1988**, *38*, 3096–3100.

[47] A. D. Becke, *J. Chem. Phys.* **1993**, *98*, 5648–5652.

[48] C. Lee, W. Yang, R. Parr, *Phys. Rev.* **1988**, *37*, 785–789.

[49] J. P. Perdew in *Electronic Structure of Solids '91*, (Eds.: P. Ziesche, H. Eschrig), Akademie Verlag, Berlin, **1991**.

[50] S. H. Vosko, L. Wilk, M. Nusair, *Can. J. Phys.* **1980**, *58*, 1200–1211.

[51] A. D. Becke, *J. Chem. Phys.* **1993**, *98*, 1372–1377.

[52] M. D. Hanwell, D. E. Curtis, D. C. Lonie, T. Vandermeersch, E. Zurek, G. R. Hutchison, *J. Cheminform.* **2012**, *4*, 1–17.

[53] A. K. Rappé, C. J. Casewit, K. S. Colwell, W. A. Goddard III, W. M. Skiff, *J. Am. Chem. Soc.* **1992**, *114*, 10024–10035.

[54] N. S. R. Database, Precomputed vibrational scaling factors, `http://cccbdb.nist.gov/vibscalejust.asp`, Release 17b, September, 2015.

[55] S. Miertus, E. Scroco, J. Tomasi, *J. Chem. Phys.* **1981**, *55*, 117–129.

[56] B. L. Feringa, W. R. Browne, *Molecular Switches*, Wiley-VCH Verlag, **2011**.

[57] H. Bouas-Laurent, H. Dürr, *Pure and Applied Chemistry* **2001**, *73*, 639–665.

[58] H. Rau in *Photochromism: molecules and systems*, (Eds.: H. Dürr, H. Bouas-Laurent), Gulf Professional Publishing, **2003**, Chapter 4, pp. 165–192.

[59] J. Saltiel, Y.-P. Sun in *Photochromism: molecules and systems*, (Eds.: H. Dürr, H. Bouas-Laurent), Gulf Professional Publishing, **2003**, Chapter 3, pp. 64–162.

[60] C. Slavov, N. Bellakbil, J. Wahl, K. Mayer, K. Rück-Braun, I. Burghardt, J. Wachtveitl, M. Braun, *Phys. Chem. Chem. Phys.* **2015**, *17*, 14045–14053.

[61] S. Malkmus, F. O. Koller, B. Heinz, W. J. Schreier, T. E. Schrader, W. Zinth, C. Schulz, S. Dietrich, K. Rück-Braun, M. Braun, *Chem. Phys. Lett.* **2006**, *417*, 266–271.

[62] J. Ern, A. Bens, A. Bock, H.-D. Martin, C. Kryschi, *J. Lumin.* **1998**, *76*, 90–94.

[63] S. Shim, T. Joo, S. C. Bae, K. S. Kim, E. Kim, *J. Phys. Chem. A* **2003**, *107*, 8106–8110.

[64] C. Beyer, H.-A. Wagenknecht, *J. Org. Chem.* **2010**, *75*, 2753–2755.

[65] B. Seefeldt, R. Kasper, M. Beining, J. Mattay, J. Arden-Jacob, N. Kemnitzer, K. H. Drexhage, M. Heilemann, M. Sauer, *Photochem. Photobiol. Sci.* **2010**, *9*, 213–220.

[66] J. Kohl-Landgraf, M. Braun, C. Özçoban, D. P. N. Gonçalves, A. Heckel, J. Wachtveitl, *J. Am. Chem. Soc.* **2012**, *134*, 14070–14077.

[67] M. Hammarson, J. R. Nilsson, S. Li, T. Beke-Somfai, J. Andréasson, *J. Phys. Chem. B* **2013**, *117*, 13561–13571.

[68] C. Özçoban, T. Halbritter, S. Steinwand, L.-M. Herzig, J. Kohl-Landgraf, N. Askari, F. Groher, B. Fürtig, C. Richter, H. Schwalbe, B. Suess, J. Wachtveitl, A. Heckel, *Org. Lett.* **2015**, *17*, 1517–1520.

[69] K. Matczyszyn, J. Olesiak-Banska, K. Nakatani, P. Yu, N. A. Murugan, R. Zaleśny, A. Roztoczyńska, J. Bednarska, W. Bartkowiak, J. Kongsted, H. Ågren, M. Samoć, *J. Phys. Chem. B* **2015**, *119*, 1515–1522.

[70] A. M. Kolpak, J. C. Grossman, *Nano Lett.* **2011**, *11*, 3156–3162.

[71] A. Lennartson, A. Roffey, K. Moth-Poulsen, *Tetrahedron Lett.* **2015**, *56*, 1457–1465.

[72] D. L. Fortin, M. R. Banghart, T. W. Dunn, K. Borges, D. A. Wagenaar, Q. Gaudry, M. H. Karakossian, T. S. Otis, W. B. Kristan, D. Trauner, R. H. Kramer, *Nat. Methods* **2008**, *5*, 331–338.

[73] M. R. Banghart, A. Mourot, D. L. Fortin, J. Z. Yao, R. H. Kramer, D. Trauner, *Angew. Chem. Int. Ed.* **2009**, *48*, 9097–9101.

[74] F. Schweighöfer, L. Dworak, M. Braun, M. Zastrow, J. Wahl, I. Burghardt, K. Rück-Braun, J. Wachtveitl, *Sci. Rep.* **2015**, *5*, 1–5.

[75] L. Dworak, A. J. Reuss, M. Zastrow, K. Rück-Braun, J. Wachtveitl, *Nanoscale* **2014**, *6*, 14200–14203.

[76] G. Hartley, *Nature* **1937**, *140*, 281.

[77] G. S. Kumar, D. C. Neckers, *Chem. Rev.* **1989**, *89*, 1915–1925.

[78] J. Dokić, M. Gothe, J. Wirth, M. V. Peters, J. Schwarz, S. Hecht, P. Saalfrank, *J. Phys. Chem. A* **2009**, *113*, 6763–6773.

[79] S. Monti, G. Orlandi, P. Palmeri, *Chem. Phys.* **1982**, *71*, 87–99.

[80] J. Griffiths, *Chem. Soc. Rev.* **1972**, *1*, 481–493.

[81] I. Conti, F. Marchioni, A. Credi, G. Orlandi, G. Rosini, M. Garavelli, *J. Am. Chem. Soc.* **2007**, *129*, 3198–3210.

[82] P. Bortolus, S. Monti, *J. Phys Chem.* **1979**, *83*, 648–652.

[83] A. F. Holleman, E. Wiberg, N. Wiberg, *Lehrbuch der Anorganischen Chemie*, de Gruyter, Berlin, **1995**.

[84] H. Rau, *J. Photochem.* **1984**, *26*, 221–225.

[85] Y. Norikane, N. Tamaoki, *European J. Org. Chem.* **2006**, *2006*, 1296–1302.

[86] Y.-C. Lu, E. W.-G. Diau, H. Rau, *J. Phys. Chem. A* **2005**, *109*, 2090–2099.

[87] I. Piyanzina, B. Minisini, D. Tayurskii, J.-F. Bardeau, *J. Mol. Model.* **2015**, *21*, 1–5.

[88] T. Sueyoshi, N. Nishimura, S. Yamamoto, S. Hasegawa, *Chem. Lett.* **1974**, *3*, 1131–1134.

[89] C. R. Crecca, A. E. Roitberg, *J. Phys. Chem. A* **2006**, *110*, 8188–8203.

[90] W. Fuß, C. Kosmidis, W. E. Schmid, S. A. Trushin, *Angew. Chem. Int. Ed.* **2004**, *43*, 4178–4182.

[91] N. Biswas, S. Umapathy, *J. Chem. Phys.* **1997**, *107*, 7849–7858.

[92] I. K. Lednev, T.-Q. Ye, R. E. Hester, J. N. Moore, *J. Phys. Chem.* **1996**, *100*, 13338–13341.

[93] T. Nägele, R. Hoche, W. Zinth, J. Wachtveitl, *Chem. Phys. Lett.* **1997**, *272*, 489–495.

[94] E. W.-G. Diau, *J. Phys. Chem. A* **2004**, *108*, 950–956.

[95] T. Ishikawa, T. Noro, T. Shoda, *J. Chem. Phys.* **2001**, *115*, 7503–7512.

[96] I. Conti, M. Garavelli, G. Orlandi, *J. Am. Chem. Soc.* **2008**, *130*, 5216–5230.

[97] M. Böckmann, N. L. Doltsinis, D. Marx, *J. Phys. Chem. A* **2010**, *114*, 745–754.

[98] M. Quick, A. L. Dobryakov, M. Gerecke, C. Richter, F. Berndt, I. N. Ioffe, A. A. Granovsky, R. Mahrwald, N. P. Ernsting, S. A. Kovalenko, *J. Phys. Chem. B* **2014**, *118*, 8756–8771.

[99] T. Schultz, J. Quenneville, B. Levine, A. Toniolo, T. J. Martínez, S. Lochbrunner, M. Schmitt, J. P. Shaffer, M. Z. Zgierski, A. Stolow, *J. Am. Chem. Soc.* **2003**, *125*, 8098–8099.

[100] S. Monti, E. Gardini, P. Bortolus, *Chem. Phys. Lett.* **1981**, *77*, 115–119.

[101] S. Monti, S. Dellonte, P. Bortolus, *J. Photochem.* **1983**, *23*, 249–256.

[102] A. Cembran, F. Bernardi, M. Garavelli, L. Gagliardi, G. Orlandi, *J. Am. Chem. Soc.* **2004**, *126*, 3234–3243.

[103] J. Wachtveitl, S. Spörlein, H. Satzger, B. Fonrobert, C. Renner, R. Behrendt, D. Oesterhelt, L. Moroder, W. Zinth, *Biophys. J.* **2004**, *86*, 2350–2362.

[104] R. Siewertsen, J. B. Schönborn, B. Hartke, F. Renth, F. Temps, *Phys. Chem. Chem. Phys.* **2011**, *13*, 1054–1063.

[105] G. Floß, P. Saalfrank, *J. Phys. Chem. A* **2015**, *119*, 5026–5037.

[106] C. Slavov, C. Yang, L. Schweighauser, C. Boumrifak, A. Dreuw, H. A. Wegner, J. Wachtveitl, *Phys. Chem. Chem. Phys.* **2016**, *18*, 14795–14804.

[107] J. C. Corchado, M. L. Sánchez, F. I. Galván, M. E. Martin, A. Munoz-Losa, R. Barata-Morgado, M. A. Aguilar, *J. Phys. Chem. B* **2014**, *118*, 12518–12530.

[108] H. M. D. Bandara, S. C. Burdette, *Chem. Soc. Rev.* **2012**, *41*, 1809–1825.

[109] I. Lednev, *Chem. Phys. Lett.* **1998**, *290*, 68–74.

[110] T. Fujino, T. Tahara, *J. Phys. Chem. A* **2000**, *104*, 4203–4210.

[111] H. Satzger, C. Root, M. Braun, *J. Phys. Chem. A* **2004**, *108*, 6265–6271.

[112] Y. Ootani, K. Satoh, A. Nakayama, T. Noro, T. Taketsugu, *J. Chem. Phys.* **2009**, *131*, 194306–1–194306–10.

[113] T. Schultz, S. Ullrich, J. Quenneville, T. J. Martinez, M. Z. Zgierski, A. Stolow in *Femtochemistry and Femtobiology*, (Eds.: M. M. Martin, J. T. Hynes), Elsevier B.V., **2004**, pp. 45–48.

[114] N. Nishimura, T. Sueyoshi, H. Yamanaka, E. Imai, S. Yamamoto, S. Hasegawa, *Bull. Chem. Soc. Jpn.* **1976**, *49*, 1381–1387.

[115] S. Yamamoto, N. Nishimura, S. Hasegawa, *Bull. Chem. Soc. Jpn.* **1971**, *44*, 2018–2025.

[116] T. Asano, T. Okada, *J. Org. Chem.* **1984**, *49*, 4387–4391.

[117] G. Angelini, N. Canilho, M. Kingsley, C. Gasbarri, *J. Org. Chem.* **2015**, *80*, 7430–7434.

[118] P. Hammett, *J. Am. Chem. Soc.* **1937**, *59*, 96–103.

[119] M. R. Han, Y. Hirayama, M. Hara, *Chem. Mater.* **2006**, *18*, 2784–2786.

[120] D. G. Whitten, P. D. Wildes, J. G. Pacifici, G. Irick Jr., *J. Am. Chem. Soc.* **1971**, *93*, 2004–2008.

[121] C. Knie, M. Utecht, F. Zhao, H. Kulla, S. Kovalenko, A. M. Brouwer, P. Saalfrank, S. Hecht, D. Bléger, *Chem. Eur. J.* **2014**, *20*, 16492–16501.

[122] T. Halicioğlu, O. Sinanoğlu, *Ann. N. Y. Acad. Sci.* **1969**, *158*, 308–317.

[123] G. M. Wyman, *Chem. Rev.* **1955**, *55*, 625–657.

[124] U.-J. Paik, G. Zimmerman, L.-Y. Chow, *J. Am. Chem. Soc.* **1958**, *80*, 3528–3531.

[125] G. Hartley, *J. Chem. Soc.* **1938**, 633–642.

[126] N. Böhm, A. Materny, W. Kiefer, H. Steins, M. M. Müller, G. Schottner, *Macromolecules* **1996**, *29*, 2599–2604.

[127] M. Ueda, H. B. Kim, T. Ikeda, K. Ichimura, *Chem. Mater.* **1992**, *4*, 1229–1233.

[128] R. Kohlrausch, *Ann. Phys. (Leipzig)* **1947**, *12*, 393.

[129] G. Williams, D. C. Watts, *Trans. Faraday Soc.* **1970**, *66*, 80–85.

[130] K. Janus, J. Sworakowski, E. Luboch, *Chem. Phys.* **2002**, *285*, 47–54.

[131] J. Sworakowski, K. Matczyszyn, *Acta Phys. Pol. A* **2007**, *112*, S153–S159.

[132] B. Kumar, K. A. Suresh, *Phys. Rev. E* **2009**, *80*, 021601–1–021601–5.

[133] Y. Zhao, T. Ikeda, *Smart Light-Responsive Materials: Azobenzene-Containing Polymers and Liquid Crystals*, John Wiley & Sons, Inc., **2009**, pp. 1–514.

[134] H. Eyring, *Chem. Rev.* **1935**, *17*, 65–77.

[135] A. A. Beharry, G. A. Woolley, *Chem. Soc. Rev.* **2011**, *40*, 4422–4437.

[136] C. Brieke, F. Rohrbach, A. Gottschalk, G. Mayer, A. Heckel, *Angew. Chem. Int. Ed.* **2012**, *51*, 8446–8476.

[137] W. Szymanski, J. M. Beierle, H. A. V. Kistemaker, W. A. Velema, B. L. Feringa, *Chem. Rev.* **2013**, *113*, 6114–6178.

[138] J. García-Amorós, A. Piñol, H. Finkelmann, D. Velasco, *Org. Lett.* **2011**, *13*, 2282–2285.

[139] K. Röttger, S. Wang, F. Renth, J. Bahrenburg, F. Temps, *Appl. Phys. B* **2014**, *118*, 185–193.

[140] J. Bahrenburg, F. Renth, F. Temps, F. Plamper, W. Richtering, *Phys. Chem. Chem. Phys.* **2014**, *16*, 11549–11554.

[141] S. K. Yesodha, C. K. S. Pillai, N. Tsutsumi, *Prog. Polym. Sci.* **2004**, *29*, 45–74.

[142] F. Zhao, C. Wang, Y. Zeng, Z. Jin, G. Ma, *Chem. Phys. Lett.* **2013**, *558*, 100–103.

[143] T. Jaunet-lahary, A. Chantzis, K. J. Chen, D. Laurent, D. Jacquemin, *J. Phys. Chem. C* **2014**, *118*, 28831–28841.

[144] J. M. Abendroth, O. S. Bushuyev, P. S. Weiss, C. J. Barrett, *ACS Nano* **2015**, *9*, 7746–7768.

[145] M. Yamada, M. Kondo, R. Miyasato, Y. Naka, J.-I. Mamiya, M. Kinoshita, A. Shishido, Y. Yu, C. J. Barrett, T. Ikeda, *J. Mater. Chem.* **2009**, *19*, 60–62.

[146] T. Ube, K. Takado, T. Ikeda, *J. Mater. Chem. C* **2015**, *3*, 8006–8009.

[147] V. Marturano, P. Cerruti, C. Carfagna, M. Giamberini, B. Tylkowski, V. Ambrogi, *Polymer (Guildf).* **2015**, *70*, 222–230.

[148] F. Tanaka, T. Mochizuki, X. Liang, H. Asanuma, S. Tanaka, K. Suzuki, S. I. Kitamura, A. Nishikawa, K. Ui-Tei, M. Hagiya, *Nano Lett.* **2010**, *10*, 3560–3565.

[149] D. Bléger, S. Hecht, *Angew. Chem. Int. Ed.* **2015**, 11338–11349.

[150] C. Renner, L. Moroder, *Chembiochem* **2006**, *7*, 868–878.

[151] J. A. Ihalainen, J. Bredenbeck, R. Pfister, J. Helbing, L. Chi, I. H. M. van Stokkum, G. A. Woolley, P. Hamm, *Proc. Natl. Acad. Sci. U. S. A.* **2007**, *104*, 5383–5388.

[152] P. Hamm, J. Helbing, J. Bredenbeck, *Annu. Rev. Phys. Chem.* **2008**, *59*, 291–317.

[153] U. Kusebauch, S. A. Cadamuro, H.-J. Musiol, M. O. Lenz, J. Wachtveitl, L. Moroder, C. Renner, *Angew. Chem. Int. Ed.* **2006**, *45*, 7015–7018.

[154] L. Lorenz, U. Kusebauch, L. Moroder, J. Wachtveitl, *ChemPhysChem* **2016**, *17*, 1314–1320.

[155] F. Zhang, K. A. Timm, K. M. Arndt, G. A. Woolley, *Angew. Chem. Int. Ed.* **2010**, *49*, 3943–3946.

[156] A. Yamazawa, X. Liang, H. Asanuma, M. Komiyama, *Angew. Chem. Int. Ed.* **2000**, *39*, 2356–2357.

[157] M. Zhou, X. Liang, T. Mochizuki, H. Asanuma, *Angew. Chem. Int. Ed.* **2010**, *122*, 2213–2216.

[158] X. Liang, R. Wakuda, K. Fujioka, H. Asanuma, *FEBS J.* **2010**, *277*, 1551–1561.

[159] T. Goldau, K. Murayama, C. Brieke, H. Asanuma, A. Heckel, *Chem. Eur. J.* **2015**, *21*, 17870–17876.

[160] J. Thevarpadam, I. Bessi, O. Binas, D. P. N. Gonçalves, C. Slavov, H. R. A. Jonker, C. Richter, J. Wachtveitl, H. Schwalbe, A. Heckel, *Angew. Chem. Int. Ed.* **2016**, *55*, 2738–2742.

[161] T. Goldau, K. Murayama, C. Brieke, S. Steinwand, P. Mondal, M. Biswas, I. Burghardt, J. Wachtveitl, H. Asanuma, A. Heckel, *Chem. Eur. J.* **2015**, *21*, 2845–2854.

[162] P. Mondal, M. Biswas, T. Goldau, A. Heckel, I. Burghardt, *J. Phys. Chem. B* **2015**, *119*, 11275–11286.

[163] P. Hamm, R. A. Kaindl, J. Stenger, *Opt. Lett.* **2000**, *25*, 1798–1800.

[164] J. Broichhagen, J. A. Frank, D. Trauner, *Acc. Chem. Res.* **2015**, *48*, 1947–1960.

[165] M. A. Kienzler, A. Reiner, E. Trautman, S. Yoo, D. Trauner, E. Y. Isacoff, *J. Am. Chem. Soc.* **2013**, *135*, 17683–17686.

[166] A. Rullo, A. Reiner, A. Reiter, D. Trauner, E. Y. Isacoff, G. A. Woolley, *Chem. Commun. (Camb).* **2014**, *50*, 14613–14615.

[167] E. C. Carroll, S. Berlin, J. Levitz, M. A. Kienzler, Z. Yuan, D. Madsen, D. S. Larsen, E. Y. Isacoff, *P. Natl. A. Sci.* **2015**, *112*, E776–E785.

[168] L. S. Runtsch, D. M. Barber, P. Mayer, M. Groll, D. Trauner, J. Broichhagen, *Beilstein J. Org. Chem.* **2015**, *11*, 1129–1135.

[169] J. Wachtveitl, A. Zumbusch, *Chembiochem* **2011**, *12*, 1169–1170.

[170] M. Dong, A. Babalhavaeji, S. Samanta, A. A. Beharry, G. A. Woolley, *Acc. Chem. Res.* **2015**, *48*, 2662–2670.

[171] W. J. Schreier, T. Aumüller, K. Haiser, F. O. Koller, M. Löweneck, H.-J. Musiol, T. E. Schrader, T. Kiefhaber, L. Moroder, W. Zinth, *Biopolymers* **2013**, *100*, 38–50.

[172] R. Ochi, N. Perur, K. Yoshida, N. Tamaoki, *Tetrahedron* **2015**, *71*, 3500–3506.

[173] B. Ellis, P. J. F. Griffiths, *Spectrochim. Acta* **1965**, *21*, 1881–1892.

[174] P. Grünanger, P. Vita-Finzi in *Chem. Heterocycl. Compd.* John Wiley & Sons, Inc., **1991**, pp. 1–416.

[175] F. Halverson, R. C. Hirt, *J. Chem. Phys.* **1951**, *19*, 711–718.

[176] S. Steinwand, T. Halbritter, D. Rastädter, J. M. Ortiz-Sánchez, I. Burghardt, A. Heckel, J. Wachtveitl, *Chem. Eur. J.* **2015**, *21*, 15720–15731.

[177] J. García-Amorós, A. Sánchez-Ferrer, W. A. Massad, S. Nonell, D. Velasco, *Phys. Chem. Chem. Phys.* **2010**, *12*, 13238–13242.

[178] J. García-Amorós, M. Díaz-Lobo, S. Nonell, D. Velasco, *Angew. Chem. Int. Ed.* **2012**, *51*, 12820–12823.

[179] N. J. Dunn, W. H. Humphries, A. R. Offenbacher, T. L. King, J. A. Gray, *J. Phys. Chem. A* **2009**, *113*, 13144–13151.

[180] M. Kojima, S. Nebashi, K. Ogawa, N. Kurita, *J. Phys. Org. Chem.* **2005**, *18*, 994–1000.

[181] M. J. Frisch, G. W. Trucks, H. B. Schlegel, G. E. Scuseria, M. A. Robb, J. R. Cheeseman, G. Scalmani, V. Barone, B. Mennucci, G. A. Petersson, H. Nakatsuji, M. Caricato, X. Li, H. P. Hratchian, A. F. Izmaylov, J. Bloino, G. Zheng, J. L. Sonnenberg, M. Hada, M. Ehara, K. Toyota, R. Fukuda, J. Hasegawa, M. Ishida, T. Nakajima, Y. Honda, O. Kitao, H. Nakai, T. Vreven, J. Montgomery, J. A., J. E. Peralta, F. Ogliaro, M. Bearpark, J. J. Heyd, E. Brothers, K. N. Kudin, V. N. Staroverov, R. Kobayashi, J. Normand, K. Raghavachari, A. Rendell, J. C. Burant, S. S. Iyengar, J. Tomasi, M. Cossi, N. Rega, M. J. Millam, M. Klene, J. E. Knox, J. B. Cross, V. Bakken, C. Adamo, J. Jaramillo, R. Gomperts, R. E. Stratmann, O. Yazyev, A. J. Austin, R. Cammi, C. Pomelli, J. W. Ochterski, R. L. Martin, K. Morokuma, V. G. Zakrzewski, G. A. Voth, P. Salvador, J. J. Dannenberg, S. Dapprich, A. D. Daniels, Ö. Farkas, J. B. Foresman, J. V. Ortiz, J. Cioslowski, D. J. Fox, Gaussian 09, Revision D.01, **2009**.

[182] T. R. Cech, J. A. Steitz, *Cell* **2014**, *157*, 77–94.

[183] J. Fohrer, M. Henning, T. Carlomagno, *J. Mol. Biol.* **2006**, *356*, 280–287.

[184] S. E. Butcher, A. M. Pyle, *Acc. Chem. Res.* **2011**, *44*, 1302–1311.

[185] T. Hermann, D. J. Patel, *Science* **2000**, *287*, 820–825.

[186] R. Stoltenburg, C. Reinemann, B. Strehlitz, *Biomol. Eng.* **2007**, *24*, 381–403.

[187] R. D. Jenison, S. C. Gill, A. Pardi, B. Polisky, *Science* **1994**, *263*, 1425–1429.

[188] A. Geiger, P. Burgstaller, H. von der Eltz, A. Roeder, M. Famulok, *Nucleic Acids Res.* **1996**, *24*, 1029–1036.

[189] R. R. Breaker, Riboswitches and the RNA World. Cold Spring Harb Perspect Biol 4: a003566, **2012**.

[190] D. D. Young, A. Deiters, *Chembiochem* **2008**, *9*, 1225–1228.

[191] G. Hayashi, M. Hagihara, K. Nakatani, *Chem. Eur. J.* **2009**, *15*, 424–432.

[192] H. Asanuma, X. Liang, H. Nishioka, D. Matsunaga, M. Liu, M. Komiyama, *Nat. Protoc.* **2007**, *2*, 203–212.

[193] J. A. Phillips, H. Liu, M. B. O'Donoghue, X. Xiong, R. Wang, M. You, K. Sefah, W. Tan, *Bioconjug. Chem.* **2011**, *22*, 282–288.

[194] C. Berens, A. Thain, R. Schroeder, *Bioorg. Med. Chem.* **2001**, *9*, 2549–2556.

[195] J. Weigand, S. R. Schmidtke, T. J. Will, E. Duchardt-Ferner, C. Hammann, J. Wohnert, B. Suess, *Nucleic Acids Res.* **2011**, *39*, 3363–3372.

[196] D. H. Burke, D. C. Hoffman, A. Brown, M. Hansen, A. Pardi, L. Gold, *Chem. Biol.* **1997**, *4*, 833–843.

[197] C. Tuerk, L. Gold, *Science* **1990**, *249*, 505–510.

[198] S. D. Mendonsa, M. T. Bowser, *J. Am. Chem. Soc.* **2004**, *126*, 20–21.

[199] M. Zuker, A. B. Jacobson, *RNA* **1998**, *4*, 669–679.

[200] R. Lorenz, S. H. Bernhart, C. H. Zu Siederdissen, H. Tafer, C. Flamm, P. F. Stadler, I. L. Hofacker, *Algorithm Mol. Biol.* **2011**, *6*, 1–14.

[201] O. C. Uhlenbeck, P. N. Borer, B. Dengler, I. Tinoco, *J. Mol. Biol.* **1973**, *73*, 483–496.

[202] D. J. Williams, K. B. Hall, *Biochemistry* **1996**, *35*, 14665–14670.

[203] E. B. Brauns, R. B. Dyer, *Biophys. J.* **2005**, *89*, 3523–3530.

[204] E. E. Regulski, R. R. Breaker in *Post-Transcriptional Gene Regulation*, (Ed.: J. Wilusz), Humana Press, Totowa, NJ, **2008**, pp. 53–67.

[205] B. Suess, S. Hanson, C. Berens, B. Fink, R. Schroeder, W. Hillen, *Nucleic Acids Res.* **2003**, *31*, 1853–1858.

[206] D. H. Appella, L. A. Christianson, I. L. Karle, D. R. Powell, S. H. Gellman, *J. Am. Chem. Soc.* **1996**, *118*, 13071–13072.

[207] D. J. Hill, M. J. Mio, R. B. Prince, T. S. Hughes, J. S. Moore, *Chem. Rev.* **2001**, *101*, 3893–4012.

[208] S. Hecht, I. Huc, *Foldamers: Structure, Properties, and Applications*, Wiley-VCH Verlag, **2007**.

[209] G. Guichard, I. Huc, *Chem. Commun.* **2011**, *47*, 5933–5941.

[210] D. H. Appella, L. A. Christianson, D. A. Klein, D. R. Powell, X. Huang, J. J. Barchi Jr., S. H. Gellman, *Nature* **1997**, *387*, 381–384.

[211] B. R. Huck, J. D. Fisk, I. A. Guzei, H. A. Carlson, S. H. Gellman, *J. Am. Chem. Soc.* **2003**, *125*, 9035–9037.

[212] C. Bao, B. Kauffmann, Q. Gan, K. Srinivas, H. Jiang, I. Huc, *Angew. Chem. Int. Ed.* **2008**, *47*, 4153–4156.

[213] N. Delsuc, T. Kawanami, J. Lefeuvre, A. Shundo, H. Ihara, M. Takafuji, I. Huc, *ChemPhysChem* **2008**, *9*, 1882–1890.

[214] L. Delaurière, Z. Dong, K. Laxmi-Reddy, F. Godde, J.-J. Toulmé, I. Huc, *Angew. Chem. Int. Ed.* **2012**, *51*, 473–477.

[215] T. Qi, V. Maurizot, H. Noguchi, T. Charoenraks, B. Kauffmann, M. Takafuji, H. Ihara, I. Huc, *Chem. Commun. (Camb).* **2012**, *48*, 48–51.

[216] W. S. Horne, S. H. Gellman, *Acc. Chem. Res.* **2008**, *41*, 1399–1408.

[217] V. Berl, I. Huc, R. G. Khoury, J. M. Lehn, *Chem. Eur. J.* **2001**, *7*, 2798–2809.

[218] J. L. Hou, X. B. Shao, G. J. Chen, Y. X. Zhou, X. K. Jiang, Z. T. Li, *J. Am. Chem. Soc.* **2004**, *126*, 12386–12394.

[219] M. Inouye, M. Waki, H. Abe, *J. Am. Chem. Soc.* **2004**, *126*, 2022–2027.

[220] D. J. Hill, J. S. Moore, *Proc. Natl. Acad. Sci. U. S. A.* **2002**, *99*, 5053–5057.

[221] W. Zhang, J. S. Moore, *Angew. Chem. Int. Ed.* **2006**, *45*, 4416–4439.

[222] J. M. Cary, J. S. Moore, *Org. Lett.* **2002**, *4*, 4663–4666.

[223] H. Goto, J. M. Heemstra, D. J. Hill, J. S. Moore, *Org. Lett.* **2004**, *6*, 889–892.

[224] T. Buffeteau, L. Ducasse, L. Poniman, N. Delsuc, I. Huc, *Chem. Commun. (Camb).* **2006**, 2714–2716.

[225] D. Miguel, S. P. Morcillo, A. Martín-Lasanta, N. Fuentes, L. Martínez-Fernández, I. Corral, M. J. Ruedas-Rama, D. J. Cárdenas, L. Álvarez de Cienfuegos, A. Orte, J. M. Cuerva, *Org. Lett.* **2015**, *17*, 2844–2847.

[226] A. M. Moore, B. A. Mantooth, Z. J. Donhauser, F. Maya, D. W. Price, Y. X. Yao, J. M. Tour, P. S. Weiss, *Nano Lett.* **2005**, *5*, 2292–2297.

[227] R. B. Prince, S. A. Barnes, J. S. Moore, *J. Am. Chem. Soc.* **2000**, *122*, 2758–2762.

[228] A. Tanatani, M. J. Mio, J. S. Moore, *J. Am. Chem. Soc.* **2001**, *123*, 1792–1793.

[229] J. Garric, J.-M. Léger, I. Huc, *Angew. Chem. Int. Ed.* **2005**, *44*, 1954–1958.

[230] Y. Ferrand, A. M. Kendhale, B. Kauffmann, A. Grélard, C. Marie, V. Blot, M. Pipelier, D. Dubreuil, I. Huc, *J. Am. Chem. Soc.* **2010**, *132*, 7858–7859.

[231] K. Maeda, M. Ishikawa, E. Yashima, *J. Am. Chem. Soc.* **2004**, *126*, 15161–15166.

[232] M. Ishikawa, K. Maeda, Y. Mitsutsuji, E. Yashima, *J. Am. Chem. Soc.* **2004**, *126*, 732–733.

[233] D. Bléger, Z. Yu, S. Hecht, *Chem. Commun.* **2011**, *47*, 12260–12266.

[234] R. B. Prince, J. G. Saven, P. G. Wolynes, J. S. Moore, *J. Am. Chem. Soc.* **1999**, *121*, 3114–3121.

[235] C. R. Ray, J. S. Moore, *Adv. Polym. Sci.* **2005**, *177*, 91–149.

[236] H. H. Nguyen, J. H. McAliley, W. R. Batson, D. A. Bruce, *Macromolecules* **2010**, *43*, 5932–5942.

[237] J. C. Nelson, *Science* **1997**, *277*, 1793–1796.

[238] M. T. Stone, J. M. Heemstra, J. S. Moore, *Acc. Chem. Res.* **2006**, *39*, 11–20.

[239] K. Ghosh, J. S. Moore, *J. Am. Chem. Soc.* **2011**, *133*, 19650–19652.

[240] R. B. Prince, L. Brunsveld, E. W. Meijer, J. S. Moore, *Angew. Chem. Int. Ed.* **2000**, *39*, 228–230.

[241] L. Brunsveld, E. W. Meijer, R. B. Prince, J. S. Moore, *J. Am. Chem. Soc.* **2001**, *123*, 7978–7984.

[242] K. Matsuda, M. T. Stone, J. S. Moore, *J. Am. Chem. Soc.* **2002**, *124*, 11836–11837.

[243] Z. Yu, S. Weidner, T. Risse, S. Hecht, *Chem. Sci.* **2013**, *4*, 4156–4167.

[244] M. Banno, T. Yamaguchi, K. Nagai, C. Kaiser, S. Hecht, E. Yashima, *J. Am. Chem. Soc.* **2012**, *134*, 8718–8728.

[245] Z. Yu, S. Hecht, *Chem. Commun.* **2016**, *52*, 6639–6653.

[246] A. Khan, S. Hecht, *Chem. Eur. J.* **2006**, *12*, 4764–4774.

[247] A. Khan, C. Kaiser, S. Hecht, *Angew. Chem. Int. Ed.* **2006**, *45*, 1878–1881.

[248] Z. Yu, S. Hecht, *J. Polym. Sci. Part A Polym. Chem.* **2015**, *53*, 313–318.

[249] Z. Yu, S. Hecht, *Angew. Chem. Int. Ed.* **2011**, *50*, 1640–1643.

[250] M. M. Green, M. P. Reidy, R. D. Johnson, G. Darling, D. J. O'Leary, G. Willson, *J. Am. Chem. Soc.* **1989**, *111*, 6452–6454.

[251] R. B. Prince, J. S. Moore, L. Brunsveld, E. W. Meijer, *Chem. Eur. J.* **2001**, *7*, 4150–4154.

[252] A. Cotton, *Compt. Rend* **1895**, *120*, 989–991.

[253] S. Steinwand, Z. Yu, S. Hecht, J. Wachtveitl, *J. Am. Chem. Soc.* **2016**, DOI 10.1021/jacs.6b07720.

[254] H. Satzger, S. Spörlein, C. Root, J. Wachtveitl, W. Zinth, P. Gilch, *Chem. Phys. Lett.* **2003**, *372*, 216–223.

[255] Z. Yu, S. Hecht, *Chem. Eur. J.* **2012**, *18*, 10519–10524.

[256] Z. Yu, S. Hecht, *Angew. Chem. Int. Ed.* **2013**, *52*, 13740–13744.

[257] G. Duvanel, J. Grilj, A. Schuwey, A. Gossauer, E. Vauthey, *Photochem. Photobiol. Sci.* **2007**, *6*, 956–963.

[258] R. Binder, J. Wahl, S. Römer, I. Burghardt, *Faraday Discuss.* **2013**, *163*, 205–222.

[259] J. Wahl, R. Binder, I. Burghardt, *Comp. Theor. Chem.* **2014**, *1040–1041*, 167–176.

[260] H. Asanuma, T. Takarada, T. Yoshida, D. Tamaru, X. Liang, M. Komiyama, *Angew. Chemie* **2001**, *113*, 2743–2745.

List of Figures

List of Tables

List of Abbreviations

AO	**A**tomic **O**rbital
AFM	**A**tomic **F**orce **M**icroscopy
BBO	Beta Barium Borate, $\beta - \mathbf{B}a\mathbf{B}_2\mathbf{O}_4$
$\mathbf{CaF_2}$	**Ca**lcium **F**luoride
CD	**C**ircular **D**ichroism
CE	**C**apillary **E**lectrophoresis
CI	**C**onical **I**ntersection
CPA	**C**hirped **P**ulse **A**mplification
CPL	**C**ircular **P**olarized **L**ight
DAS	**D**ecay **A**ssociated **S**pectra
DFT	**D**ensity **F**unctional **T**heory
DMARD	**D**isease-**M**odifying **A**nti**R**heumatic **D**rug (DMARD)
DMSO	**D**i**M**ethyl**S**ulf**O**xide
DNA	**D**esoxyribo**N**ucleic **A**cid
DTE	**D**i**T**hienyl**E**thenes
DTT	**D**i**T**hio**T**hreitol
EDTA	**E**thylene**D**iamine**T**etraacetic **A**cid
eIFs	**E**ukaryotic **I**nitiation **F**actor**s**
ESA	**E**xcited-**S**tate **A**bsorption
ESIPT	**E**xcited **S**tates **I**ntramolecular **P**roton **T**ransfer
EET	**E**xcitation **E**nergy **T**ransfer
FWHM	**F**ull **W**idth at **H**alf **M**aximum
GGA	**G**eneralized **G**radient **A**pproximation
GSB	**G**round-**S**tate **B**leach
GTO	**G**aussian-**T**ype **O**rbital
GVD	**G**roup **V**elocity **D**ispersion
HeLa	**He**nrietta **La**cks, cancer patient, †1951
HF	**H**artree **F**ock
HK	**H**ohenberg-**K**ohn
HOMO	**H**ighest **O**ccupied **M**olecular **O**rbital
IC	**I**nternal **C**onversion
IFs	**I**nitiation **F**actor**s**
IR	**I**nfra**R**ed
ISC	**I**nter**S**ystem **C**rossing
ITC	**I**sothermal **T**itration **C**alorimetry
IVR	**I**ntramolecular **V**ibrational **R**elaxation
KTP	**KT**iO**P**O_4, Potassium Titanyl Phosphate
LCAO	**L**inear **C**ombination of **A**tomic **O**rbitals
LDA	**L**ocal **D**ensity **A**pproximation
LUMO	**L**owest **U**noccupied **M**olecular **O**rbital

LYP	**L**ee, **Y**ang, **P**arr
MCT	**M**ercury **C**admium **T**elluride
MD	**M**olecular **D**ynamics
MO	**M**olecular **O**rbital
MPE	**M**ulti-**P**hoton **E**xcitation
mRNA	**M**essenger **R**ibo**N**ucleic **A**cid
NOPA	**N**on-colinear **O**ptical **P**arametric **A**mplifier
NHS	**N**-**H**ydroxy**S**uccinimidyl
NMR	**N**uclear **M**agnetic **R**esonance
O*m*PE	**O**ligo-***m****eta***-**P**henylene-**E**thynylene
OPA	**O**ptical **P**arametric **A**mplifier
PA	**P**roduct **A**bsorption
PBE	**P**erdew, **B**urke, **E**rnzerhof
PBS	**P**hosphate-**B**uffered **S**olution
PCM	**P**olarized **V**alence **D**ouble **Z**eta
PE	**P**henylene-**E**thynylene
PEG	**P**oly**E**thylene **G**lycol
PFID	**P**erturbed **F**ree **I**nduction **D**ecay
PPLN	**P**eriodically **P**oled **L**ithium **N**iobate
PSS	**P**hoto-**S**tationary **S**tate
PVDZ	**P**olarized **V**alence **D**ouble **Z**eta
RBS	**R**ibosomal **B**inding **S**ite
RNA	**R**ibo**N**ucleic **A**cid
RP-HPLC	**R**eversed-**P**hase **H**igh-**P**erformance **L**iquid **C**hromatography
RT-PCR	**R**everse **T**ranscription **P**olymerase **C**hain **R**eaction
SCF	**S**elf-**C**onsistent **F**ield
SD	**S**hine-**D**algarno
SDS	**S**odium **D**odecyl **S**ulfate
SELEX	**S**ystematic **E**volution of **L**igands by **EX**ponential enrichment
SF	**S**elf-**F**ocusing
SPC	**S**imple **P**oint **C**harge models
SPM	**S**elf-**P**hase **M**odulation
STO	**S**later-**T**ype **O**rbital
TD	**T**ime-**D**ependent
TIP3P	**T**ransferable **I**ntermolecular **P**otential with **3** **P**oints
tRNA	**T**ransfer **R**ibo**N**ucleic **A**cid
UFF	**U**niversal **F**orce **F**ield
UTR	**U**n**T**ranslated **R**egion
UV	**U**ltra**V**iolet
vis	**VIS**ible
VWN	**V**osko, **W**ilk, **N**usair
XPM	**C**ross-**P**hase **M**odulation

Eidesstattliche Erklärung

Ich, Sabrina Steinwand, erkläre an Eides statt, dass ich die bei der promotionsführenden Fakultät der Johann Wolfgang Goethe-Universität zur Promotionsprüfung vorgelegte Arbeit mit dem Titel:

„Conformational control of organic molecules by azobenzene-based photoswitches – a spectroscopic study“

im Institut für Physikalische und Theoretische Chemie unter der Anleitung und Betreuung durch Prof. Dr. Josef Wachtveitl ohne sonstige Hilfe erstellt und bei der Abfassung nur die angegebenen Hilfsmittel benutzt habe.

- Ich habe keine Organisation eingeschaltet, die gegen Entgelt Betreuerinnen und Betreuer für die Anfertigung von Dissertationen sucht, oder die mir obliegenden Pflichten hinsichtlich der Prüfungsleistungen für mich ganz oder teilweise erledigt.
- Ich habe die Dissertation in dieser oder ähnlicher Form in keinem anderen Prüfungsverfahren als Prüfungsleistung vorgelegt.
- Ich habe den angestrebten Doktorgrad noch nicht erworben und bin nicht in einem früheren Promotionsverfahren für den angestrebten Doktorgrad endgültig gescheitert.

Die öffentlich zugängliche Promotionsordnung der Johann Wolfgang Goethe-Universität ist mir bekannt, insbesondere habe ich die Bedeutung von § 15 (Aberkennung des Doktorgrades) zur Kenntnis genommen. Ich bin mir der Konsequenzen einer falschen Eidesstattlichen Erklärung bewusst.

Frankfurt, den _____ _____

Unterschrift

Scientific Contributions

Publications within the Context of this Thesis

- S. Steinwand, Z. Yu, S. Hecht, and J. Wachtveitl, "*Ultrafast Dynamics of Photoisomerization and Subsequent Unfolding of an Oligoazobenzene Foldamer*", J. Am. Chem. Soc. **2016**, *accepted*, **DOI**: 10.1021/jacs.6b07720

- S. Steinwand, T. Halbritter, D. Rastädter, J.-M. Ortiz-Sánchez, I. Burghardt, A. Heckel, and J. Wachtveitl, "*Ultrafast spectroscopy of hydroxy-substituted azobenzenes in water*", Chem. Eur. J. **2015**, 21, 15720-15731

- C. Özçoban*, T. Halbritter*, S. Steinwand*, L.-M.Herzig, J. Kohl-Landgraf, N. Askari, F. Groher, B. Fuertig, C. Richter, H. Schwalbe, B. Suess, J. Wachtveitl, and A. Heckel, "*Water-Soluble Py-BIPS Spiropyrans as Photoswitches for Biological Applications*", Org. Lett. **2015**, 17, 1517-1520

- T. Goldau, K. Murayama, C. Brieke, S. Steinwand, P. Mondal, M. Biswas, I. Burghardt, J. Wachtveitl, H. Asanuma, and A. Heckel, "*Reversible photoswitching of RNA hybridization at room temperature with an azobenzene C-nucleoside*", Chem. Eur. J. **2014**, 21, 2845-2854

Other Publications

- A. T. Messmer, S. Steinwand, K. M. Lippert, P. R. Schreiner, and J. Bredenbeck, "*Ultrafast two-dimensional infrared spectroscopy resolves the conformational change of an Evans auxiliary induced by $Mg(ClO_4)_2$*", J. Org. Chem. **2012**, 77, 11091-11095

- A. T. Messmer, K. M. Lippert, S. Steinwand, E.-B. W. Lerch, K. Hof, D. Ley, D. Gerbig, H. Hausmann, P. R. Schreiner, and J. Bredenbeck "*Two-Dimensional Infrared Spectroscopy Reveals the Structure of an Evans Auxiliary Derivative and Its $SnCl_4$ Lewis Acid Complex*", Chem. Eur. J. **2012**, 18, 14989-14995

Oral Contributions to Conferences

- "*Azobenzenes as Ligands for Riboswitches*", Sommerschule **2014**, Lyon/Frankreich

Poster Contributions to Conferences

- "*In-vitro Selection of RNA Aptamers against Photoswitchable Molecules*", Symposium on Selective Regulation in Nanoscaled Systems **2013**, Kloster Banz/Deutschland
- "*Azobenzene-based photoswitchable OmPE-foldamer: Conformational changes due to photoisomerization*", International Symposium on Photochromism **2013** (ISOP 13), Berlin/Deutschland
- "*Conformational change of azobenzene-based photoswitchable OmPE-foldamer due to photoisomerization*", Conference on time-resolved vibrational spectroscopy **2013** (TRVS 2013), Beppu, Oita/Japan
- "*Time-resolved UV/vis-spectroscopic studies on isomerization dynamics of photoswitchable foldamers*", XXIVth IUPAC Symposium on Photochemistry **2012**, Coimbra/Portugal

Oral Presentations

- Internal group seminar **2016**
- Annual seminar of the Institute of Physical and Theoretical Chemistry, Goethe University, Hirschegg/Austria, **2015**
- Internal group seminar **2015**
- Internal group seminar **2014**
- Internal group seminar **2013**
- Internal group seminar **2012**